OBSERVATIONAL ANALYSIS OF THE PHYSICAL CONDITIONS IN GALACTIC AND EXTRAGALACTIC ACTIVE STAR FORMING REGIONS

LARS EGSTRØM KRISTENSEN

LERMA   LAMAP

OBSERVATOIRE DE PARIS-MEUDON   UNIVERSITÉ DE CERGY-PONTOISE

Laboratoire d'Étude du Rayonnement et de la Matière en Astrophysique

RAPPORTEURS:	MR. M. WALMSLEY	INAF, FIRENZE
	MR. F. BOULANGER	IAS, ORSAY
EXAMINATEURS:	MR. D. NEUFELD	JOHNS HOPKINS, BALTIMORE
	MME. B. NISINI	OAR, ROMA
	MR. D. ROUAN	LESIA, PARIS
INVITÉS:	MR. D. FIELD	IFA, ÅRHUS
	MR. G. PINEAU DES FORÊTS	IAS, ORSAY & LERMA, PARIS
DIRECTEUR DE THÈSE:	MR. J.-L. LEMAIRE	LERMA, PARIS/CERGY

Abstract

English

In my thesis observations of near-infrared rovibrational H_2 emission in active star-forming regions are presented and analysed. The main subject of this work concerns mainly new observations of the Orion Molecular Cloud (OMC1) and particularly the BN-KL region. The data consist of images of individual H_2 lines with high spatial resolution obtained both at the Canada-France-Hawaii Telescope and the ESO Very Large Telescope (VLT). With the high spatial resolution of the VLT it is possible to analyse in detail (down to 60 AU $\sim 0\farcs13$) individual objects in the region. I have also analysed H_2 and [FeII] emission from outflows in two dark clouds (Bok globules BHR71 and BHR137) and a high excitation blob in the Magellanic Clouds (N159-5). In the latter, data consist of long-slit spectra obtained at the ESO-VLT.

In order to facilitate this work I ran a large grid of $\sim$25 000 shock models, producing almost 400 Gb of results. These models are state-of-the-art and there is a large number of free parameters which can be adjusted. A large part of my project has been to analyse the results from this grid and make it publically available. Furthermore, as it turned out, not all results are equally reliable and I have had to develop methods for checking the consistency of the wealth of results obtained. But with the model results and a sound knowledge of shock physics it is now relatively straightforward to interpret the H_2 and [FeII] data.

The models allow me to predict the large-scale physical conditions in OMC1 such as density, shock velocities, magnetic field strengths, etc. Overall the preshock density is of the order of $\sim 10^5$-10^7 cm^{-3} and shock velocities are in the interval 10-40 km s^{-1}. Another very interesting result is a new method developed for analysing bow shocks observed at high spatial resolution. For one isolated bow shock in OMC1 I predict a shock velocity of 50 km s^{-1} and a preshock density of the order of 5×10^5 cm^{-3}. The 3D velocity has recently been measured to 55 km s^{-1} providing an independent check on our results.

Français

Je présente et j'analyse dans ma thèse des observations de l'émission dans l'infrarouge proche de transitions rovibrationelles de H_2 dans des régions de formation stellaire. Le sujet principal de ce travail concerne de nouvelles observations du nuage moléculaire d'Orion (OMC1) et en particulier de la région BN-KL. Les données sont constituées d'images des raies individuelles de H_2 obtenues à haute résolution spatiale avec le Telescope Canada-France-Hawaii et avec l'ESO VLT. Grâce à la haute résolution spatiale du VLT il est possible d'analyser en détail (jusq'à 60 UA $\sim0''.13$) des objets individuels dans cette région. De plus, j'ai analysé l'émission de H_2 et [FeII] dans des écoulements (« outflows ») présents dans deux nuages sombres (les globules de Bok BHR71 et BHR137) ainsi que dans un « blob » à haute excitation dans le grand nuage de Magellan (N159-5). Ici les données sont constituées de spectres en fente longue obtenus à l'ESO-VLT.

Pour réaliser ce travail j'ai tout d'abord calculé une grille complète de modèles de chocs composée de $\sim25\,000$ simulations (correspondant à 400 Go, environ). Ces modèles qui sont les plus récents comportent un grand nombre de paramètres libres qui peuvent être ajustés. Une grande partie de mon travail a été d'analyser les résultats de cette grille avant de les mettre en ligne. En effet les résultats ne sont pas tous crédibles, et il m'a donc fallu de développer des méthodes pour les vérifier. Mais avec une bonne compréhension du modèle et un solide sens de la physique des chocs, il est maintenant assez facile d'interpréter les données sur H_2 et [FeII].

Les modèles me permettent ensuite de prédire les conditions physiques à grande échelle dans OMC1, par exemple la densité, la vitesse des chocs, l'intensité du champ magnétique, etc. En général la densité du milieu avant le choc est $\sim10^5$-10^7 cm^{-3} et la vitesse de choc est dans la gamme 10-40 km.s^{-1}. Un autre résultat très interessant de mon travail est le développement d'une nouvelle méthode pour analyser les chocs en arc (« bow shocks ») observés à une haute résolution spatiale. Pour un choc en arc isolé je prédis une vitesse de choc de ~50 km.s^{-1} et une densité avant le choc de 5×10^5 cm^{-3}. La vitesse 3D a été mesurée très récemment à 55 km.s^{-1}. Cela donne une confirmation indépendante de nos résultats.

Publications

Refereed publications (see also Appendix D):

I "Excitation conditions in the Orion Molecular Cloud obtained from observations of ortho- and para-lines of H_2", **L.E. Kristensen**, T.L. Ravkilde, D. Field, J.-L. Lemaire, G. Pineau des Forêts 2007, *A&A*, 469, 561

II "Observational 2D model of H_2 emission from bow shocks in the Orion Molecular Cloud", **L.E. Kristensen**, T.L. Ravkilde, G. Pineau des Forêts, S. Cabrit, D. Field, J.-L. Lemaire, M. Gustafsson, submitted to *A&A*

III "VLT/NACO near-infrared imaging and spectroscopy of N159-5 in the LMC HII complex N159", G. Testor, J.L. Lemaire, **L.E. Kristensen**, D. Field, S. Diana 2007, *A&A*, 469, 459

IV "Model predictions of shock excited gas in the interstellar medium", **L.E. Kristensen**, G. Pineau des Forêts, S. Cabrit, D. Field & J.-L. Lemaire, in final stages of preparation

- "3D modeling of H_2 emission from bowshocks in the Orion Molecular Cloud", T.L. Ravkilde, **L.E. Kristensen**, S. Cabrit, G. Pineau des Forêts, D. Field and J.-L. Lemaire, in preparation

Proceedings:

- "Excitation Mechanisms in the Orion Molecular Cloud Deduced from H_2 Ortho- and Para-Lines Emission at High Spatial Resolution." at "La sémaine Française d'Astronomie et d'Astrophysique", Strasbourg, France, 2005

- "Model results for shocked gas in active star forming regions", at the Molecules in Space and Laboratory conference, Paris, France, 2007

Contents

Introduction

In this introduction I will go through the basics and the background knowledge needed to understand the work I have been doing as a part of my thesis. This includes a basic review of what is already known about star formation (Sect. 1.1). This review is far from complete, as this is beyond the scope of this thesis. I will then proceed to give a short introduction to the H_2 molecule. This is done in Sect. 1.2. H_2 is basically excited in either shock waves or in photo dissociation regions (PDRs). It is the cooling process which is observed. In Sect. 1.3 I will give an introduction to shocks and PDRs.

I have been spending most of my time analysing and interpreting physical conditions in the Orion Molecular Cloud (OMC1). OMC1 is the nearest active massive star forming region and is therefore considered the archetypical active massive star forming region. A short review will be given of this object in Sect. 1.4. With more than 100 refereed papers published on this complicated object each year (O'Dell 2001) the review is not complete. I will be focusing on the aspects of OMC1 which are relevant for our observations.

I have also been working on observations of two regions of isolated star formation, BHR71 and BHR137, two Bok globules located in the southern hemisphere. Both objects show signs of active isolated star formation. None of them have been observed nearly as extensively as OMC1, so a more complete review will be given in Sect. 1.5.

Furthermore I have been working on observations of a single object in the Large Magellanic Cloud (LMC), N159-5, part of the greater N159 complex. This complex is in turn part of the 30 Doradus star forming complex. I will focus on how star formation in LMC is different from galactic star forming regions. This is done in Sect. 1.6.

1.1   Star Formation

References in this Section are mostly from the proceedings of the Protostars and Planets V conference, held in Waikoloa, Hawaii, October 2005, which I

Table 1.1: Physical properties of interstellar clouds. Size, density, mass and temperature are from Mac Low & Klessen (2004). The Jeans mass is calculated from Eqn. 1.1.1 (Evans 1999).

	Giant molecular cloud complex	Molecular cloud	Star-forming clump	Protostellar core
Size (pc)	10–60	2–20	0.1–20	$\lesssim 0.1$
Density (cm^{-3})	1–5×10^2	10^2–10^4	10^3–10^5	>10^5
Mass ($M_\odot$)	10^4–10^6	10^2–10^4	10–10^3	0.1–10
Temperature (K)	7–15	10–30	10–30	7–15
M_J ($M_\odot$)	15–100	6–300	2–90	1–3

attended. Other references are primarily review articles.

1.1.1 Molecular clouds

Stars form in Molecular Clouds (MCs). MCs span a wide range of masses and sizes from the Giant Molecular Clouds (GMCs) with masses of 10^5–10^6 $M_\odot$ and sizes of 10–60 pc to MCs with masses of 10^2–10^4 $M_\odot$ and sizes 2–20 pc (Mac Low & Klessen 2004). Within MCs there may be denser condensations (typically 10^4–10^6 cm^{-3}) which are called clumps or cores. Table 1.1 lists a range of commonly accepted properties (Mac Low & Klessen 2004).

The Jeans mass is defined as the mass where thermal is equal to the gravitational energy (Jeans 1928). It may be calculated as (Evans 1999):

$$M_J = 18 \, M_\odot \, T_K^{1.5} \, n_{\mathrm{H}}^{-0.5} \,, \tag{1.1.1}$$

where M_J is the Jeans mass, T_K the kinetic temperature and n the total particle density [$n_{\mathrm{H}} \approx 2n(\mathrm{H}_2) + n(\mathrm{He})$]. Interstellar clouds typically have masses greatly exceeding their Jeans mass and they should all undergo gravitational collapse and form stars. This would lead to a star formation rate much higher than the observed (e.g. Scalo 1986).

Something must be slowing down the rate of star formation, that is, something is preventing MCs from collapsing on a global scale. It has been proposed that magnetic fields may support the clouds from collapse as well as supersonic turbulent motion. Observations of CO line profile widths show that turbulence alone is sufficient to support against collapse. However, the exact role of turbulence and the characteristics of turbulence at the star-forming scale is not known (Ballesteros-Paredes et al. 2007).

Star forming objects are typically divided into four classes from 0 to III. Young stellar objects are starting their evolution as class 0 objects and finish their early evolution as class III objects. The classes are characterized in the following way (e.g. André et al. 2000):

Class 0: In a class 0 object the mass of the protostellar envelope is greater than the mass of the protostellar object itself. Accretion occurs directly from the envelope onto the protostar. Class 0 objects show strong molecular outflows.

Class I: The protostar is still accreting from the envelope, but the mass of the envelope is lower than the mass of the protostar. The envelope is beginning to form a protostellar disk. Here we also see strong molecular outflows.

Class II: The remaining parts of the envelope have collapsed into a protostellar disk. There is still accretion onto the protostar from the accretion disk and we still see jets and outflows. It is in this class we find the so-called classical T Tauri stars (CTTSs).

Class III: In this class we find the naked young stars without disks and without accretion. Jets and outflows are not observed from this class. Planets may have formed or be forming at this stage.

1.1.2   Jets and outflows

We will use the following definitions of jets and outflows:

- Jets are visible, they have a high collimation and they are fast. They may be observed in both atomic and molecular lines.

- Outflows consist of swept up ambient material behind jets. They are slower and traced by molecular emission.

Launch mechanism

Star formation is always accompagnied by jets and outflows. This is an observational fact and was not predicted by any early model of star formation. In current theoretical models of star formation where rotation and magnetic fields are included, jets are predicted (e.g. Banerjee & Pudritz 2006). The launch mechanism is connected with the infall of material onto the protostar as well as removal of angular momentum by the magnetic field. As material accretes some of it is ejected centrifugally away from the protostar and then focused by the magnetic

field forming a protostellar jet (Ray et al. 2007). There are a number of theoretical models describing how exactly this launch mechanism works (Pudritz et al. 2007, and references therein), but it is not yet possible to distinguish between different models. To distinguish different models it is necessary to observe the protostellar objects at high spatial and spectral resolution. This is best achieved at optical/near infrared (NIR) wavelengths. However at these wavelengths the central class O/I object is still hidden from view.

For class II objects and especially the classical T Tauri stars (CTTSs), the central object is optically visible. Therefore launch models are usually tested against observations of this type of protostars (Pudritz et al. 2007). Currently the central 100 AU are being probed, but to understand the details of the launch mechanism it is necessary to probe the central few AU (e.g. Dougados et al. 2000; Ray et al. 2007). This is currently not possible, although with the VLT interferometer (VLTI) and the Large Binocular Telescope in Arizona it should be possible in the very near future.

Jet and outflow properties

Jets and outflows are typically very luminous at longer wavelengths, i.e. in the far-infrared and at sub-mm. This often makes them the only signpost of very recent star formation. In general jets and outflows from class 0 objects are brighter in molecular emission than class I objects. This is probably caused by a higher accretion rate in class 0 objects (Richer et al. 2000). The bulk of mm-wavelength CO emission have velocities of the order of a few to ten $\mathrm{km\,s^{-1}}$. However, NIR lines of H_2 and [FeII] show velocities of several tens of $\mathrm{km\,s^{-1}}$. At visual wavelengths observations of forbidden atomic and ionic lines show velocities of tens to hundreds of $\mathrm{km\,s^{-1}}$ (Bally et al. 2007).

Typically outflows are more collimated from class 0 objects. The reason for this is not well understood. Since class 0 objects are still enshrouded in their parental gas, it is probably only the central, high velocity part of the jet that escapes the cloud. As the parental cloud collapses into a protostellar disk, it is easier for the wide angle, low velocity component of the jet to escape and the outflow appears less collimated as shown in Fig. 1.1. Furthermore, at this late stage the jets may be accompagnied by stellar winds. This would also give the result that the outflow is less collimated (Arce & Sargent 2006; Arce et al. 2007). It is currently debated whether the wind component is present at all times, but only becomes visible at later stages, or if the stellar wind becomes active at this late stage.

In general outflows from low-mass protostars are better understood than outflows from high-mass protostars (Arce et al. 2007). This is due to observational facts. As high-mass stars form, their evolution towards the main sequence pro-
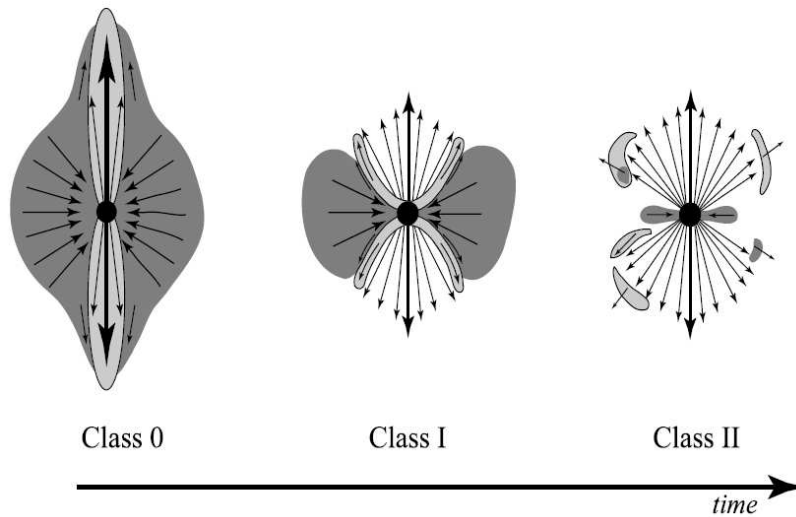
Figure 1.1: Differences between outflows from class 0, I and II sources. In class 0 sources the outflow is very collimated, whereas in class II sources the ouflow resembles a stellar wind. From Arce & Sargent (2006).

ceeds more rapidly than for low-mass stars. Accretion also stops while the star is deeply embedded due to radiation pressure. The closest sites of active massive star formation is located in Orion at a distance of ~450 pc while several sites of low mass star formation are found at ~150 pc. Thus it is difficult to observe young massive protostars because their very early evolution proceeds very rapidly and because they are located far away.

Jets and outflows are not always ejected in a continuous manner. Typically there are several outburst events, where clumps of gas are ejected. In massive O-stars the outflow sometimes appear to be explosive in nature (Arce et al. 2007), as for example in Orion (we return to this below, Sect. 1.4).

The jets and outflows from protostellar objects have a profound influence on their surroundings. They drive shock waves into the ambient medium, which heat the gas. The temperature typically exceeds 1000 K. As the temperature increases, neutral-neutral chemical reactions with relatively high activation energies may occur. This leads to a molecular enrichment of the postshock gas. We return to the effects of shocks in more detail in Sect. 1.3.2. Jets and outflows are also injecting a significant amount of turbulence into the ambient medium, but they are probably not the major source of turbulent motion (Mac Low & Klessen 2004; Arce et al. 2007).

1.1.3   Star formation in associations

Massive O and B stars only form in associations[1]. This is an observational fact, not something proposed by theory. As a MC or GMC collapses, it will break up into smaller fragments, each fragment may go on to form a star. Massive stars are typically located at the centre of MCs (Evans 1999). Currently there are two competing scenarios for the formation of massive stars: either they form in the same way as low mass stars, that is by accreting matter from a protostellar envelope, or they form from several low mass stars which coalesce into a single massive star (Bally & Zinnecker 2005; Beuther et al. 2007).

Elmegreen & Lada (1977) originally proposed that the massive OB stars form first. Outflows and winds from these stars then impact on the surrounding material, and the shock waves compress local density perturbations in the MC leading to a new generation of low mass stars. This is known as triggered star formation. It is also expected to occur in clusters and associations with no massive stars but to a lesser degree.

An important parameter in determining whether triggered star formation is efficient, is the shock velocity. For shock velocities greater than $\sim$50 km s^{-1}, shock waves disperse clumps (Briceño et al. 2007). Shock velocities below 15 km s^{-1} only cause slight temporary compression of cloud cores, so in order for this mechanism to be efficient, shocks should have a velocity in the range of $\sim$15–50 km s^{-1} (Briceño et al. 2007). Several examples of triggered star formation have been discovered (Arce et al. 2007) including the Orion OB association (see below, Sect. 1.4 and Vannier et al. 2001).

Besides driving strong stellar winds and outflows, massive stars will also ionize their surroundings. Ionization fronts are also driving shock waves into the MC with a typical velocity of $\sim$10–15 km s^{-1} (Elitzur & de Jong 1978). The strong far-UV radiation fields of massive O and B-stars also powers photo dissociation regions (PDRs). We return to PDRs below in Sect. 1.3.3.

The closest active massive star forming region is the Orion Molecular Cloud (OMC1). The distance is $\sim$500 pc. I will return to OMC1 in Sect. 1.4 and Chapters 3–5.

1.1.4   Isolated star formation

Isolated star formation is much better understood than clustered star formation. Part of this is because in clusters it can be difficult to disentangle the effects caused by numerous high- and low-mass protostellar objects. Also the closest sites of isolated star formation are much closer to Earth ($\sim$150 pc; Taurus,

---

[1]We here reserve the term cluster for a gravitationally bound collection of stars, while associations are groups of stars, but not necessarily gravitationally bound.

Chaemeleon and ρ Oph), meaning that it is possible to observe physical and chemical processes in greater detail.

In general the mass and column density of isolated cores is lower for isolated protostellar and prestellar objects than cluster objects (e.g. Jijina et al. 1999). This could imply that the formation mechanism is different for cores in isolated and clustered regions, with the latter formed by fragmentation of higher-mass, more turbulent cores (Ward-Thompson et al. 2007). However, more observations are required to quantify this.

1.2   H$_2$ Molecule

The hydrogen molecule, H$_2$ is the most abundant molecule in the Universe. Since it is a homonuclear molecule it posseses no permanent dipole moment and rovibrational transitions are forbidden electric quadrupole transitions. This implies that the lifetime of H$_2$ in rovibrationally excited states is high, typically of the order of a year (Wolniewicz et al. 1998). Even though heteronuclear excited molecules have much shorter lifetimes, they are at least four orders of magnitude less abundant. Therefore H$_2$ remains one of the most observed molecules.

1.2.1   Rovibrational transitions

In this thesis we are only considering rovibrational transitions in the electronic ground state of H$_2$, X^1 Σ_g^+. For rovibrational transitions we have the following selection rule for the rotational quantum number, J: ΔJ=0,±2. There are no selection rules for vibrational quantum numbers, v. The nomenclature for the rotational selection rules is as follows

$$\Delta J = \left\{ \begin{array}{ll} -2 & \text{S-branch} \\ 0 & \text{Q-branch} \\ +2 & \text{O-branch} \end{array} \right.$$

Rovibrational transitions are located in the near- and mid-infrared (NIR and MIR, respectively) part of the spectrum. A transition is denoted by first writing the vibrational transition followed by the relevant branch and the lower rotational level. Thus the transition from v=1 to v=0, J=3 to J=1 is written v=1-0 S(1). In this thesis the main focus is put on the three rovibrational transitions v=1-0 S(0), v=1-0 S(1) and v=2-1 S(1). In Table 1.2 some properties of these transitions are given.

Because the molecule is light, the energy levels are widely spaced. For example the v=0, J=1 level has an energy of 170 K. The energy difference between

Table 1.2: Properties of the three rovibrational transitions, v=1-0 S(0), v=1-0 S(1) and v=2-1 S(1). Here I list the energy of the upper level (E_u), the wavelength in air and the frequency in vacuum (Black & van Dishoeck 1987), degeneracy and Einstein A coefficient (Wolniewicz et al. 1998).

	v=1-0 S(0)	v=1-0 S(1)	v=2-1 S(1)
E_u/k_B (K)	6474	6947	12551
λ (μm)	2.22268	2.12125	2.2471
ν (cm^{-1})	4497.84	4712.91	4448.96
$g_I g_J$	5	21	21
A (10^{-7} s^{-1})	2.53	3.47	4.98

the v=0, J=2 and J=0 levels is 510 K, which corresponds to the lowest rovibrational transition, v=0-0 S(0) at 28 μm. As we will see below, this implies that a high kinetic temperature is required to collisionally excite H_2.

1.2.2   Excited H_2

Consider a gas consisting of H_2 molecules. We assume that the gas is in local thermodynamic equilibrium (LTE). This implies that the level population distribution is a Boltzmann distribution and that for a given level i, the population is

$$n_i \propto g_I g_J \exp\left(-\frac{E_i}{k_B T}\right) , \qquad (1.2.1)$$

where $g_I g_J$ is the level degeneracy (see below), E_i the energy of the level, k_B the Boltzmann constant and T the temperature. If the populations of two levels are known from observations, it is possible to calculate a corresponding temperature, the excitation temperature, T_{ex}. If the H_2 gas is in LTE, the excitation temperature corresponds to the kinetic temperature. In the interstellar medium this is typically not the case because of the low density.

If we assume that the line is optically thin for a given H_2 line, it is possible to calculate the column density, N from the observed line brightness, I. The probability for spontaneous emission is given by the Einstein A-coefficient. The column density of the upper level is given by:

$$N = \frac{4\pi\lambda}{hc}\frac{I}{A} . \qquad (1.2.2)$$

To estimate whether the assumption that the line is optically thin, we may calculate the optical depth, τ, for a transition between an upper and lower level:

$$\tau = \frac{A}{8\pi} \frac{1}{v} \frac{g_u}{g_l} \lambda^3 N \, , \qquad (1.2.3)$$

where v is the line width and $g_{u,l}$ is the degeneracy of the upper and lower level. For the v=1-0 S(1) transition we find

$$\tau = 3.07 \times 10^{-24} \frac{N[\mathrm{H}_2\,(\mathrm{cm}^{-2})]}{v\,(\mathrm{km\,s}^{-1})} \, . \qquad (1.2.4)$$

In OMC1 the total H$_2$ column density is of the order of 10^{22} cm^{-2} (e.g. Masson et al. 1987; Genzel & Stutzki 1989; Rosenthal et al. 2000) and v=1-0 S(1) linewidths are of the order of ~30 km s^{-1} (e.g. Chrysostomou et al. 1997). The optical depth is ~10^{-3}. Therefore the assumption that the line is optically thin to H$_2$ emission is fulfilled. Typically only dust grains will prevent H$_2$ emission from escaping the gas.

To evaluate the state of the gas, it is often usefull to make a Boltzmann plot or excitation diagram. In such a diagram $\log(N/g_I g_J)$ is plotted versus the upper level energy. If the gas is in LTE the points will lie on a straight line with a slope of $-1/T$ according to Eqn. 1.2.1. If the gas is not in LTE, the points will typically lie on a curve and display a range of excitation temperatures.

1.2.3 Ortho/para ratio

H$_2$ is a diatomic, homonuclear molecule, and as such the total nuclear spin will be either I=0 or 1 corresponding to the nuclear spins being anti-parallel or parallel, respectively. The degeneracy caused by the nuclear spin is given by g_I=2I+1 and is thus either 1 or 3. The rotational degeneracy is g_J=2J+1. The total wavefunction of the molecule must be anti-symmetric which means that if the nuclear spins are anti-parallel the rotational quantum number must be even and vice versa. These two states are known as para-H$_2$ and ortho-H$_2$ respectively. For any H$_2$ molecule it is only possible to change the rotational quantum number, J, by 0 or $\pm$2, so if a H$_2$ molecule is in the para-state, it will remain there, unless it exchanges a proton with another species (e.g. H, H$^+$, H$_3^+$; see below). The same is true for ortho-H$_2$.

If the gas is in local spin equilibrium (LSE) the ortho/para ratio is given by

$$\begin{aligned} ortho/para(\mathrm{LSE}) = \frac{N_{\mathrm{ortho}}}{N_{\mathrm{para}}} &= \frac{\sum_{J\,\mathrm{odd}} g_I g_J \exp\left(\frac{-E_J}{k_\mathrm{B}T}\right)}{\sum_{J\,\mathrm{even}} g_I g_J \exp\left(\frac{-E_J}{k_\mathrm{B}T}\right)} \\[2mm] &= \frac{\sum_{J\,\mathrm{odd}} 3\,g_J \exp\left(\frac{-E_J}{k_\mathrm{B}T}\right)}{\sum_{J\,\mathrm{even}} g_J \exp\left(\frac{-E_J}{k_\mathrm{B}T}\right)} \, . \qquad (1.2.5) \end{aligned}$$
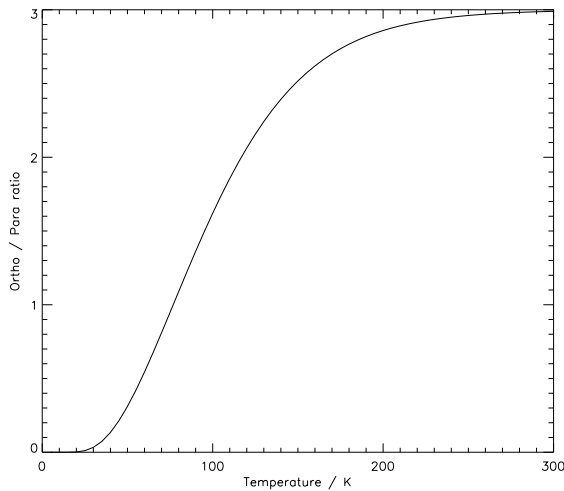
Figure 1.2: LSE ortho/para ratio as a function of kinetic temperature. For temperatures greater than ~300 K the ortho/para ratio is 3, while it is ~0 for temperatures lower than 20 K.

In the high temperature limit the LSE ortho/para ratio is equal to 3. This is illustrated in Fig. 1.2 where it may be seen that for temperatures greater than ~300 K the ortho/para ratio is equal to 3. As it is possible to determine an excitation temperature observationally, so it is also possible to determine an ortho/para ratio observationally by using a Boltzmann diagram. If the ortho/para ratio is different from 3, the high temperature LSE value, ortho-points will be displaced with respect to their para-counterparts. The amplitude of the displacement will give the ortho/para ratio. If the displacement is independent of the level, then the measured ortho/para ratio will be equal to the total ortho/para ratio. In general this is not the case in the interstellar medium.

In this case it is necessary to evaluate the ortho/para ratio for each level. For a given level, (v,J), this is done by first calculating the excitation temperature from the levels (v,$J-1$) and (v,$J+1$). This temperature is then inserted into Eqn. 1.2.5 and the ortho/para ratio is calculated (Wilgenbus et al. 2000).

It is only possible to change the ortho/para ratio through reactive collisions involving proton exchange reactions. According to Schofield (1967) the exchange reaction between H_2 and H shows an activation energy of ~3900 K and is therefore insignificant in the cold interstellar medium. In a cold dark cloud, only slow exchange reactions with H^+, H_3^+ and other protonated species will occur (Flower et al. 2006). In a cold dark cloud with $T = 10$ K, density $n_H = 10^5$ cm^{-3}, cosmic ray ionization rate 5×10^{-17} s^{-1} per H atom and an initial degree of ionization of ~10^{-8} it will take more than 10^7 years to go from an ortho/para ratio of 3 to the equilibrium value at 10 K of ~2×10^{-3} as illustrated in Fig. 1.3. The conversion timescale is only weakly dependent on density.

In hot gas it is possible to overcome the activation energy barrier, and ex-
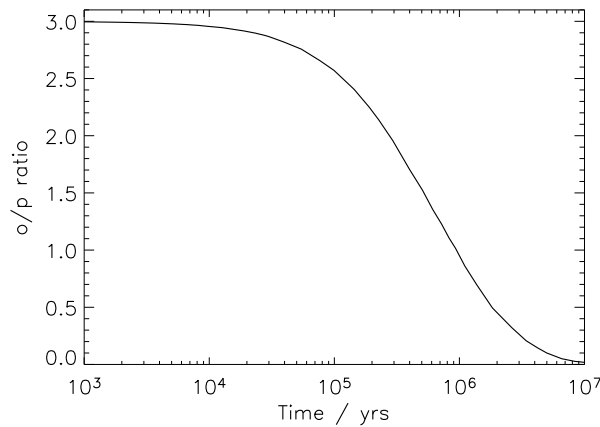
Figure 1.3: Ortho/para ratio as a function of time in a cold dark cloud (Kristensen et al. 2007a). See text for initial conditions.

change reactions with H are the most efficient method for interconversion. In Sect. 2.2.2 we show that this process will become efficient at kinetic temperatures greater than ~800 K.

1.3   H$_2$ excitation mechanisms

It is possible to excite H$_2$ in one of three ways (e.g. Tielens 2005; Habart et al. 2005):

1. Formation excitation, in which a H$_2$ molecule is formed in an excited state

2. Collisional excitation, where the gas is heated, and collisions with other molecules excite H$_2$

3. Radiative excitation, where the gas is subjected to a strong radiation field and H$_2$ molecules are excited by absorbing this radiation

In the following I will briefly go through each of these three mechanisms. Of the three mechanisms I will focus on collisional excitation, as this is the main interest of this thesis.

1.3.1   H$_2$ formation excitation

The binding energy of H$_2$ is ~4.5 eV or ~51 000 K. This binding energy is divided between the grain (internal heating), kinetic energy of the H$_2$ and internal energy in H$_2$ (i.e. the molecule is formed in a rovibrationally excited state). At

the moment several experiments are underway to determine how the binding energy is partitioned among the constituents, and in particular what the internal energy distribution is and what the ortho/para ratio is.

In cold molecular clouds H_2 is formed on the surface of ice-covered dust grains, the ice is primarily composed of H_2O and CO. Experiments have already shown that the formation of H_2 may proceed quite rapidly on ice surfaces (e.g. Manicò et al. 2001; Hornekær et al. 2003; Perets et al. 2005; Amiaud et al. 2007).

In hot regions, such as close to stars or in shocks, the icy mantles covering the dust grains will evaporate. Therefore it is also necessary to perform the experiments on grain surfaces that simulate bare grains, such as silicate and carbonaceous surfaces. This is also currently a work in progress (e.g. Pirronello et al. 1997a,b; Perry & Price 2003; Hornekær et al. 2006).

The energetics of the formation process has been measured by different groups, both on bare grain analogues and ice-covered grain analogues (e.g. Hornekær et al. 2003; Creighan et al. 2006; Amiaud et al. 2007). Very recently the ortho/para ratio of newly formed H_2 has also been measured (Amiaud et al. 2007, F. Dulieu, priv. comm.).

In principle it should be possible to observe the formation excitation directly in cold dark clouds. As mentioned previously, H_2 lines are optically thin under interstellar conditions, so any H_2 emission will escape the gas. Several surveys have been performed of dark clouds, but so far without results (Tiné et al. 2003, and references therein).

1.3.2   Shocks

A shock may be defined as "*any pressure-driven disturbance which is time-independent (in a co-moving reference frame) and which effects an irreversible change in the state of the medium*" (Draine 1980). A more popular definition of a shock is that it is a "*hydrodynamical surprise*" (Chernoff 1987). For a few reviews of shock physics and chemistry I refer the reader to e.g. Draine (1980); McKee & Hollenbach (1980); Chernoff (1987); Hollenbach et al. (1989); Hollenbach & McKee (1989); Draine & McKee (1993); Hartigan (2003).

Rankine-Hugoniot Equations

The Rankine-Hugoniot equations are the fundamental equations describing how physical properties of a medium change across a shock front. The derivation of the equations is made by assuming the shock-front is infinite and plane-parallel. Using the conservation laws for mass (ρ), momentum and energy flux over the shock front it is now possible to derive the following equations (subscript 1 de-

notes the pre-shock zone and 2 the post-shock zone):

$$\rho_1 v_1 = \rho_2 v_2 \tag{1.3.1}$$

$$\rho_1 v_1^2 + p_1 = \rho_2 v_2^2 + p_2 \tag{1.3.2}$$

$$\rho_1 v_1 U_1 + p_1 v_1 + \frac{1}{2}\rho_1 v_1^3 = \rho_2 v_2 U_2 + p_2 v_2 + \frac{1}{2}\rho_2 v_2^3, \tag{1.3.3}$$

where p is the pressure, U is the internal energy of the molecules and v the velocity of the flow in the reference frame of the shock. The first equation (1.3.1) concerns the conservation of mass across the shock front, the second (1.3.2) the conservation of momentum and the third (1.3.3) the conservation of energy.

The above equations are only valid in the absence of a magnetic field. In the presence of a magnetic field the Rankine-Hugoniot equations are somewhat modified (e.g. de Hoffmann & Teller 1950; Draine 1980).

J-Type versus C-Type Shocks

In the absence of a transverse magnetic field neutral particles (atoms, molecules and grains) and charged particles (ions, electrons and grains) all behave in the same way, as a single-fluid medium with the same velocity and temperature. It is impossible for the medium in the preshock zone to receive information about the shock-front, as the shock-front is moving at a supersonic speed. Thus the temperature and density changes over a distance corresponding to the mean free path of the particles. This type of shock is called a jump-type shock (J-type), as the change in temperature and density resembles a discontinuity. In the post-shock zone the medium cools under constant pressure.

Introducing a non-zero transversal magnetic field will separate the constituents into neutral, positively and negatively charged particles and it behaves as a multifluid medium. In a multifluid medium the charged particles couple to the magnetic field and they will gyrate around the magnetic field lines. The neutral particles are not directly affected by the magnetic field, only through collisions with charged particles. Charged dust grains will also couple to the magnetic field.

A mechanical signal can propagate at several distinct velocities: The sound speed, c_s, the Alfvén velocity, v_A and the ion magnetosonic speed, v_{ims}. The sound speed is

$$c_s = \sqrt{\frac{\gamma k_B T}{\mu}}, \tag{1.3.4}$$

where γ is the heat capacity ratio (5/3 for a monatomic gas and 7/3 for a diatomic gas), k_B Boltzmann's constant, T the temperature, μ the mean molecular weight

and m_H the mass of H. c_s is typically less than ~1 km s^{-1} in a cold dark cloud. The Alfvén velocity is given as (Alfven 1950)

$$v_A = \sqrt{\frac{B^2}{4\pi\rho}},\qquad\qquad(1.3.5)$$

where B is the transverse magnetic field strength and ρ the density. In a cold dark cloud it is of the order of a few km s^{-1}. Similarly the ion magnetosonic speed is given as

$$v_{ims} = \sqrt{\frac{B^2}{4\pi\rho_i}},\qquad\qquad(1.3.6)$$

where ρ_i is the ion density. A typical value is ~1000 km s^{-1} in a cold dark cloud.

For small transverse magnetic fields the shock still contains a J-type shock front, because, even though the charged particles react to the magnetic field and form magnetic precursors, the neutral particles will not have time to recouple to the ions before the arrival of the discontinuity. When the magnetic field surpasses a critical value, B$_{crit}$ the neutrals have time to recouple to the ions (Draine 1980).

When the magnetic field strength is greater than B_{crit} the precursor is long enough that the neutrals do not undergo a discontinuity, and the shock is now a continuous (C) type shock. This evolution is illustrated in fig. 1.4, where a J-type shock progresses into a C-type shock as the magnetic field increases. The value of B_{crit} can only be determined analytically for adiabatic shocks.

In a C-type shock the shock velocity must be greater than the Alfvén velocity and the local sound speed. Otherwise information about the arrival of the shock front is directly relayed to the neutrals and the gas will only be pushed, not shocked. In fact in the reference frame of a C-type shock, the gas flow is always supersonic. Information about the shock front can travel faster than the shock through the charged particles if the shock speed is lower than v_{ims}. The information is then relayed to the neutral particles through collisions with the charged particles.

The magnetic field is usually assumed to be frozen into the into the charged particles (Draine 1980). The parametrization of the preshock transverse magnetic field is

$$B_0 = b \times \sqrt{n_H\,(\text{cm}^{-3})}\,\mu\text{Gauss},\qquad\qquad(1.3.7)$$

where n_H is the number density of the ambient medium in units of cm^{-3}, and b is the magnetic scaling factor. In the interstellar medium b is typically 0.1–3 (Draine 1980). This relation has been validated for regions with densities higher than ~10^3 cm^{-3} both through observations (e.g. Troland et al. 1986; Crutcher & Troland 2007; Crutcher 2007) and simulations (e.g. Padoan & Nordlund 1999).

FLOW ⟶

a

V

J – TYPE,
NO PRECURSOR
(V$_s$ > V$_{ims}$

B$_0$ = 0

V$_n$, V$_i$

b

V

J – TYPE,
NO PRECURSOR
(V$_s$ > V$_{ims}$)

L

small B$_0$

V$_i$

V$_n$

c

V

J – TYPE, V$_i$
WITH PRECURSOR
(V$_s$ < V$_{ims}$)

L

moderate B$_0$

V$_n$

d

V

J – TYPE,
WITH PRECURSOR
(V$_s$ < V$_{ims}$)   V$_i$

L

larger B$_0$

V$_n$

e

V

C – TYPE,
(V$_s$ < V$_{ims}$)

L

V$_n$ B$_0$ > B$_{crit}$

V$_i$

POSITION   z
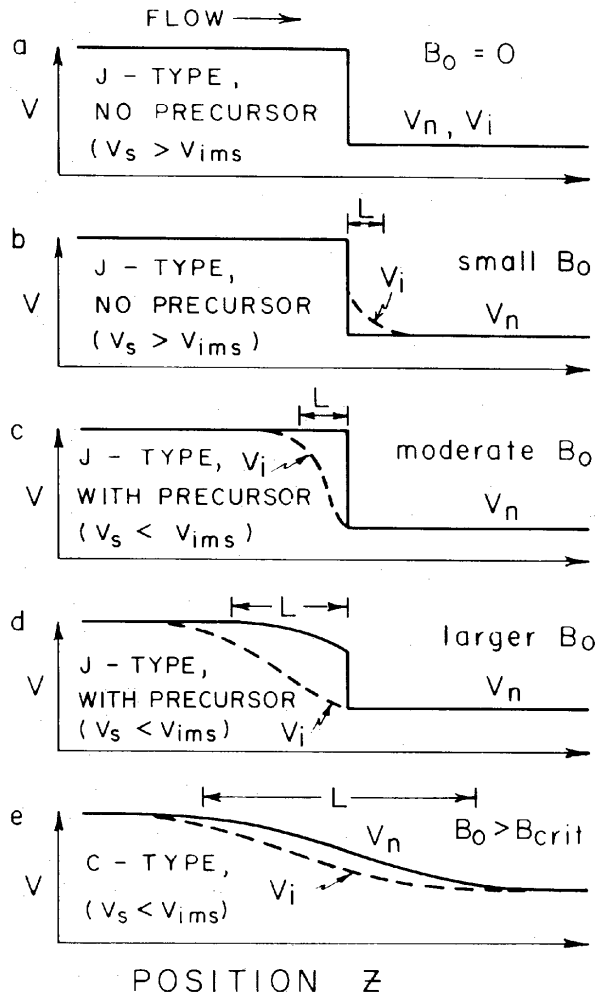
Figure 1.4: Evolution from a J-type shock to a C-type shock by increasing the magnetic field. In the top panel (a) there is no magnetic field, and the shock is a J-type shock. Increasing the magnetic field causes the origin of magnetic precursors, and when the magnetic field is larger than some critical value, the shock is a C-type shock. L is the typical length scale. Velocities are given in the restframe of the shock-front (Draine 1980).

The heating associated with the passing of a shock wave causes excitation and (possibly) dissociation of H$_2$. The main coolant in the wake of a shock is H$_2$. If H$_2$ is dissociated, the gas temperature will increase rapidly because the main coolant is lost. The sound speed increases as $\sqrt{T}$ so the temperature increase leads to an increase in sound speed. However, as the sound speed increases rapidly the gas flow will become subsonic in the reference frame of the shock. The point of transition between super- and subsonic gas flow is known as a sonic point. During such a transition, the C-type shock will collapse into a J-type shock.

H$_2$ rot, low-J CO
[OI]
H$_2$ ro-vibe, high-J CO
CO, H$_2$O vibe, OH
H$_2$O rot.
[SII],
Hα
`cold'        `warm'   `hot'
J-shock
C-shock
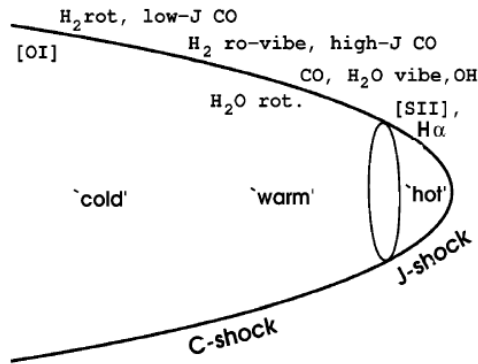
Figure 1.5: Schematic of a bow shock. The bow shock is dissociative at the tip. The locations where radiative coolants make their primary contributions are indicated. From Smith et al. (2003).

Jets, outflows and bow shocks

Shock waves in the interstellar medium are observed through their cooling mechanisms. The origin of these shock waves includes numerous phenomena such as supernova explosions, supersonic turbulent motion (which again may originate in different ways), cloud-cloud collisions, jets and outflows from young stellar objects or from active galactic nuclei. In this thesis I only consider shock waves originating in young stellar objects.

Shock waves may either be created by jets impinging in the ambient material or by bullets which are individual clumps of gas moving at supersonic velocities. In both cases the shock wave will take the shape of a bow as preshock material is being shocked and pushed aside.

At the head of the bow the shock speed will be at a maximum leading to a maximum in temperature. Often, but not always, the shock at the tip of a bow shock will be a dissociative J-type shock. The main coolants are then atomic or ionic, as molecules have been dissociated. Further down the wings the shock velocity will decrease. This leads to a decrease in temperature. In this part of the shock the molecules will not dissociate and they will be the dominants coolants. This is illustrated in Fig. 1.5 and has been observed in a number of objects, e.g. several Herbig-Haro (HH) objects (Bally et al. 2007, and references therein) and the Orion bullets (Allen & Burton 1993).

If the shock wave is generated by a jet, the structure is more complex as illustrated in Fig. 1.6. We here follow the description outlined in Raga & Cabrit (1993). As the jet reaches the ambient medium it is slowed down. However as material from the jet is continuously flowing from behind the shock surface at a velocity v_s, this creates an internal working surface (also known as the Mach disk) where the jet is pushing from behind and the ambient material is pushing from the front. The trapped material is ejected sideways and interacts with the ambient gas. The ejected material will form a bow shock on the outside and a jet-shock on the inside. In between the two is a mixing layer consisting of
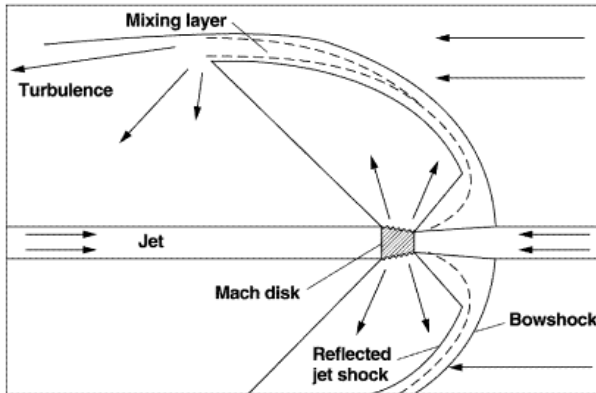
Figure 1.6: Detailed view of the internal shock structures in a bow shock as seen from the reference frame of the internal working surface (Mach disk). The jet and ambient material are both impinging on the Mach disk in the reference frame of the shock. From Hollenbach (1997).

a mixture of the jet material and the ambient gas. The mixing layer expands and fills the cavity created by the bow shock.

Shock velocity

Observationally, it is often difficult to measure the shock velocity. While it is relatively straightforward to measure the velocity of an object, v_{obj}, through radial velocity and proper motion studies, this is typically not the shock velocity, v_s. If the preshock medium is moving at a certain velocity, v_{pre} with respect to the shock wave, the shock velocity is given as $v_s = v_{obj} - v_{pre}$.

This has been observed with knots of excitation in protostellar jets, where the preshock gas has been swept up by previous shocks, and is then being overrun by new shock waves (e.g. Arce & Goodman 2002). It has also been observed in large scale outflows, where an initial outflow accelerates the surrounding gas. Outflow events following the initial one will then encounter the postshock gas of the first shock wave, and the shock velocity is lower than the observed velocity of the shock wave. this has been observed in planetary nebulae (e.g. NGC 7027; Latter et al. 2000) and regions of massive star formation (e.g. OMC1; Stone et al. 1995, and see below, Sect. 1.4).

Models

Some of the first shock models created were published in 1977 (Hollenbach & Shull 1977; Kwan 1977; London et al. 1977). These were all planar J-type shock models. Later Draine (1980) introduced C-type shocks and provided the first planar C-type shock model (Draine & Roberge 1982; Draine et al. 1983). Over the years several groups have published planar shock models, but a general review is considered beyond the scope of this thesis. The shock model used in

this work was first described in Flower et al. (1985) and most recently in Flower et al. (2003) and Flower & Pineau des Forêts (2003).

What is common for these models is that they model a 1D plane-parallel shock front impinging on a preshock medium. In the model the MHD equations are integrated and typically the chemistry is rather extended with at least several tens of different chemical species linked by hundreds of reactions. Because the models are 1D, it possible to calculate the models self-consistently (see Chapter 2 for details).

It is also possible to put more emphasis on the 2D or 3D geometry rather than the detailed physical and chemical modelling. Usually the chemistry is rudimentary at best. For examples of this type of model, see e.g. Smith et al. (2003); Raga et al. (2002); Smith & Brand (1990) for 3D models or e.g. Raga & Cabrit (1993); Lee et al. (2001); Ostriker et al. (2001); Lim et al. (2002); Fragile et al. (2005) for 2D models. 1D models have also been combined to produce 2D or 3D models. This has previously been done by e.g. Smith & Brand (1990); Smith et al. (2003). Here we will also construct a 3D model from 1D models, this is the subject of Sect. 2.3.

1.3.3   Photo-Dissociation Regions

Another important excitation mechanism of H_2 in the interstellar medium is found in photodissociation regions or photon dominated regions (PDRs). Here the UV and far UV radiation fields of massive OB stars are strong enough to excite a substantial part the surrounding molecular gas. Close to massive stars the gas is ionized and we find the bright HII regions. As we move away from the star the radiation field weakens and at a certain point H recombination is more effective than ionization. This marks the beginning of the PDR. Moving further away from the star there will be a transition zone where H reforms H_2. Other species are also ionized/ recombined, dissociated/ reformed. The end of the PDR is typically marked by the reformation of O_2 (Hollenbach & Tielens 1999). The structure of a PDR is shown in Fig. 1.7 where some of the important ionization/recombination and dissociation/reformation zones are displayed. Kinetic temperatures in PDRs are lower than in shocks. Typically it is ∼a few hundred K, but it may be as high as 1000 K in very dense regions.

In a PDR H_2 may be excited rovibrationally by first being UV-pumped to an electronically excited state. The excited molecule will then fluoresce back into the ground electronic state, from which it will cascade down through rovibrational transitions (Hollenbach & Tielens 1997). However, in ∼10–15% of the electronic excitations the molecule will dissociate. Because molecules are first electronically excited, (high v, high J) lines are characteristic of PDRs. In shocks

Photodissociation region
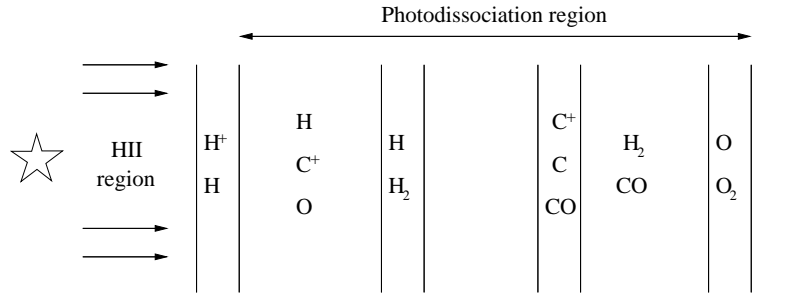
Figure 1.7: Schematic view of a PDR, showing the different zones surrounding an O or B star. Adapted from Hollenbach & Tielens (1999).

very high temperatures are required to collisionally excite H$_2$ to (high v, high J) levels. Typically H$_2$ molecules are dissociated before reaching these levels.

The radiation field of the massive stars is measured either units of the radiation field of the interstellar medium. values are typically quoted in either "Draine-units", χ (Draine 1978) or "Habing-units", G$_0$ (Habing 1968). The Habing-unit has a value of G$_0$=1.6×10^{-6} Wm^{-2} in the range 6 eV $< h\nu <$ 13.6 eV (Habing 1968) whereas the Draine-unit is a spectral distribution between ∼5-13.6 eV.

Models

Recently a meeting was held with the sole purpose of comparing ten PDR codes. The detailed results of the meeting are given in Röllig et al. (2007). In this work, two different models will be used to estimate the brightness observed in PDR zones. The first model is a steady-state, stationary model, the so-called "Meudon PDR code" Le Petit et al. (2006) while the other has been made to model the proplyds observed in Orion (Störzer & Hollenbach 1999).

The "Meudon PDR code" model models a semi-infinite slab of molecular gas illuminated from one side by an intense FUV radiation field. The density throughout the slab is considered to be constant. The model then calculates the level populations for H$_2$ through the PDR, as well as including 491 chemical reactions with 72 species. The model does not consider the motion of the ionization front into the medium or advective heating of the gas. The latter is of importance as shown by Lemaire et al. (1996).

Störzer & Hollenbach (1999) calculates a model where the molecular gas is spherically shaped with varying densities throughout the sphere. The sphere is illuminated from one side by an FUV radiation field. Advection is included in the models as well as mass loss from the sphere due to ionization by the radiation field.

1.4   Orion

The Orion Giant Molecular Cloud (OGMC) is a large complex of molecular clouds covering more than 150 deg^2 on the sky. The largest is the Orion A Molecular Cloud, which itself is a complex of molecular clouds covering 29 deg^2 on the sky (Maddalena et al. 1986). An image of OGMC recorded in CO emission is shown in Fig. 1.8. For a full description of the environment see e.g. Genzel & Stutzki (1989).

One of the components of the Orion A cloud is the visible Orion Nebula (ON; also known as M42+43 and NGC1976). ON is described in a recent review by O'Dell (2001). The ON is an HII region generated by the Trapezium cluster, a group of five O and B-stars, and the Orion Nebula Cluster (ONC). These stars (primarily the Trapezium stars) are forming a blister of ionized hydrogen from OMC1 and that the Trapezium is slowly ionizing more and more material from OMC1, eating into the molecular cloud (Wen & O'Dell 1995). The location of the ionization front with respect to the Trapezium stars is illustrated in Fig. 1.9.

The brightest member of the Trapezium cluster, θ^1Ori C, is an O6 star. θ^1Ori C is located 0.25 pc from the main ionization front (O'Dell 2001). O'Dell et al. (1993) have published images obtained from the Hubble Space Telescope (HST) revealing protoplanetary disks (proplyds) surrounding low mass stars. These proplyds appear as dark silhouettes against the bright background of the HII region. It is believed that the part of the proplyds facing the Trapezium stars are being eaten away by the strong stellar winds and radiation fields emitted by these stars.

ONC is a cluster with ~3500 stars all located within 2.5 pc (~18.′7) of the centre (Hillenbrand 1997). Using Hertzsprung-Russel diagrams it is possible to infer that the age of the cluster is ~ 10^6 yrs (Hillenbrand 1997). ONC is located on top of the greater Orion Molecular Cloud 1 (OMC1), which is a part of the Orion A complex.

Approximately 70″ (~0.16 pc) north of the Trapezium stars is the Becklin-Neugebauer object (BN). It is a B3-star deeply embedded in the molecular cloud (A_V = 17 mag; Gezari et al. 1998), and was first observed in the K-band by Becklin & Neugebauer (1967). Since then it has been observed at almost every wavelength from X-ray to radio (e.g. Garmire et al. 2000; Churchwell et al. 1987). The BN object is located at the heart of the BN-KL nebula, which is located on the surface of OMC1. Below we describe the BN-KL nebula in greater detail.

θ^1Ori C is responsible for forming a PDR in the Orion Nebula. The radiation field of θ^1Ori C near the BN-KL nebula is estimated to be 2–3×10^5 times the Habing field including attenuation by dust (Störzer & Hollenbach 1999). However, the magnitude of the radiation field may be underestimated by an order of
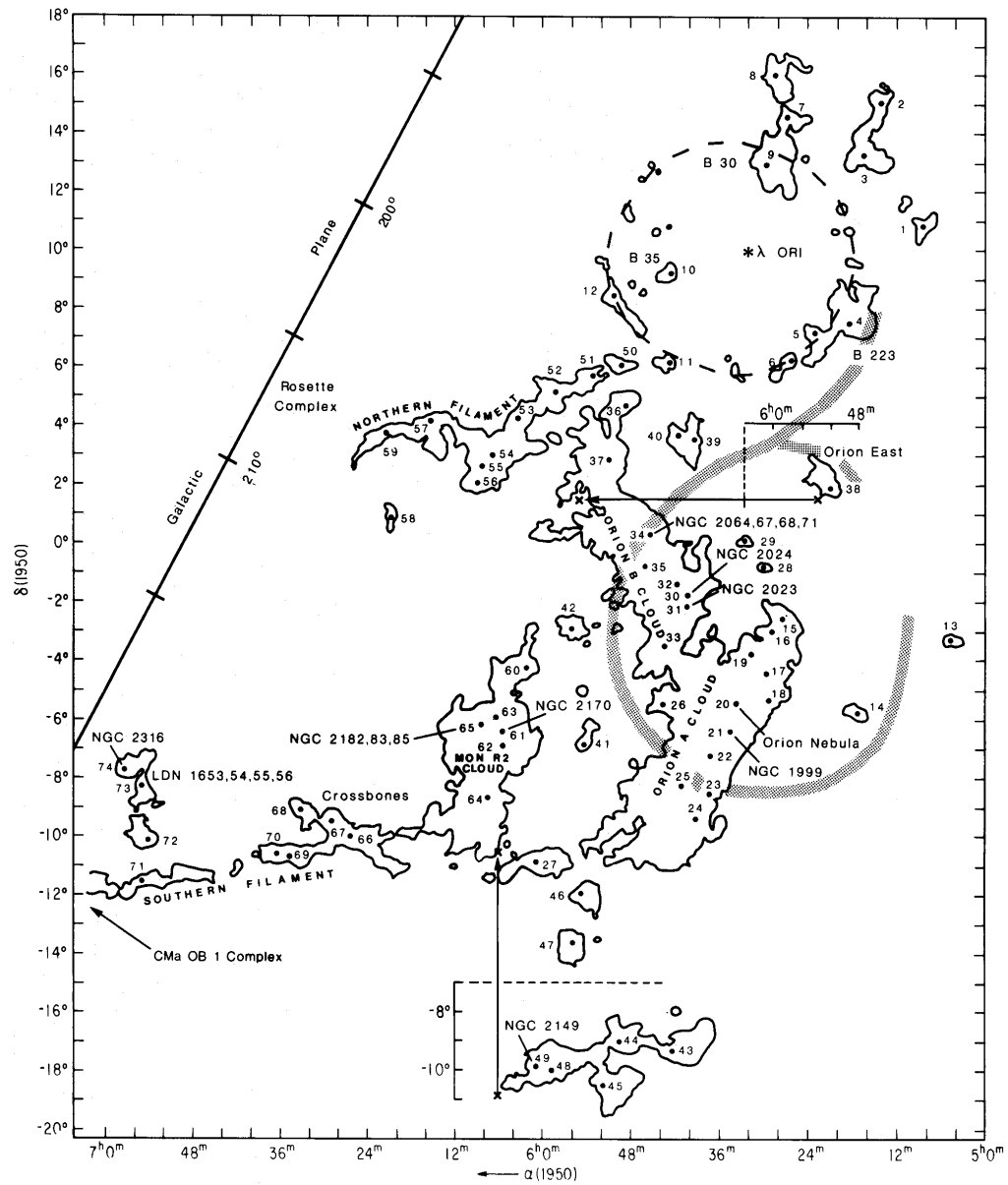
*Figure 1.8: The Giant Orion Molecular Cloud as observed through CO emission.
The Orion Nebula is shown at co-ordinates $-5°\,32'$, 5^h25^m (Maddalena et al.
1986).*
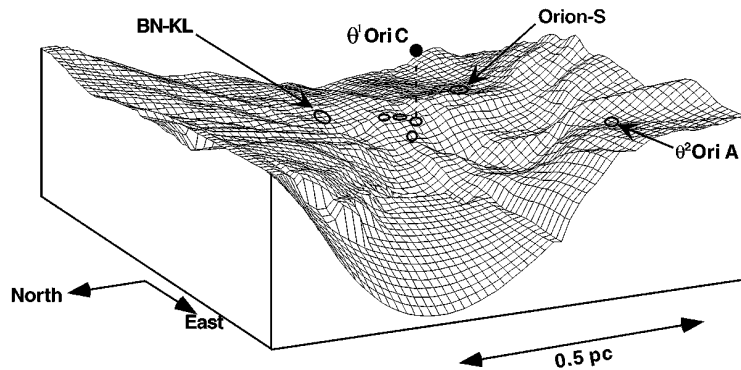
Figure 1.9: Three-dimensional image showing the surface described by the main ionization front on OMC1. θ^1Ori C is located 0.25 pc above the ionization front (O'Dell 2001).

magnitude (Ferland 2001).

1.4.1 Outflows in the BN-KL nebula

The BN object is located at the heart of the infrared KL nebula (Kleinmann & Low 1967). This nebula consists of two butterfly shaped wings that has later been resolved into numerous smaller objects (e.g. Stolovy et al. 1998, and see below). The outflow is shown in Fig. 1.10. Three different types of outflow has so far been connected with the BN-KL nebula. The outflows are schematically shown in Fig. 1.11 and briefly described below.

1. A fast outflow where bullets are moving radially outwards from the centre of the nebula at velocities of several hundred $\mathrm{km\,s^{-1}}$ (e.g. Axon & Taylor 1984; Allen & Burton 1993; Burton 1997; Lee & Burton 2000; Kaifu et al. 2000; Doi et al. 2002). These bullets are primarily located far to the NW of BN-KL, although a few are found SE (Kaifu et al. 2000). At the head of each bullet is a bright cap of [FeII] emission with H_2 emission trailing behind (Allen & Burton 1993). Based on proper motions, the dynamical age has been determined to ~1000 years (Lee & Burton 2000; Doi et al. 2002).

2. A bipolar molecular outflow oriented NW-SE. This outflow was first detected in CO (Kwan & Scoville 1976; Zuckerman et al. 1976) and the outflow speeds are of the order of 30–100 $\mathrm{km\,s^{-1}}$. This is the outflow giving rise to the butterfly shape of the KL-nebula. The outflow is one of the
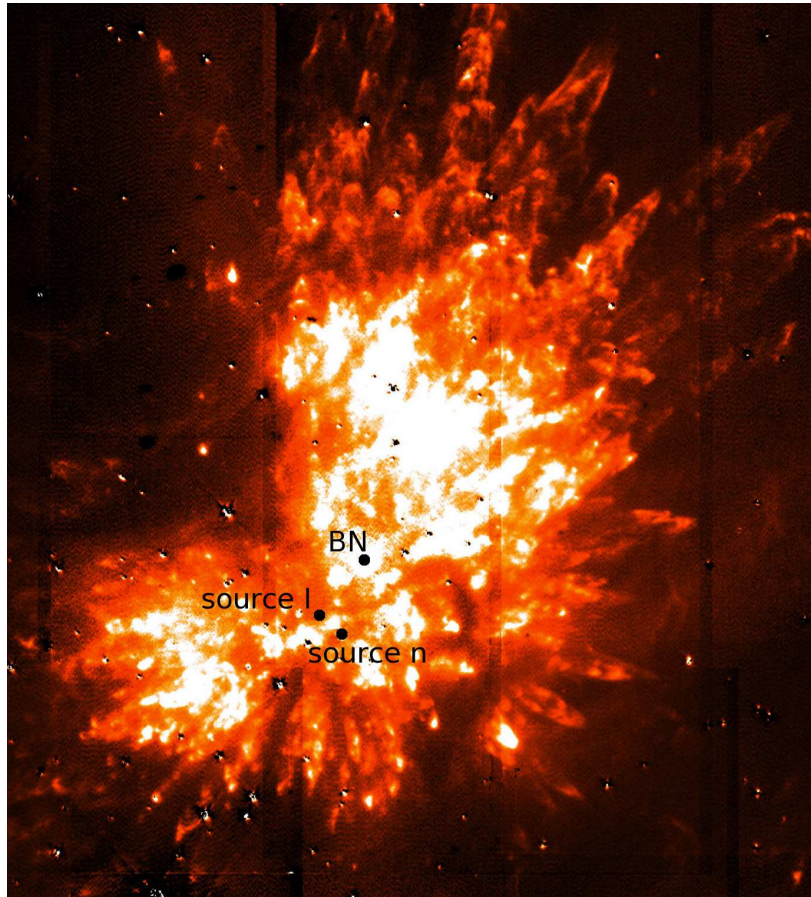
Figure 1.10: Structure of continuum-subtracted H_2 2.12 μm emission in OMC1. The positions of BN, radio source I and radio source n are marked. The image was obtained with the Subaru Telescope.

most luminous H_2 emitting objects in the sky. Recent measurements of the 3D velocity of H_2 clumps show that their velocities are similar to the velocities of the CO outflow. We name the northern wing of H_2 emission Peak 1 and the southern Peak 2 following (Beckwith et al. 1978). The origin of this outflow is possibly similar to the one described above.

3. A slower outflow perpendicular to the previous outflow, first described by Genzel et al. (1981). This outflow is primarily observed in maser emission from H_2O, OH, SiO and methanol masers (e.g. Genzel et al. 1981; Menten & Reid 1995; Greenhill et al. 2004a). The 3D velocities of masers have been measured to be ~18 km s^{-1} (Genzel et al. 1981; Hirota et al. 2007). This outflow has a NIR counterpart as decribed in Chrysostomou
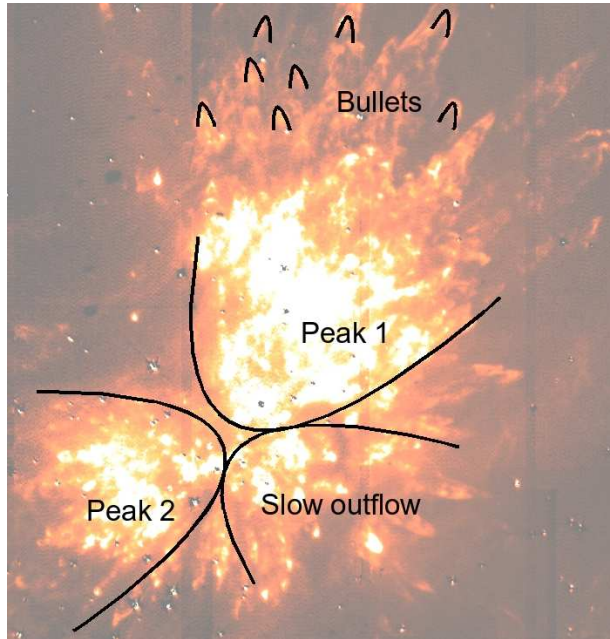
Figure 1.11:   Schematic showing the distinct outflows in the OMC1, BN-KL region. The bullets, the bipolar outflow and the slower outflow are illustrated (see text for descriptions).   The background image shows continuum-subtracted v=1-0 S(1) emission; from the Subaru Telescope.

et al. (1997); Nissen et al. (2007); Lemaire et al. (2007). The SW part is blue-shifted and only this part of the outflow has been detected in the NIR. The NE part is probably deeply buried in the molecular cloud. This outflow is older than the other outflow with a dynamical age of ∼3000 years. Furthermore this outflow is centered on radio sources I and n (Genzel et al. 1981; Johnston et al. 1989; Menten & Reid 1995).

The origin of the outflows is not yet clear. This outflow is unique and no other sites of active massive star formation has shown similar activity, where more than 50 jets or "fingers" have been launched (Schultz et al. 1999). Furthermore the nature of the outflow itself is not clear. Two scenarios have been proposed: In the first the outflow is caused by an explosive event in which all bullets and clumps have been ejected from a central source and it is these objects we are now observing (e.g. Allen & Burton 1993; Doi et al. 2002). In the second scenario the bullets and clumps are caused by shock instabilities in a swept-up shell driven by a large scale stellar wind from a central source (e.g. Stone et al. 1995; McCaughrean & Mac Low 1997). Nissen et al. (2007) propose that at least some of the objects are caused by small protostellar outflows in the region and Gustafsson et al. (2006a) show that some of the emission is caused by a turbulent cascade. According to the authors both of these contributions are small compared to the energetics of the overall outflow.

1.4.2   Central engine

There are several massive stars near the centre of the outflows. First of all there are radio sources I and n. Radio source I is a deeply embedded massive star, so far only observed in radio (Menten & Reid 1995; Greenhill et al. 2004b; Beuther et al. 2005). Radio source n is another massive star, however less massive and less buried in the molecular cloud than source I (Greenhill et al. 2004a,b; Beuther et al. 2004) and observed in the NIR (e.g. Lemaire et al. 2007). Both of these sources show evidence of protostellar disks (Greenhill et al. 2004a,b; Shuping et al. 2004). The disks have position angles of ~135° (Greenhill et al. 2004b; Reid et al. 2007). Both sources are surrounded by a ring of maser emission from H_2O, OH and methanol masers (Genzel et al. 1981; Johnston et al. 1989; Menten & Reid 1995; Greenhill et al. 2004b) and source I is also surrounded by SiO masers (Menten & Reid 1995). The luminosity of source I is $\sim 10^4\ L_\odot$ while it is ~2000 $L_\odot$ for source n (Dougados et al. 1993; Shuping et al. 2004; Greenhill et al. 2004b).

BN is the brightest object at NIR wavelengths, however it contributes little to the overall luminosity. The total luminosity from BN is ~2500 $L_\odot$ (Gezari et al. 1998). It is not as embedded as radio sources I and n and shows no disk-structure. Measurements of the proper motion of BN show that it is possibly an ejected member of the Trapezium cluster (Tan 2004; Rodríguez et al. 2005; Gómez et al. 2005).

The IRc2 complex consists of five bright condensations with a total luminosity of ~1000±500 $L_\odot$ (Dougados et al. 1993; Shuping et al. 2004). It is not clear whether all condensations are indeed protostars or if they are externally illuminated by for example source I. Recent observations show that the latter is probably the case for at least some of the condensations (Shuping et al. 2004).

Some 500 years ago three of the massive stars, BN, radio source I and radio source n, were located within ~2″ (~900 AU) of each other (Tan 2004; Rodríguez et al. 2005; Gómez et al. 2005). If one or more of the massive stars were still accreting mass, then the proximity of other massive stars could disrupt the process and launch an explosive event such as the observed fast bipolar outflow (Bally et al. 2005). This does not explain the slower outflow connected with maser emission. Nissen et al. (2007) argue that the slower outflow could be caused by either source I or n, but that the most likely candidate is source I due to its higher luminosity.

1.4.3   Observations of H_2 emission in OMC1

As mentioned above, OMC1 is one of the best studied regions of the sky and there are more than ~100 refereed papers published each year on this object

(~4500 papers between 1977 and now). To give a complete review of OMC1 is beyond the scope of this thesis. Instead I will focus on observations and analysis of the hert of OMC1 based on NIR observations, primarily in the *K*-band. That is, I ignore the emission created by the famous H_2 bullets north of BN. I will begin by giving a very brief historical introduction before presenting the status today.

Historical introduction

OMC1 has been observed in the NIR ever since the first discovery of rovibrationally excited H_2 here (Gautier et al. 1976). At first it was proposed that H_2 was radiatively excited (i.e. in a PDR Black & Dalgarno 1976). In 1977 several models of shocked gas were published (Hollenbach & Shull 1977; Kwan 1977; London et al. 1977). At this point only J-type shocks were considered. The following year, Beckwith et al. (1978) measured the excitation temperature in OMC1 to be ~2000 K and soon after the v=1-0 S(1) line width was observed to be greater than 100 $km\,s^{-1}$ (Nadeau & Geballe 1979; Nadeau et al. 1982; Brand et al. 1989a). This linewidth was interpreted as originating from bulk motion rather than turbulent motion (e.g. Nadeau & Geballe 1979), thus providing evidence that the H_2 emission was generated by shocks rather than in a PDR. However, a major problem with this interpretation was, that H_2 is dissociated at velocities greater than 24 $km\,s^{-1}$ (Kwan 1977).

In a very important paper (Draine 1980) proposes that the magnetic field could help in softening the shock, and he thereby introduced C-type shock waves. This was later expanded in Draine et al. (1983). At the time the models provided reasonable fits to the observed H_2 emission (Chernoff et al. 1982; Draine & Roberge 1982).

However, observations made by Brand and his group of Peak 1 north of BN seemed to rule out planar C-type shocks. These observations include spectra showing rovibrational H_2 transitions in the *K*-band (Brand et al. 1988), emission from the 0-0 S(13) and v=1-0 O(7) lines (Brand et al. 1989b), emission from the v=3 and v=4 lines (Moorhouse et al. 1990) and emission from the v=0-0 S(1) line (Burton 1997). More interestingly, the observations reported in Brand et al. (1989b); Burton (1997) also seem to rule out planar J-type shocks. They conclude that C-type bow shocks are responsible for the emission (Smith et al. 1991a,b). C-type bow shocks would also be able to explain the observed linewidth of the v=1-0 S(1) line. But even with a C-type bow shock, it would require an unusually high transverse magnetic field strength of the order of 10 mGauss (Smith et al. 1991a,b).

More recently Rosenthal et al. (2000) observed OMC1 with the ISO-satellite. They observed 56 pure rotational and rovibrational H_2 lines. Le Bourlot et al.

(2002) found that it was possible to reproduce the observations with a two-component planar C-type shock model.

The common trait for most of the above results (except Brand et al. 1989b) is that they seek to reproduce most of the emission in Peak 1 by a single shock model. There is no *a priori* reason why this should be so. Indeed high spatial resolution observations clearly indicate that the medium is clumpy and show a large range of both radial velocities and proper motions. But the observations reported in Brand et al. (1989b) show that at least the v=0-0 S(13) and v=1-0 O(7) line ratio is constant over most of the BN-KL nebula at a spatial resolution of 5″. Later observations reported in Smith et al. (1997) confirms that line ratios are almost constant over the entire region of OMC1, even if emission is not. They discuss observations of v=1-0 S(0), S(1) and S(2) emission. This is in contrast to reports made by e.g. Schild et al. (1997) where the line ratio of several H_2 transitions in the *K*-band is shown. These ratios vary over OMC1. The spectral resolution is comparable in both cases, 1″ and 0.″8 respectively.

Present status

The highest spatial resolution images now have resolutions of ∼0.″06–0.″20. These have been obtained with the HST (Stolovy et al. 1998; Chen et al. 1998; Schultz et al. 1999; Doi et al. 2002), the Canada-France-Hawaii Telescope (Gustafsson et al. 2003; Nissen et al. 2007), the ESO 3.6 m telescope (Vannier et al. 2001; Kristensen et al. 2003), the ESO VLT (Lacombe et al. 2004; Gustafsson 2006; Lemaire et al. 2007) and other telescopes (e.g. McCaughrean & Mac Low 1997; Schild et al. 1997; Kaifu et al. 2000; Cunningham 2006). In Fig. 1.10 we show the structure of the H_2 emission from OMC1 along with the positions of radio sources I and n and BN, as discussed above. Observations show that

- H_2 emission is obscured by dust over the entire region. An often quoted number for the extinction is 1mag at 2.12 μm (e.g. Brand et al. 1988; Rosenthal et al. 2000), but this may vary locally. It is very possible that we are only observing H_2 emitting clumps moving out of the molecular cloud or very close to the edge, and that weak features are bright but obscured (e.g. Brand et al. 1988; Rosenthal et al. 2000; Vannier et al. 2001).

- The structure of H_2 emission in OMC1 is not fractal, but instead shows a preferred scale of ∼1000 AU (∼2″; Vannier et al. 2001; Gustafsson et al. 2006b; Gustafsson 2006). This is consistent with a protostellar population (Nissen et al. 2007).

- The primary excitation mechanism for H_2 is shocks (e.g. Kwan 1977; Smith & Brand 1990; Rosenthal et al. 2000; Vannier et al. 2001; Kristensen et al. 2003; Lacombe et al. 2004; Nissen et al. 2007) rather than the PDR generated by θ^1Ori C (e.g. Sternberg & Dalgarno 1989). Kristensen et al. (2003) showed that the contribution from the PDR is of the order of ~10% in bright clumps located in a small region in Peak 2 (see also France & McCandliss 2005).

- There is not a lot of [FeII] emission at the heart of OMC1 (Schultz et al. 1999; Takami et al. 2002). The [FeII] emission that is detected is located at the tip of well-known HH-objects similar to the bullets north of BN. This indicates that the bulk of emission from shocked H_2 is caused by non-dissociative shocks (see Sect. 2.2.2).

- The proper motions of the objects in the inner region of OMC1 has recently been measured (Cunningham 2006). These data confirm the dynamical age of the outflow to be less than ~1000 years.

Even though it is clear that the bulk of emission is generated in shocks, the exact mechanism and, in particular, shock type is still a mystery. As noted in the historical introduction, Smith et al. (1991a,b) argue that C-type bow shocks with high magnetic field strengths are the solution. Kristensen et al. (2003) note that for a limited region in Peak 2 it is possible that H_2 emission is generated by a combination of C- and J-type shocks. Lacombe et al. (2004) resolve individual shock widths of shocks located between Peaks 1 and 2. This provides a very strong argument that shocks in this part of OMC1 are very likely C-type shocks.

A detailed analysis of a significant portion of individual clumps at the heart of OMC1 has not been done so far. Radial velocities and proper motions have now been reported for individual objects where they are resolved (Cunningham 2006; Nissen et al. 2007), but more work is clearly required.

1.4.4 Distance to Orion

The distance to Orion and in particular OMC1 is a source of much debate. In Chapter 5 we wish to use the size of individual objects as a constraint on theoretical shock models, and therefore it is important that the distance to OMC1 is known.

The distance to Orion is generally determined from

- Constructing Hertzsprung-Russel diagrams and fitting theoretical isochrones to the observed distribution. This method is highly model dependent and there are large uncertainties involved with this method. Results are between 363±25 pc (Penston 1973) and 525 pc (Strand 1958).

- Observations of proper motion and radial velocities of H_2O masers near source I. Genzel et al. (1981) assumed a spherical, uniformly expanding shell of masers and found a distance of 480±80 pc. However the geometry is more complex (e.g. Greenhill et al. 2004a).

- Measured parallaxes of stars or masers in the ONC. This has been done by the Hipparcos once for a single star and the result was 361^{+168}_{-87} pc (Bertout et al. 1999). Recently the parallax of a radio-flaring star was measured using the Very Long Baseline Array. This gave a distance of 389^{+24}_{-21} pc (Sandstrom et al. 2007). It is difficult to use the method of parallax for stars, since the underlying molecular cloud prevents observation of background stars. For the stars at the edge of the cloud, it is necessary to verify that they are cluster members. Recently the parallax of a maser spot near source I was measured by Hirota et al. (2007). They find a distance of 445±42 pc.

Results from stellar observations tend to be lower than maser-observations. This could indicate that the distance between ONC and OMC1 along the line of sight is larger than previously assumed. Here we are interested in the distance to OMC1 and we adopt a distance of 460 pc throughout, both following the example of Bally et al. (2000) but also since this is the average distance measured from the above observations of masers.

1.4.5 Magnetic field

Two direct measurements of the magnetic field strength in OMC1 exist. Through observations of OH-masers near IRc2, Norris (1984) was able to infer that the masers are subject to a magnetic field with a strength of ~3 mGauss. Using the Zeemann splitting of CN, Crutcher et al. (1999) argue that the magnetic field strength along the line of sight is -0.36 ± 0.08 mGauss at a position 24″ north of IRc2. Both of these measurements are very localized, and it is quite possible they do not apply to all of OMC1.

Chrysostomou et al. (1994) estimate the magnetic field strength by estimating the Alfvén velocity, v_A from the dispersion of the position angle of the polarization vectors. The Alfvén velocity is approximately equal to $b \times 1.5$ km s^{-1}. They estimate that $b \sim 10$ which at a density of 10^6 cm^{-3} corresponds to 10 mGauss. Their lower limit is $b \sim 3$. The same method was used by Gonatas et al. (1990) but observations were made at a wavelength of 100 μm. They estimate b to be ~4. Following the discussion in Crutcher (2007) this method for estimating the magnetic field may be in error by a factor ~2.

From polarization measurements in the near-infrared (e.g. Hough et al. 1986; Chrysostomou et al. 1994; Simpson et al. 2006; Tamura et al. 2006) and far-

infrared (Schleuning 1998) it is possible to derive the position angle of the field in the plane of the sky. This has been done on a large scale. For individual clumps and objects the magnetic field orientation may be different as the medium is very clumpy.

1.5   BHR71 and BHR137

The two Bok globules (Bok & Reilly 1947) BHR71 and BHR137 (Bourke et al. 1995a) are examples of isolated star formation. They are both located on the southern hemisphere and both show signs of active star formation. Both objects have associated outflows, but whereas the BHR71 outflow has already been described in detail in the litterature, very little is known of the BHR137 outflow. In fact we are the first to report of observations in the NIR *K*-band of this outflow (Chapter 6). The two objects are located at a distance of ~175 pc and ~700 pc, respectively (Bourke et al. 1995b). Below I will describe in more detail what is already known about these two objects, with emphasis on properties relevant for this work.

1.5.1   BHR71 outflow

The BHR71 outflow consists of two different outflows (Bourke 2001; Parise et al. 2006) centered on two different protostellar sources, IRS1 and IRS2 (Bourke et al. 1997) separated by ~3400 AU. IRS1 is coincident with IRAS 11590-6452 (Bourke et al. 1995a). IRS1 is a Class 0 source (Bourke et al. 1997) and IRS2 is more evolved, probably a Class I object (Bourke 2001).

Bright HH objects are associated with the blue-shifted lobes of each outflow (Corporon & Reipurth 1997), HH320 and HH321. They have been imaged in the [SII] transition at 6711 Å, indicating that at least part of the outflows are dissociative. The dynamical age of the HH321 outflow is estimated to be ~400 years (Corporon & Reipurth 1997). It has not been possible to determine the dynamical age of the HH320 outflow yet. In Fig. 1.12 we show a finding chart of the BHR71 outflow, with the positions of IRS1 and 2 marked as well as the HH objects.

H_2 was first detected by observations of the v=1-0 S(1) line at 2.12 μm (Bourke 2001). Recently NIR *JHK*-band spectra were obtained by Giannini et al. (2004). Here the spectra cover both HH320 and 321. Through detailed shock modelling they report of a preshock density of HH320A of 10^4 cm^{-3} and shock velocity of 41 km s^{-1}. This is found by fitting a non-steady-state shock model with the observed H_2 brightness. The age of the non-steady-state shock is 475 years, which is in agreement with dynamical age of the HH321 flow. The
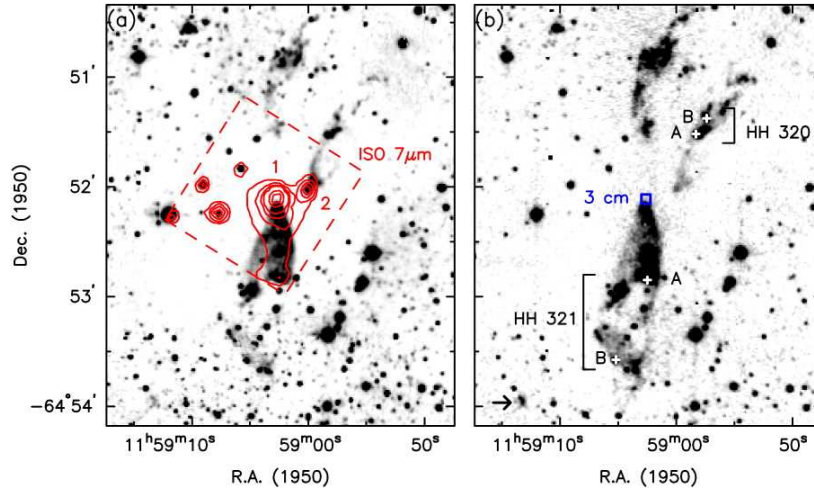
Figure 1.12: Finding chart for the BHR71 region. (a) Image shows K'-band emission with ISO LW2 contours (5.0–8.5 μm) showing the locations of IRS1 and 2. (b) H₂ v=1-0 S(1) emission + continuum. The locations of HH320A/B and HH321A/B are marked with plus signs.

preshock density is lower than what is predicted on basis of CO observations, 10^5 cm^{-3} (Parise et al. 2006). However, the latter is the density of the molecular outflow which is compressed compared to the ambient preshock cloud.

1.5.2   BHR137 outflow

The BHR137 region is home to one IRAS source (IRAS17181-4405) and at least three YSOs and a mm source. The IRAS source is classified as a Class 0 source (Yun et al. 1999) while the YSOs are more evolved, probably Class II sources (Santos et al. 1998). The mm source appears to be a molecular core (Reipurth et al. 1996). For the outflow associated with BHR137 only the blue wing has been detected through CO observations (Henning & Launhardt 1998), implying that the red wing could be emerging from the core. There are currently no published maps of the CO outflow. Santos et al. (1998) performed NIR *JHK*-band photometry of the region detecting the three YSOs. Although they imaged the region, they did not detect the BHR137 outflow in H₂. In Fig. 1.13 we show a finding chart of the BHR137 region based on our data (see Chapter 6).
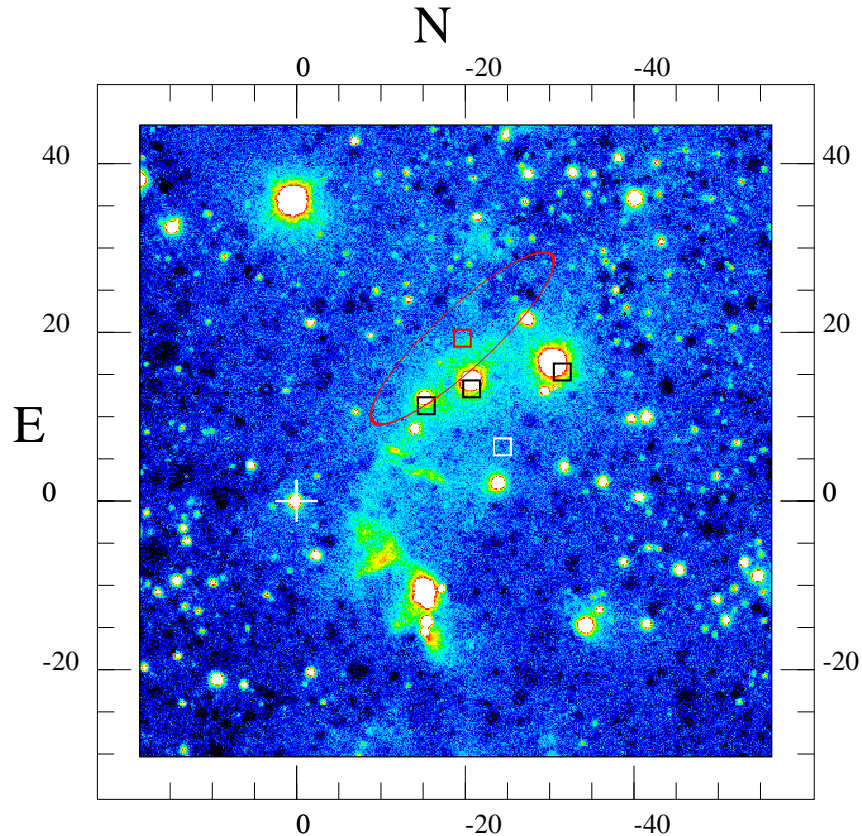
Figure 1.13: H$_2$ v=1-0 S(1) + continuum finding chart for the BHR137 region. The red box marks the location of the IRAS source with its associated error ellipse, the three black boxes show the YSOs (Santos et al. 1998) and the white box shows the location of the mm source (Reipurth et al. 1996).

1.6 Star formation in the Large Magellanic Cloud

The Magellanic Clouds are the nearest moderate-size galaxies to the Milky Way at a distance of ~50 kpc (Storm et al. 2004). They are out of the plane of the Galaxy and are relatively free of foreground extinction. Furthermore the Magellanic Clouds are relatively low metallicity compared to the Galaxy (0.33 times the Solar metallicity Fukui 2007). This makes them an ideal testbed for understanding star formation in external galaxies.

A particular type of compact HII region has been discovered in the Magellanic Clouds, the so-called high excitation blobs (HEBs; Heydari-Malayeri et al. 1982). They are characterized by a small size, high density, high extinction and high excitation. Typically they are excited by more than one central source. They are thought to represent the early stages of massive star formation (Hoare et al.
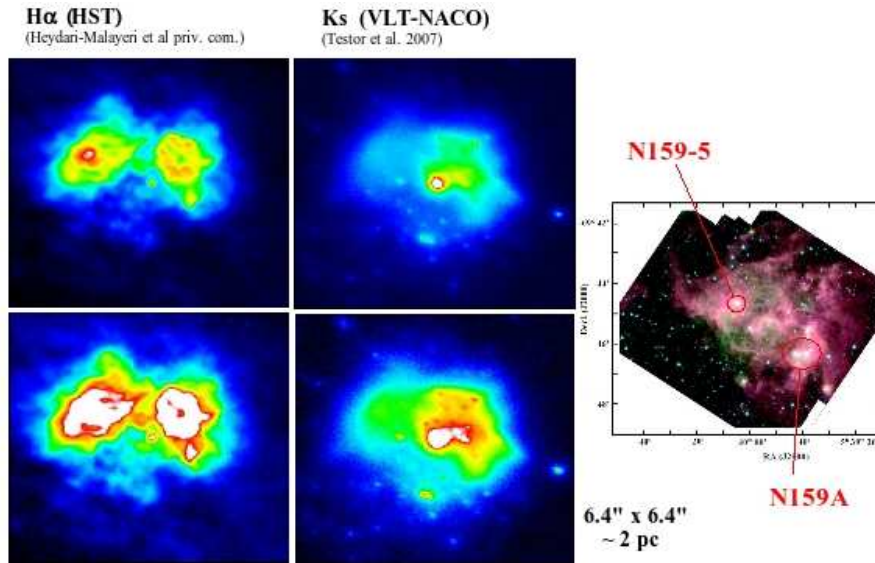
Figure 1.14: (Left) Hα emission (Meynadier et al. 2004) and K_S emission (Testor et al. 2007) of the N159-5 region. The colour scale has been chosen so as to emphasise both faint and bright structures. (Right) Spitzer Space Telescope image of the entire N159 complex (Jones et al. 2005). From Lemaire et al. (2007).

2007, and references therein).

30 Doradus is a giant star forming complex located in the Large Magellanic Cloud (LMC). The actual size of the 30 Dor complex is unknown, but it probably stretches over more than 1000 pc (Blitz et al. 2007). Some ~600 pc south of the centre of 30 Dor a chain of HII regions are located (Henize 1956). It is believed that the star formation process started at the centre of 30 Dor and is now continuing towards the south (Israel et al. 1996). N159 is the southernmost HII region in this association, containing the first extragalactic YSO detected (Gatley et al. 1981).

N159 is further divided into three giant molecular clouds, N159E, W and S. Of the three, N159E has the highest dust mass (Rantakyrö et al. 2005). The HEB N159-5 is located in N159E (Heydari-Malayeri et al. 1982). It is a HII region with a size of ~6″ (~1.5 pc). It is associated with the IRAS source 05405-6946. Spitzer observations show that it is one of the brightest members of N159 (Jones et al. 2005). H_2 emission has previously been detected in the region (Israel & Koorneef 1991; Krabbe et al. 1991; Nakajima et al. 2005). NIR data give a clear indication that star formation is continuing in this object. In fig. 1.14 we show a finding chart of the entire N159 region.

N159-5 is also known as the Papillon Nebula (Heydari-Malayeri et al. 1999)

because Hubble Space Telescope images of Hα resolved N159-5 into two lobes of emission shaped like a butterfly (see Fig. 1.14). The two lobes are located in the western and eastern part of N159-5 respectively. Of the two lobes, the western shows continuum emission at 3 and 6 cm (Indebetouw et al. 2004). The central exciting source could be an O4 star (Martín-Hernández et al. 2005) or a 50 $M_\odot$ star (Meynadier et al. 2004). It is located at the centre of the Hα "butterfly".

1.7   Outline

questions to be answered: - shock type in omc1 - possible to use single shock model for peak1 - more conclusions on interaction

This thesis is roughly divided into two parts, models and observations. In Chapter 2 I will describe the 1D shock model which I have used, and I will give some of the results of a large grid of models I ran. I will also discuss methods for verifying model results. Tis Chapter may be considered a "tool"-chapter, where I decribe the tools (i.e. shock models and model results) that will be used in the analysis of observations.

We have observed OMC1 in H$_2$ rovibrational emission lines at high spatial resolution using both the Canada-France-Hawaii Telescope (CFHT) and the ESO Very Large Telescope (VLT). The observations and data reduction are described in Chapter 3. Here I also provide details of data reduction that are specific for comparing images.

In Chapters 4 and 5 I analyse and interpret the observations of OMC1. This analysis is ordered chronologically, that is, when I started my thesis work I began by analysing the data from the CFHT and large-scale structures in OMC1 (Chapter 4). Later I went on to work on the data from the VLT, which are at a higher spatial resolution and sensitivity. Here I have analysed individual objects in terms of a 2D shock model I have developed using results from the above mentionned grid of shock models. The most recent result is the comparison of a single object with a newly developped 3D shock model (Chapter 5). In these two Chapters I will provide a contribution to the ongoing discussion of the source of H$_2$ emission, in particular whether emission arises in C- or J-type shocks. I will also reflect on the impact of the massive stars in the region on their surroundings, where I focus on whether the outflow is triggering a new wave of star formation.

In Chapter 6 I analyse H$_2$ emission from the outflows originating in BHR71 and BHR137 observed using the VLT. Here, data consist of long-slit spectra, thus increasing the number of observed H$_2$ lines. Again the analysis has been made using the results from the grid of models, which was not as straight-forward as

for OMC1. Both this and the following Chapter have only been a minor part of my thesis work, and so the Chapters are relatively short.

In Chapter 7 I analyse long-slit spectra of the extra-galactic HII region N159-5 obtained at the VLT. I discuss the origin of rovibrational H_2 emission and also the morphology of the region. In particular I compare the morphology to OMC1.

Finally I will give concluding remarks in Chapter 8 where I also provide an outlook for the continuation of this work.

Theoretical shock models

My thesis work is centered on the use of a detailed and sophisticated shock model, `MHD_VODE`. The first paper describing this model was published in 1985 (Flower et al. 1985). The last two papers describing the most recent developments in the shock model were published in 2003 in Flower et al. (2003) and Flower & Pineau des Forêts (2003) respectively. Since all developments in the model happened before starting my thesis work I have not been involved in the development itself.

However, I have been a frequent user of the model. I have calculated a large grid of shock models which I have analysed. This analysis includes exctraction of a large number of model parameters and a verification of the validity of each model. This is the basis of Publication III which is a pure theoretical work. I have used this grid of models to analyse and interpret emission arising from shocks observed in the interstellar medium.

In this chapter I will first give a rather detailed description of the shock model itself particularly the input and output parameters. I will also review some of the shortcomings of the model and its future evolution. Then I will describe the grid of shock models and the results predictions. Finally I will describe how to construct a 3D bow shock model based on the 1D model. This model is the basis of Publication IV and forms the basis of the Master Thesis by Thomas Ravkilde (September 2007, University of Aarhus, Denmark).

2.1   Model description

The shock model is integrating the magnetohydrodynamic equations (see Sect. 1.3.2) in parallel with the H_2 level population rates. Abundances of 136 species linked by 1040 chemical reactions are determined in parallel with the above. This is done in a self-consistent manner using the `DVODE` integrator routine (Brown et al. 1989)[1].

---

[1]Available on `http://www.netlib.org/ode/vode.f`

The model is modular thus making it easy to change a number of parameters directly in the input files of the model. Here we will go through these parameters. Then we will give an overview of the large number of output models.

2.1.1 Input parameters

As specified above, the model is modular. This allows the user to easily change a large number of parameters for each model, both to test parameter space but also to allow for easy changes when new calculations or experimental results become available. In the following we will go through a number of these.

Chemistry

The chemistry consists of two parts: species abundances and chemical reactions. Here we will briefly discuss both.

Abundances   The 136 species are composed of 9 elements (H, He, C, O, N, S, Si, Mg and Fe) but it is easy to include other elements such as D, and it is also easy to include a deuterated chemistry (Flower et al. 2006). We use the initial chemical abundances of Flower & Pineau des Forêts (2003), see Table 2.1. The abundances are either solar abundances (Anders & Grevesse 1989) or from absorption-line abundances obtained with the Huble Space Telescope (Savage & Sembach 1996). For the abundances in grain mantles and cores, we have used the results from Gibb et al. (2000) and Sofia & Meyer (2001). A representative PAH is included in the models, $C_{54}H_{18}$ with an abundance of 10^{-6}. This abundance is high, as we are trying primarily to model shocks in OMC1. Here PAH-features are observed to be very strong (e.g. van Dishoeck et al. 1998; Rosenthal et al. 2000) and it is expected that the PAH abundance is high. All elemental abundances may be modified according to preference.

Initial species abundances of the 136 species are determined before any shock model calculation, see Table B.1 in the Appendix for a list of species and an example of initial species abundances. This is done in a chemical steady-state model where we do not include adsorption on grains to avoid complete freeze-out onto grains. The output abundances of the chemical steady-state model are then used as input abundances in the shock models.

Chemical reactions   The chemistry in both the shock models and the chemical steady-state models may be modified easily in the input files. For the moment 1040 chemical reactions are included. These are listed in Appendix B. These reactions include (with examples in parentheses):

- Gas phase chemistry (CRP: cosmic ray particle; SECPHOT: secondary photon):

  - Neutral-neutral, ion-neutral, recombination reactions

  - Endothermic reactions

  - Collisional ionization/dissociation

  - Secondary photons from cosmic ray particles (H_2O + SECPHOT $\rightarrow$ OH + H)

  - Possibility to add photoreactions (if UV field included; but self-shielding of H_2 and CO is not calculated)

- Grain chemistry (*: the species is found in the grain mantle; **: the species is found in the grain core):

  - H_2 formation (H + H $\rightarrow H_2$)

  - Sputtering of grain mantles (CH_4^* + He $\rightarrow CH_4$ + He + GRAIN)

  - Erosion of grain cores (Si^{**} + O $\rightarrow$ GRAIN + Si + O)

  - cosmic ray induced desorption from grains (CH_4^* + CRP $\rightarrow CH_4$ + GRAIN)

  - Adsorption and saturation of species on grains (C + GRAIN $\rightarrow CH_4^*$)

The grain charge is explicitly calculated. As mentioned above a chemistry induced by cosmic rays is included. It is possible for the user to set the cosmic ray ionization rate, and here we set it to 5×10^{-17} s^{-1} per H atom.

Shock type

The user is free to choose one of the following types of model:

1. Chemical steady state model. This type of model is run before each shock model in order to determine the composition of the preshock gas.

2. J-type shock. The "discontinuity" found in J-type shocks is treated with an artificial viscosity method (this is discussed in Flower et al. 2003)[2].

---

[2]A viscous length has to be entered into the models. This viscous length is of the order of the mean free path. It is possible to verify the viscous length by comparing the results with predictions of the Rankine-Hugoniot relations.

Table 2.1: Initial species abundances as given by Flower & Pineau des Forêts (2003). Numbers in parentheses are powers of 10. The fractional abundance of PAH is 10^{-6}.

Element	Fractional abundance	Gas phase	PAH	Grain mantles	Grain cores
H	1.00	1.00			
He	1.00(-1)	1.00(-1)			
C	3.55(-4)	8.27(-5)	5.40(-5)	5.53(-5)	1.63(-4)
N	7.94(-5)	6.39(-5)		1.55(-5)	
O	4.42(-4)	1.24(-4)		1.78(-4)	1.40(-4)
Mg	3.70(-5)				3.70(-5)
Si	3.37(-5)				3.37(-5)
S	1.86(-5)	1.47(-5)		3.93(-6)	
Fe	3.23(-5)	1.50(-8)			3.23(-5)

3. C-type shock. For C-type shocks the gas is treated as 3 fluids consisting of neutral species, positively and negatively charged species. We assume that the initial transverse magnetic field is frozen into the charged fluid of the preshock gas and that the transverse magnetic field strength is given by $B_0 = b \times \sqrt{n_H(\text{cm}^{-3})}\,\mu$Gauss. The user may change b, the magnetic scaling factor. For J-type shocks b is not necessarily 0.

4. Non-steady state C-type shock. This shock-type is also called a truncated shock. At a predefined time, t_0 a "snapshot" is taken of a C-type shock. The non-steady state C-type shock develops as a steady state shock up until the time t_0. At this point the shock is truncated causing the gas flow to become subsonic in the reference frame of the shock. This leads to a sonic point and the development of a J-type front (see Sect. 1.3.2 and Chièze et al. 1998; Lesaffre et al. 2004).

The models have been designed to specifically simulate molecular outflows and not very high speed shocks. This means that the limit of J-type shocks is ~60-70 km s^{-1}. At higher velocities the temperature is high enough to doubly ionize species, which is not taken into account in the models. Furthermore J-type shocks should not be simulated with densities much higher than 10^6 cm^{-3}. The postshock densities predicted by the models become so high that 3-body gas phase reactions become feasible (including H$_2$ formation in the gas phase). This is not included in the models.

H$_2$

The models treat H$_2$ in a very detailed manner. Collisional excitation with H, H$_2$ and He is included. Also H$_2$ formation on grains is included. It is possible to choose the number of rovibrational levels that we take into account and specifically set output parameters. In the following we will go through these points in more detail.

Collisional excitation   In the models collisional excitation of H$_2$ is treated with respect to H, H$_2$ and He. The rate coefficients for H$_2$-H$_2$ and H$_2$-He collisions are given in Le Bourlot et al. (1999). For H$_2$-H collisional rates it is possible to choose between a quasi-classical approach (Martin & Mandy 1995) or the full quantum mechanical approach (Flower 1997; Flower & Roueff 1998). Unfortunately in this latter case the rate coefficients have only been calculated for the first 49 rovibrational levels of H$_2$. New rate coefficients for the first 108 rovibrational levels of H$_2$ have recently been calculated (Wrathmall et al. 2007), but these have not been included in the model yet. It is possible to use the rate coefficients from Flower (1997); Flower & Roueff (1998) for the first 49 levels and use the Martin & Mandy rate coefficients for the rest. In the models it is possible to include up to 317 levels corresponding to the dissociation limit for H$_2$. Of course the computing time for a model is strongly dependant on the number of H$_2$ levels taken into account.

H$_2$ formation on grains   In the models it is possible to choose between 3 different scenarios for H$_2$ formation on grains. H$_2$ formation is important mainly in dissociative J-type shocks where molecular reformation takes place in the postshock gas. As grains are not included in the chemical steady-state model, molecular formation is not an issue there. The formation scenarios are:

1. Energy equipartition: One third of the formation energy (4.4781 eV ~ 51 747 K) goes into internal energy of H$_2$ and is Boltzmann distributed. Another third goes into kinetic energy and the last third goes into grain heating.

2. Formation at the dissociation limit: The H$_2$ is formed with v=14, J=0,1 (corresponding to an energy of 4.4781 eV).

3. H$_2$ is formed in the v=6, J=0, 1 state (vibrationally hot, rotationally cold)

These different scenarios are not based directly on laboratory experiments but they are currently works in progress (e.g. Hornekær et al. 2003; Creighan et al. 2006; Amiaud et al. 2007).

In the models the probability that an H atom sticks to the surface of a grain (the sticking coefficient) is given as (Hollenbach & McKee 1979; Flower et al. 2003):

$$S = \frac{1}{1 + 0.04 \sqrt{T + T_{\text{grain}}} + 2 \, 10^{-3} \, T + 8 \, 10^{-6} \, T^2} \qquad (2.1.1)$$

where T is the kinetic gas temperature and T_{grain} is the grain temperature. We have set the gas temperature equal to 15 K throughout. The formation rate is given by (Le Bourlot et al. 2002):

$$n(\text{H})n(\text{grain})\pi r_{\text{grain}}^2 S \left(\frac{8 k_{\text{B}} T}{\pi m_{\text{H}}} \right)^{0.5} \qquad (2.1.2)$$

where $n(\text{grain})$ and r_{grain} are the local values of the grain number density and the root mean square grain radius.

H_2 output   As mentioned above it is possible to manually set the number of H_2 levels included in the models, up to 317. It is also possible to set the number of H_2 transitions recorded in the output file. The time it takes to calculate a model is strongly dependant on the number of H_2 levels.

Furthermore we can specify whether line brightness should be recorded as local or integrated brightness, and we can choose whether the level populations should be recorded as local or integrated (column density) populations. When integrating either the H_2 brightness or level population, the integration is performed through the shock.

Grains

Grains are assumed to be composed of olivine, $MgFeSiO_4$. The size distribution is assumed to be $\mathrm{d}n_g(a)/\mathrm{d}a \propto a^{-3.5}$ where a is the grain radius (the o-called MRN distribution Mathis et al. 1977). The radius is taken to be in the range of 10-300 nm. The total mass density (including mantles) of the grains is taken to be $0.0119 n_{\text{H}} m_{\text{H}}$. The grain temperature is not calculated in the models but remains constant at a user specified value. Here we use 15 K. The rate coefficients for charge transfer with grains is also taken into account into the model, allowing for the grain charge distribution to be calculated for each step of the model. In the latest version of the model (Flower & Pineau des Forêts 2003), grain collisions are also taken into account, which may lead to shattering of grains and even destruction.

It is possible to release the grain core elements (Mg, Fe, Si and O) into the gas phase through sputtering. Sputtering yields are given in May et al. (2000). It is an important process both in J- and C-type shocks. In J-type shocks the

high kinetic temperature ensures that sputtering is an efficient process, while in C-type shocks it is due to the velocity difference between neutral and charged species.

2.1.2   Output parameters

Profiles

The model runs on an adaptive grid routine. This means that when a model is started, it solves all equations and calculates species abundances, physical parameters, etc. It then takes a step forward (in time and space, see below Sect. 2.2.2). The length of this step is determined by how much the parameters have changed compared to previous steps. When properties are changing rapidly, as for example close to the maximum kinetic temperature, stepsizes are small compared to the cold postshock gas, where prperties change very little from one step to another. In the model input it is possible to set the precision for the `vode` integrator.

One of the strengths of this model is that everything is recorded as profiles. This means that for each step of the model most of the output parameters are recorded. It is possible to specify the number of steps between each output. A typical model contains 2500-5000 steps for a precision of 10^{-7}.

This makes it easy to visualize most profiles, such as temperature (of neutrals, ions and electrons), density, velocity (neutral, ions and electrons), H_2 line brightness and level populations, species abundances, etc.

H_2

For H_2 an excitation diagram (Boltzmann plot) is calculated directly, making it very easy to compare with observations and visualise the excitation. Again all H_2 level populations and line brightness are calculated at each step of the model, allowing for brightness profiles to be made.

Other lines

A number of level populations of different species are calculated. For some of these levels the deexcitation is explicitly calculated and stored. These include fine-structure lines of Fe^+ and several meta-stable lines of C, N, O, etc. We list the lines for which the brightness is explicitly calculated in Table B.2 in Appendix B with the species and the wavelength. Doubly ionized species are not taken into account in the models. Furthermore, OH and H_2O spectra are not calculated even though they are expected to be observed in the near-future by e.g. Herschel (see below, Sect. 2.1.4). Furthermore, at each step in the models

the abundances of all 136 species (see Appendix B) are of course calculated and recorded.

In particular we note the importance of [FeII] emission. This emission is mainly generated in dissociative J-type shocks, as will be discussed later (see Sect. 2.2.2). Therefore [FeII] emission may be used as a discriminator between dissociative J-type shocks and non-dissociative C- and J-type shocks.

[FeII] emission   As shown in Table B.2 the line brightness for 21 Fe^+ transitions are calculated. However the populations of 35 levels are calculated. In Fig. 2.1 we show the position of these levels in a Grotrian diagram (energy level diagram) as well as the 21 transitions.

It is thus straightforward to calculate line brightness for any transition originating from an upper level already calculated, assuming that the Einstein coefficient is known. For a recent list of Einstein A-coefficients, see e.g. Quinet et al. (1996), and see Bautista & Pradhan (1998) for a discussion of these values.

In particular we note that three transitions have been observed by the Spitzer Space Telescope (Neufeld et al. 2007) for which the line brightness has not been calculated. These transitions are marked in Fig. 2.1 in black.

Energy budget

The conservation equations are calculated at each step with source terms (these include energy, momentum, mass and number densities). This allows for direct visualisation of for example the mass flux through the shock.

The cooling function of a large number of species, both molecular, atomic and ionic, is also recorded:

- Molecular: H_2, ^{13}CO, CO, OH, NH_3 and H_2O

- Atomic and ionic: Si, C, O and C^+, Si^+, S^+, N^+, Fe^+

It is assumed that all of the above are optically thin. In the model it is possible to distinguish between the cooling caused by rotational de-excitation and the cooling caused by vibrational de-excitation. This cannot be done for all molecules, but only CO and H_2O. This is done by using an escape probability method as described in Kaufman & Neufeld (1996a,b). Implementing this option allows for a more accurate calculation of the cooling functions in general, which is especially important at lower temperatures. However, it comes at the cost of computing time. This option has not been used here.
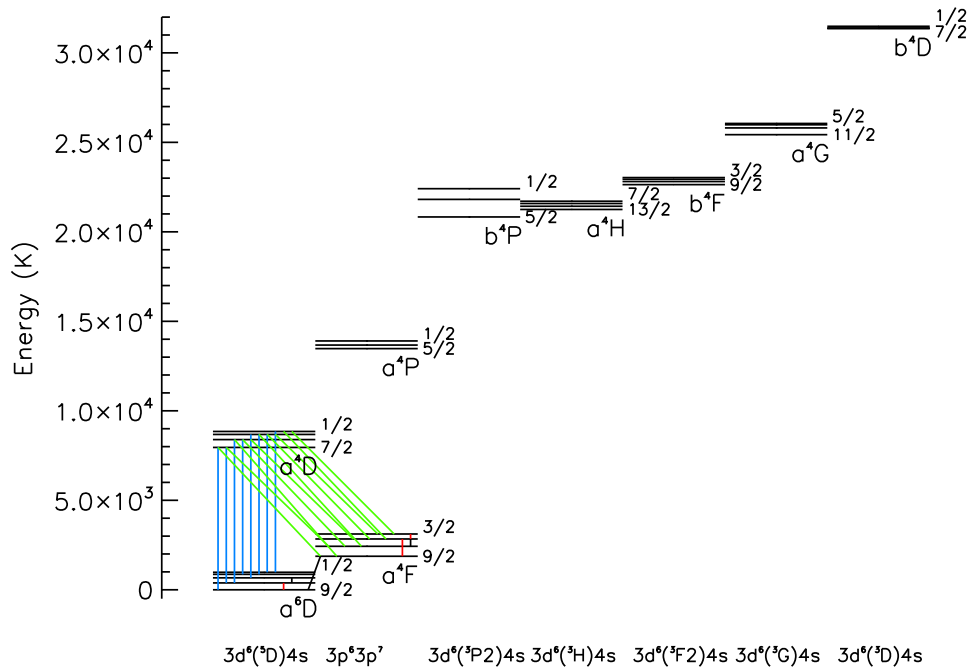
Figure 2.1: Grotrian diagram showing the levels of Fe^+ for which populations are calculated in the models. On the abscissa the electronic configuration is shown. We display levels according to terms ($^{2S+1}L_J$) where the range of J is shown for each level. Line brightness for eight transitions between the a^4D and a^6D terms (blue), ten transitions between the a^4D and a^4F terms and three fine-structure transitions (red) are calculated. Furthermore three transitions observed by Spitzer (Neufeld et al. 2007) are shown (black).

2.1.3 Shortcomings of the model

The shock model described here is not complete and do not, at the moment, include all known physical and chemical processes which are thought to be occuring in interstellar shocks. Below I list some examples.

- Geometry: in the 1D model, when the postshock gas has been compressed it remains compressed at a higher pressure than the preshock gas. In nature the postshock gas would diffuse into the surrounding medium seeking to equilibrate the pressure. This is especially important in J-type shocks where compression factors of more than 10^4 are predicted from the models. This could in some cases lead to number densities greater than 10^{10} cm^{-3}. It is unlikely that such high densities exist in the ISM, except

in regions close to massive stars. In C-type shocks the problem is also important. Here the compression is not as high as in J-type shocks, but the compression remains for a much longer period of time. Therefore H_2 emission, for example, may be over-estimated because the number density in the hot postshock gas is overestimated.

- Doubly ionized species: doubly ionized species are not included in the models, and they will probably not be included in the very near-future. For the work and observations presented here, this is not a big problem. The problem arises in J-type shocks with velocities greater than ~60-70 $km\,s^{-1}$, where temperatures reach more than a few $100\,000$ K. Thus at the moment the model is best adapted to reproduce molecular shocks.

- Grains: currently there is work in progress to treat the grains in a more realistic manner in the model. This is done by determining the 2D grain dynamics, including effects of grain inertia and charge fluctuations. In particular the gyration of charged grains around magnetic field lines is calculated (V. Guillet et al. in preparation).

2.1.4   Future

HD

One of the things that should be included in the model in the near future is a more detailed treatment of HD. This should be included because rotational transitions of HD has already been observed by the Spitzer Space Telescope (Neufeld et al. 2007). We are hoping it will not prove too difficult to include as collisional rate coefficients already exist (Flower et al. 2000). In principle the approach would be to copy the treatment of H_2 but apply it to HD. This will eventually also include line brightness calculations.

The Herschel telescope

For the interpretation of observations made with the new Herschel Telescope (the launch date is set for July, 2008) it would be necessary to include a more detailed treatment of OH, H_2O, CO, SiO, etc. into the model and calculate spectra. The best way to do this would be to add a Large Velocity Gradient (LVG) model and calculate the spectra separately, i.e. calculating the shock model and afterwards calculate an H_2O spectrum. However this is not a completely self-consistent approach. Furthermore it is not at all done at the moment, although they are included in the chemistry as well as their cooling rates.

2.2   Grid of models

During the summer of 2005 I ran a large grid of ~25 000 shock models. This grid is designed to reproduce observations of OMC1. Therefore the density is relatively high ($\geq 10^4$ cm^{-3}) and the resolution in the magnetic scaling factor is high. A current work in progress is to expand the grid to lower densities and include the results in the grid and analysis. This has not been done at present.

In this section I will first describe the grid in terms of input parameters and output parameters that I have already recorded. Following this I will give a brief overview of what can be learned from the results. This is not meant to be a complete analysis of the results, as this would be too overwhelming a task. I will primarily focus on predictions of H_2 rotational and rovibrational emission. These can be observed by the Spitzer Space Telescope and ground-based facilities, respectively.

Running a large grid like this has now been completely automated, as well as the extraction process and verification of output results. Thus if a user wishes to run a new grid of models and/or extract other results than I provide, it is a simple matter of modifying my programs.

2.2.1   Grid description

Input parameters

The grid of 25 000 shock models was obtained by varying the shock velocity, preshock density, magnetic scaling factor and initial H_2 ortho/para ratio. The parameter space is as follows

- Shock velocity, v_s: 10-50 km s^{-1} (step-size: 1 km s^{-1})

- Preshock density, n_H: 10^4, 5×10^4, 10^5, 5×10^5, 10^6, 5×10^6 and 10^7 cm^{-3}

- Magnetic scaling factor, b:

  - J-type shocks: 0.0 and 0.1
  - C-type shocks: 0.5-10.0 (step-size: 0.5)

- Initial H_2 ortho/para ratio: 0.01, 1.0, 2.0 and 3.0

For all models in the grid we have set the cosmic ray ionization rate to 5×10^{-17} s^{-1} per H atom. We have used the initial elemental abundances given in Table 2.1 (Flower & Pineau des Forêts 2003), see also Table 2.1. In the models we have included 100 H_2 rovibrational levels (up to an upper level energy of ~30 000 K, corresponding to v=6). The line emissivities of 150 rovibrational

lines are recorded as integrated emissivities (integrated through the shock; units of $erg\,s^{-1}\,cm^{-2}\,sr^{-1}$) and the 100 H_2 level populations are recorded as local level populations (units of cm^{-3}). The latter is used in calculating the H_2 ortho/para ratio.

The PAH-abundance have been set to 10^{-6} (see Table 2.1). As opposed to cold dark clouds where it is assumed that PAHs are frozen out onto grain surfaces, in warmer, more turbulent media like OMC1 the PAHs will have desorbed and are present in the gas phase. This is important for the critical velocity, i.e. the maximum velocity for a C-type shock (Flower & Pineau des Forêts 2003) as effective electron attachment to PAHs will increase the density of the charged fluid and thereby changing the ion magnetosonic velocity (Sect. 1.3.2 and e.g. Field et al. 1999, 2004). When the PAH abundance is increased from 10^{-8} to 10^{-6} the critical velocity is increased from $\sim$25 $km\,s^{-1}$ to $\sim$50 $km\,s^{-1}$ for preshock densities in the range of 10^3–10^5 cm^{-3} (Flower & Pineau des Forêts 2003).

For H_2 reformation on grains in dissociative shocks, we have chosen the equipartition scenario (scenario 1, previous section). That is one third of the formation energy goes to heating of the grain, one third goes to kinetic energy and one third goes to internal energy.

In the grid the vode precision is set to 10^{-7} and the output has been recorded at every 5 steps, meaning there are 500-1000 lines of output for each parameter. This has been done in order to save disk space. As a gzipped archive containing all the model outputs, the grid takes up a total of $\sim$80 Gb. The option of Kaufman & Neufeld cooling (see above; Kaufman & Neufeld 1996a,b) has not been included in the grid of models, as it substantially increases computing time. The models have been running on a 2 GHz server and the average computing time for a model was $\sim$8.3 min. Thus for 25 000 models this resulted in a total computing time of $\sim$4.8 months.

The grid may be used to reproduce observations. Once a specific model has been found to reproduce a set of observations, it is possible to refine the choice of model by running a limited number of models close to the best-fit model in a miniature grid.

Output already recorded

For the large grid of models all output files have been saved for each model. Thus, should the need arise, it is possible to extract any of the information mentioned in the previous section.

We have already selected and extracted some properties. These include H_2 data, Fe^+ and Si^+ data as well as a number of macroscopic parameters. These are listed below:

- H_2 line brightness for 61 lines. These lines are listed in Table B.3 in Appendix B. These correspond to the H_2 lines observable in the near-infrared *J*, *H* and *K*-bands and the Spitzer IRS band.

- Fe^+ and Si^+: All line brightness from the recorded lines (see Table B.2). These are observable either in the NIR or by Spitzer.

- Macroscopic parameters: Maximum kinetic temperature, postshock density, size (in terms of width and age) and maximum H_2 ortho/para ratio

Details on the extracted predictions will be discussed in the following section.

2.2.2 Model predictions

Here some of the model predictions will be reviewed. This is only meant as an overview of what can be done with the models, and should not be considered complete. As mentioned previously we have for each model recorded almost 100 parameters. Here we do not take into account the huge number of output results not yet recorded.

Profiles

One of the most important output parameters and model predictions is the temperature profile of the shock. In Fig. 2.2 such a profile is displayed for a C-type shock with a preshock density of 10^6 cm^{-3}, shock velocity 20 km s^{-1}, initial ortho/para ratio 0.01 and *b* equal to 1.

In this figure local brightness profiles for the H_2 v=1-0 S(0), v=1-0 S(1) and v=2-1 S(1) lines are also shown. Naturally it is not useful to record and compare every profile in detail. However the width (see below) and maximum temperature have been recorded for each model, providing some information on the temperature structure (see below). The FWHM of the local emission profile of the three lines shown in Fig. 2.2 and the total integrated brightness (again, see discussion below) have been recorded also.

Kinetic temperature

The maximum kinetic temperature in J-type shocks may be calculated using the Rankine-Hugoniot equations (see Sect. 1.3.2). Assuming that the shock velocity is much greater than the speed of sound (i.e. the Mach-number is $\gg$1) and that the shock is a J-type shock the postshock temperature is given by (e.g. Flower et al. 2003)

$$T = \frac{2\gamma(\gamma - 1)}{(\gamma + 1)^2}\mathcal{M}^2 \, , \tag{2.2.1}$$
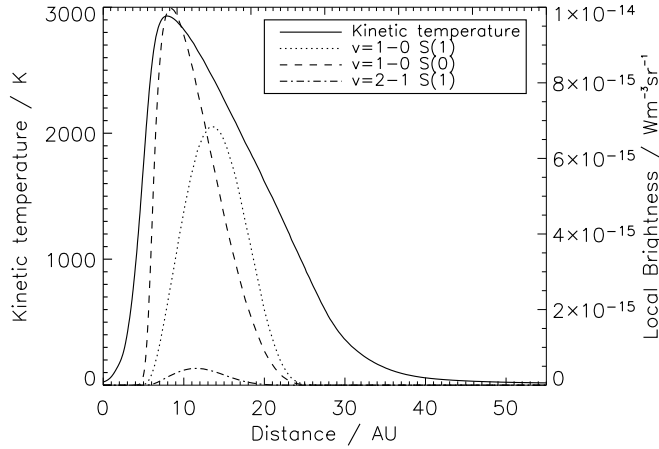
Figure 2.2: The temperature profile of a C-type shock with preshock density 10^6 cm^{-3}, shock velocity 20 km s^{-1}, initial ortho/para ratio 0.01 and b equal to 1. Also shown are local brightness profiles for the H$_2$ v=1-0 S(0), v=1-0 S(1) and v=2-1 S(1) lines. Zero distance is set to be the pointat which the kinetic temperature starts to rise (Kristensen et al. 2007a).

where $\mathcal{M}$ is the Mach-number, $\mathcal{M}^2 = (\mu v_s^2)/(\gamma k_B)$, μ is the mean molecular weight. In a monatomic gas γ=5/3, and γ=7/5 in a diatomic gas. The main preshock gas component is H$_2$. However, as discussed in Flower et al. (2003), γ should be taken as 5/3 since the H$_2$ level populations of H$_2$ do not react instantaneously to the temperature jump. The maximum kinetic temperature in J-type shocks is shown in Fig. 2.3.

We observe that for high velocities there is a small departure from the maximum temperature predicted by Eq. 2.2.1. Because of the higher temperature the H$_2$ is more rapidly thermalized and the gas is closer to a diatomic gas. It can easily be shown from the above equation that a diatomic gas is ~25% cooler than a monatomic gas.

For a C-type shock it is not possible to reduce the Rankine-Hugoniot equations to a simple analytical expression as Eq. 2.2.1. Therefore we do not have any independent means of verifying our results for the maximum kinetic temperature in C-type shocks. Results for the maximum temperature are displayed in Fig. 2.4 as a function of b and shock velocity v_s for four different preshock densities.

For a given preshock density and b the maximum kinetic temperature in a C-type shock will increase as a function of increasing velocity. At a certain point in the C-type shock the temperature will be so high that H$_2$ is dissociated. The increase in temperature caused by the loss of the principal coolant and the increase in pressure, will increase the sound speed and the gas flow (in the ref-
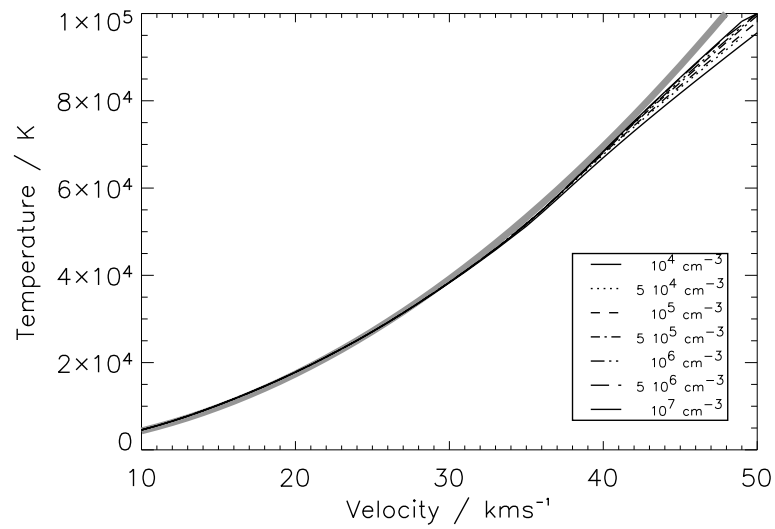
Figure 2.3: *The kinetic temperature in J-type shocks as a function of shock velocity. The gray line shows the prediction from Eq. 2.2.1.*
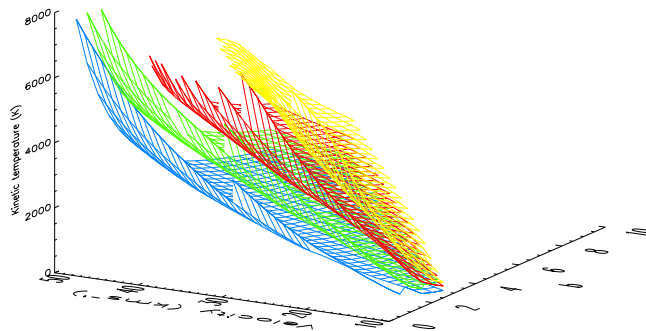
Figure 2.4: *The kinetic temperature in C-type shocks as a function of shock velocity and magnetic scaling factor, b. Different sheets corresponds to different preshock densities. Blue: 10^4 cm^{-3}, green: 10^5 cm^{-3}, red: 10^6 cm^{-3} and yellow: 10^7 cm^{-3}.*
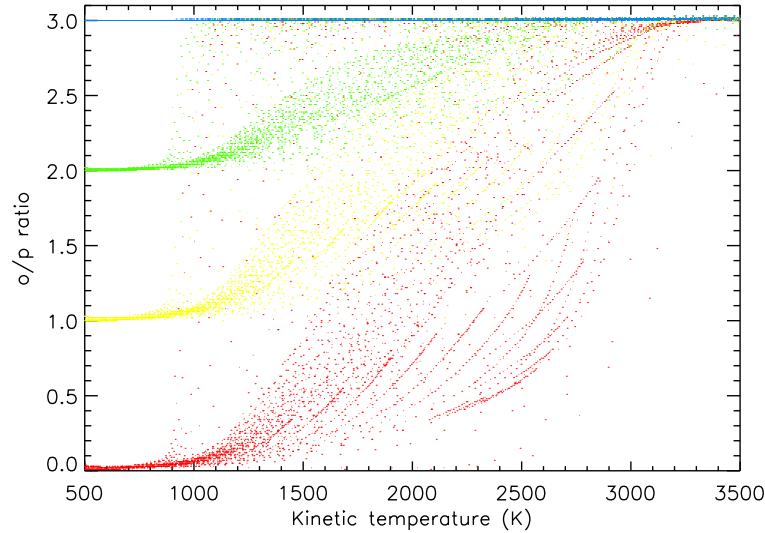
Figure 2.5: The H_2 ortho/para ratio as function of the maximum kinetic temperature reached in C-type shocks. Each dot corresponds to a shock model. Red is for an initial ortho/para ratio of 3, green for 2, yellow for 1 and red for 0.01. The ortho/para ratio only changes between 800 and 3200 K.

erence frame of the shock) becomes subsonic. Therefore the shock becomes a J-type shock. Above this critical velocity, v_{crit}, it is not possible for steady-state C-type shocks to exist (see also Sect. 1.3.2).

Ortho/para ratio as function of temperature

The H_2 ortho/para ratio is not easily changed. At low temperatures and in equilibrium most of the H_2 is found in the ground state, J=0, giving an ortho/para ratio of ~0. An efficient conversion from para-H_2 to ortho-H_2 is done through reactive collisions with H:

$$H_2^{para} + H \rightarrow H_2^{ortho} + H \tag{2.2.2}$$

This reaction shows an activation energy of ~3900 K (Schofield 1967). By plotting the maximum ortho/para ratio predicted in a shock model as a function of maximum kinetic temperature we can show over which temperature interval effective para- to ortho-conversion takes place. This is shown in Fig. 2.5 for all C-type shock models calculated. We show that over our range of input parameters the para- to ortho-conversion takes place between ~800 K and 3200 K. That is, the conversion effectively begins at 800 K and is complete at 3200 K where the ortho/para ratio will be 3.
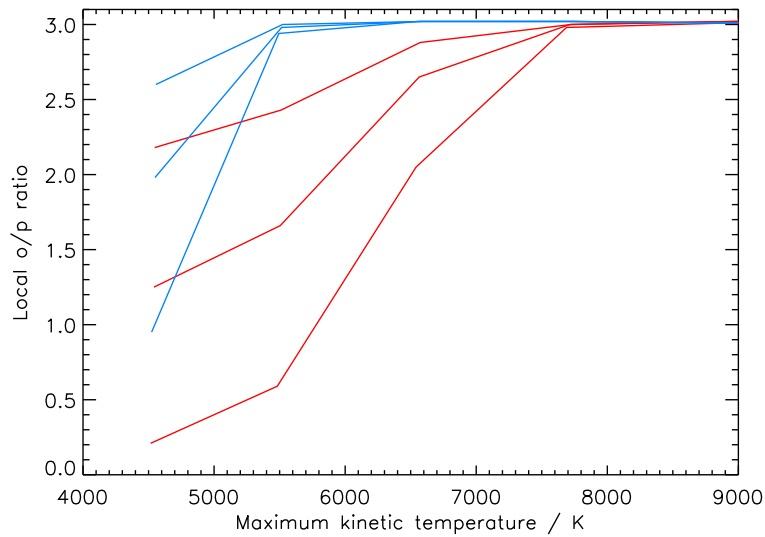
Figure 2.6: The H_2 ortho/para ratio as function of the maximum kinetic temperature reached in J-type shocks. Results are displayed for preshock densities of 10^4 cm^{-3} (red) and 10^5 cm^{-3} (blue) and for initial ortho/para ratios of 0.01, 1.0 and 2.0.

This prediction was initially based on C-type shock models only. In J-type shocks the maximum kinetic temperature is greater than ~3200 K fr velocities greater than ~10 km s^{-1}. But as we show in Fig. 2.6 para- to ortho-conversion is not complete for temperatures less than ~8000 K, corresponding to a velocity of ~13 km s^{-1}. However, in a J-type shock the width is much smaller (see below, Sect. 2.2.2) and there is not enough time for the ortho- to para-conversion to be complete. Only results for preshock densities lower than 10^6 cm^{-3} are shown in this figure as the conversion is complete for higher densities. Results are identical for models with b=0.0 and b=0.1.

H_2 emission

One of the primary diagnostic tools for analysing shocks in the interstellar medium is the emission from collisionally excited species. The primary coolant of the hot gas (between ~800 and ~8000 K) is H_2 as it is the most abundant species. However, H_2 only cools the hot gas whereas other species (primarily H_2O, CO and OH) cool the warm and cold gas (below ~800 K).

Therefore predictions of H_2 emission brightness are of great importance in analysing observations. When discussing the brightness in the following we
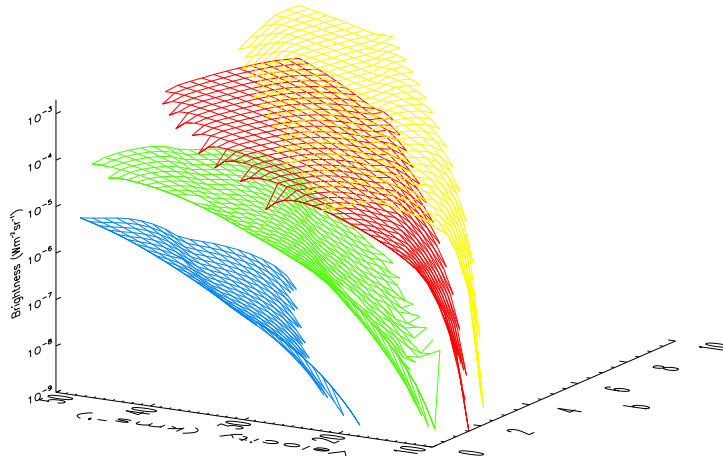
Figure 2.7: The H_2 v=1-0 S(1) brightness in C-type shocks as a function of shock velocity and b for four different preshock densities, 10^4 cm^{-3} (blue), 10^5 cm^{-3} (green), 10^6 cm^{-3} (red) and 10^7 cm^{-3} (yellow).

will always be discussing the brightness integrated over the length of the shock unless otherwise specified. This is the brightness we would observe if we were observing the shock in a face-on geometry. As the models are 1D this is the best estimate of the total brightness emitted. Later, in Sect. 5.2 another estimate of the brightness will be discussed. In Fig. 2.7 we display the brightness of the H_2 v=1-0 S(1) line as a function of shock velocity, v_s and b for four different values of the preshock density.

One of the methods used in analysing H_2 emission is the so-called diagnostic diagram. In such a diagram model input parameters are displayed as a function of observable constraints. An example is given in Fig. 2.8 (Neufeld et al. 1998) where shock velocity and initial ortho/para ratio are displayed as a function of the S(2)/S(1) and S(3)/S(1) line ratios. In this case, it is assumed that b=1.0 and that the preshock density is 5×10^5 cm^{-3}. By plotting the observed line ratios it is possible to show the range of shock velocities and initial ortho/para ratios that will reproduce observations.

However, to make s similar diagram with four input parameters is not possible. So even though diagnostic diagrams are well-suited for gaining insights into physical processes at play in shocks and their effect on, for example, the H_2 brightness, they may be more appropriately used if there are only one or two input parameters as in the example above.
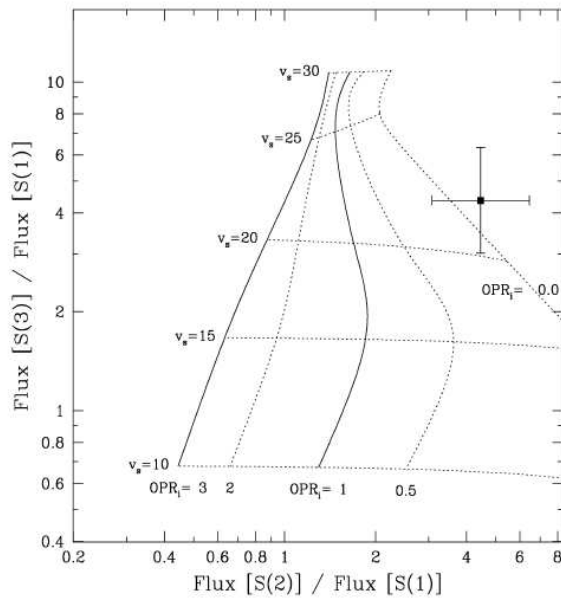
Figure 2.8: Diagnostic diagram of pure rotational H_2 emission. Model predictions are shown for a C-type shock model with preshock density 5×10^5 cm^{-3} as a function of shock velocity and initial ortho/para ratio (OPR). Predictions are from (Timmermann 1998). Taken from Neufeld et al. (1998).

Initial ortho/para ratio   In J-type shocks the initial ortho/para ratio has a small effect on the v=1-0 S(1) brightness. This is shown in Fig. 2.9. The lower the initial ortho/para ratio, the lower the brightness is. This is a time-scale effect. For a low initial ortho/para ratio most of the H_2 is of course in the J=0 para-state. The effective interconversion between para- and ortho-H_2 does not start until the temperature reaches ~800 K. Therefore the ortho-H_2 levels cannot begin to be populated until the temperature reaches 800 K causing a delay. This delay is responsible for the lower brightness in transitions between ortho-levels at low initial ortho/para ratio. Vice versa, the brightness from transitions between para-levels is higher for low initial ortho/para ratio. Fig. 2.9 also shows that even though the ortho/para ratio in the shock reaches a value of 3 at v=13 km s^{-1} the brightness varies with ortho/para ratio up to ~15 km s^{-1}.

The same effect is observed in C-type shocks (see Fig. 2.10). Here the effect is very clear when the temperature is below ~3200 K (black part of the curves in Fig. 2.10) even for high densities. From Fig. 2.7 and 2.10 it is also clear that for the combination of high density, high velocity the brightness decreases. The reason for this is twofold: first of all the temperature is very high and so higher rovibrational levels are becoming populated. This decreases the number of H_2 molecules in the v=1, J=3 state [the upper state of the v=1-0 S(1) transition] and so decreases the brightness. Furthermore H_2 is beginning to dissociate which also decreases the v=1, J=3 level population.
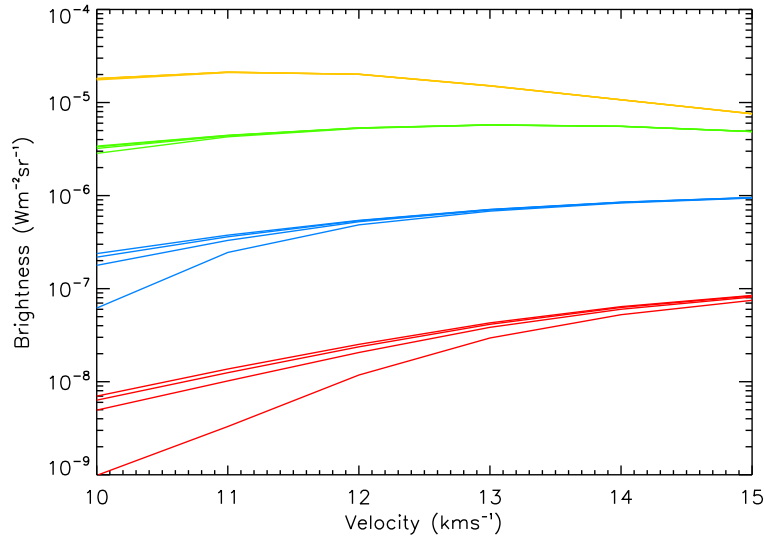
Figure 2.9: The H$_2$ v=1-0 S(1) brightness in J-type shocks for different preshock densities, 10^4 cm^{-3} (red), 10^5 cm^{-3} (blue), 10^6 cm^{-3} (green) and 10^7 cm^{-3} (yellow) and different initial ortho/para ratios. For each value of the preshock density, the lower the line the lower the value of the initial ortho/para ratio.
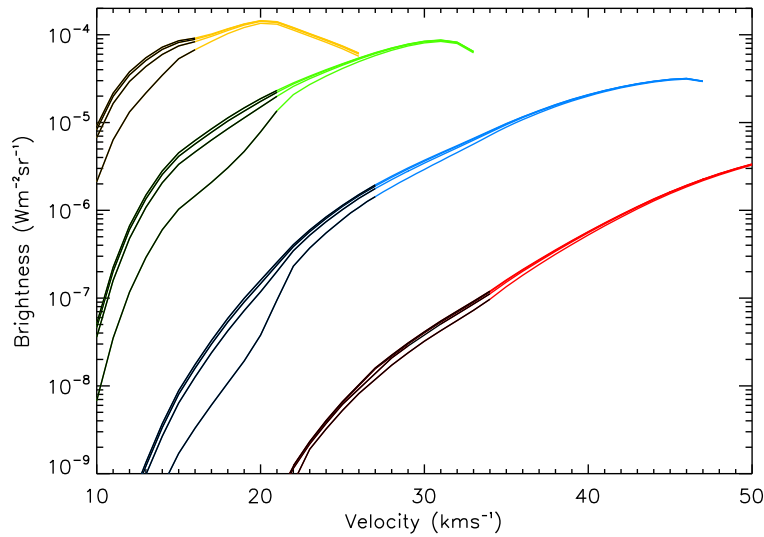
Figure 2.10: As in Fig. 2.9 but for C-type shocks. The black section of each line indicate where the kinetic temperature is less than 3200 K and there is ongoing para- to ortho-interconversion. b is equal to 1.
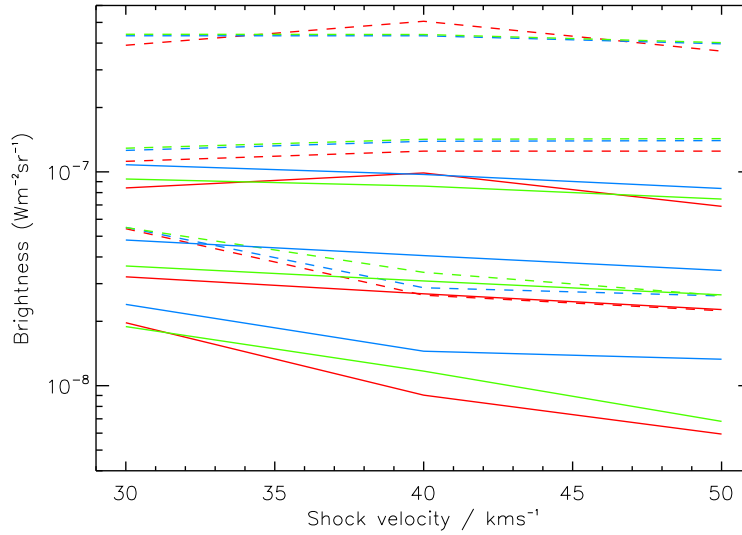
Figure 2.11: Effects of H_2 reformation in the postshock zone of dissociative J-type shocks. The brightness of the $v=1-0$ $S(1)$ transition (dashed line) and the $v=2-1$ $S(1)$ transition (full line) are shown. Formation scenario 1 is displayed in red, scenario 2 in blue and scenario 3 in green (see text for explanation of formation scenarios). Preshock densities are 10^3, 10^4 and 10^5 cm^{-3}, where lower preshock density results in lower brightness.

H_2 reformation in dissociative shocks In dissociative J-type shocks H_2 will reform in the postshock zone. As described above in Sect. 2.1.1 there are three different possibilities for reforming H_2: *(i)* equipartition *(ii)* formation at the dissociation limit *(iii)* formation in a rotationally cold, vibrationally hot state. The results of the different formation scenarios are displayed in Fig. 2.11. For the $v=1-0$ $S(1)$ transition the differences in formation scenarios are hardly visible independent of preshock density. For higher vibrational states the differences are more clear, as illustrated by the $v=2-1$ $S(1)$ transition in Fig. 2.11.

It should also be noted that the ratio in line brightness between the two lines is between ∼2 and 5. These values of the $v=1-0$ $S(1)$ to $v=2-1$ $S(1)$ line ratio are typically taken as a sign of UV-pumping, i.e. they are supposed to be observed in PDRs. From these results it is clear, that it is not possible to distinguish between a PDR and a shock based only on this ratio.

Shock width and age

When discussing the width and age of a shock it is important to realize that there is no one definition used by the community. This implies there is no standard definition of the shock width. The timescale in the models, t, is defined as the neutral flow timescale where

$$t = \int \frac{dz}{v} \ . \tag{2.2.3}$$

We note here that the velocity decreases through the shock. In the following we will use the terms width and age interchangeably. For the models considered here there is a one-to-one correspondance although this correspondance is not linear.

We will be using three different definitions of shock width and age for different purposes. These are illustrated in Fig. 2.12 and are as follows:

1. Steady-state width and age: the width and age of a shock measured between 50 K in the preshock gas and 50 K in the postshock gas.

2. Width and age at 1000 K: H_2 is vibrationally excited at temperatures greater than 1000 K.

3. Width and age of H_2 emitting zone: this may be used for direct comparison with observations of spatially resolved shocks.

Below we will discuss each of these definitions in the case of C-type shocks. The main reason for focusing on C-type shocks is that here it is often possible to directly resolve the shock width in high spatial resolution observations. In J-type shocks the width is typically less than 1 AU and always below 10 AU. This is at the limit of what can be observed today in near-infrared with the large ground-based facilities such as the ESO-VLT, assuming that the nearest objects are located at ~150 pc, the distance of the closest low-mass star formating regions.

Definition 2 and 3 above relate directly to high spatial resolution observations of shocks in the ISM. When discussing the observed width of a shock it is always implicitly assumed that the shock is moving close to the plane of the sky. The use of shock width as a direct observational constraint is new and has been used for the first time in this work (Kristensen et al. 2007a,b). With new high spatial resolution observations it will probably become more wide-spread in the near future.

It is well-known that the width of a C-type shock depends strongly on the ion-neutral coupling (Draine 1980) and thus the degree of ionization (see below). For the C-type shock models presented here the initial degree of ionization is typically of the order of 10^{-7}-10^{-8}.
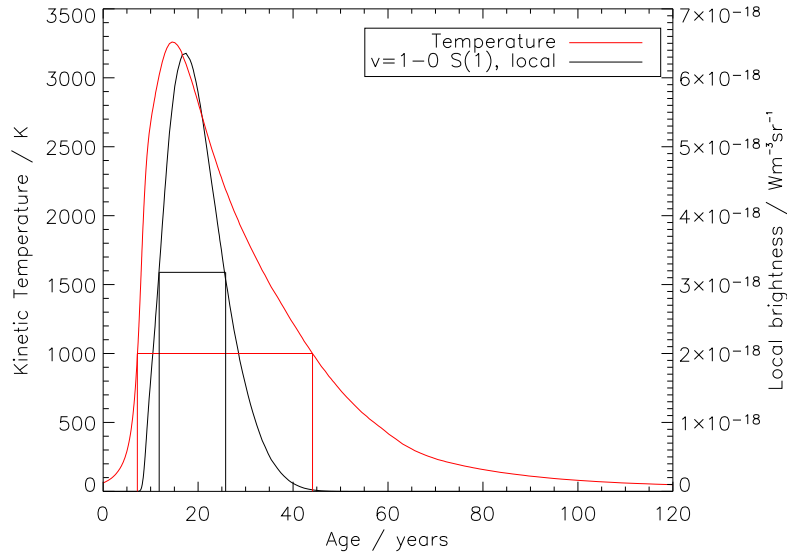
Figure 2.12: The three different definitions of shock age displayed for a C-type shock with preshock density 5×10^5 cm^{-3}, shock velocity 49 km s^{-1}, initial ortho/para ratio 3.0 and b is 6.0. The kinetic temperature and H_2 v=1-0 S(1) local emissivity profiles are shown. The ordinate displays the steady-state timescale (age at 50 K; 120 years) and the red vertical lines display the age at 1000 K (37 years). The black vertical lines display the H_2 v=1-0 S(1) local emission FWHM (14 years) (Kristensen et al. 2007b).

Steady-state width and age   The steady-state age is also known as the dynamical age. Observationally the dynamical age may be determined as the distance between shock launcher (i.e. protostellar object) and the shock itself divided by the shock velocity. It is an upper limit since the shock may have decelerated passing through the ambient medium. If the dynamical age is shorter than the modelled steady-state age, the observed shock has not had enough time to reach steady-state and the shock must be modelled as a truncated shock (Chièze et al. 1998; Lesaffre et al. 2004).

In one of the first papers on C-type shocks (Draine 1980) the typical length-scale for the magnetic precursor is calculated as

$$L \approx \frac{(\mu_{\mathrm{n}} + \mu_{\mathrm{i}}) \, B_0^2}{\pi \, \rho_{\mathrm{i}} \, \rho_{\mathrm{n}} \, \langle \sigma v \rangle \, v_{\mathrm{s}}} \tag{2.2.4}$$

where $\mu_{\mathrm{i,n}}$ are the mean molecular weights, indices i,n referring to ions and neutrals, B_0 the initial transverse magnetic field strength, $\rho_{\mathrm{i,n}}$ the density and $\langle \sigma v \rangle$ the ion neutral scattering rate coefficient. In the model we calculate this as (Os-

terbrock 1961; Flower et al. 1985)

$$\langle \sigma v \rangle = 2.41 \pi e \left[\frac{(\mu_n + \mu_i)\alpha}{\mu_n \mu_i} \right]^{1/2} \tag{2.2.5}$$

where e is the electron charge and α the polarizability of the neutral partner. The neutral partner is primarily H or H_2 and we calculate α as the weighted average

$$\alpha = \frac{n(H)\alpha_H + n(H_2)\alpha(H_2)}{n(H) + n(H_2)} \tag{2.2.6}$$

where $\alpha(H) = 6.67 \times 10^{-25}$ cm^{-3} and $\alpha(H_2) = 7.70 \times 10^{-25}$ cm^{-3} (Osterbrock 1961). As a numerical example we examine a shock with a shock velocity of 20 km s^{-1}, preshock density 10^5 cm^{-3} and $b=1.0$. The initial values of μ_i and μ_i are 3.94×10^{-23} g and 7.65×10^{-23} g, respectively. The neutral and ionic densities are 2.37×10^{-19} g/cm^3 and 1.52×10^{-25} g/cm^3, respectively. The abundance of H in the preshock gas is negligible. Thus we find $L \approx 1440$ AU. For the particular model, we find $L(50\,K)=350$ AU, a factor of four lower. In order to estimate the validity of Eqn. 2.2.4 we may reduce the expression and consider how it depends on initial conditions.

As usual we introduce $B_0 = b \times \sqrt{n_H\,(\text{cm}^{-3})}\ \mu$Gauss and we find that

$$
\begin{aligned}
L \quad &\approx \quad \frac{(\mu_n + \mu_i)B_0^2}{\pi \rho_i \rho_n \langle \sigma v \rangle v_s} \\[6pt]
&\propto \quad \frac{B_0^2}{\rho_i \rho_n v_s} \\[6pt]
&\propto \quad \frac{b^2}{x_i\, n_H\, v_s}
\end{aligned}
\tag{2.2.7}
$$

where x_i is the degree of ionization. Thus we expect the shock width to be comparable to this result which is indeed what we find. To display it nicely, we plot $L\, x_i\, n_H\, v_s/b^2$ as a function of v_s, see Fig. 2.13. This should give the proportionality constant of Eqn. 2.2.7. We do not find that it is exactly true, but to a first approximation it looks reasonable. The reason there is no exact match may be that Draine is making a number of simplifications whereas in these models all of the chemistry is included. This will almost certainly affect the results.

Width and age at 1000 K   At a temperature of $\sim$1000 K exchange reactions between H and H_2 are feasible and an effective para- to ortho-state conversion begins. Furthermore, H_2 is efficiently vibrationally excited above $\sim$1000 K. Therefore this is a good estimate of the H_2 rovibrationally emitting hot zone and may be used to compare directly with observations of excited H_2 (see Fig. 2.12).
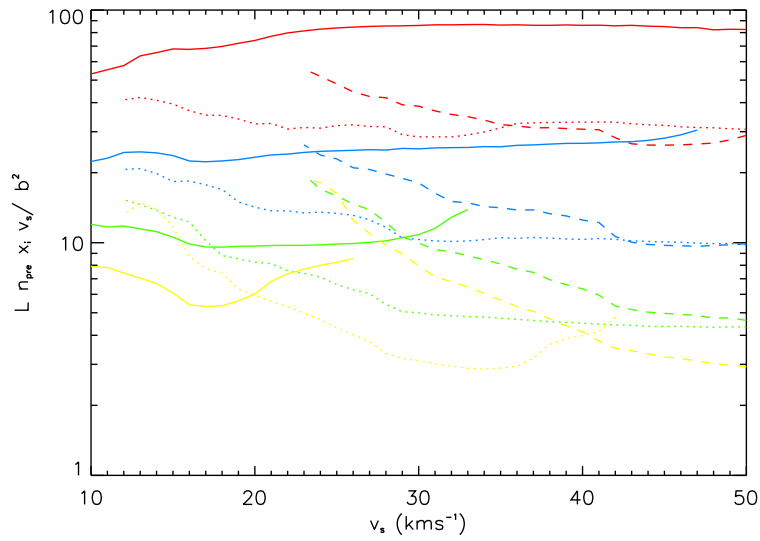
Figure 2.13: ($L\,n_{pre}\,x_i\,v_s/b^2$) as a function of v_s (see Eqn. 2.2.7). Results are displayed for four different preshock densities, 10^4 cm^{-3} (red), 10^5 cm^{-3} (blue), 10^6 cm^{-3} (green) and 10^7 cm^{-3} (yellow) and three different values of b, b=1.0 (full line), b=5.0 (dotted line) and b=10.0 (dashed line).
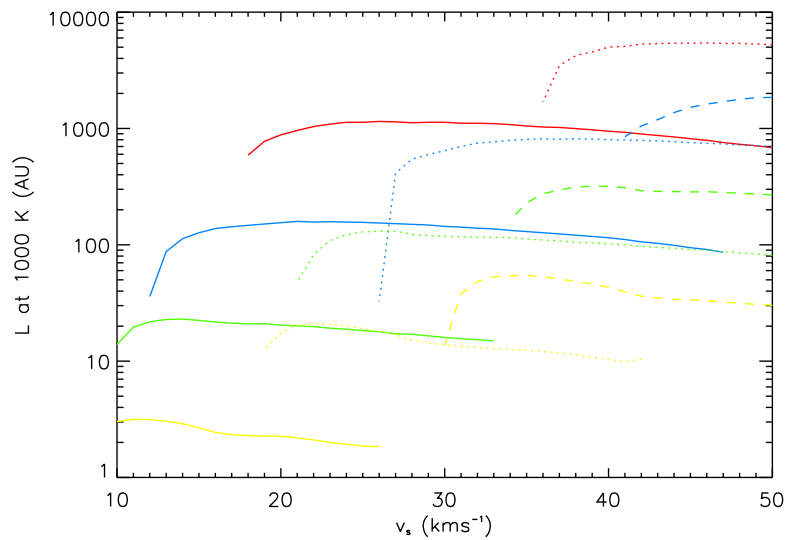
Figure 2.14: Width of C-type shocks at 1000 K as a function of shock velocity. Colours and line styles are as above in Fig. 2.13.
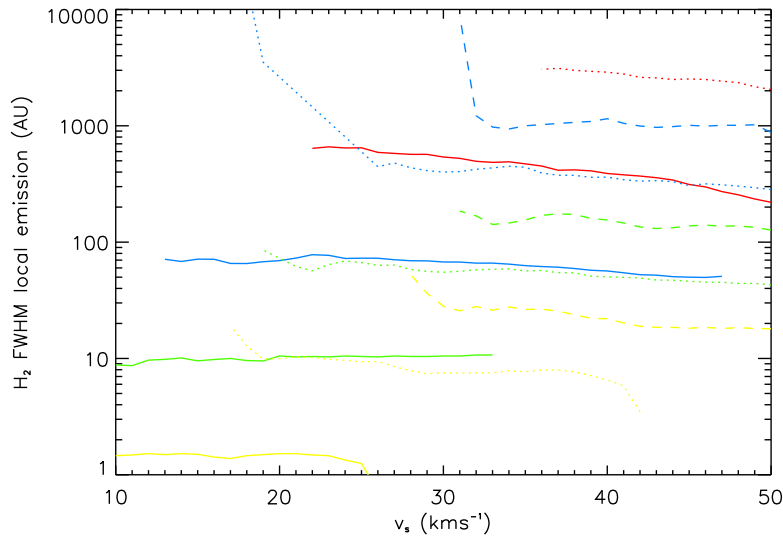
Figure 2.15: Width of C-type shocks as FWHM of local H_2 v=1-0 S(1) emission as a function of shock velocity. Colours and line styles are as above in Fig. 2.13.

Even though H_2 is primarily vibrationally excited above 1000 K it is still possible to have a high brightness from rovibrational transitions in shocks where the maximum kinetic temperature only reaches a few hundred K. This is typically attained in shocks with very high b and low shock velocity. However these shocks are very broad and so the temperature of a few hundred K is sustained over a long period of time allowing for the integrated brightness to build up slowly.

As for the steady-state width this is largely dependent on the shock density, b and v_s. In Fig. 2.14 the width is displayed as is. The dependance on preshock density, degree of ionization, b and shock velocity is not as good as for the steady-state width. The reason for this is as follows. By definition it is only possible to measure the width at 1000 K if the maximum kinetic temperature is above 1000 K. Hence the temperature is another parameter in determining the width. This is also the reason why widths are seen to decrease for the combination of low shock velocities and preshock densities (Fig. 2.14).

Width and age of H_2 emitting zone   If the shock is moving in the plane of the sky, it may be more appropriate to estimate the size of the shock by measuring the FWHM of the emitting zone. This is done by measuring the FWHM of the local emissivity profile of any given line (see Fig. 2.12). This has only been done for shocks with a total H_2 v=1-0 S(1) brightness greater than 10^{-13} W m^{-2} sr^{-1}

(see below, Sect. 2.2.3 and Wilgenbus et al. 2000).

This width depends not only on density, magnetic field and shock velocity but also the initial ortho/para ratio as discussed above. Adding an extra parameter of course adds to the complexity and it is no longer possible to find a clear correspondance between the independent parameters and the width. For purposes which will become clear later (see Sect. 5.2) I have extracted the H_2 FWHM of local emissivity profiles of the three rovibrational lines, v=1-0 S(0), v=1-0 S(1) and v=2-1 S(1). In Fig. 2.15 the width is shown as is. As predicted it is of the same order of magnitude as the width at 1000 K.

[FeII] emission

To generate [FeII] emission two processes are important:

- Releasing Fe^+ from grain cores through sputtering and erosion

- Allowing Fe^+ to contribute significantly to the cooling process

In J-type shocks it is relatively easy to release Fe^+ into the gas phase due to the high gas temperature. In dissociative J-type shocks Fe^+ becomes one of the main coolants when typical molecular coolants such H_2, OH and H_2O are dissociated. Hence bright [FeII] emission is primarily associated with dissociative J-type shocks as can be seen from Fig. 2.16, where the brightness of three very luminous transitions is shown. These are the transitions $a^4D_{7/2}-a^6D_{9/2}$ at 1.257 μm, $a^4D_{7/2}-a^4F_{9/2}$ at 1.644 μm and $a^4F_{7/2}-a^4F_{9/2}$ at 17.936 μm.

In C-type shocks the temperature is significantly lower than in J-type shocks. However because of the magnetic field there is a velocity difference between neutral and charged species. This velocity difference is high enough that sputtering of grains is feasible. Of course the stronger the magnetic field is, the larger the velocity difference is and the more efficient the sputtering process becomes. In general C-type shocks are not dissociative and the main coolants are molecular in nature with H_2 being the primary coolant. At shock velocities just below the critical velocity a non-negligible part of the H_2 will dissociate along with other molecules. As the main coolants are reduced in abundance other species, such as O end Fe^+ will take over. Therefore at velocities just below the critical velocity a sudden rise in [FeII] emission is seen in C-type shocks. The emission is stronger as the magnetic field is increased. We display this in Fig. 2.17.

2.2.3   Verifying model results

Sometimes a model will produce results that are not trustworthy or wrong. It is important to weed out models that do not produce credible results and to have
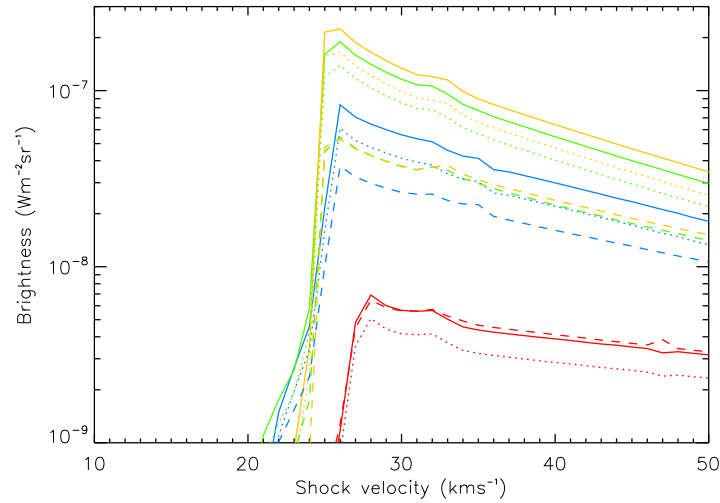
Figure 2.16: [FeII] emission in J-type shocks as a function of shock velocity. Brightness is shown for the transitions at 1.257 µm (full line), 1.644 µm (dotted line) and 17.936 µm (dashed line). Brightness is displayed for four different preshock densities: 10^4 cm^{-3} (red), 10^5 cm^{-3} (blue), 10^6 cm^{-3} (green) and 10^7 cm^{-3} (yellow).
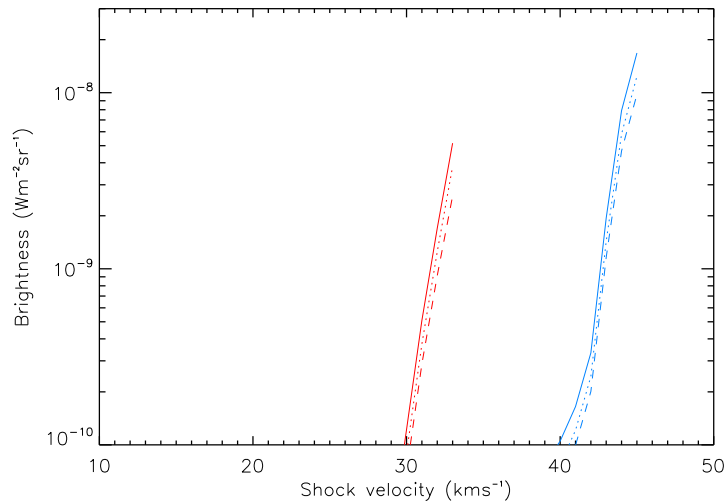
Figure 2.17: [FeII] emission in C-type shocks as a function of shock velocity. Linestyles are as above, Fig. 2.16. Brightness is displayed for a preshock density of 10^6 cm^{-3} and b is 1.0 (red) and 3.0 (blue).

methods to recognize whether a model result should be considered as faulty or not. The sources for wrong results are summarized here and detailed below:

- C- to J-type shock (sonic point; only valid for C-type shocks)

- No shock (pushed gas; only valid for C-type shocks)

- Unphysical results

- Random, but persistent errors

C- to J-type shock

As the temperature in a C-type shock increases H_2 will eventually be dissociated. When H_2 dissociates the main coolant of the shock is removed causing a rapid increase in temperature. A sonic point forms which in effect turns the C-type shock into a J-type. The velocity at which this happens is called the critical velocity, v_{crit}. It is not possible to treat this in the models and it is not possible to predict v_{crit} analytically. Therefore if the input velocity is greater than v_{crit} the model will collapse. In this case the model always collapses at the point of maximum temperature. Hence all models where the last point contains the maximum temperature are excluded.

No shock

If b is very high or the velocity very low, the gas will never be shocked. This is because the Alfvén velocity of the neutrals will exceed the shock velocity and the gas will only experience a gentle push from the shock front. Thus we find

$$
\begin{aligned}
v_s > v_A \quad &= \quad \frac{B}{\sqrt{4\pi\rho}} \\
&= \quad \frac{b\,\sqrt{n_{pre}[\mathrm{cm^{-3}}]}\,[\mu\mathrm{Gauss}]}{\sqrt{4\pi\,\mu\,n_{pre}}} \\
&= \quad 2.18\,b\,\sqrt{\frac{m_H}{\mu}}\ \mathrm{km\,s^{-1}}
\end{aligned}
\tag{2.2.8}
$$

where ρ is the density and μ the mean molecular weight. Typically μ is of the order of 2-2.5 m_H and the shock speed must then be greater than (1.38-1.54)$\times b$ km s^{-1}.

In a C-type shock the compression factor is given by (e.g. Draine & McKee 1993)

$$
\frac{n_{post}}{n_{pre}} = \sqrt{2}\,\mathcal{M}_A
\tag{2.2.9}
$$
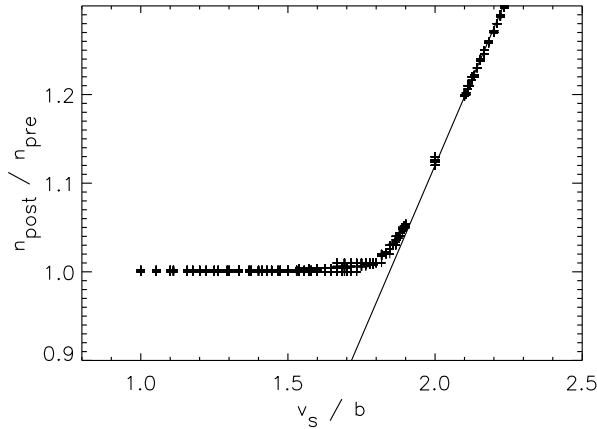
Figure 2.18: The compression factor in C-type shocks as a function of v_s/b. Each cross corresponds to a model result. The line corresponds to Eqn. 2.2.10.

where $\mathcal{M}_A$ is the Alfvénic Mach number defined as v_s/v_A. In the models we find that

$$\frac{n_{\text{post}}}{n_{\text{pre}}} = 0.775 \frac{v_s \, [\text{km s}^{-1}]}{b} - 0.5 \qquad (2.2.10)$$

as shown in Fig. 2.18. For a shock to occur the compression must be greater than 1 resulting in

$$\begin{aligned} \frac{n_{\text{post}}}{n_{\text{pre}}} &= 0.775 \frac{v_s \, [\text{km s}^{-1}]}{b} - 0.5 > 1 \;\Rightarrow \\ v_s &> 1.94 \, b \, \text{km s}^{-1} \end{aligned} \qquad (2.2.11)$$

This value corresponds to $\sqrt{2} \mathcal{M}_A$ for a mean molecular mass of 2.5 m_H.

Eqn. 2.2.11 poses the stronger constraint of the two. Furthermore the models themselves predict no compression if v_s/b is less than ~2. This is shown in Fig. 2.18 where the compression factor is displayed as a function of v_s/b. Therefore this is the constraint we will be using throughout.

Unphysical results

A number of model predictions may be tested to see whether they produce results that agree with simple physical predictions or arguments. Below I will explain the tests used to verify model results. If the model predictions are not in concordance with these simple predictions, some of them may result from discrepancies in the model itself and others may be due to the programs that extract results.

Maximum kinetic temperature in J-type shocks   We have seen that it is possible to use the Rankine-Hugoniot equations to predict the maximum kinetic temperature in J-type shocks (see Eqn. 2.2.1). This may also be used to verify the temperature predicted by the models. If the temperature varies more than 20% from that calculated in Eqn. 2.2.1, the results are excluded. The value of 20% is chosen so as to allow for small numerical discrepancies.

Low brightness   To avoid confusion any brightness below 10^{-13} W m^{-2} sr^{-1} is set equal to zero following the example of Wilgenbus et al. (2000). If the brightness is so low it implies that the upper level of the transition is not significantly populated.

Width   If the width at 50 K is smaller than the width at 1000 K obviously something is wrong. Models where this happened have been listed and examined by hand (two J-type shock models and three C-type shock models). In all cases the temperature profile was irregular and the models have been eliminated.

   Furthermore, if the integrated brightness of an H_2 level is less than 10^{-13} W m^{-2} sr^{-1} the local line profile is not used to calculate the H_2 FWHM. In C-type shock models it is also a requirement that the v=2-1 S(1) local emission FWHM is less than the v=1-0 S(1) and v=1-0 S(0) local emission FWHM.

Random discrepancies in results

Even with all of the above filtering there are still results that are not trustworthy. When displaying a certain prediction, such as a line brightness as in Fig. 2.16, these discrepancies will show up as peaks and the the given property will not be a continuous function of the input parameters.

   Because the resolution in the grid in terms of v and b is relatively high, it is possible to locate these discrepancies by looking at neighbouring values. I designed a routine that went through all input-points and compared them with their nearest neighbours in (v,b)-space. If the point was more than a factor of two off from the mean of the nearest neighbours, the point was discarded and set equal to zero. Other results from the same model are considered valid, unless they are also significantly different from their nearest neighbours.

   I tested that the model results are reproducable by rerunning a large number of the "faulty" models. Model results were always consistent. Once the models have been identified it is possible to overcome these discrepancies by for example choosing a velocity that is 0.1 km s^{-1} higher. This has not been done in the present work.

2.2.4   Strategy for reproducing observations

With the above discussed results and predictions it is possible to construct a strategy for reproducing observations effectively. Ideally the following constraints are possible to observe directly:

- Velocity: Proper motion and/or radial velocity

- [FeII] emission

- Shock width

- Dynamical age

- Absolute H_2 brightness of at least one line

- Line ratios of several H_2 lines (excitation diagram)

The input parameters that we wish to determine are: shock type, shock velocity, preshock density, b, initial ortho/para ratio.

Velocity

One should be careful when using the observed velocity as a constraint. As discussed in the introduction (Sect. 1.3.2) the shock velocity may be significantly lower than the observed object velocity.

[FeII] emission

If [FeII] emission is observed, it can be used as a discriminator between C- and J-type shocks. As discussed above, [FeII] emission is predicted primarily in dissociative J-type shocks. Lack of [FeII] emission does not imply that the shock is of C-type, however.

Shock width and dynamical age

The shock width and age depends on b, preshock density, shock velocity and degree of ionization as discussed above. The degree of ionization is determined in the models and is not a free parameter. Since the width depends on b^2, and we consider the preshock density over four orders of magnitude, these two parameters are more important than the shock velocity. If the shock width is resolved it implies that the shock is of C-type as discussed above.

Absolute H_2 brightness and H_2 excitation diagram

The absolute H_2 brightness and H_2 line ratios depends on all five input parameters (shock type, preshock density, shock velocity, *b*, initial ortho/para ratio). Previously we have used the observational constraints to determine four of them, shock type, preshock density, shock velocity and *b*, it is now possible to determine the initial ortho/para ratio.

The above strategy is very idealized. In general it is necessary to have at least five constraints to determine the five input parameters. But even with five constraints it is not always possible to reproduce observations. There may be several reasons for this. First of all, the preshock density may be lower than the densities in the grid, the velocity higher, etc. Second of all, the shock may be a non-steady state C-type shock. In this case we may observe a shock that emits [FeII] emission indicating it is a dissociative J-type shock. But at the same time the H_2 emission, which is primarily generated in the magnetic precursor, may indicate that we are observing a C-type shock. Or we may resolve the shock width, which clearly indicates a C-type shock. But, as is often observed, HH-objects are capped by atomic and ionic emission (such as [FeII] emission) and in the wake H_2 emission is observed in C-type shocks.

All in all, a good common physical sense is needed when interpreting observations. Even though the grid proposes one model as a best-fit model, it may not necessarily be the best-fit model when considering all the data available. Examples of this is given in Chapter 6.

2.3   3D model construction

Here I will provide a description of the method for constructing 3D models. These models will be used in analyzing bow shocks observed in the Orion Molecular Cloud. This description will not contain all details, for that I refer the reader to the M.Sc. thesis of T.L. Ravkilde[3], who has done all of the technical work in close collaboration with Sylvie Cabrit (Observatory of Paris), Guillaume Pineau des Forêts (IAS, Orsay) and myself. This work is currently in preparation for publication.

2.3.1   Recipe for model construction

To construct a 3D bow shock model the following is done:

---

[3]The thesis is available at `http://www.phys.au.dk/~ravkilde/msc/`

- Define an algorithm which dictates how your velocity, density and magnetic field strength shall change along the bow.

- Define a 2D bow shape and cut it into a number of discrete segments.

- Assign a 1D shock model with the given velocity, density and magnetic field strength to each segment.

- Bend your model results along the predefined bow shape.

- If the bow model is axisymmetric, it can be rotated into 3D, and maybe inclined.

In the following I will discuss these points. However I will try to keep the technical details at a minimum and instead refer the reader to the M.Sc. thesis by T.L. Ravkilde.

Continuity of physical properties along the bow

In the frame of the shock, the gas is streaming by the shock at a velocity of v_s. However, only the component of the gas moving perpendicular to the surface is interacting with the surface. Thus the shock velocity at any given point P on the bow surface is given as $v_P = v_\perp = v_s \sin\varphi$. For a definition of the different angles, points, etc. see Fig. 2.19. v_P is used as the input shock velocity for the 1D shock models. We define the apex of the shock to be at point A marked on Fig. 2.19.

The magnetic field must be transverse to the shock propagation direction to act on the ions in the shock by implication of the Lorentz force, $\vec{L} = q(\vec{E} + \vec{v} \times \vec{B})$. Hence the component of the magnetic field of interest in our shock model is expressed by $B_P = \vec{B}_\parallel$ such that $B_P = B\cos\eta$.

The inclination of the bow shock to the line-of-sight ψ is also an important parameter when trying to decipher the nature of a bow shock, since it determines the projection onto the plane-of-the-sky, and may obscure the bow shock nature completely if $\psi = 0$. We define a bow shock with $\psi < 90°$ to be blueshifted.

Assigning models to the bow shape

In this section we will describe how to align shocks onto a regular rectangular surface, which we will then later bend to the correct shape. All 1D models are calculated using an adaptive mesh routine, so the steps in a model are not of the same size. So the first thing to do, is to regrid the model results so that all models along the bow have the same step-size. In doing so, we are only considering model points where the kinetic temperature is greater than 1000 K. This is done
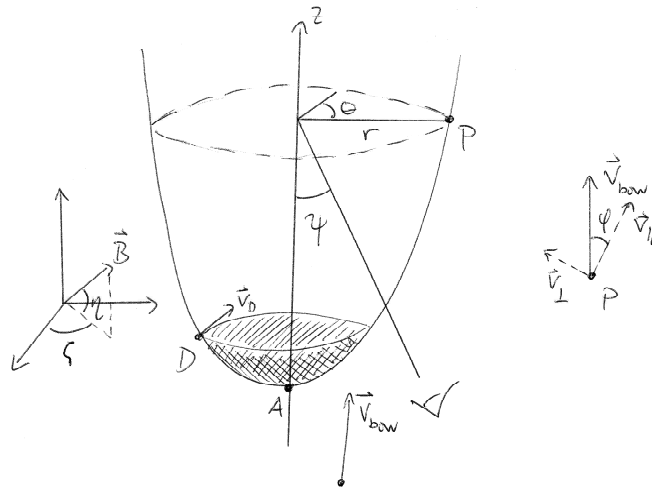
Figure 2.19: Schematic presentation of a bow shock from the reference frame of the shock. The ambient gas is streaming past the shock at a velocity, v_s.

to limit the number of model points considered. The temperature of 1000 K has been chosen because it is above this temperature that H_2 is vibrationally excited, as discussed above. The models are then aligned according to maximum kinetic temperature.

When models have been regridded and aligned we make an interpolation between different models so that output parameters will vary continuously. The model results are stored in a 2D array.

Bending model results

With this recipe it is in principle possible to use any shape one can think of. For the present work we will be examining axisymmetrical bow shocks of the form

$$z = f(r) = L_{\text{bow}} \left(\frac{r}{R_{\text{bow}}} \right)^s , \tag{2.3.1}$$

where L_{bow} and R_{bow} are the length and radius of the bow from the apex to the truncation point of the wings, respectively. We will limit ourselves to paraboloids here, that is $s = 2$.

With the 2D array that we have calculated it is in principle fairly simple to bend it along any predefined shape, in our case a paraboloid. Even though

bending the data bar is fairly simple, a lot of technical details are needed to make sure that the parameters in the bended result are continuous, that there are no gaps, etc. Gaps may arise as points who were previously neighbours are now further apart. This we name the fishbone effect because the 2D array containing our model results will be bent like a set of fishbones.

Rotation into 3D

We now have a two dimensional profile of half a bow shock. It is now a matter of rotating the 2D profile along the axis of symmetry. The result at this point is a data cube containing the full physics-chemistry coupled model of a bow shock. Different levels of the shock may be investigated by simply looking at slices of the data cube. In this work, we want to compare directly with observations, i.e. we require projections of the data cube onto a plane perpendicular to the line-of-sight.

There are several ways to achieve an arbitrary point of view through the data cube. Here we simply rotate the 2D slices lying in a plane spanned by two of the x, y, and z axes along the third axis, like turning parts of a Rubik's cube one after the other. This method was chosen because of its ease of implementation.

While the shocks in OMC1 have local preshock densities of 10^5–10^6 cm^{-3} (Kristensen et al. 2003, 2007a), they are still optically thin. We therefore ignore any opacity effects when looking through the volume and instead treat it as completely transparent.

Results of 3D model

We will not show any results of the 3D modelling in this Section. There are several examples in the thesis by T.L. Ravkilde. However we will return to the 3D model in Sect. 5.2 where we will compare the model directly with observations of a bow shock in OMC1. By way of examples we will show some of the shortcomings of the 3D model and discuss the errors that are inherent in this method for constructing 3D models.

2.4   Concluding remarks

We have here presented some results of a large grid of 1D shock models. We are currently preparing the model results given in Sect. 2.2 for publication. This publication will include both a general review of some of the more important results, but we will also make the recorded model outputs publically available on the "Centre de Donnée astronomiques de Strasbourg" (CDS) site.

The results may be applied to the interpretation of observations of any type of molecular shock almost regardless of origin. As such they will serve as a valuable tool for the astrophysical community (once they have been published). However, it is of course still important not to regard the model results presented here as the absolute truth. As discussed in Sect. 2.1.3 the model is still suffering from several shortcomings, one of the most important being the 1D geometry. Furthermore the model is in a continuous state of evolution, so model results presented here will almost certainly be outdated at some point.

Therefore one of the other major contributions is the programs that run the grid, extract the results and verify that they are not seriously flawed. Thanks to these programs this process is now fully automated and the only limitation on running large grids of models is computing time. It is possible that we have not detected all criteria for deciding whether a model result is to be trusted or not, and this will also be a continuing work.

In the following Chapters I will provide examples on how to interpret observations of jets and outflows associated with young stellar objects. I will also show, that often it is not straight-forward to interpret the data, and often it is not possible to reproduce observations by a single shock model or by a steady-state shock model.

There still exists a vast amount of results which have not been analysed at all. These include the species abundances and a more detailed analysis of the cooling functions. However, since all the results have been stored, it is possible to extract them. For any given set of result, it typically takes ~1 day to extract them.

Observations of the Orion Molecular Cloud

I have been working on two different sets of observations of the Orion Molecular Cloud (OMC1). The first was taken in December 2000 using the Canada-France-Hawaii Telescope (CFHT) the other is from December 2004 and was obtained with the European Southern Observatories (ESO) Very Large Telescope (VLT), UT4. These two datasets will in the following be referred to as the CFHT and VLT data respectively.

In this chapter I will go through the data reduction of the two datasets. Even though I have not been part of the observation team, I have worked on the data reduction and subsequent analysis.

Both observations have been performed using adaptive optics (AO) systems and a short introduction to observing with AO will be given. In the CFHT data, narrow-band filters have been used to isolate emission from H_2 rovibrational transitions, whereas in the VLT data a Fabry-Perot interferometer has been used. There are a number of common traits in data reduction and issues that need to be considered. These will be dealt with in this chapter.

3.1 Adaptive optics

Both sets of observations have been performed with the use of adaptive optics (AO) systems and a short introduction will be provided here. At CFHT the PUEO adaptive optics system was used (Rigaut et al. 1998), while at VLT NAOS was used (Lenzen et al. 2003; Rousset et al. 2003).

AO systems are of crucial importance for the observations performed here. Without AO the resolution would be limited by the seeing, which in even the best cases rarely fall below $0\rlap{.}''3$. By comparison the diffraction-limited resolution of a telescope with a given diameter, D, at a wavelength λ is given as $\theta_0 \approx 1.22\ \lambda/D$. In the case of the VLT where $D = 8.2$ m the diffraction-limited resolution at 2.1 μm is $0\rlap{.}''064$.
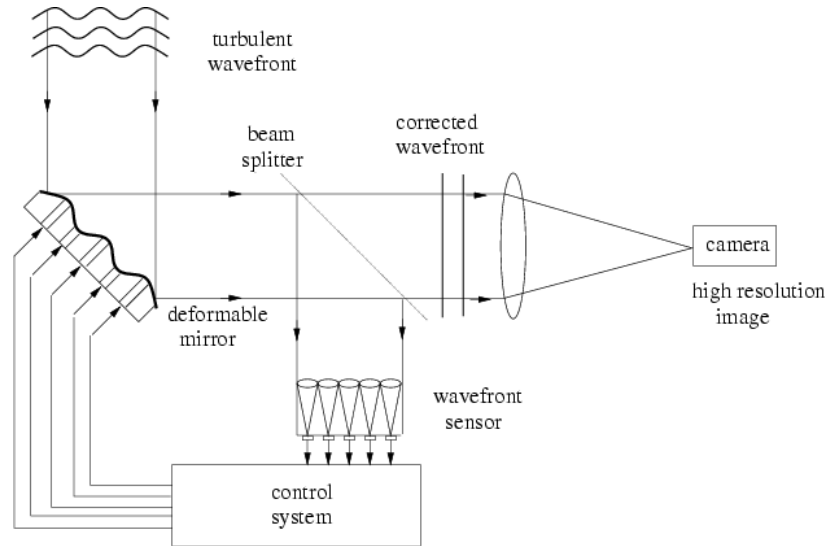
Figure 3.1: Schematic view of an adaptive optics system.

An AO system works by imaging a star (the guide star) at a high sampling-frequency. For both PUEO and NAOS the sampling frequency is several hundred Hz. This means that an image is taken and processed and the information is passed to actuators that change the shape of a deformable mirror several hundred times per second (see schematic in Fig. 3.1). For this reason the guide star must be bright (for brightness limits, see Sect. 3.2.1 and 3.2.2).

Turbulence is not uniform across the sky. The isoplanatic angle is the angle over which the turbulence may be considered uniform and it depends on the wavelength as $\lambda^{6/5}$. For K-band observations at a wavelength of ~2.2 μm the angle is of the order of $20''$. The distance between the guide star and the science target should be smaller than the isoplanatic angle. For these observations it was possible to find stars bright enough and close enough to make the AO system work.

The AO systems work in closed-loops. When the AO is locked on an object it will monitor the behavior and calculate the parameters needed to correct for atmospheric distortions. However in general the loops should not stay closed for more than one hour under average tip-tilt conditions as atmospheric conditions can change drastically over this time-period. After one hour of observing the AO should be re-locked on a medium position on the guide star. This was especially important for the VLT data (see below Sect. 3.2.2).

Finally the atmospheric conditions at the time of the observations also play an important role. The more stable the atmosphere is, the more efficiently the

AO system will work. One method to measure the efficiency of the AO system is through the Strehl ratio. The Strehl ratio is defined as the ratio of the peak intensity of the measured point spread function (PSF; the function describing the distortion of the star) to the theoretical maximum for a telescope with perfect optics and no atmosphere. For good corrections the Strehl ratio is above ~30%.

3.1.1 Strehl ratio

For a perfect spherical mirror the intensity distribution in the focal plane is given as (e.g. Kitchin 1984):

$$I = I_0 \left(\frac{J_1(\beta)}{\beta} \right)^2 \, , \tag{3.1.1}$$

where $\beta = (\pi D \sin \theta)/\lambda$, D is the diameter of the main mirror, θ the radial co-ordinate of the focal plane, λ the wavelength and J_1 is the first degree Bessel-function of the first order.

When comparing the integrated brightness of the star as measured with perfect optics and no atmosphere, it is clear that it must equal the observed integrated brightness of the star. This allows the determination of I_0 in eq. 3.1.1:

$$
\begin{aligned}
I_{\text{obs}}^{\text{total}} &= I_{\text{perfect}}^{\text{total}} \\
&= \int I_0 \left(\frac{J_1(\beta)}{\beta} \right)^2 \, \mathrm{d}A \\
&= I_0 \int_0^{2\pi} \int_0^{\infty} \beta \left(\frac{J_1(\beta)}{\beta} \right)^2 \, \mathrm{d}\beta \mathrm{d}\theta \\
&= I_0 2\pi \int_0^{\infty} \frac{J_1(\beta)^2}{\beta} \, \mathrm{d}\beta \\
&= \pi I_0 \, .
\end{aligned}
\tag{3.1.2}
$$

The maximum intensity of the perfect optics system is

$$I_{\text{perfect}}^{\text{max}} = \lim_{\beta \to 0} I_0 \left(\frac{J_1(\beta)}{\beta} \right)^2 = \frac{I_0}{4} \, . \tag{3.1.3}$$

Thus the Strehl ratio may be calculated in the following way:

$$
\begin{aligned}
S r &= \frac{I_{\text{obs}}^{\text{max}}}{I_{\text{perfect}}^{\text{max}}} = \frac{I_{\text{obs}}^{\text{max}}}{I_0/4} \\
&= \frac{I_{\text{obs}}^{\text{max}}}{I_{\text{obs}}^{\text{total}}/(4\pi)} = 4\pi \frac{I_{\text{obs}}^{\text{max}}}{I_{\text{obs}}^{\text{total}}} \, .
\end{aligned}
\tag{3.1.4}
$$

3.2 Observation runs

First I will give a brief summary of how the observations were performed. This is only meant as a short introduction to the two datasets and further details will be given later. The positional reference we use throughout, when discussing observations of OMC1 is the position of TCC0016: $05^h35^m14\overset{s}{.}91$, $-05°22'39\overset{''}{.}31$ (J2000).

3.2.1 CFHT December 2000

Observations were performed at the Canada-France-Hawaii Telescope on Mauna Kea, Hawaii on the nights of the 6 to 8 December 2000. Observations are centered on the BN-object situated 45″ northwest of the Trapezium stars. The total field of view is shown in Fig. 3.2. Observations cover the regions designated as Peak 1 and 2 by Beckwith et al. (1978).

   The PUEO adaptive optics system was used with the KIR detector (1024×1024 pixels). The lens set used gave a pixel scale of 0″035 per pixel resulting in a field of view of 36″×36″. Narrow-band filters were used to isolate individual H_2 rovibrational line emissions. Altogether data were recorded for ten different filters corresponding to seven different H_2 lines, Brγ and two continuum filters. Specifications for the filters used are given in Table 3.1.

   Data consist of seven overlapping individual frames of which only three have been analysed (see below for further details). The observation log is shown in Table 3.2. The weather conditions at the time of the observations were rather poor, the seeing was typically $\geq 1\overset{''}{.}5$. No observations of calibration stars were performed.

   Several guide stars were used for locking the PUEO AO system: TCC0016 (m_V=14.0), Parenago 1839 (m_V=14.6) and Parenago 1819 (m_V=14.4). Under optimal conditions the limiting magnitude for guide stars is ~17. Exposure time was 300 s for each field and each filter.

   We only use the 6307, 6310 and 6323 filters here (continuum, H_2 v=1-0 S(1) and H_2 v=1-0 S(0) respectively). In the other filters the signal to noise (S/N) ratio were either too low or there is significant atmospheric absorption of the line. Only in one or two very bright objects was it possible to detect a signal. Atmospheric absorption will be discussed below in Sect. 3.3.3.

Data rejection

Unfortunately it was necessary to reject a large amount of data for several reasons. The three main reasons for this are

- Some of the observed lines are simply too faint to be observed.
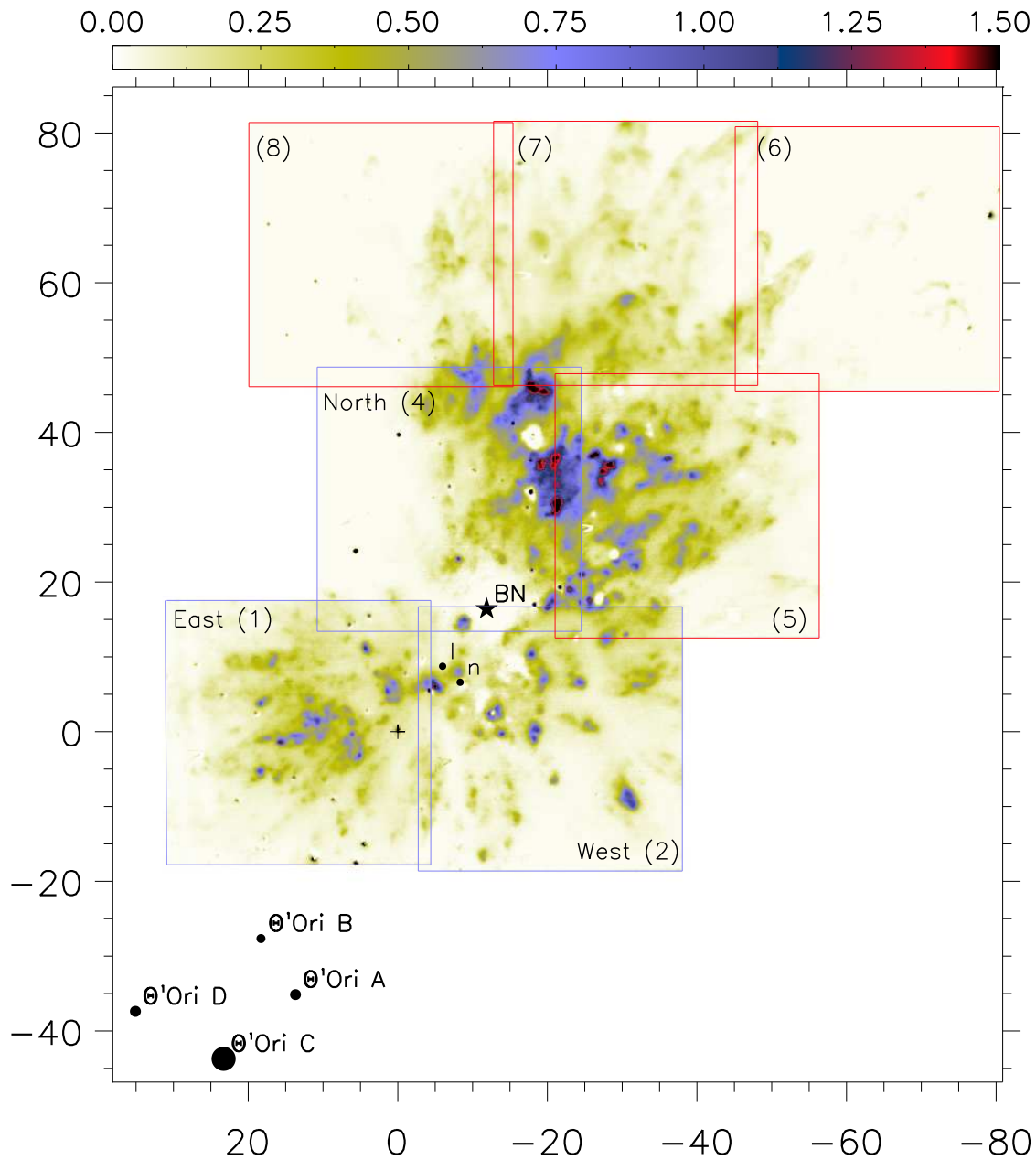
Figure 3.2: Finding chart of CFHT observations. Data show continuum-subtracted H_2 emission in the v=1-0 S(1) line at 2.12μm. The colourbar is in units of 10^{-5} W m^{-2} sr^{-1}. The positions of the Trapezium stars are marked. Axes are in arcseconds and offsets are given with respect to TCC0016 marked by a cross (+). The position of radio sources I and n are also given as well as BN (Menten & Reid 1995). Boxes indicate the location of our 7 fields of view, each measuring 36″×36″. Blue boxes marks fields which have been used in the data-analysis while red fields have not (see text for further details). Numbers in parentheses are the region numbers.

Table 3.1: *Specifications of the narrow-band filters used during the CFHT observations. Obtained from the CFHT website. Only data obtained with the filters marked with a 'y' were actually analysed.*

Number	Filter	Central wavelength (μm)	Bandwidth (nm)	Used
6306	H_2 v=1-0 S(1), z=0.01	2.143	30.0	n
6307	Brγ, z=0.01	2.183	30.0	y
6310	H_2 v=1-0 S(1)	2.122	20.0	y
6311	Brγ	2.166	20.0	n
6217	H_2 v=1-0 S(3)	1.957	25.5	n
6320	H_2 v=2-1 S(2)	2.154	26.7	n
6323	H_2 v=1-0 S(0)	2.223	24.9	y
6321	H_2 v=3-2 S(1)	2.386	31.0	n
6317	H_2 v=1-0 S(2)	2.030	21.0	n
6312	H_2 v=2-1 S(1)	2.248	20.0	n

Table 3.2: *Observation log for the CFHT observations performed on the 6 to 8 December 2000. Filter numbers are given in Table 3.1. The exposure time was 300 s for each observation. Region numbers refer to Fig. 3.2. N1, N2 and N3 refer to the nights of the 6th, the 7th and the 8th December, respectively.*

Filter	Reg. 1	Reg. 2	Reg. 4	Reg. 5	Reg. 6	Reg. 7	Reg. 8
6306	2×N1	N1	N1	N1			
6307	2×N1	N1	N1	N1	N1	N1	N1
6310	N1, N2	N1	N1	N1	N2	N2	N2
6311	2×N1	N1	N1	N1	N1	N1	
6217	N2	N2	N2	N2	N2	N2	
6320	N3	N3	N3	N3			
6323	N2	N2	N2	N2	N2	N2	N2
6321	N3	N3	N3	N3			
6317	N2	N2	N2	N2	N2	N2	
6312	N3	N3	N3	N3			

- Some lines are strongly affected by atmospheric absorption.

- Some data show artefacts which cannot be removed.

In the following I will go through each of these points.

Faint lines   The noise level for the CFHT data is of the order of $10^{-7}\,\mathrm{W\,m^{-2}\,sr^{-1}}$ for all filters. This is mainly due to the relatively short exposure times of 300 s. Some of the lines we observe fall below this noise level. We do not detect the following lines: H_2 v=1-0 S(2), H_2 v=3-2 S(1) and Brγ. In principle this gives us an upper limit for emission in these lines which we can use later on. However, since the noise level is relatively high the constraint is very weak, and we have chosen not to use it. Furthermore the H_2 v=2-1 S(1) line is very weak and we only detect it in the brightest regions.

In the three northern-most regions (regions 6, 7 and 8) we only detect H_2 v=1-0 S(1) emission. Due to this we choose not to include them in our analysis, and instead focus on the inner part of OMC1. Region 1 corresponds to Peak 2 of Beckwith et al. (1978) and regions 4 and 5 correspond to Peak 1.

Atmospheric absorption   As discussed below atmospheric absorption may strongly affect our results. Certain lines will be more affected than others, including in particular lines at the edge of the K-band, close to 2 μm and to 2.5 μm. The following two lines were excluded on this basis: H_2 v=1-0 S(2) and H_2 v=1-0 S(3) with wavelengths of 2.03 μm and 1.96 μm respectively. Both lines are very risky to use, and should in principle only be used if the velocity of the emitting gas is well-known, that is, the velocity has been measured at the level of our spatial resolution. In principle this should have been possible with the radial velocity data reported in Gustafsson et al. (2003); Gustafsson (2006); Nissen et al. (2007), but they have no local standard of rest.

Wiggles in ratio maps   In some cases we discovered that artefacts were showing up superposed on the emission. These artefacts appeared as wiggles in primarily the left side of the images. An example is shown in Fig. 3.3. In the case of strong emission the problem is not important, as it seems the intensity of the wiggles are constant. When examining faint emission however, the wiggles are relatively strong. We did not find a method for removing the wiggles. Instead we discarded data were the wiggles were too prominent.

Unfortunately this involved most of region 5. For region 5 we found that it was only possible to use the H_2 v=1-0 S(1) line emission and none of the others. Therefore we have also excluded region 5 from our analysis.
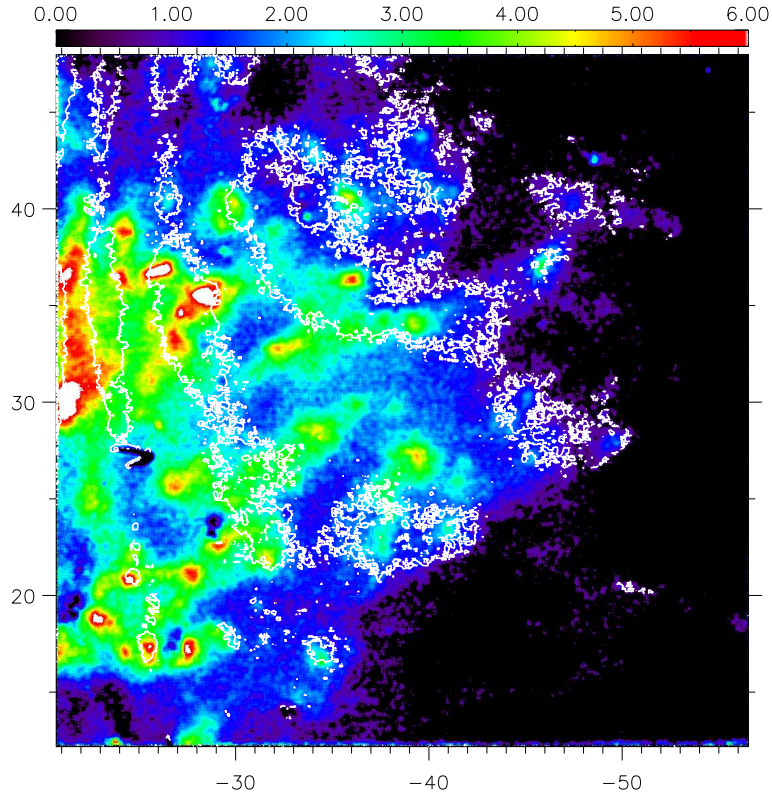
Figure 3.3: An example of the wiggles found in the CFHT data. Here we show a continuum-subtracted image of H_2 v=1-0 S(0) emission in region 5 (Fig. 3.2). The wiggles are not so clear in the emission image, but when making a ratio map between this line and the v=1-0 S(1) line the wiggles appear. The ratio is shown as white contours. The colour bar is for v=1-0 S(0) brightness in units of 10^{-6} $W\,m^{-2}\,sr^{-1}$ and coordinates are relative to TCC0016.

Strehl ratio and spatial resolution

The Strehl ratio has been calculated for 6–10 stars in each field using Eqn. 3.1.4. To measure I_{obs}^{total} we perform aperture photometry of the stars using an aperture of varying radius. The radius at which the S/N ratio is maximized is used as the aperture radius. This is measured independently for each star. Furthermore we subtract the sky emission by estimating the sky contribution in an annulus surrounding the star. Therefore it is imperative that the stars used are as free as possible from background emission and nebula emission and that they are non-saturated.

The Strehl ratio is found to be typically 8–16% for all fields and filters. The further the star is from the guide star the lower the Strehl ratio is, as expected. The low Strehl ratio reflects the poor seeing conditions at the time of the observations.

As a measure of the spatial resolution we adopt the FWHM of the point spread function (PSF) of stars. We use the same stars as above. The spatial resolution was found to be ~$0\farcs45$ corresponding to 200 AU at the adopted distance to Orion.

Data reduction

Data reduction to obtain H_2 images is performed so as to take account of any temporal variability of the sky background, spatial variations in the sensitivity of the detector (flat-fielding), differences in the sky brightness at different wavelengths and differing efficiencies of the detection system for the different filters used (see below). Dark counts are subtracted and bad pixels and noise due to cosmic rays removed.

Deconvolution

Because of the relatively low spatial resolution, we tried deconvolving the data with the method of Subtractive Optimally Localized Averages (SOLA; Pijpers 1999). SOLA has been shown to conserve information of the very smallest scale and we judge it to be superior for this work.

However as with all deconvolution techniques the S/N ratio is lowered. We find that it is possible to increase the resolution to $0\farcs24$ for the v=1-0 S(1) line while degrading the S/N ratio by $\sim 40\%$. For the much weaker v=1-0 S(0) line we could not afford to lower the S/N ratio. Therefore it was not possible to increase the spatial resolution. In the following we seek to compare data from different lines and we thus do not perform any deconvolution an any of the data.

Continuum subtraction

The continuum background emission is subtracted from each filter. The continuum is weak, that is, typically less than 10% of either major line brightness. We choose the emission from the Brγ, z=0.01 filter as continuum emission since emission in this filter shows very little emission save that from stars.

Absolute calibration

No calibration star was observed and we are therefore forced to use other means to obtain an absolute brightness. This has been done in two ways:

1. We tried to make an absolute calibration using the two stars TCC0031 ($m_{K'}$=9.86) and TCC0044 ($m_{K'}$=10.50) (McCaughrean & Stauffer 1994). These stars are both located in field East. We performed aperture photometry in much the same way as described in the following Sect. 3.2.2. The spectral types are M2 and M3e for TCC0031 and TCC0044 respectively. By looking at the ISAAC standard spectra (Pickles 1998) we find that for spectral type M2 there is a factor of 4 in difference between spectral type M2II and M2V. For spectral type M3 only M3III has an absolute calibration. But the difference between each subclass is probably of the same order of magnitude as for M2, so since the subclass is unknown we cannot determine an absolute calibration with any kind of accuracy.

2. We may compare the peak brightness of the brightest H_2 emitting region located 15″2 east and 2″1 south of TCC0016[1]. Here Vannier et al. (2001) have measured a brightness of $3.0\pm0.15\times10^{-5}$ $W\,m^{-2}\,sr^{-1}$. This may be directly compared to our observations.

By comparing our observations to previously calibrated data we are adding a layer of uncertainty to the absolute brightness. However for comparing the observations with shock- or PDR-models it is absolutely imperative that we have at least an estimate of the absolute brightness. This just goes to show the importance of always observing a calibration star.

3.2.2 VLT/NACO-FP December 2004

Data were obtained on December 3 to 5 2004 using the European Southern Observatories (ESO) Very Large Telescope (VLT). We used the UT4 (Yepun) equipped with the NAOS adaptive optics system and Conica infrared camera (NACO). Furthermore the telescope was equipped with a Fabry-Perot (FP) interferometer. The S27 setting was used which gives a pixel scale of 27.15mas and a field of view of 27″8×27″8.

Data were recorded in 3 fields centered around BN. These 3 fields are labelled East, West and North and are identified in Fig. 3.4. We obtained data for 3 rovibrational H_2 lines: v=1-0 S(1) at 2.12 μm, v=1-0 S(0) at 2.22 μm and v=2-1 S(1) at 2.25 μm. Each line was observed one or more times in each field, except the v=1-0 S(1) line in field East. There are no observations of the v=1-0 S(1) line in this field due to a lack of time. A log of the observations is given in table 3.3.

The same stars as for the CFHT observations were used as reference stars for the AO system, that is, TCC0016 for field East (m_V=14), Parenago 1819 for

---

[1] $05^h35^m14^s91, -05°22'39″31$ (J2000)

field North (m_V=14.4) and Parenago 1839 for field East (m_V=14.6). The visible wavefront sensor was used. The limiting magnitude of NAOS is 16.7.

The star HR1950 (HD37744) was observed for absolute calibration purposes. The coordinates are $05^h40^m37\overset{s}{.}2959$; $-02°49'30\overset{''}{.}851$ (J2000). Thus it has approximately the same airmass as OMC1. We will return to the absolute calibration in sect. 3.2.2.

The Fabry-Perot (FP) interferometer was used both to isolate individual spectral emission lines but also to scan over each spectral line to measure any Doppler shift and thus determine the radial velocity. This is done by using the FP as a tunable narrow-band filter with a bandwidth of $\lambda/\Delta\lambda \sim 1000$ that is ~ 2 nm. The central wavelength is then changed in very small steps, typically less than 1 nm while scanning over the spectral line. Each field was scanned in 15 to 18 steps. Each H_2 line was scanned from the far blue to the far red wing. The frames obtained in the wings are free from H_2 emission and have been used as continuum frames. The frames are also referred to as channel maps. It is desirable to have as many steps as possible in each scan and have as long an exposure time as possible. However the AO system should not stay locked for more than one hour at a time as discussed above, limiting both of these parameters. It is imperative that each field is completely scanned without re-locking the AO as this may cause differential effects to appear.

For this work the FP has only been used as a narrow-band filter. As it turned out there were problems with fringes appearing when trying to extract radial velocities from these data, and so far the problems have not been completely resolved. This is in spite of having worked closely together with Markus Hartung, ESO, the FP instrument scientist at the VLT. For a full account of the problems I refer the reader to Gustafsson (2006). In this work we are interested by the absolute brightness and there have been no problems extracting this from the data. In fact the problem with the fringes arises from the settings of the FP. The absolute brightness is obtained from an integration over several FP settings and so the fringes are completely smeared out in the brightness data.

Strehl ratio and spatial resolution

The atmospheric conditions were better for the VLT observations than for the CFHT observations. Typically the seeing was $\sim 1''$. This is reflected in a much higher Strehl ratio and better spatial resolution. Typically the spatial resolution was $0\overset{''}{.}10$–$0\overset{''}{.}20$ with a Strehl ratio of 25–60%. Average resolution and Strehl ratio are reported in Table 3.3 with the statistical uncertainty for each field.
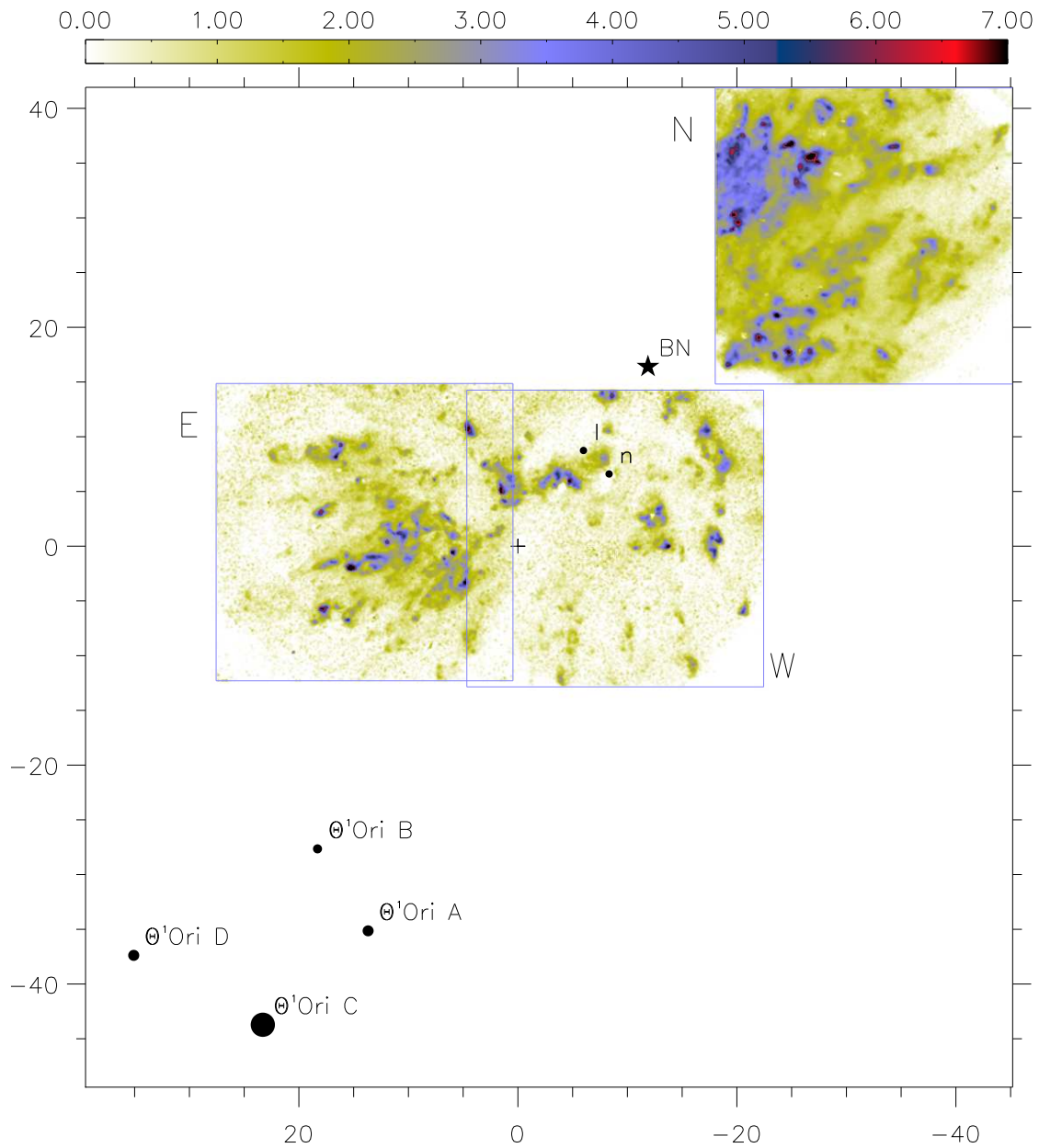
Figure 3.4: Finding chart for VLT-NACO/FP observations. Data show continuum-subtracted H_2 emission in the v=1-0 S(0) line at 2.23μm. The colour-bar is in units of 10^{-6} W m^{-2} sr^{-1}. The positions of the Trapezium stars are marked. Axes are in arcseconds and offsets are given with respect to TCC0016 marked by a cross (+). Our observed fields are outlined in blue boxes, each with a size of 27″×27″. The position of radio sources I and n are also given as well as BN (Menten & Reid 1995).

Table 3.3: Observation log for the VLT-NACO/FP observations performed on December 3-5 2004. We list the field (see Fig. 3.4 for location), line, exposure time per frame and the number of steps per scan. Furthermore the average spatial resolution and Strehl ratio are listed.

Field	Line	Night	Exp. time (s)	Steps	Resolution	Strehl ratio (%)
North	v=1-0 S(1)	1	120	15	0.″24±0.″07	14±09
	v=1-0 S(0)	1	240	16	0.″18±0.″08	25±10
		3	240	18	0.″19±0.″08	29±11
	v=2-1 S(1)	1	240	16	0.″21±0.″06	23±10
		3	240	18	0.″13±0.″05	43±13
West	v=1-0 S(1)	2	120	17	0.″16±0.″03	30±11
	v=1-0 S(0)	2.1	120	18	0.″12±0.″02	47±12
		2.2	120	18	0.″11±0.″02	49±15
		2.3	120	18	0.″11±0.″01	52±14
		3	120	18	0.″10±0.″01	59±16
	v=2-1 S(1)	2.1	120	18	0.″11±0.″01	56±15
		2.2	120	18	0.″13±0.″02	40±11
		2.3	120	18	0.″17±0.″05	25±11
		3	120	18	0.″10±0.″01	59±17
East	v=1-0 S(0)	3	120	18	0.″13±0.″03	47±16
	v=2-1 S(1)	3	120	11	0.″19±0.″04	25±14

Reducing FP data

As for the CFHT data, initial data reduction to obtain H_2 images is performed so as to take account of any temporal variability of the sky background, spatial variations in the sensitivity of the detector (flat-fielding), differences in the sky brightness at different wavelengths and differing efficiencies of the detection system for the different wavelength settings used. Dark counts are subtracted and bad pixels and noise due to cosmic rays removed. This has been done for each channel map.

Afterwards the channel maps were collected into data cubes, one for each emission line and each field. The channel maps were carefully registered with respect to each other, the accuracy being better than 1 pixel. This was done using stars in the field. The continuum was then subtracted from each channel map. We used the channel maps in the far wings as continuum maps.

Before each science scan the Ar line at 2.0992 μm was scanned to give the wavelength correction for each pixel. Next a lorentzian is fitted and integrated through each pixel as a function of the corrected wavelength. The integrated lorentzian is the line emission observed. The width of the lorentzian profile corresponds to the observed line width. In our case this was limited by the spectral resolution of the FP interferometer which is ~3000 km s^{-1}.

In order to fully reduce a FP data set and obtain accurate radial velocities many more steps are necessary. For a full account of FP data reduction and the involved problems I refer the reader to Gustafsson (2006) as this is not something I have been directly involved in.

Absolute calibration

For calibration purposes the star HR 1950 (HD 37744) was observed. The star has approximately the same airmass as OMC1. Observations of the star were performed on the first and second night and in the same manner as the science observations. The only difference was that the exposure time was set to the lowest possible value, 1.793s. This is due to the relatively high magnitude of the calibration star. All observations cover the same wavelength ranges as the three science lines. An absolute calibration has been performed for each frame and the results are listed in table 3.4 at the end of this section. Here we will only go through the absolute calibration for one frame in the v=1-0 S(1) line at 2.12 μm.

The *K*-band magnitude is 6.785±0.024 (Skrutskie et al. 2006) and the spectral type is B1.5V. For absolute calibration we use the observed calibration spectra given on the ESO-VLT ISAAC webpage[2]. The calibration spectra are reported in Pickles (1998). They do not supply a calibration spectrum for the spectral type B1.5V. However the calibration spectra for types B1V and B2IV show a difference of less than 4% in the *K*-band. We therefore assume that the absolute flux of our calibration star is identical to that of a star with spectral type B1V.

According to the ISAAC spectra the absolute brightness at 2.1185 μm (the wavelength of the first image in our scan of the v=1-0 S(1) line) is 0.007095 F_λ. The F_λ unit is the brightness of Vega (spectral type AOV) at a wavelength of 5556.0 Å. This brightness is observed to be $F_{5556.0\text{Å}}$(Vega)=(3.44±0.05)×10^{-9} erg cm^{-2} s^{-1}Å^{-1} (Hayes 1985).

We use the distance modulus to calculate the flux emitted by our calibration star. The relative flux is given by:

$$\frac{f_1}{f_2} = 10^{-0.4\ (m_1 - m_2)} \tag{3.2.1}$$

---

[2]Available at `http://www.eso.org/instruments/isaac/tools/lib/index.html`
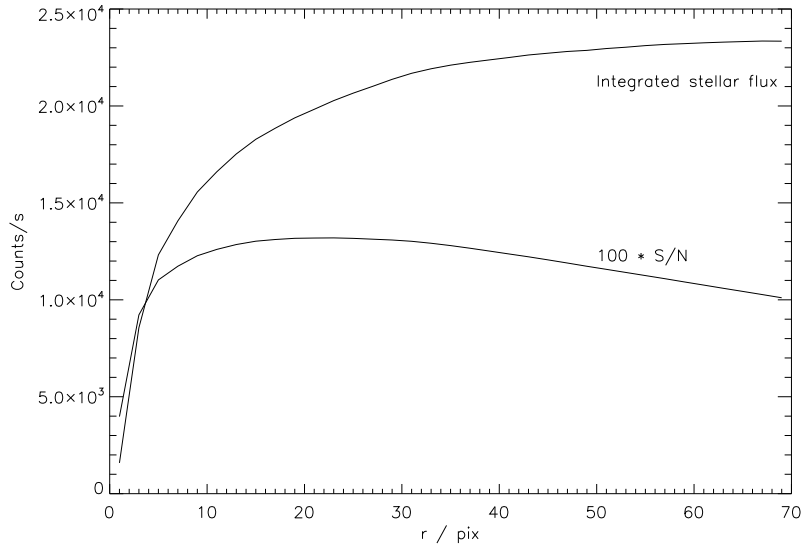
Figure 3.5: Aperture photometry of the calibration star HR1950. The total count rate within radius r is shown as well as the S/N ratio. The latter has been multiplied by 100. The S/N ratio peaks at a radius of ~23 pixels.

where index 1 and 2 indicate our calibration star and Vega respectively.

To estimate the total flux observed from the star we perform simple aperture photometry of the star. That is, we measure the total flux in an aperture centered on the star for varying radii, r from which we subtract the sky contribution. The sky contribution has been estimated from an annulus centered on the star, but with an inner and outer radius of 69 and 89 pixels respectively. As r increases so does the total stellar flux until it is almost constant. This is achieved at ~13 FWHM of the star. The FWHM is ~4.4 pixels.

For each r we also calculate the total signal to noise ratio (S/N) for the star. This is done using the "CCD equation" (e.g. Howell 2000). The maximum S/N is reached at a radius of 23 pixels (~5.3 FWHM) and has a value of 132. The flux inside this radius is what we use as the total stellar flux and it is $\phi_{obs} = 20274.8$ counts / 1.793 s = 11307.8 counts/s. This is shown in Fig. 3.5.

The FP interferometer acts as a filter with a width of $\lambda/\Delta\lambda = 1000$, that is, $\Delta\lambda = 2.12$ nm. The pixel scale (ps) in steradians is:

$$
\begin{aligned}
1 \text{ pixel} \quad &\sim \quad 0\farcs027 \times 0\farcs027 \\
&= \quad 1.713 \times 10^{-14} \text{ sr} \tag{3.2.2}
\end{aligned}
$$

Altogether we find that the calibration is

$$
\begin{aligned}
\text{cal} \quad &= \quad \frac{f_{2.1185\mu\text{m}}(\text{HR1950}) \, \Delta\lambda}{\phi_{\text{obs}} \, \text{ps}} \, 10^{-0.4 \, m_K} \\
&= \quad \frac{0.007095 \times 3.44 \times 10^{-9} \, \text{erg} \, \text{cm}^{-2} \, \text{s}^{-1} \, \text{\AA}^{-1} \times 2.12 \, \text{nm}}{11307.8 \, \text{counts/s} \times 1.713 \times 10^{-14} \, \text{sr}} \, 10^{-0.4 \times 6.785} \\
&= \quad 5.157 \times 10^{-6} \, \text{Wm}^{-2} \, \text{sr}^{-1} \, (\text{counts/s})^{-1} \, . \qquad\qquad (3.2.3)
\end{aligned}
$$

The S/N ratio for the stellar flux is 132 leading to an uncertainty of 0.76%. The RMS error on the calibration spectra is <1% (Pickles 1998). To calculate the total uncertainty on our calibration, we assume that it is equal to 1%. The error on the value of F_λ is 1.5% (Hayes 1985). We ignore systematic errors in the pixel scale and the effective filter width. As stated above, the uncertainty on the magnitude of HR1950 is 0.35% (Skrutskie et al. 2006).

Calculating the standard uncertainty on the calibration I find σ=3.2%. This is the systematic uncertainty combined with the uncertainty obtained from photon statistics. The fact that we are using a calibration for type B1V instead of B1.5V has not been included as this is difficult to estimate. If the star was of type B2IV instead of B1V we find a difference of ~4%. Including this will increase the uncertainty to ~5%.

It is possible to compare with the calibration performed by Vannier et al. (2001). They found that the brightest part of Peak 2 (field East) had an absolute brightness in the v=1-0 S(1) line of $(3.00\pm0.15)\times10^{-5}$ W m^{-2} sr^{-1}. Unfortunately it is not possible to perform a direct comparison, as we do not have data for field East in the v=1-0 S(1) line. Instead we chose to compare this calibration with data from CFHT (see Sect. 3.2.1) which have been directly compared to the calibration from Vannier et al.. This of course adds another layer of uncertainty, and we will only use this as a guideline instead of an absolute verification.

We will do two comparisons. (1) We may compare our calibration of the v=1-0 S(0) line in field East with field South-East of the CFHT data. (2) We can also compare the brightness of the v=1-0 S(1) line in another field.

1. The v=1-0 S(0) line is a factor of 2.04 weaker than the v=1-0 S(1) line at the centre of the brightest object in field East. Thus the absolute brightness is 1.50×10^{-5} W m^{-2} sr^{-1}. In this dataset we find that the absolute brightness is $\sim1.9\times10^{-5}$ W m^{-2} sr^{-1}. Thus the two are in good agreement with eachother, considering the different conditions and the method of comparison.

2. In field West there is a bright bow shock located at a position 20.″5 west and 6″ south of TCC0016 (see sect. 5.2). The peak brightness according

Table 3.4: Absolute calibration results for each of the lines observed. The wave-length range of the v=2-1 S(1) line was scanned on nights 1 and 2.

Line	Night	Scans	Calibration 10^{-6} W m^{-2} sr^{-1} (counts/pixel)$^{-1}$
v=1-0 S(1)	1	15	5.15±0.04
v=1-0 S(0)	1	16	3.98±0.03
v=2-1 S(1)	1	15	3.73±0.03
v=2-1 S(1)	2	8	4.02±0.05
v=2-1 S(1)	2	8	4.02±0.05

to the CFHT data in the v=1-0 S(1) line is 0.8×10^{-5} W m^{-2} sr^{-1}. We now find that the peak brightness is $(2.06\pm0.11)\times10^{-5}$ W m^{-2} sr^{-1}. Here the difference is a factor of 2.5.

We conclude that the calibration shows the same order of magnitude as the CFHT data when they have been compared to the data from Vannier et al. (2001). It clearly displays why it is imperative always to observe a standard star if the data are to be absolute flux calibrated. Differences between observations may be significant. These include differing weather conditions, which result in different atmospheric transmissions and different spatial resolutions, but different instruments may also play an important role. For example in the CFHT data narrow band filters were used to isolate spectral lines. These had a spectral resolution of $\lambda/\Delta\lambda \sim 100$ whereas the bandwidth of the FP is an order of magnitude lower. Thus the sky contribution to the CFHT data will be significantly higher than here.

The results of the absolute calibration of the VLT data is sumarized in table 3.4. Here we list the calibration for each wavelength range. The calibration for the v=1-0 S(0) and v=2-1 S(1) are on average 25% lower than that for v=1-0 S(1). This is caused by the difference in absolute magnitude of the reference star at the different wavelengths.

3.3   Comparing emission maps of different lines

There are a number of issues that need to be considered when comparing emission maps of different lines. These considerations are common both for the CFHT and VLT data and we will go through them here. They include:

- Image registration

- Differential reddening

- Atmospheric absorption

- Relative calibration of line emissivities

- Contamination from other lines

In the following we will go through each of these factors discussing their impact on our observations.

3.3.1   Image registration

Image registration is imperative when comparing emission obtained at different wavelengths, even though they may be obtained with the same instrument. Image registration has been performed by fitting a 2D Gaussian to the emission from a star and then using the centroid position as the position of the star. Depending on the number of stars used this will lead to a registration of better than ±1 pixel over the entire field.

For the CFHT data we discovered that from a simple comparison between two images it was not possible to do a very accurate registration. By comparing the position of stars in one filter with the position of stars in another filter, it was found that it was necessary to change the image size to produce an accurate registration. In Fig. 3.6 we show the relative position of stars taken in the continuum filter (Brγ, z=0.01) and v=1-0 S(1) filter as a function of absolute position in the v=1-0 S(1) filter. For this particular combination of filters it was necessary to increase the size of the Brγ, z=0.01 image by 6 and 5 pixels in the x- and y-directions respectively to a size of 1030×1029 pixels. This has been checked for each filter-combination we used. After the rescaling of the images registration was better than ±1 pixel corresponding to 35mas or 1/13 of the PSF. For each field we used between 6 and 10 stars.

The reason for this is unknown. At first we suspected that it was due to a form of micro-lensing in the filters themselves, but the change in size is independent of filter, so we conclude that the filters do not play an important role.

The VLT data did not show similar problems. For these data it was possible to use between 6 and 11 stars resulting in an image registration better than ±1 pixel. This corresponds to 27mas or 1/5 of the PSF.

3.3.2   Differential reddening

The v=1-0 S(0) and v=2-1 S(1) lines will be less reddened than the v=1-0 S(1) line. The relative magnitude difference between the two is $\sim(\lambda_1/\lambda_2)^{-1.7}$ (Mathis
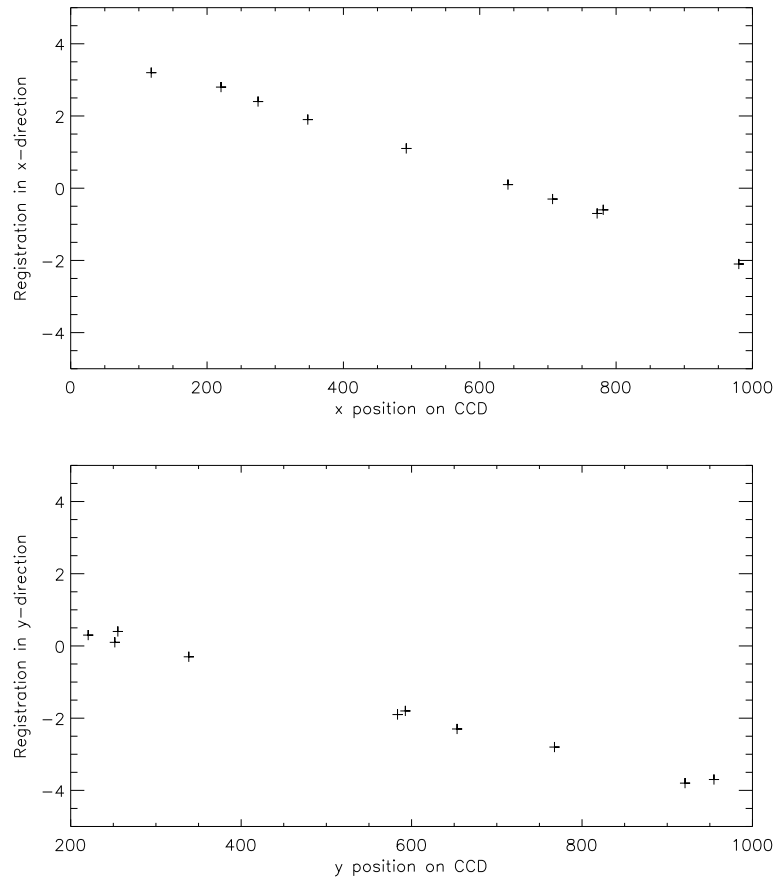
Figure 3.6: Registration in the CFHT data. The relative position of stars taken in the continuum filter (Brγ, z=0.01) and v=1-0 S(1) filter as a function of absolute position in the v=1-0 S(1) filter for 10 stars.

1990). If we assume that the extinction at 2.12 μm is 1^{mag} (Brand et al. 1989a; Rosenthal et al. 2000) the relative reddening or extinction is 0.106^{mag} or 0.90^{mag} at 2.25 μm. From the relation $m_1 - m_2 = -2.5 \log(F_1/F_2)$ we find that the flux ratio $F_{2.12}/F_{2.25}$ is 0.915 or that the v=2-1 S(1) emission may be overestimated be ~9%. Results for the v=1-0 S(0) line are similar due to the proximity in wavelength. Here we present results for data uncorrected for this imprecisely known and spatially variable differential absorption.

3.3.3   Atmospheric absorption

It is essential that brightness estimates are as free as possible from atmospheric absorption. The velocity of the gas must be considered in this context, as this will cause the lines to be Doppler-shifted. Data obtained (Dec. 2000) on the Canada-France-Hawaii Telescope, using a combination of the PUEO adaptive optics system and Fabry-Perot interferometry ("GriF"; Clénet et al. 2002; Gustafsson et al. 2003; Nissen et al. 2007), as well as extensive data in Chrysostomou et al. (1997), reveal that the region of OMC1 observed contains H_2 v=1-0 S(1) emission which shows velocity shifts, relative to Earth, of between +60 to -10 km s^{-1}. We are implicitly assuming that the v=1-0 S(0) and v=2-1 S(1) emitting gas are moving at identical velocity to the v=1-0 S(1) emitting gas.

Using the atmospheric absorption line atlas of Livingston & Wallace (1991), we find that there is negligible absorption for the v=1-0 S(1) line in all cases, save over a very narrow range of velocities around +30 km s^{-1} for which an absorption of 7% is found. For the v=1-0 S(0) line, the situation is similar with a weak absorption feature again of 7% at around +43 km s^{-1}. For the v=2-1 S(1) line there is also an absorption feature at +33 km s^{-1} of ~7%. GriF data show that the regions studied span the range of velocities which includes these values. Thus differential absorption may introduce systematic errors when comparing line brightness from the three lines, but of only a few per cent. The effect cannot be accurately determined and we choose to ignore it in the present work.

3.3.4   Relative calibration of line emissivities

To compare line emissivities obtained from different filters with different transmission profiles it is necessary to do a relative calibration. This is done by comparing the flux for each star and compare it to the flux of the same star in different filters. Fluxes are measured using aperture photometry as previously discussed. Here we are assuming that the stellar flux is constant over the wavelength range from 2.12 μm to 2.25 μm. It may not be constant, depending on the spectral type. For a star with spectral type K7 as TCC0016, the difference in brightness at 2.12 μm and at 2.25 μm is ~10% according to the ISAAC standard spectra (Pickles 1998). This has been ignored throughout, because the spectral type for most of the stars we are using is unknown.

We are also assuming that measured stellar fluxes are not affected by atmospheric absorption as discussed above. Within each filter there are several absorption features which may lead to an underestimation of the fluxes. However all features are very narrow and not very deep (typically less than 20%) and they are present in all filters. As above we choose to ignore this effect.

It is also possible to assume that the sky contribution in the two filters should be identical. This is a much less certain method as the count rates are much lower. We do not use this method except for verification purposes.

For the CFHT data this was done using the same 6 to 10 stars as for image registration. It is very important that the relative calibration is as accurate as possible since we do not have any independent means of verifying the result. In the case of the VLT data the observations of the calibration star will provide absolute calibration and hence relative calibration. However we do also compare the stars in the science scans as an independent check on the absolute calibration already performed. We find that the results are in very good agreement.

3.3.5 Contamination from other lines

It is possible that other line transitions, both H_2 lines and atomic lines, are located within the wavelength range of our filters, thus adding to the line brightness and leading to a systematic over-estimation.

Line contamination in filters

Within the v=1-0 S(1) filter only additional (high v, high J) lines may be present such as v=8-6 O(4) and v=3-2 S(4). These lines are negligibly weak in shocks but may be found in PDRs. However PDRs are intrinsically one to two orders of magnitude lower in brightness than the C-type shocks encountered here. Moreover these very high v lines are weak in PDRs (Black & van Dishoeck 1987).

Within the v=1-0 S(0) filter there is also contamination from the (high v, high J) lines, e.g. v=8-6 O(5). There may also be a weak contamination from the v=2-1 S(1) line, which lies 0.024 μm to longer wavelength than the v=1-0 S(0) line. However transmission through the S(0) filter of the v=2-1 S(1) line is only 3%. We conclude that contamination by other lines is not a problem for either the S(1) or the S(0) filters.

The continuum filter has a line centre 2.183 μm. Within this filter there are no H_2 lines. There may be some weak contribution from Brγ which we neglect here.

Line contamination in FP data

Using an FP practically eliminates this problem. Since each channel map is very narrow, ~2 nm, there is almost no line contamination. Even though 15–18 channel maps were obtained covering each line, the effective filter width is typically 10–15 nm or about half the width of the narrowband-filters. In any case, the arguments given above are certainly still true for the FP.

For the v=2-1 S(1) line at 2.247 μm there are no contaminating lines in the vicinity. Again we conclude that contamination by other lines is not a problem.

CFHT observations of OMC1: Results and discussion

In this chapter I will present the results we obtained from the CFHT data. This is a work mainly done by me and which is published in Kristensen et al. (2007a); Publication I. Since the spatial resolution of the CFHT data is significantly lower than for VLT data, we will primarily describe and examine large-scale properties of OMC1 here. For the VLT data where the spatial resolution and sensitivity is much higher we will examine in detail individual objects.

I will first describe how we can obtain important information on the state of the gas through comparison of ortho- and para-H_2 lines. The results that we obtain will then be compared with the shock models that was previously described in Chapter 2. We will also show how it is possible to compare individual shocks with the shock models. This we will refine in the following chapter.

4.1 Ortho/para ratios and their relationship to v=1-0 S(0) and S(1) line brightness

In principle it is necessary to obtain the full set of ortho- and para-lines for all vibrational levels in order to evaluate the real ortho/para ratio. A Boltzmann plot would then show departures from the high temperature equilibrium value of ortho/para = 3, if such departures exist (see Sect. 1.2.3). However we show below that because of the proximity in energy of the J=2 and J=3 levels in v=1, it is possible to obtain approximate values of an ortho/para ratio which are meaningful, using only S(0) and S(1) v=1-0 emission line data. To differentiate these values from the ortho/para ratio global to all lines, we name the term derived purely from v=1-0 S(0) and S(1), ϕ_{10}.

We use the definition of the ortho/para ratio found in standard textbooks and used in Hoban et al. (1991); Chrysostomou et al. (1993); Ramsay et al. (1993); Hora & Latter (1996); Neufeld et al. (1998); Wilgenbus et al. (2000), see also Sect. 1.2.3. The ortho/para ratio at local spin equilibrium (LSE) at a rotational

temperature of $T_{\rm rot}$ is given by (Sect. 1.2.3)

$$ortho/para({\rm LSE}, T_{\rm rot}) = \frac{\sum_{J \ {\rm odd}} 3(2J+1)\exp\left(\frac{-E_J}{k_{\rm B}T_{\rm rot}}\right)}{\sum_{J \ {\rm even}} (2J+1)\exp\left(\frac{-E_J}{k_{\rm B}T_{\rm rot}}\right)} \qquad (4.1.1)$$

where J is the rotational quantum number and E_J the energy of the rotational state for a given vibrational level v.

If the ortho/para ratio is different from 3 the data points of ortho-levels will be displaced as described above. In that case it is only meaningful to calculate the excitation temperature between neighbouring ortho data points and neighbouring para data points. Furthermore, in principle it is only possible to calculate an ortho/para ratio for one ortho data point and compare it to the two neighbouring para data points. In that case, the non-equilibrium ortho/para ratio is given by (Wilgenbus et al. 2000):

$$\frac{ortho/para(J)}{ortho/para({\rm LSE}, T_{\rm rot})} = \frac{N_J}{N_J({\rm LSE}, T_{\rm rot})} \qquad (4.1.2)$$

where N_J is the value of the column density of the non-equilibrium ortho-line and $N_J({\rm LSE}, T_{\rm rot})$ is the expected column density of the ortho-line, had it been observed at LSE at a rotational temperature of $T_{\rm rot}$. Note that we deal throughout with column density, unless otherwise specified, as this relates directly to observations. This implicitly ignores any spatial variation in the line of sight, though such variations must of course be present.

Referring to the upper state of the transition v=1-0 S(0), that is v=1, $J=2$, as $i=0$ and the upper state of v=1-0 S(1) that is v=1, $J=3$, as $i=1$, one obtains the approximate ortho/para ratio, ϕ_{10}:

$$\phi_{10} = \frac{N_1}{N_0}\frac{g_0}{g_1}\exp\left(\frac{E_1 - E_0}{k_{\rm B}T_{\rm rot}}\right)ortho/para({\rm LSE}, T_{\rm rot}) \qquad (4.1.3)$$

where g_i [$=(2I+1)(2J+1)$] is the total multiplicity and $(E_1 - E_0)/k_{\rm B} = 473$ K (see Table 1.2).

The column densities, N_i, in Eqns. 4.1.2 and 4.1.3 can be obtained from the observed brightness, I_i, using

$$N_i = \frac{4\pi\lambda_i}{hc}\frac{I_i}{A_i} \qquad (4.1.4)$$

where λ is the wavelength and A is the Einstein A-value for the corresponding

line (Table 1.2). Inserting Eqn. 4.1.4 in Eqn. 4.1.3 gives (Harrison et al. 1998):

$$\phi_{10} = \frac{I_1}{I_0}\frac{\lambda_1}{\lambda_0}\frac{A_0}{A_1}\frac{g_0}{g_1} \times$$

$$\exp\left(\frac{E_1 - E_0}{k_B T_{rot}}\right) ortho/para(\text{LSE}, T_{rot})$$

$$= 0.4970 \frac{I_1}{I_0} \exp\left(\frac{473\text{K}}{T_{rot}}\right) \qquad (4.1.5)$$

where we assumed $T_{rot}>300$ K for which ortho/para(LSE,T_{rot})=3.

Using ISO-SWS observations, Rosenthal et al. (2000) find that the rotational temperature measured with an aperture of ~15″ by 30″ is of the order of 3000 K. Le Bourlot et al. (2002) reanalysed the data and found the rotational temperature to be 3300 K. In Kristensen et al. (2003) it was found that the excitation temperature over a small field in region East varied between 2000 and 5000 K. This excitation temperature was calculated from the v=1-0 S(1) and v=2-1 S(1) H_2 lines using high spatial resolution data from the ESO 3.6 m telescope (see also Vannier et al. 2001). Unpublished data recently obtained from the VLT in the same two lines show that the excitation temperature in Peak 1 (NW of BN) is ~2000 K (see Sect. 5.1. In the following we have chosen a constant value of T_{rot}=3500 K based on all of the above observations.

The systematic errors generated by the energy term in Eqn. 4.1.5 are small. For example, given that the rotational temperature, T_{rot} is in the interval from 2000 K to 5000 K as suggested by the observations just mentioned, the error introduced by taking a constant value of the rotational temperature in the energy term $\exp(473 \text{ K}/T_{rot})$ is no greater than ~10%.

We emphasise that ϕ_{10} refers only to the ratio in the v=1, J=2 and 3 excited states in that part of the medium in which they are populated, and does not represent the ortho/para ratio of all the molecular H_2 present in the medium.

The resulting ϕ_{10} map can be seen in Fig. 4.1. To avoid unacceptable levels of noise in forming this image, all emission in the v=1-0 S(1) and v=1-0 S(0) lines weaker than 8×10^{-7} W m^{-2} sr^{-1} was excluded. This represents ~2.5% of the maximum in the v=1-0 S(1) line and 9% of the maximum in the weaker v=1-0 S(0) line. Prior to obtaining the ratio the v=1-0 S(1) and v=1-0 S(0), images were smoothed using 7×7 boxcar averaging. This degraded the spatial resolution by ~15%. The map shows surprisingly clear structure in ϕ_{10}, ranging from ϕ_{10} of 1 to 3. In particular, individual clumps of material in region West in Fig. 4.1 each show structure where ϕ_{10} is low (1–1.5) at the centre of emission rising to 3 at the edges.

A comparison may be made between our values of ϕ_{10} and the ISO-SWS data reported in Rosenthal et al. (2000). We have performed a weighted average over
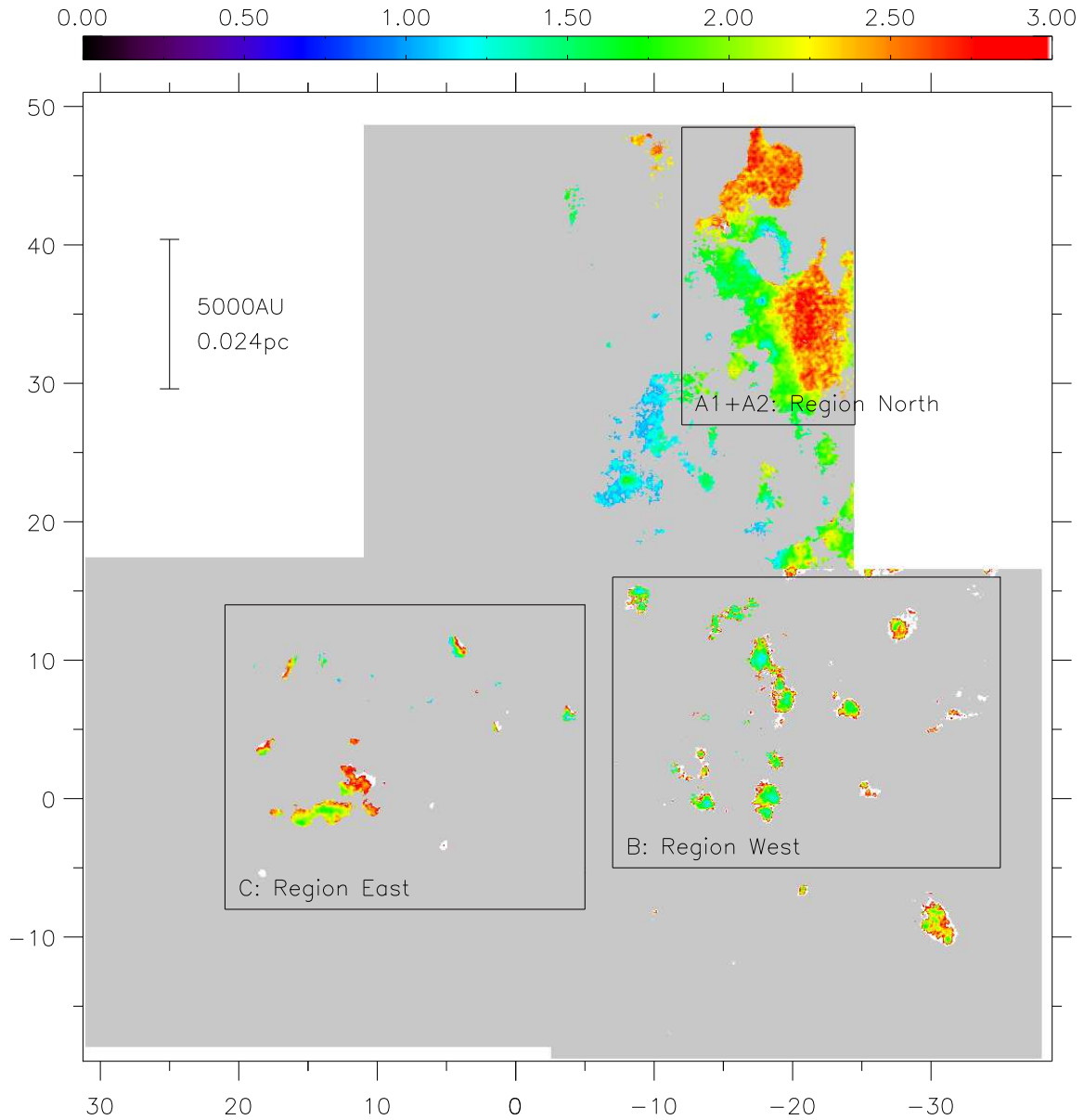
Figure 4.1: A map of the approximate ortho/para ratio, ϕ_{10}, calculated from v=1-0 S(0) and S(1) emission, for the field identified in Fig. 3.2 estimated using Eqn. 4.1.5. The area in grey represents regions in which emission is below specified signal levels (see text). The colour bar is for ϕ_{10}. Coordinates are relative to TCC0016 as in Fig. 3.2. The absolute coordinates of TCC0016 are $05^h 35^m 14^s.91$, $-05° 22' 39''.31$ (J2000). Original images have been smoothed using a boxcar average over 7×7 pixels. The three large squares delineated by grey borders are named East, West and North, as illustrated in Fig. 3.2. The black rectangles, A1+A2, B and C, delineate regions which have been chosen for special study.

the aperture of the ISO-observations, using the S(1) brightness as weight. We find that ϕ_{10}=2.5±0.3 similar to the value of 3 quoted in Rosenthal et al. (2000).

4.1.1 Variations caused by differential extinction?

If the variation in ϕ_{10} that we observe ($1 \leq \phi_{10} \leq 3$ corresponding to variations in flux ratio between ~2 and 6, Eqn. 4.1.5) is only due to variations in extinction then the minimum flux ratio must be ~2/6≈0.3 leading to a relative difference in magnitudes of 1.2^{mag}. If we use the extinction law of Mathis (1990), that is the relative extinction is ~$(\lambda_1/\lambda_2)^{-1.7}$, we find that the extinction at 2.12 μm is 6.5^{mag}. This is in contrast to the extinction estimated from several H_2 lines which is ~1mag at 2.12 μm (e.g. Brand et al. 1988; Rosenthal et al. 2000).

If we assume that the extinction at 2.12 μm is 6.5^{mag} we receive 1/400 of the emitted light. As stated above the noise level is at ~8×10^{-7} $\text{Wm}^{-2}\text{sr}^{-1}$. Thus if the extinction is 6.5^{mag} then the noise level (or minimum brightness) would have a real brightness of 3.2×10^{-4} $\text{Wm}^{-2}\text{sr}^{-1}$ or an order of magnitude higher than the maximum brightness of the brightest object in OMC1. This is true for both the v=1-0 S(1) and the v=1-0 S(0) lines as the noise level is the same.

Furthermore, where we observe a low value of ϕ_{10}, as in the objects in region West, we measure the lower value of ϕ_{10} at the centre of brightness where we have a surface brightness of ~10^{-5} $\text{W m}^{-2}\text{ sr}^{-1}$in the v=1-0 S(1) line. If this is due to extinction alone, then that would mean that the objects are emitting more than ~100 times what we are observing. This is much higher than any H_2 brightness observed so far. Moreover such a high H_2 brightness is not reproducable by any theoretical shock or PDR models.

To translate this magnitude into a column density we note that it is mainly dust grains that are responsible for extinction. Thus in principle it is necessary to know the size distribution of the grains, the extinction cross section (C_{ext}) at the appropriate wavelength and the albedo of the dust grains. For simplicity we assume that the albedo is 1 and that the average size of the grains is a=0.1 μm. The cross section may be described by an efficiency factor, Q_{ext}, so that C_{ext}=$\pi a^2 Q_{\text{ext}}$. For a wavelength of 2 μm, Q_{ext} is typically ~0.1 (e.g. Voshchinnikov et al. 2006) resulting in a cross section at 2 μm of ~3×10^{-11} cm^2. We know that for every 400 photons emitted, 1 will escape. This gives a column density of ~3×10^{10} cm^{-2}.

We note that this is the column density of the grains. To translate this into total column density we assume a dust/gas mass ratio of 0.01. We also assume that the dust grains are composed of a mixture of silicates and carbonaceous materials with an average density of 3 g/cm^3. The mass of dust grains is thus ~4×10^{-4} g/cm^2 resulting in a total mass of the column of ~4×10^{-2} g/cm^2. Assuming that the column is only consisting of H we get a total column density of ~2.4×10^{22} cm^{-2}.

Such a high column density is not unreasonable in OMC1. Beuther et al. (2004) observes a total column density of 8×10^{24} cm^{-2} towards radio source I. However radio source I is a very deeply embedded massive star, as discussed in the introduction (Sect. 1.4.2). In general the H_2 column density in OMC1 is of the order of 10^{22} cm^{-2} (e.g. Masson et al. 1987; Genzel & Stutzki 1989; Rosenthal et al. 2000). Even though the extinction leads to a column density which is consistent with previous observations, it is still not possible to reproduce the high brightness with theoretical models. Therefore the conclusion is that the ratio variations observed are not caused by extinction variations.

Data in van Dishoeck et al. (1998) show that H_2 emission lies in part in front of the 9.7 μm silicon absorption feature. These data indicate that at least some of the H_2 emission is generated in a region relatively unobscured by the main absorbing material. The H_2 data from Rosenthal et al. (2000) indicates that the extinction at 2.12 μm is 1^{mag}. Since this is based on the H_2 emission itself it is independent of where the main absorbing material is.

4.2 Observational constraints on models

In the inner zone of OMC1 studied here, which omits the Orion fingers or bullets to the NW (e.g. Allen & Burton 1993), we may divide the H_2 emission into the following groups, based upon the general characteristics of the emission. The first group consists of blue-shifted emission representing a massive outflow originating between Peaks 1 and 2, in the north-eastern part of region West in Fig. 3.2. This group of objects is discussed in detail in Nissen et al. (2007). Data obtained with VLT using the NACO adaptive optics system resolve the widths of isolated shocks in this region in a very graphic manner (Lacombe et al. 2004,Sect. 4.4.3). The second group belongs to Peak 1 and Peak 2 (North and East in Fig. 3.2). These are especially bright, with overlapping interconnected features and a complex velocity structure (Gustafsson et al. 2003; Nissen et al. 2007). The third group is represented by the faint background emission observed in region North. This does not show small scale spatial structure at our level of sensitivity and spatial resolution. The brightness of this pervasive emission in the v=1-0 S(1) line is $(4.0\pm1.3)\times10^{-6}$ W m^{-2} sr^{-1}. Brightness in v=1-0 S(0), corresponding to this level of emission in v=1-0 S(1), lies below the noise level. However there remains a good deal of diffuse S(0) emission detectable at around $(2.0\pm1.3)\times10^{-6}$ W m^{-2} sr^{-1}, noting the brightness ratio of S(1) to S(0) lies between a factor of 2 and 6. This type of emission as characterized by the S(1) line shows no detectable velocity structure (Nissen et al. 2007).

In the following we seek to find a generalized set of shock and PDR models which are consistent with our observations. These observations include both

the line brightnesses in v=1-0 S(0) and S(1) as well as the ratio and also radial velocities as measured with GriF (Gustafsson et al. 2003; Nissen et al. 2007). In the next section we will also include the width of the bowshock-structures observed in VLT-NACO data (Lacombe et al. 2004). For part of the East field, we also have brightness data for the v=2-1 S(1) line (Kristensen et al. 2003).

We choose to analyse three large regions, which we name A1+A2, B and C. The choice of location and size of these regions was made partly on the basis of the map of ϕ_{10} in Fig. 4.1 and partly following the results in Nissen et al. (2007). Region A1+A2 corresponds to what we observe of Peak 1, region B corresponds to the blue-shifted outflow located between Peaks 1 and 2 and region C corresponds to Peak 2. We have chosen to divide the data into these three regions as we expect physical conditions to vary over OMC1, but that they may be constant in each of these regions. Below we will justify the quantitatively.

Note that the zone north-east of BN which lies at $-15''$,$+17''$ relative to TCC0016, south-east of A1+A2, has been excluded because of possible artefacts associated with strong continuum emission in this region.

To put our data in a generalized form, we plot the absolute brightness of the v=1-0 S(1) vs. the line ratio, R_{10} defined as $I_{v=1\text{-}0\ S(1)}$ / $I_{v=1\text{-}0\ S(0)}$ for the regions A1+A2, B and C whose locations are given in Fig. 4.1. Results are shown separately for the regions A1+A2, B and C in Fig. 4.2. Very similar results are obtained with the v=1-0 S(0) data. In the following we will summarize the properties of each region.

Region A1+A2 In the A1+A2 region, Fig. 4.2a, there is a clear tendency for pixels with higher brightness to have higher R_{10}. Two condensations of points located at R_{10}=3.2, $I_{S(1)}$=7×10^{-6} W m^{-2} sr^{-1} and R_{10}=4.2, $I_{S(1)}$=1.2×10^{-5} W m^{-2} sr^{-1} are clearly seen in Fig. 4.2a. These two classes of points were identified according to the following criterion. The two condensations were first separated by locating the minimum in point density between the two condensations. The contour of this minimum point density was then used around each condensation to form a locus defining each class. These loci are shown in Fig. 4.2a schematically as oblongs, defining the range of properties which specify points of class A1 and A2.

It is evident that certain regions are associated with either the A1 or A2 classes. That is, the low R_{10} are found in a restricted zone in the southern and eastern half of the A1+A2 region. Thus the A1 region is specifically that part of the emission. This also turns out to be the more weakly emitting zone. The A2 class of points is restricted to the two high ratio zones in Fig. 4.1. Fig. 4.2a also shows that a minimum value of brightness is associated with each ratio. This is not an artefact due to a noise level cut-off, which lies at
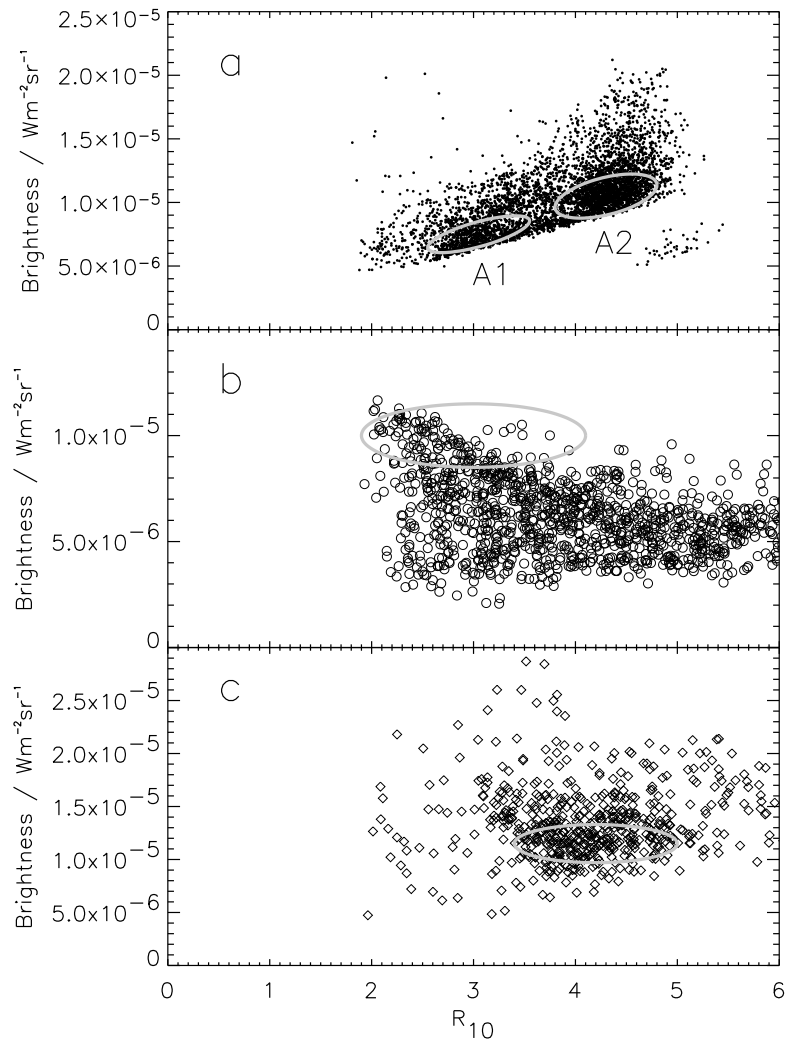
Figure 4.2: **a**: *Region North: brightness of v=1-0 S(1) vs. the line ratio R_{10}. **b**: Region West : similarly for the blueshifted clumps in this zone. **c**: Region East. All data have been rebinned to 500×500 pixels from the original field size of 2000×2000 pixels. The effective pixel size becomes 0.''14 or 3 times better than the resolution. The grey oblongs identify those parts of the data whose characteristics are given in Table 4.1.*

~8×10^{-7} W m^{-2} sr^{-1}, but arises because of the diffuse background. This has a brightness of ~4.0×10^{-6} W m^{-2} sr^{-1} in the S(1) line (see above).

Table 4.1: Characteristics of the four classes of points described in the text and displayed in Fig. 4.2. Brightness is given in units of 10^{-5} W m^{-2} sr^{-1}. The v=2-1 S(1) brightness and R_{12} are from Kristensen et al. (2003) and radial velocities are from Gustafsson (2006) and Nissen et al. (2007) (see Sect. 4.4.2). The figures shown as ± represent the range of values.

Observations	class A1	class A2	class B	class C
Brightness v=1-0 S(1)	0.67±0.11	1.15±0.10	0.90±0.08	1.05±0.18
Brightness v=1-0 S(0)	0.24±0.04	0.28±0.04	0.31±0.09	0.31±0.08
Brightness v=2-1 S(1)				0.15±0.05
R_{10}	3.2±0.6	4.2±0.5	3.2±1.1	4.2±0.8
R_{12}				7±2
ϕ_{10}	1.8±0.3	2.4±0.3	1.8±0.6	2.4±0.5
Associated radial velocity (km s^{-1})	11	11	18	8

Region B   Fig. 4.2b shows data for the blue-shifted clumps in region West. Similar plots restricted to individual blue-shifted clumps show the same structure of higher brightness towards lower values of R_{10} (Sect. 4.4.3). Thus here, in contrast to class A1 or A2, positions of data points within the scatter plot are not associated with any particular spatial sub-zone of the chosen region. The loci of points which we call class B is defined by the oblong in Fig. 4.2b. The criterion here is that we have chosen the subset of data with >65% of the maximum brightness. The reason for this restriction is as follows. In class B, which represents the blue outflow region, much of the data arises from highly localized shocks, some of which take a bow form, judging from the morphology in Lacombe et al. (2004); see also Chapter 5. Data in our chosen subset refer to that brighter emission which lies near the tip or centre of the bow shock. We therefore do not consider the fainter wings of the bow shocks.

Region C   Fig. 4.2c, for Region East, shows a different structure, with a central condensation around R_{10}=4.0 and $I_{S(1)}$=1.2×10^{-5} W m^{-2} sr^{-1}. We have v=2-1 S(1) data for part of region C (Kristensen et al. 2003) and these yield a diagram of very similar appearance to that shown in Fig. 4.2c. We define R_{12} as the line ratio of v=1-0 S(1) to v=2-1 S(1). The oblong, defining points of class C, was obtained as follows. Contours of density were obtained and all data above the half-maximum were included, as schematically outlined by the oblong in Fig. 4.2c.

Our task now is to identify shock models which satisfy the characteristics of data of classes A1, A2, B and C as specified in Fig. 4.2a, b, c. These characteris-

tics are listed in Table 4.1. Each class is defined by a range of characteristic values of absolute brightness and line ratio(s). Also included in Table 4.1 are values of average radial shock velocities taken from GriF data reported in Gustafsson (2006); Nissen et al. (2007).

4.3   PDR as a possible source of excitation

H_2 emission in OMC1 arises from both heating through shocks (e.g. Vannier et al. 2001; Kristensen et al. 2003) and from photon excitation in PDRs (e.g. Black & Dalgarno 1976; Black & van Dishoeck 1987; Sternberg & Dalgarno 1989; Störzer & Hollenbach 1999). We turn first to PDRs.

We now show that the diffuse background of H_2 emission which permeates most of region North (but not region East or West), and to which we have drawn attention in Fig. 4.2a, may be approximately modelled using results reported from existing PDR codes. In our region θ^1Ori C, an O6 star in the Trapezium located at a projected distance of 0.09 pc from BN, generates a radiation field of $2\text{--}3\times10^5$ times the standard interstellar field in Habing units, G_0 (Habing 1968). Combined with a high density, for example exceeding $n_H>10^5$ cm^{-3}, collisional events result in a kinetic temperature in a PDR with values greater than 800 K (Störzer & Hollenbach 1999; Sternberg & Dalgarno 1989; Kaufman et al. 1999; Le Petit et al. 2006). The importance of this figure here is that interactions between H and H_2 begin to overcome the activation energy barrier for H atom exchange at these temperatures, scrambling the ortho- and para- populations and creating ortho/para=3, as mentioned in the introduction (Sternberg & Neufeld 1999).

We use results from the PDR models of both Störzer & Hollenbach (1999) and the "Meudon PDR code" (Le Petit et al. 2006). We focus upon the weaker background emission without measurable velocity structure because (i) PDRs are unable to reproduce the high brightness of many localized regions (ii) the large bulk motions in the gas, associated with very bright regions, are not characteristic of PDRs. We therefore seek to reproduce a brightness in v=1-0 S(1) of $\sim 4.0\times10^{-6}$ W m^{-2} sr^{-1}, with an upper limit of $\sim 8\times10^{-7}$ W m^{-2} sr^{-1} in S(0), the noise level. This implies that R_{10} must be greater than 5 resulting in a lower limit of ϕ_{10} of 2.8 close to the high temperature equilibrium value of the ortho/para ratio of 3.

Using the model of Störzer & Hollenbach (1999) with a radiation field of 2.4×10^5 G_0, $n_H=4.0\times10^6$ cm^{-3}, including 2.6 km s^{-1} of advection, a value of 4.2×10^{-6} W m^{-2} sr^{-1} arises in the S(1) line. This is in fact the maximum that any models in Störzer & Hollenbach (1999) report and reproduces the observed

value of the S(1) background emission seen in region North. The corresponding brightness for the S(0) line is not reported in Störzer & Hollenbach (1999).

Turning to use of the "Meudon PDR code", we first note this does not include advection. This has the result that the high brightness in v=1-0 S(1) is more difficult to match, at any rate for a simple face-on model. The most extreme conditions explored use n_H=5×10^6 cm^{-3} and a radiation field of 5×10^5 G$_0$. These yield S(1) brightness of 3.0×10^{-6} W m^{-2} sr^{-1}. The ratio R_{10} is calculated to be 3.8 and thus S(0) is predicted to be close to the noise level but a little too bright. In this connection, R_{10} is insensitive to the intensity of the radiation field in the range of high number densities and high values of the radiation field strength used here.

We conclude that a significant part of the diffuse background in region North is due to the direct action of a PDR generated by θ^1Ori C. We also conclude that the density here is higher than 10^6 cm^{-3} implying that the temperature is >1500 K. Hence changes in the ortho/para ratio occur through reactive collisions. The region is of course also subject to the well-known major outflow from the general area of BN/IRc2. Thus diffuse shocked gas also makes a contribution to the emission (see Sect. 4.4.2).

4.4   Shocks as a source of H$_2$ excitation

In this section we will compare the observations with the model and model results described in Chapter 2 and Flower & Pineau des Forêts (2003). We compare observations with a subset of the grid already calculated and described previously (Sect. 2.2). In the case of C-type shocks we only consider values of the magnetic scaling factor, b, of 1.0 and 5.0. This is done because the number of observational constraints is low and it is not possible to constrain b.

In a shock, H$_2$ is excited through mechanical heating, at the microscopic level through high temperature H$_2$-H$_2$, H-H$_2$ and He-H$_2$ collisions (Le Bourlot et al. 1999). As the shock develops, the temperature becomes sufficient that excited vibrational states become significantly populated. Emission is observed in the IR, for example, from J=2 or J=3 states in v=1 to form respectively the S(0) and S(1) lines. We first consider the type of shocks relevant here, that is, whether they are J- or C- type.

4.4.1   C-type vs. J-type shocks

As we now show it appears very likely that the shocks which give rise to localised bright emission in the central region of OMC1 are magnetic C-type shocks, rather than non-magnetic J-type. First, it has been demonstrated that

the region can support substantial magnetic fields (Norris 1984; Chrysostomou et al. 1994; Crutcher et al. 1999; Simpson et al. 2006) and the gas is at least weakly ionized. Second, there are numerous features, especially in the central zone (region West in Fig. 3.2) between Peaks 1 and 2 (regions North and East), which are clearly individual shocks, as imaged at 70 mas resolution (30 AU) using the NACO-VLT adaptive optics system (Lacombe et al. 2004). We return to individual objects in the NACO-VLT field in Sect. 4.4.3. The component of magnetic flux density transverse to the direction of shock propagation in a C-type shock softens the shock and makes very extensive the region in which high temperatures and accompanying excitation of H_2 are encountered. We find below that it is possible to model observed shock widths of 40–80 AU in dense regions only with C-type shocks.

The occurrence of J-type, non-magnetic shocks (Hollenbach & McKee 1989; Lim et al. 2002) has been discussed in detail in Kristensen et al. (2003). It was shown there, for data in region East, that J-shocks contribute in very restricted areas at the edges of clumps. These zones are not resolved here. From observations of v=3 and v=4 lines, Moorhouse et al. (1990) finds that it is impossible to reproduce the observed brightness by C-type shock models, but that J-type shock models are required. These observations were made of Peak 1. Therefore it is very likely that there is a contribution to the brightness from J-type shocks. However the effect is probably not strong since the H_2 brightness in J-type shocks is generally lower than for C-type shocks.

4.4.2 Physical conditions associated with different classes of data

Our aim is primarily to establish shock velocities and preshock density for all four classes of data defined in Sect. 4.2. This may be successfully achieved through comparison with a very large number of models taken from the grid described in Sect. 2.2. From the outset we note that there are generally insufficient constraints to exclude anything but a large range of initial ortho/para values for any of the four classes. The same is true of the magnetic field.

We use a χ^2-method to quantify the best fit models of our observations, calculating $\chi^2 = \sum_{\mathrm{obs}} \left(\frac{X_{\mathrm{obs}} - X_{\mathrm{model}}}{\sigma_{\mathrm{obs}}} \right)^2$ where X_{obs} and X_{model} refer to the observed and modelled quantities, respectively. σ_{obs} refers to the uncertainty in the parameter associated with any class, that is, effectively the range of values appropriate to that class. These ranges of values are given in Table 4.1 for the line brightness. In the case of the velocity, Gustafsson (2006); Nissen et al. (2007) reports only radial velocities. They measure the radial velocity by comparing the peak radial velocity of a given object with the radial velocity of the material surrounding
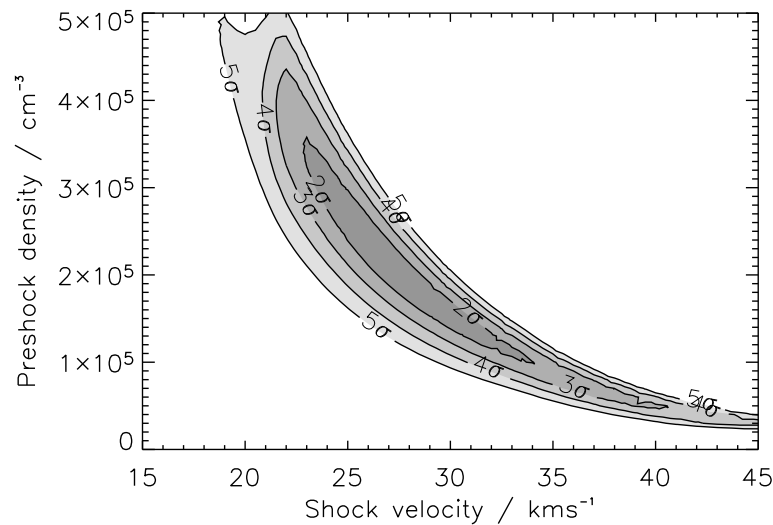
Figure 4.3: The confidence intervals of class A1. The contours are given at intervals of σ from 2σ to 5σ. The models used to make this plot all have an initial ortho/para ratio of 0.01 and b=1.0. See Sect. 4.4.2 for further description.

the object, thus measuring the radial velocity compared to the ambient material. These are effectively minimum velocities and are shown as such in Table 4.1. The value of σ associated with these velocities was the standard deviation of the sample used.

A typical contour plot of confidence intervals, in this case for class A1 data and initial ortho/para=0.01, with b=1, defining the transverse magnetic flux, can be seen in Fig. 4.3. Contours of 2, 3, 4 and 5σ are shown corresponding to each level of certainty. Similar contour plots were obtained for each value of the initial ortho/para ratio and of the value of b, for each class. Each contour plot typically covers 200–300 individual shock models. Common to all these contour plots is that they cover a combination of high preshock density with low shock velocity to low preshock density with high shock velocity. The criterion of fit for each class is taken to be the 3σ limit (99.7% confidence). For each value of the initial ortho/para ratio, the derived range of values of shock velocity and preshock density are shown in the appendix in Table C.1, for both b=1 and b=5. We also show the corresponding range of the postshock density, the shock width, the integrated ortho/para ratio and the maximum kinetic temperature, where all values are generated by the shock model.

There turn out to be rather few general conclusions that may be drawn at this stage from the results in Table C.1 despite the detailed analysis. The underlying

reason for this is that we are attempting in the case of data class C, for example, to model all the emission in Region East, which comprises most of Peak 2, in terms of a single set of shock conditions. Nevertheless various general statements may be made which give a useful overview of the characteristics of shocks in the inner part of OMC1. These may be summarised as follows:

- Class C objects, in region East, cannot be modelled with b=5, that is with high magnetic fields for any initial ortho/para ratio. High magnetic fields are also excluded for classes A2 and B for values of the initial ortho/para ratio of 0.01. Isolated regions of parameter space may in principle exist where agreement is possible but are not accessed by our model grid.

- Initial ortho/para = 0.01 tends to require velocities higher than ~25 km s^{-1} whereas for higher values of the initial ortho/para ratio the velocity may be as low as ~10 km s^{-1}. This may suggest that higher velocities should be rejected since the required delay between successive shocks to reset the initial ortho/para to 0.01 is 10^7 years, whereas the OMC1 complex is no older than ~10^6 years (Hillenbrand 1997; O'Dell 2001).

- The higher the initial ortho/para ratio is the higher the preshock density must be leading to higher postshock densities. This favours high densities in OMC1 clumps, given that low initial ortho/para seems unlikely for reasons of cloud lifetime.

- The predicted width, in particular the lower limit decreases as higher initial ortho/para ratios are used. Where widths can be measured, typically values are of the order of 50 to 100 AU (Lacombe et al. 2004). For b=1, this tends to exclude an initial ortho/para = 3 in all classes.

- For initial ortho/para values greater than 1, higher magnetic fields may also be used to fit the observations. Higher velocities (i.e. greater than 20 km s^{-1}) are naturally required because of the cushioning effects of higher fields.

A general conclusion from the above items is that the initial ortho/para ratio probably lies between 1 and 2. This implies an upper limit of the order of 10^6 years between successive shocks, consistent with the lifetime of OMC1.

The kinetic gas temperature in OMC1 as measured from for example NH_3, CO or CH_3CCH is ~45–75 K (Churchwell & Hollis 1983; Liszt et al. 1974; Sweitzer 1978). At equilibrium the ortho/para ratio would be in the range ~0.25–0.9, lower than the initial ortho/para ratio which we find above. Again this indicates that the gas has probably been shocked previously by jets from protostellar

objects in the region or that the PDR generated by massive stars in the region (e.g. θ^1Ori C or BN) have raised the ortho/para ratio of the gas.

If the shock velocity is less than $\sim$10 km s^{-1} shock waves tend to cause only a very temporarily compression of the medium, while if it is greater than $\sim$50 km s^{-1} they will disperse the medium. All our predicted shock velocities fall in this range, which implies that they are compressing the density perturbations that already exist in the medium.

We may estimate the Jeans mass of individual clumps by using the derived postshock density and the kinetic temperature. The Jeans mass is given as (see Eqn. 1.1.1; Evans 1999):

$$M_J = 18 \ M_\odot \ T_K^{1.5} \ n_{\mathrm{H}}^{-0.5} \ . \tag{4.4.1}$$

As an example we consider a clump with a kinetic temperature of 50 K (as indicated above) and a postshock density of 10^8 cm^{-3}. This is at the upper limit for predicted postshock densities. The Jeans mass is then $\sim$0.6 $M_\odot$. The characteristic scale size of objects in the region has been estimated to be $\sim$1000 AU (Vannier et al. 2001; Gustafsson et al. 2006b; Gustafsson 2006). Consider a clump with this diameter. If we assume the density is uniform, then the total clump mass is $\sim$0.15 $M_\odot$. This is four times lower than the Jeans mass and the clump will not collapse. However, if the temperature is lowered to 10 K the Jeans mass is $\sim$0.7 $M_\odot$ or half the clump mass, resulting in gravitational collapse.

It is very likely that the density is lower than 10^8 cm^{-3}, that is, the Jeans mass is higher and the clump mass lower than above. Therefore it not likely that the outflow in OMC1 is causing a small starburst. Individual, dense, cold condensations may undergo collapse because of shock compression, but the general conclusion is that this will not be wide-spread. This is in contrast to Vannier et al. (2001) who predict that at least some clumps in Peak 2 have been compressed sufficiently to undergo collapse.

We are also not ruling out that there already is a pre- or protostellar population located within the outflow as discussed in Nissen et al. (e.g. 2007). But results here show that the formation has not been triggered by the general outflow.

4.4.3   Individual objects in region West

In region West a group of objects located between 7″ to 35″ west and –5″ to 16″ north of our reference, TCC0016, show similar properties regarding the absolute brightness, ϕ_{10} and velocity structure (Nissen et al. 2007). For example, the maximum absolute brightness of these objects is $\sim$1.0×10^{-5} W m^{-2} sr^{-1}, ϕ_{10} is $\sim$1.0–1.5 at the centre of the objects rising to 3 at the edges (see Fig. 4.4).
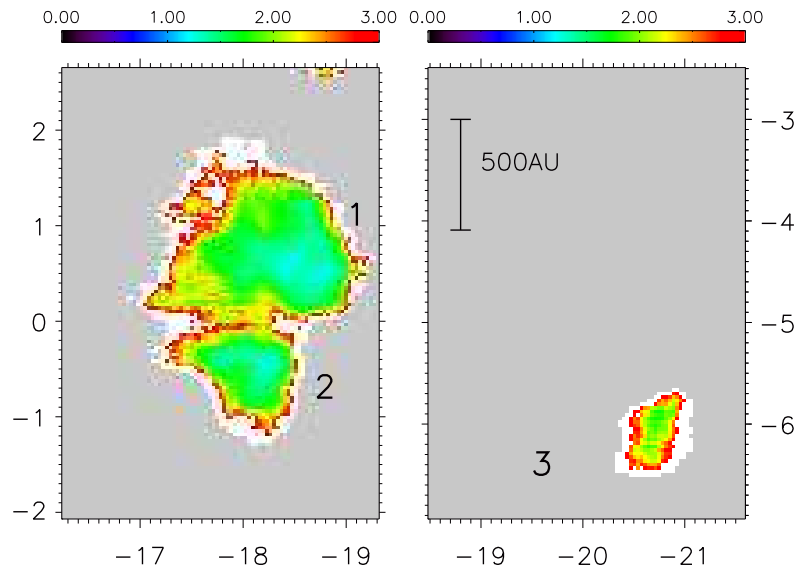
Figure 4.4: Map showing ϕ_{10} in objects 1, 2 and 3 identified in Fig. 4.5. The area in grey represents regions in which emission is below specified signal levels (see text). The colour bar is for ϕ_{10} and coordinates are in arcsec and relative to TCC0016 (see Fig. 3.2).
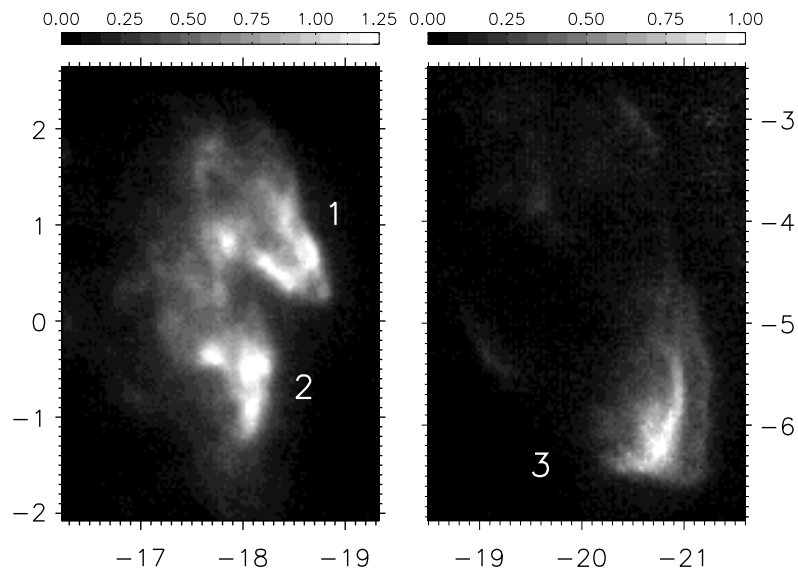
Figure 4.5: ESO-VLT NACO images of three objects where the bowshocks have been resolved. The greyscale bar is in units of 10^{-5} W m^{-2} sr^{-1} (Lacombe et al. 2004). Coordinates are as in Fig. 3.2.

These objects are of special interest since they are part of the IR counterpart of an outflow identified originally in the radio, originating from a highly obscured massive star (or stars) buried in the depths of OMC1 (source I or n; Menten & Reid 1995; Greenhill et al. 2004c; Shuping et al. 2004; Gustafsson 2006; Nissen et al. 2007).

We have chosen three objects to model, selected on the basis of their bow shapes. These objects are shown in Fig. 4.5. Their characteristics are given in Table 4.2 where widths are obtained from ESO VLT-NACO observations of the region (Lacombe et al. 2004). The width has been measured in the wing of each shock as the width of the region where the brightness is greater than 65% of the peak brightness. We have chosen this value since we only consider brightness higher than 65% of the peak brightness. Note that we now have the additional constraints of shock velocity (but see below) and shock width. In this connection an observed (radial) shock velocity is a few km s^{-1} lower in velocity than the lower limit of the shock speed, since energy is taken into heating in the shock impact and velocity is lost from the impacting material.

In Fig. 4.6 we show brightness versus R_{10} for Object 1 (see Fig. 4.5 for labelling of objects). The oblong identifies the subset of points that we use for comparison with models. Note also the similarity in form with the data in Fig. 4.2b, which defines this class of objects.

Again we use a χ^2 method to quantify which models fit observations of objects 1,2 and 3 at the 3σ level, using the same grid as earlier. We treat the observed velocity data in the following manner. If the shock velocity in any model is less than the observed radial velocity, then the velocity is included as a constraint in the χ^2 fit. If the velocity is greater than the observed radial velocity, then we do not include this as a constraint. This is in recognition of the fact that the radial velocity is a lower limit to the true velocity. We find below that a fit at 3σ is given with a shock velocity essentially equal to the observed radial velocity.

If the velocity predicted by the best-fit model is indeed the shock velocity, then this would imply that the shock is moving along the line-of-sight. In this case, the width is no longer a valid constraint. Moreover the morphology of the objects suggest that they are not moving completely along the line-of-sight. The reason that the best-fit model velocities are close to the lower velocity limits may be that the actual shock velocity is lower than the measured radial velocity. This would be the case, if the gas ahead of each object has already been shocked and is moving parallel to the objects. The actual shock velocity would then be the difference of the velocity of each object and the velocity of the preshock gas. In Chapter 5 we will analyse objects 1 and 3 in more detail.

A contour plot of confidence intervals for object 2, initial ortho/para in the preshock gas =0.01, b=1 can be seen in Fig. 4.7. Full results are summarized in
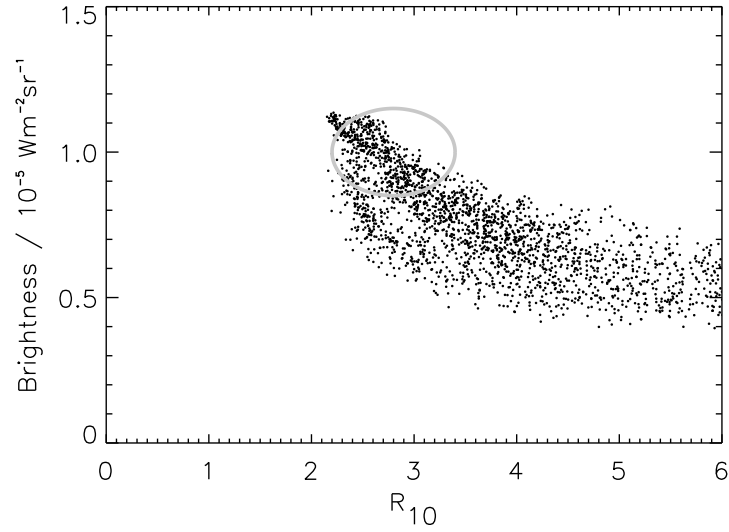
Figure 4.6: A plot of brightness in the v=1-0 S(1) line for object 1 similar to Fig. 4.2 for object 1, but without spatial rebinning. The oblong encloses those data used for comparison with models.

Table 4.2: Characteristics of the three objects described in the text and displayed in Fig. 4.5. The brightness is given in units of 10^{-5} $W\,m^{-2}\,sr^{-1}$. The velocities are from Nissen et al. (2007) and the widths from Lacombe et al. (2004).

	Object 1	Object 2	Object 3
Location	$-18\rlap{.}''5$; $+0\rlap{.}''5$	$-18\rlap{.}''1$; $-0\rlap{.}''8$	$-20\rlap{.}''8$; $-6\rlap{.}''2$
Brightness S(1)	0.94±0.10	0.87±0.10	0.65±0.07
Brightness S(0)	0.34±0.08	0.29±0.08	0.34±0.08
R_{10}	2.8±0.5	3.2±0.7	2.8±0.5
ϕ_{10}	1.6±0.3	1.8±0.4	1.6±0.3
Width / AU	80±30	80±30	40±20
Velocity / $km\,s^{-1}$	18±1	37±1	36±1

Table C.2 in the appendix. Because of the extra constraints and our limitation to a single object, we obtain a much narrower range of physical conditions. In fact we can show that object 1 is distinct from objects 2 and 3, reflected in the much lower observed radial velocity.

The physical conditions in our three objects may be summarised as follows:

- Object 1 requires that the initial ortho/para ratio be around 1 or above. Moreover the magnetic field cannot be high, that is, $b<5$. It appears difficult to reproduce the observed width, which may be an order of magnitude too low. Whilst strictly the full range of models for object 1 in Table C.2 are of equal validity, on the basis of the width criterion alone perhaps the most satisfactory model overall is that with initial ortho/para = 2, shock velocity 18 ± 2 km s^{-1}, preshock density $1\pm0.5\times10^6$ cm^{-3}. At all events, all models at the 3σ level show the same preshock density, which implies a transverse magnetic flux of 1 mGauss.

- Objects 2 and 3 may be classed together. For $b=1$, the preshock density lies an order of magnitude lower than in Object 1 and is $7.5\pm2.5\times10^4$ cm^{-3} with a corresponding transverse magnetic flux of 0.3 mGauss. Once more the widths are not well reproduced, though in this case they are too large. Higher magnetic fields cannot strictly be excluded but widths are still greater for higher fields. The initial ortho/para ratio cannot be determined.

4.5   Concluding remarks

The results presented here show that observations of ortho- and para- lines of H_2 present a useful way of probing the physical conditions in shocked zones. We have introduced the quantity ϕ_{10}, based on the 2 rovibrational H_2 lines v=1-0 S(0) and S(1), as defined in Eqn. 4.1.3. A map of ϕ_{10}, a quantity which we have shown is approximately equal to the true ortho/para ratio given a high rotational temperature, demonstrates strong spatial variation, ranging from 1 to the high temperature equilibrium value of 3. Spatially averaged values however are close to 3, in agreement with earlier work.

We have identified four classes of objects in OMC1, classified through similar properties with respect to line brightness and values of ϕ_{10}. This allowed the identification of a diffuse background emission in region North (but not elsewhere) whose presence may be partly attributed to a general PDR arising from the action of θ^1Ori C. The bulk of the work is devoted to the development of a large grid of shock models with a view to identifying the physical conditions associated both with the four classes of object and also with specific chosen
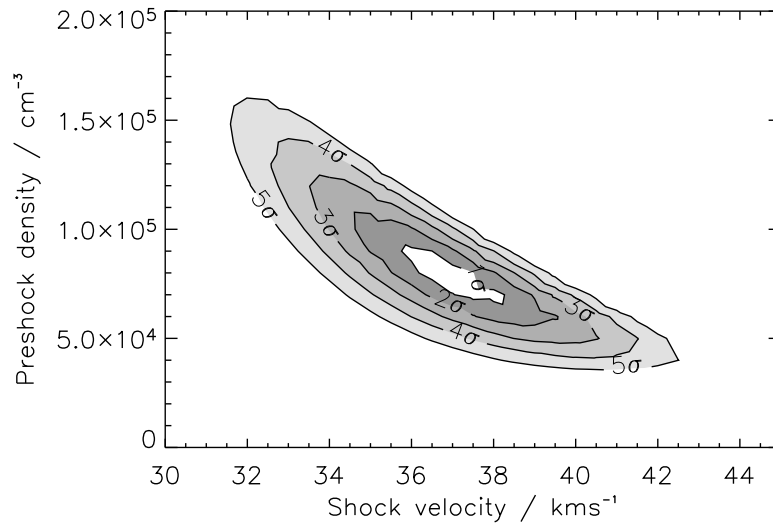
Figure 4.7: Confidence intervals for object 2. Model parameters are initial ortho/para=0.01 and b=1.0.

shocked regions in the field. At the 3σ level it was possible to determine a range of shock-models that fit our observations with preshock densities ranging from ~10^5–10^7 cm^{-3} and shock velocities in the range of 10–40 km s^{-1}. It was found that no J-type shock models fit our observations at the 3σ level if we restrict preshock densities to <10^7 cm^{-3} for which models are valid.

It was found that even though shock velocities are not so high that shock waves disrupt star formation, the postshock compression is not high enough to cause gravitational collapse in typical clumps. Individual cold, dense clumps may undergo collapse because of the outflow, but it will not be a wide-spread phenomena and results here imply that the outflow is not causing a local starburst.

For individual bow-shocks it was possible to identify relatively precise shock conditions. Working with objects in the massive blue-shifted outflow emerging from between peaks 1 and 2, three objects were examined. A velocity of ~18 km s^{-1} and preshock density of 10^6 cm^{-3} apply to one such object and a shock velocity of ~36 km s^{-1} and preshock density of 7.5×10^4 cm^{-3} apply to the other two. Derived transverse magnetic flux was 1 mGauss and 0.3 mGauss respectively. These magnetic fields are similar to those derived from observational data of Norris (1984) and Crutcher et al. (1999).

VLT observations of OMC1: Results and discussion

The work done in this chapter has primarily been done by me and corresponds to publication II. In this Chapter I will mainly focus on the analysis of one particular object located in our field. This is done to illustrate the power of high spatial resolution observations vs. lower spatial resolution as was done in the previous Chapter.

It is essentially possible to redo the work done in the previous Chapter with these new observations. However in some points the two data sets are very different. First and foremost the spatial resolution is typically a factor of 3 better for the VLT observations and the sensitivity is much higher, typically a factor of 4. This allows us to observe the region in much greater detail and resolve even more objects than previously possible. Thus the data will inevitably have a different appearance. Furthermore we have no data for the v=1-0 S(1) line in Region East and Region North is not identical in the two datasets (see Figs. 3.2 and 3.4).

Because of the higher spatial resolution and higher sensitivity, it is feasible to analyse each individual object in OMC1 and reproduce observations in terms of shock models. With this we can in principle map the preshock density, shock velocity, magnetic field strength and initial ortho/para ratio throughout OMC1 at the level of individual objects. This is in contrast to the previous Chapter were large-scale properties of OMC1 were analysed. Sofar this is very much a work in progress.

In Sect. 5.1 I will do a brief comparison between the CFHT and VLT data before analysing an individual object in Sect. 5.2. This analysis is done using a new method developped here.

5.1   Comparison of CFHT and VLT data

It is possible to compare a part of the VLT data with the CFHT data. We can make a full comparison for region West (class B) and for part of region North
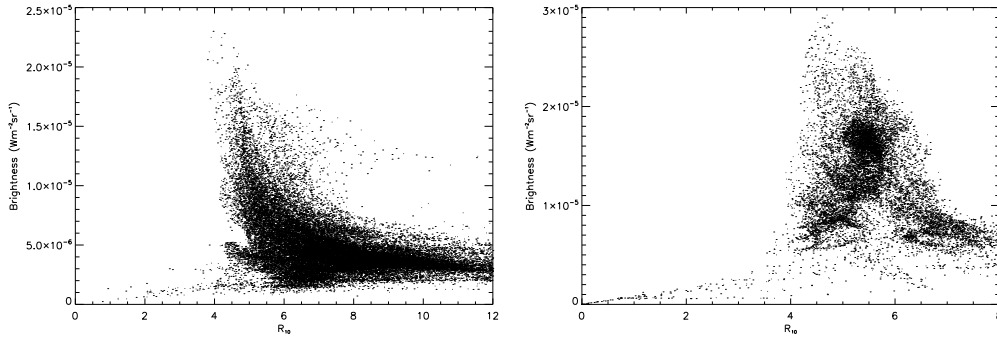
Figure 5.1: Brightness of the v=1-0 S(1) line vs. the line ratio, R_{10} in region West (left) and north (right). Data have been rebinned to a third of the original size, so the effective pixel size is $0\overset{\prime\prime}{.}081$, slightly lower than the resolution.

(class A1+A2). It is not possible to compare region East (class C) since we do not have data for the v=1-0 S(1) line here. For definitions of classes and regions, see Sect. 4.2 and Figs. 4.1 and 4.2.

5.1.1   Region West

In Fig. 5.1 we plot the absolute brightness of v=1-0 S(1) versus the brightness ratio of v=1-0 S(1) and v=1-0 S(0), R_{10}, for region West. Quantitatively the results are identical to Fig. 4.2b in that high brightness is associated with a low line ratio. Also there is a sharp limit in R_{10} below which we find no points.

However, in the CFHT data this limit was observed to be at ∼2 while in the VLT data it is found at ∼4. Also the absolute v=1-0 S(1) brightness is higher in the VLT data. To verify whether this is due to the higher spatial resolution, we tried convolving the VLT data with a Gaussian with a FWHM of $0\overset{\prime\prime}{.}40$ corresponding to the spatial resolution of the CFHT data. This lowered the maximum absolute brightness to $1.4{\times}10^{-5}$ W m^{-2} sr^{-1} which is in better agreement with the CFHT data. This did not affect the line ratio which remains greater than ∼4. A line ratio of 4 corresponds to ϕ_{10}=2.3 (Eqn. 4.1.5) assuming that the excitation temperature is 3500 K as discussed in Sect. 4.1.

5.1.2   Region North

In region North the image is slightly different. Here it is not possible to reproduce the CFHT observations even qualitatively, see Fig. 5.1. There is a small tendency for a condensation around R_{10}=5.5 and $1.75{\times}10^{-5}$ W m^{-2} sr^{-1} but it is

not as strong as for the CFHT data. The second condensation of points is not existing. Furthermore the sharp line, below which very few points were found in the CFHT data is missing.

Part of the explanation is that we are not comparing the full field of view from the CFHT data with the VLT data, as this is not possible. So there are less points for the VLT data than for the CFHT data. This might explain the missing second condensation. It cannot explain why there are a lot of points with low brightness, high line ratio in the VLT data.

As above but for region West, we find that there are very few points below a line ratio of ~4 and that the maximum brightness is higher. If we convolve the image, as above, the maximum absolute brightness is lowered to 2.6×10^{-5} W m^{-2} sr^{-1}. The convolution does not change the minimum line ratio.

5.1.3   Excitation temperature

With these data we may calculate the excitation temperature directly from the v=1-0 S(1) and v=2-1 S(1) lines. The excitation temperature may be calculated as

$$T_{ex} = \frac{E_2 - E_1}{k_B \ln \frac{g_2 N_1}{g_1 N_2}} \tag{5.1.1}$$

where E is the upper level energy, k_B the Boltzmann constant, g the level degeneracy and N the column density of the upper level. The column density may be obtained from Eqn. 4.1.4. Index 1 and 2 refer (in this case) to the v=1-0 S(1) and v=2-1 S(1) transitions respectively. Inserting Eqn. 4.1.4 in the above equation we find

$$
\begin{aligned}
T_{ex} &= \frac{E_2 - E_1}{k_B \ln \frac{g_2 N_1}{g_1 N_2}} \\
&= \frac{E_2 - E_1}{k_B \ln \frac{g_2 A_2}{g_1 A_2} \frac{\lambda_1 I_1}{\lambda_2 I_2}} \\
&= \frac{5600 \text{ K}}{\ln\left(1.355 \frac{I_1}{I_2}\right)} \ .
\end{aligned}
\tag{5.1.2}
$$

H$_2$ properties are given in Table 1.2. We display the v=1-0 S(1) absolute brightness vs. excitation temperature for both region West and North in Fig. 5.2.

In general the excitation temperature is higher in region North than in region West. However for the zones of high v=1-0 S(1) brightness the excitation temperature is ~2300 K in both regions. If this is used as excitation temperature rather than the 3500 K we used previously, the estimate of the ortho/para ratio, ϕ_{10} would be ~7% higher. This is still well below the equilibrium value of 3.
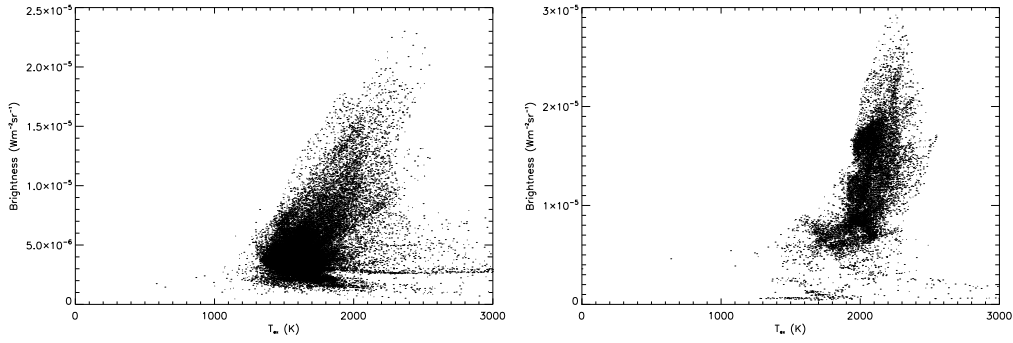
Figure 5.2: Brightness of the v=1-0 S(1) line vs. excitation temperature for region West (left) and North (right). Data have been rebinned to a third of the original size, so the effective pixel size is $0\rlap{.}''081$, slightly lower than the resolution.

5.1.4 Conclusion

Differences in absolute brightness between the two datasets may be attributed to differences in spatial resolution. The main difference is in the value of the ratio. In the CFHT data the minimum value of the line ratio R_{10} is found to be ~2 while it is ~4 in the VLT data. Due to the higher spatial resolution and higher signal/noise ratio in the VLT data, it would seem evident that there is something wrong with the CFHT data.

However, R_{10} is found to be significantly higher than 6 in the VLT data. This is important, since this value is the highest possible if the ortho/para ratio is equal to 3. If R_{10} is higher than 6 it would imply that the ortho/para ratio is higher than 3 (see Eqn. 4.1.3). If R_{10} is as high as 12 in region West (see Fig. 5.1) this would imply a value of ϕ_{10} of 6.8 assuming that $T_{\rm rot}$ is 3500 K. If the temperature is lowered to 1500 K, ϕ_{10} would be 8.2.

Another way to visualise this is by calculating $\ln(N/g)$ for the two upper level populations. By choosing a v=1-0 S(1) brightness of 5×10^{-5} W m^{-2} sr^{-1} and R_{10}=12 I find that $\ln(N/g)$ is ~36.1 for the v=1, J=2 level and ~36.8 for the v=1, J=3 state. That is, the higher the level energy, the higher the excitation!

A possible explanation may be that the relative calibration of the CFHT data was not satisfactory. We assumed (Sect. 3.3.4) that the stellar flux is constant between 2.1 and 2.2 μm which could add an uncertainty of ~10% to each relative calibration. We also estimated that the total uncertainty on R_{10} is of the order of 25% resulting in a combined uncertainty of ~27%. This could increase the minimum value of R_{10} in the CFHT data from 2 to ~2.5, which is far from

enough. At the moment I do not have an explanation for the differences.

With the VLT data it is possible to calculate the excitation temperature from the v=1-0 S(1) and v=2-1 S(1) transitions. The excitation temperature confirms our choice of excitation temperature in the previous Sect. 4.1.

5.2   2D bow shock model

As has been discussed previously, there are currently no 3D bow shock models that include complex chemistry and the full set of MHD equations in a self-consistent manner. To compensate for this, several groups have created 2D bow shock models, which may then be rotated to yield 3D results. These models are made by taking a number of 1D models and aligning them along a predefined bow structure. The input parameters of these model are changed through a pre-defined algorithm. Both the shape and the variation of input parameters can be changed to reproduce observations.

Here we will take another approach. We will ignore the 3D structure of the bow shock and assume that it is moving in the plane of the sky This *a priori* assumption will later be verified by analysing the results from 3D modelling (Sect. 5.3). We then cut the shock into pieces or segments. The width of the segments corresponds to the spatial resolution, and they are aligned perpendicular to the bow shock. We then seek to reproduce the observed properties of each segment by a plane-parallel shock model. We are implicitly assuming that the curvature of the bow shock is negligible over the width of segments. We are thus letting nature dictate how the preshock properties change along the bow.

To illustrate this we have chosen a bow shock located $20\rlap{.}''5$ west and $6''$ south of TCC0016 (see Fig. 5.3) itself located at $05^h35^m14\rlap{.}^s91$, $-05°22'39\rlap{.}''31$ (J2000). This bow shock was chosen because it is relatively isolated and show a very well defined morphology. The bow shock is not moving in the plane of the sky, but it was not possible to find a shock with a well-defined bow morphology with no radial velocity in our data. There are ~30 objects moving in the plane of the sky, especially in region North, but none of them resemble bow shocks. in region West, on the other hand, there are plenty of bow shocks, but none of them are moving in the plane of the sky. Typically the radial velocity is greater than $10–15 \mathrm{\,km\,s}^{-1}$.

In the following we will go through the method in more detail. We will discuss the results and compare the predictions of our model to other independent observations. We will also discuss the assumptions and their validity in the case of this particular object. We will then compare our results with the 3D bow shock model described in Sect. 2.3. We choose to first demonstrate the 2D method because it is easy to implement compared to a 3D model and may be
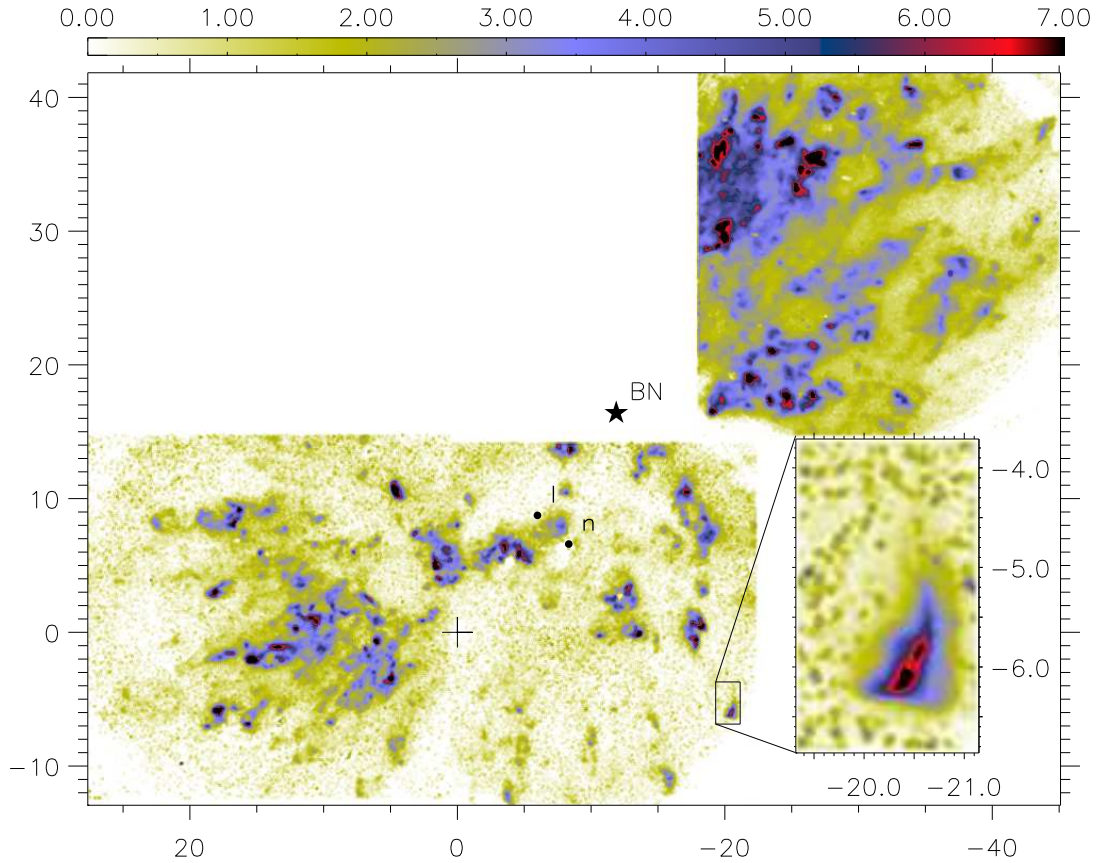
Figure 5.3: Finding chart for the bow shock we analyse with our 2D model. The map shows the VLT observations of continuum-subtracted H_2 emission in the v=1-0 S(0) line at 2.23 μm. The colourbar is in units of 10^{-6} $W\,m^{-2}\,sr^{-1}$. Axes are in arcseconds and offsets are given with respect to TCC0016. The box, which is magnified in the inset, shows the bow shock we are analysing.

used for other objects which are not necessarily bow-shaped. The results from the 2D modelling will serve as an initial guess for the 3D modelling. Finally we will do a similar analysis for another nearby object.

5.2.1   Results and 2D model description

We choose to limit this section to the description of one bow shock in our field of view. This object is located $20\rlap{.}''5$ W and $6''$ S of TCC0016, our positional reference point ($05^h35^m14\rlap{.}^s91$, $-05°22'39\rlap{.}''31$; J2000). The object is shown in the inset in Fig. 5.3 in v=1-0 S(0) emission. The peak brightness in the strong

v=1-0 S(1) line is $(2.06\pm0.09)\times10^{-5}$ W m^{-2} sr^{-1}, whereas it is 3.3 times lower in the v=1-0 S(0) line and 5.6 times lower in the v=2-1 S(1) line.

This object has previously been described in Kristensen et al. (2007a) (labelled object 3; see Chap. 4) and Nissen et al. (2007) (labelled B43). In Kristensen et al., it was found that a shock with velocity ∼35–40 km s^{-1} and preshock density ∼10^5 cm^{-3} could reproduce the line brightness of the v=1-0 S(1) and v=1-0 S(0) H$_2$ lines. In that analysis the shock width was also used as an observational constraint. The shock width was obtained from ESO-VLT/NACO observations where the spatial resolution was 80mas (Lacombe et al. 2004).

Using the GriF FP interferometer on CFHT Nissen et al. (2007) measured radial velocities of H$_2$ emitting in the v=1-0 S(1) line. They measured a peak radial velocity of –36 km s^{-1}, that is, the object is moving towards us at 36±1 km s^{-1} with respect to the ambient medium. Recent proper motion studies performed by Cunningham (2006) indicate that this object has a proper motion of 41 km s^{-1}±25 km s^{-1}. The full 3D velocity of this object is then ∼55±25 km s^{-1} and the angle with respect to the plane of the sky is ∼40°±27°. We acknowledge that the shock is not moving in the plane of the sky, but for the moment we are ignoring this. Later, in Sect. 5.2.3, we will discuss the effect of this, and we will return to it when trying to reproduce observations with a 3D model in Sect. 5.3.

Using a single parabolic curve we determine the position angle to be 235°. This angle has been determined by rotating the shock in steps of 5° and fitting a single parabola to the location of the peaks in brightness and calculating χ^2. At an angle of 235° we find a minimum in χ^2 and we choose this as our position angle. We also tried fitting the bow with a rotated parabola, where the rotation angle is another free parameter. This gives a position angle of 240°±12°. In Sect. 5.2.2 and 5.2.2 we refine this choice.

This is higher than the position angle given by Cunningham (2006) of 184° and of Nissen et al. (2007) (221°). The position angle given in Nissen et al. is very close to the position angle towards radio source I and source n (223°) both likely candidates as the source of the outflow (Nissen et al. 2007, and references therein). Given the uncertainty of our method (±10°) and the uncertainty in the angle determined by Nissen et al. (±5°) there is no significant disagreement. Based on the data given in Cunningham we estimate that the 1σ uncertainty is of the order of ∼55°. Thus our result for the position angle is within the error bars of that of Cunningham (2006).

In the bow shock we seek to reproduce line emission properties along the bow thus predicting physical conditions along the bow. We do this by slicing the bow into 9 segments shown in Fig. 5.4, with a width corresponding to the resolution (0.″15 ∼ 70 AU). We align each of the segments so they are perpendicular to the bow front. In order to define the bow shape we have chosen to fit two parabolic curves to the points of maximum brigtness along the bow, one for each
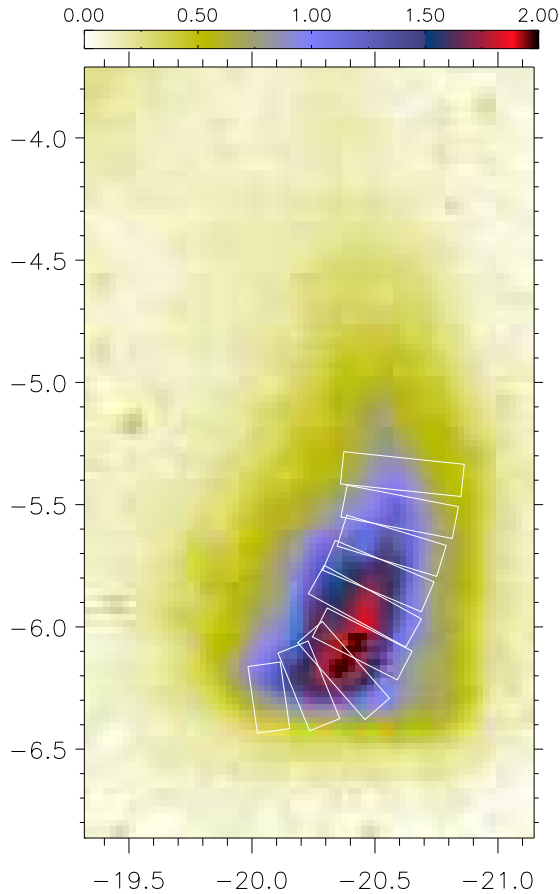
Figure 5.4: Location and extent of the 9 segments we have chosen to study overlaid on a map of continuum subtracted H_2 v=1-0 S(1) emission. Coordinates are relative to TCC0016 and the colorbar is given in units of 10^{-5} $W\,m^{-2}\,sr^{-1}$. The location of the shock is shown in Fig. 5.3. We have labelled segments 1 and 9 for easy identification. The arrow shows a position angle of 235° and the length corresponds to 150 AU.

side of the bow. We fit each side of the brightest pixel in the bow with a different parabolic curve as the object is slightly asymmetric. The position angles of the individual segments as obtained from the parabolic curves are listed in Table 5.1.

We now average the segments in the direction perpendicular to the bow to increase the S/N ratio. For each segment along the bow we obtain a brightness profile perpendicular to the bow (see Fig. 5.5). This is done for all of the three H_2 rovibrational lines. For each of the three brightness profiles we now measure the FWHM. We then average the brightness over the FWHM of the profile. FWHM is chosen because it does not depend on the noise level. For the segments analysed here, the FWHM is always measured well above the noise level, which is also clear from Fig. 5.5.

For each segment we thus have 6 observational constraints:

- FWHM measurements of emission perpendicular to the bow profile for each of the 3 lines.
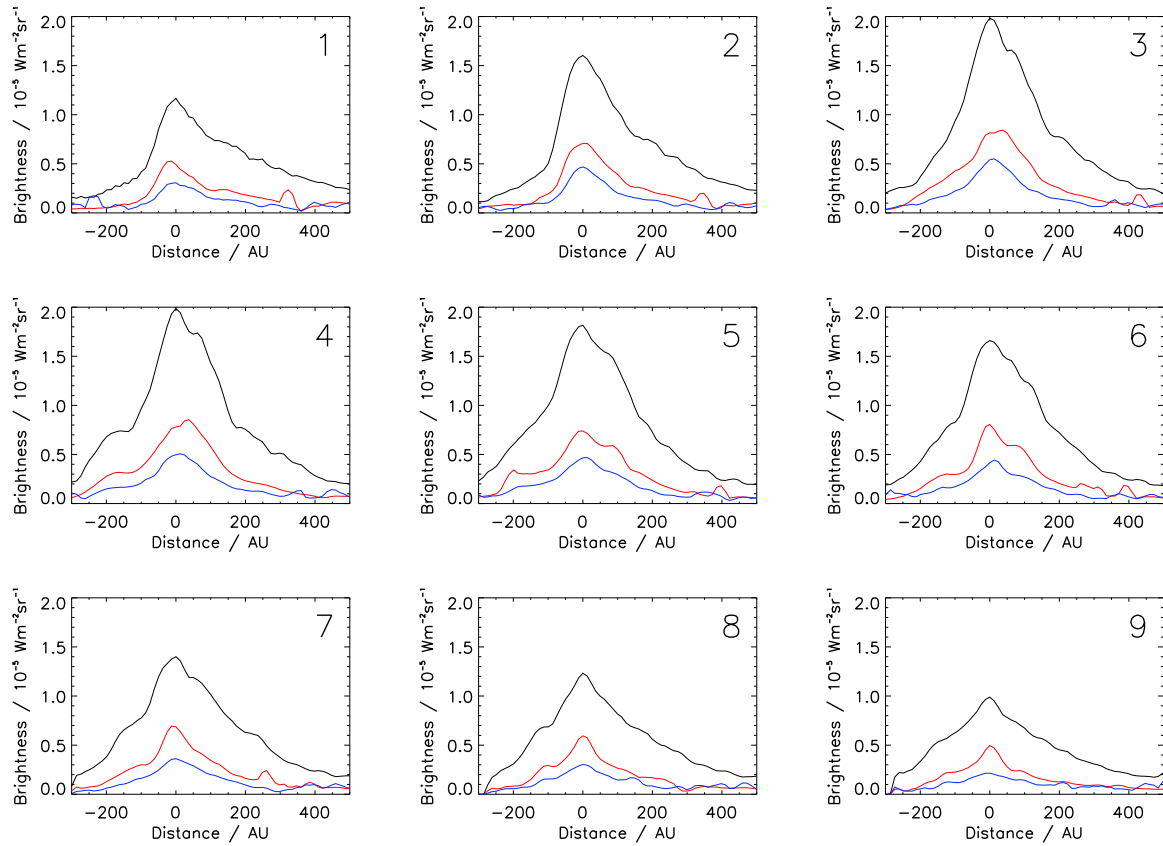
Figure 5.5: *Intensity cuts through the bow of the H$_2$ v=1-0 S(1) (black), v=1-0 S(0) (red) and v=2-1 S(1) (blue) lines in each segment. Distances are given in AU and the zero point is the location of the brightness maximum. This point does not change significantly for the other two lines. Negative distances indicate that this brightness is outside the bow, while positive distances are inside. The number in each profile refers to the segment number (see Fig. 5.4).*

Table 5.1: Characteristics of the 9 segments of the bow object described in the text and displayed in Fig. 5.4. Brightness is averaged over each segment and is given in units of 10^{-5} $W\,m^{-2}\,sr^{-1}$ and FWHM perpendicular to the bow surface in units of AU. The uncertainties σ_{obs} given are 1σ.

Seg.	p.a.	Brightness (10^{-5} $W\,m^{-2}\,sr^{-1}$)			FWHM (AU)		
		1-0 S(1)	1-0 S(0)	2-1 S(1)	1-0 S(1)	1-0 S(0)	2-1 S(1)
1	188°	0.86±0.03	0.32±0.02	0.18±0.01	130±30	100±60	80±70
2	202°	1.24±0.04	0.44±0.02	0.28±0.02	160±20	130±40	120±50
3	221°	1.55±0.05	0.50±0.02	0.32±0.02	190±15	170±20	140±40
4	243°	1.57±0.05	0.53±0.02	0.29±0.02	180±15	160±20	140±40
5	241°	1.42±0.05	0.45±0.02	0.26±0.01	210±15	160±20	180±30
6	247°	1.32±0.04	0.47±0.02	0.24±0.01	200±15	130±20	160±30
7	253°	1.05±0.04	0.41±0.02	0.21±0.02	200±20	120±40	160±40
8	259°	0.87±0.03	0.34±0.02	0.16±0.01	210±25	140±50	170±50
9	264°	0.70±0.03	0.28±0.02	0.11±0.01	230±30	110±60	150±60

- line brightness of the H_2 lines v=1-0 S(1), v=1-0 S(0) and v=2-1 S(1) averaged over the FWHM of the bow profile.

In Fig. 5.4 we display the location and extent of each segment and in Table 5.1 we list the 6 observational constraints for the segments and we display them in Fig. 5.6 and 5.7. For the moment we have chosen not to include the velocity as an observational constraint for the following reason. We do not know how the proper motion changes along the bow. Thus we only know the peak or apex velocity. In order to use the velocity as a constraint it would have been necessary to have detailed information of the measured 3D velocities along the bow and to take the inclination of the shock into account.

As can be seen from VLT images in these observations and those of Lacombe et al. (2004), the object is elongated along the direction of motion (Cunningham 2006) near the centre. This can be seen as a secondary brightness peak slightly downstream around 50 AU in segments 3–6 in Fig. 5.5. The separation between the two centres of brightness is ~55 AU (0.′′12) which is comparable to our resolution. The position angle between the two is ~206°±20°. This is consistent with the position angle determined here as well as the position angle determined in the proper motion studies by Cunningham (2006) and radial velocity measurements by Nissen et al. (2007). This secondary brightness may be due to a Mach disk. For the moment we choose to ignore this, but we will return to it in Sect. 5.2.3.
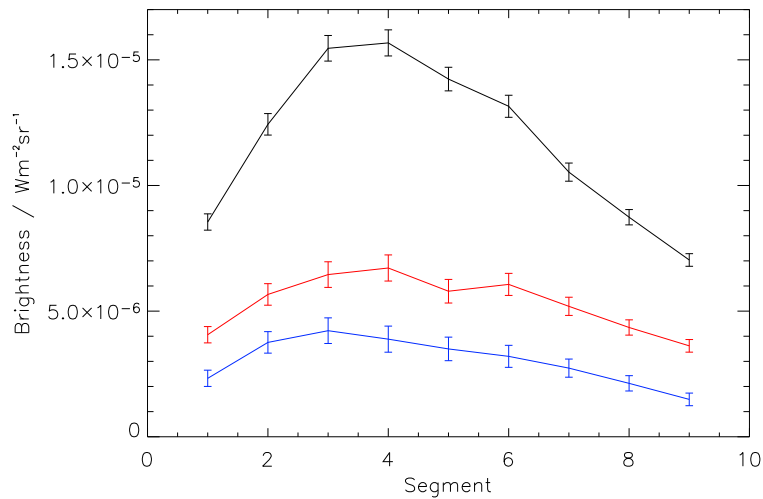
Figure 5.6: Brightness integrated over the FWHM along the bow for the three lines v=1-0 S(1) (black), v=1-0 S(0) (red) and v=2-1 S(1) (blue) in each segment. Error bars show 1σ uncertainties.
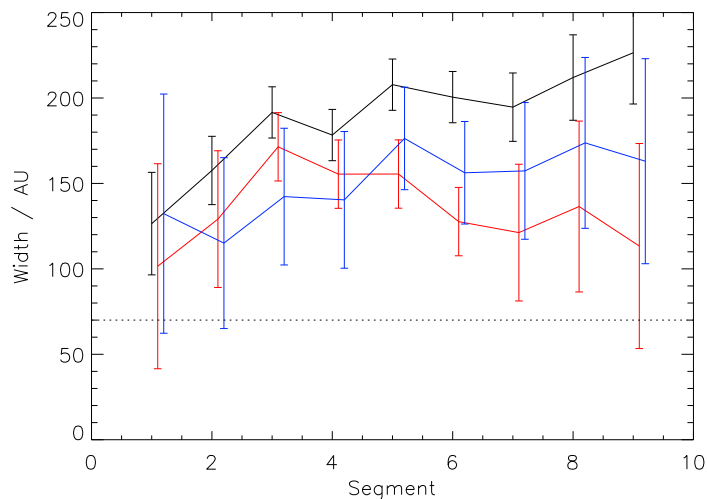
Figure 5.7: The FWHM of H_2 emission for the three lines v=1-0 S(1) (black), v=1-0 S(0) (red) and v=2-1 S(1) (blue) in each segment. The dotted line at 70 AU shows the spatial resolution (see text). Errorbars show 1σ uncertainties. Points representing v=1-0 S(0) and v=2-1 S(1) widths have been shifted horizontally by 0.1 and 0.2 respectively so as to clearly separate the error bars.

5.2.2 Shock model

C- versus J-type shock

In the following we will only consider C-type shocks and J-type shocks with magnetic precursors for the following two reasons.

(i) The main reason is that FWHM of the H_2 emission in the different segments is observed to be $\gtrsim 100$ AU. In J-type shocks this is impossible to reproduce, even with a weak component of the transverse magnetic field (Kristensen et al. 2007, in preparation). The width is however readily reproduced by C-type shock models, where widths between 1 and 10^5 AU can be achieved, depending on initial conditions.

(ii) [FeII] emission at the heart of OMC1 is primarily observed around well-known HH-objects such as HH208 (Schultz et al. 1999) and the Orion bullets (e.g. Allen & Burton 1993). For the object we examine here, no [FeII] emission has been observed (Takami et al. 2002). Therefore it is likely that the shock observed is not dissociative (Kristensen et al. 2007 in preparation). Given the relatively high velocity ($\sim$40–60 km s^{-1}; Cunningham 2006; Nissen et al. 2007) J-type shocks are fully dissociative and we would expect a brightness of the strong [FeII] line at 1.257 μm of $\sim 10^{-7}$ W m^{-2} sr^{-1} (Kristensen et al. 2007, in preparation) which is above the noise limit of Takami et al. (2002). In a C-type shock very little [FeII] emission is predicted (i.e. less than 10^{-8} W m^{-2} sr^{-1}) along with very little or no H_2 dissociation.

We do not exclude the existence of J-type shocks in OMC1. As has previously been shown (e.g. Brand et al. 1988, 1989a; Moorhouse et al. 1990) H_2 excitation of the v=3 and 4 levels cannot be reproduced by C-type shock models. Therefore part of the excitation mechanism is due to PDR excitation and J-type shocks. For this particular object emission arising from PDRs/J-type shocks is probably weak. At this stage we do not rule out that there may be an additional J-type component in the observed (C-type) shock. If such a component exists, it would be located close to the apex (see Sect. 5.2.3).

Reproduction of observations

We will now attempt to reproduce the observed properties (line brightness and width) for all segments of the object. We do this by fitting a plane parallel C-type shock model to each segment. We are interested in obtaining values for the preshock density, shock velocity, transverse magnetic field strength and the value of the initial H_2 ortho/para (o/p) ratio.

To reproduce the observed brightness we have extracted the brightness and width from the models in the same manner as in the observations. That is, for every 1D shock model we have calculated the brightness profile of each of our

H_2 lines as a function of distance along the shock. We have measured the spatial extent of the FWHM of our emissivity profile and we use this to compare with our observed FWHM. The emissivity profile is then integrated over the FWHM to yield the brightness. In this last step, we are implicitly assuming that the average depth in the line of sight of the shock in each segment is comparable to the FWHM given in Table 5.1, columns 6, 7 and 8.

Values corresponding to the six observational constraints (three line brightness and three widths) were extracted from the models and we use a χ^2 analysis to determine how well individual models reproduce the observations. For each model we thus calculate $\chi^2 = \frac{1}{n} \sum \left(\frac{X_{\text{obs}} - X_{\text{model}}}{\sigma_{\text{obs}}} \right)^2$ where n is the number of observational constraints (i.e. six), X_{obs} and X_{model} refer to observed and modelled property respectively and σ_{obs} is the observed uncertainty. These are all given in Table 5.1.

For each segment we list the best fit models with corresponding confidence intervals in Table 5.2 and show our results in Fig. 5.8. The results are as follows:

- The shock speed decreases from $\sim$50 km s^{-1} at the apex to $\sim$40 km s^{-1} in the southern wing (segment 1, Fig. 5.4) and $\sim$35 km s^{-1} in the northern wing (segment 9, Fig. 5.4).

- The magnetic scaling factor b varies from $\sim$6.0 at the apex to $\sim$3.5 in the southern wing and to $\sim$3.0 in the northern wing.

- The density is constant at 5×10^5 cm^{-3}.

- The initial o/p ratio does not change from 3. This is the value the o/p ratio is expected to have at high temperatures (i.e. greater than 300 K).

This result is very similar to that obtained by Draine & Roberge (1982). Here the authors find a shock velocity of $\sim$38 km s^{-1}, preshock density 7×10^5 cm^{-3} and a transverse magnetic field strength of 1.5 mGauss (corresponding to b=1.8). They obtain this result by fitting one of the first C-type shock models to observations of H_2, CO, OH, OI and CI emission from Peak 1.

In Fig. 2.12 we showed the local brightness profile of the v=1-0 S(1) line as well as the kinetic temperature profile. This is shown for the model corresponding to the best fit model of segment 3, which is the segment containing the apex of the shock. The figure shows that the v=1-0 S(1) FWHM is 97 AU, that is the width is underestimated by 51% (the observed FWHM is 190 AU, see Table 5.1). The total size of the H_2 emitting zone corresponds very well to the zone in which the kinetic temperature is greater than 1000 K. The size of this zone is 216 AU. The time to reach steady-state at 50 K is 120 years.

We now discuss what can be learned from these results.

Table 5.2: Input parameters of the models which best reproduce observations. Results (confidence intervals) are listed for each segment (see Fig. 5.4).

Seg.	Preshock density (cm^{-3})	Shock velocity ($km\,s^{-1}$)	b	o/p_{ini}
1	5×10^5 (5×10^5–10^6)	38 (29–39)	3.5 (2.0–4.5)	3.00 (0.01–3.0)
2	5×10^5 (5×10^5–10^6)	42 (37–45)	4.0 (3.0–6.5)	3.00 (2.0–3.0)
3	5×10^5 (5×10^5–10^6)	49 (41–50)	6.0 (4.5–8.5)	3.00 (2.0–3.0)
4	5×10^5 (5×10^5–10^6)	47 (40–50)	5.0 (4.0–8.0)	3.00 (2.0–3.0)
5	5×10^5 (5×10^5–10^6)	46 (39–49)	5.0 (4.0–8.0)	3.00 (2.0–3.0)
6	5×10^5 (5×10^5–10^6)	44 (39–45)	4.5 (3.5–6.5)	3.00 (2.0–3.0)
7	5×10^5 (5×10^5–10^6)	41 (36–43)	4.0 (2.5–5.0)	3.00 (2.0–3.0)
8	5×10^5 (5×10^5–10^6)	38 (37–42)	3.5 (3.0–6.5)	3.00 (2.0–3.0)
9	5×10^5 (5×10^5–5×10^5)	35 (32–39)	3.0 (2.0–4.5)	3.00 (0.01–3.0)

Shock velocity

It is possible to compare our predicted peak velocity to the measured 3D velocity. The measured 3D velocity is ~55 $km\,s^{-1}$ ± 25 $km\,s^{-1}$ (Nissen et al. 2007; Cunningham 2006) and we predict a shock velocity of ~50 $km\,s^{-1}$. Thus there is good agreement between our results. Furthermore we predict how the velocity will change along the bow as illustrated in Fig. 5.8.

If the bow shape remains steady over time, the shock velocity perpendicular to the bow surface should vary along the bow as

$$v_\perp = v_0 \times \cos(pa - pa_0) \qquad (5.2.1)$$

where v_0 is the maximum velocity, pa the position angle of the given segment and pa_0 the position angle of the shock. In Fig. 5.9 we show the velocity component perpendicular to the surface and the best fit results of Eq. 5.2.1. As a result we find that the position angle for the bow shock is 225°±9° and that the maximum velocity is 47 $km\,s^{-1}$±2 $km\,s^{-1}$. The position angle is in agreement with other position angles as discussed in Sect. 5.2.1.

With future high spatial resolution observations of this object it should be possible to observe the proper motion of the individual segments. If the shock is moving at an angle of ~40° with respect to the plane of the sky, then at a spatial resolution of ~0″.15 it should be possible to resolve the differential motion over a period of 13 years.
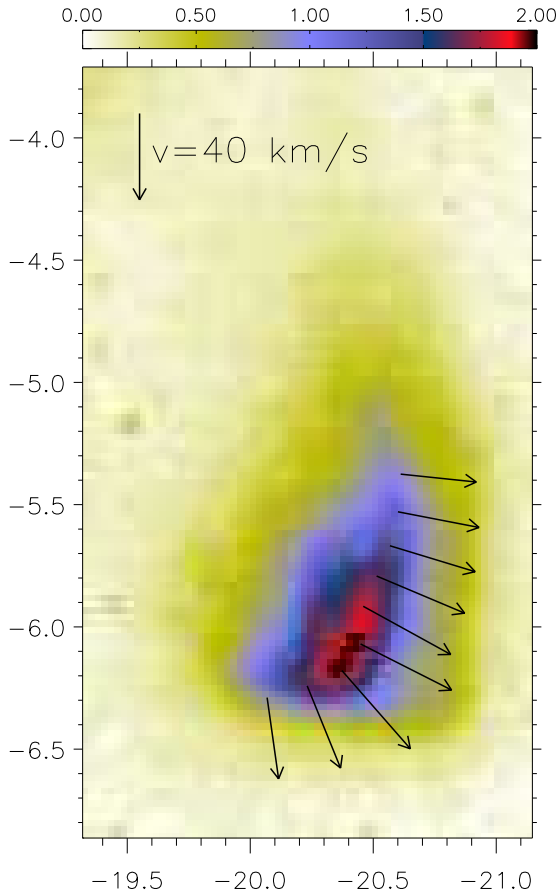
Figure 5.8: Velocity variations along the bow superposed on an image of the bow shock as observed in v=1-0 S(1). Coordinates and colour bar are as in Fig. 5.4. The lengths of the arrows are scaled with velocity and the arrow in the top left corner has a length corresponding to 40 km s^{-1}.

Transverse magnetic field

If we assume that the magnetic field is uniform, we may deduce the position angle, pa_B. The position angle is determined in much the same way as the position angle of the shock above. Quantitatively we compare the changes in the magnetic field tangential to the bow with a simple model where

$$b_{\parallel} = b_0 \times \cos\left[(pa \pm \pi/2) - pa_B\right] = b_0 \times |\sin(pa - pa_B)| \qquad (5.2.2)$$

as in Eq. 5.2.1. Here b_0 is the maximum value of the magnetic scaling factor, $(pa\pm\pi/2)$ is the position angle of the local tangent to the bow surface and pa_B is the position angle of the ambient magnetic field. This is shown in Fig. 5.10.

With this model we find that b_0=4.8±0.7 and pa_B is 133°±16°. Observations of polarized light in the region (e.g. Hough et al. 1986; Chrysostomou et al. 1994; Simpson et al. 2006; Tamura et al. 2006) indicate that the magnetic field has a position angle of ~140°. The position angle of our shock was determined to
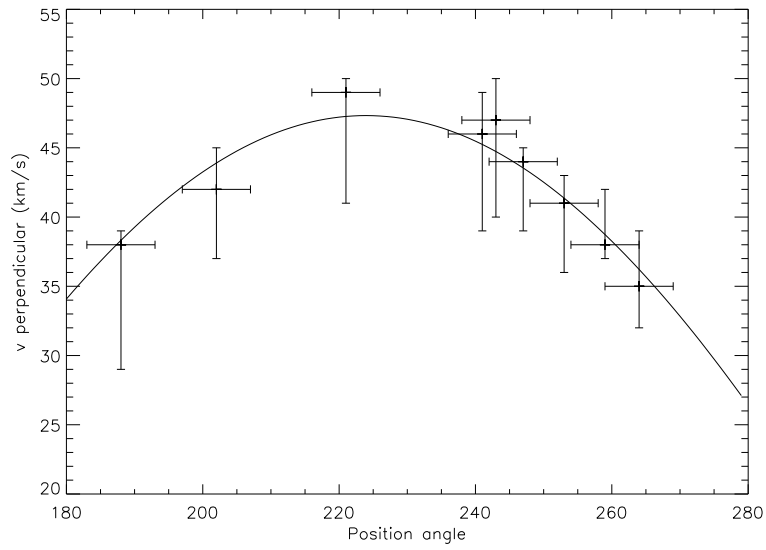
*Figure 5.9: The shock velocity perpendicular to the bow, as a function of position
angle. The curve shows the best-fit solution to Eqn. 5.2.1.*
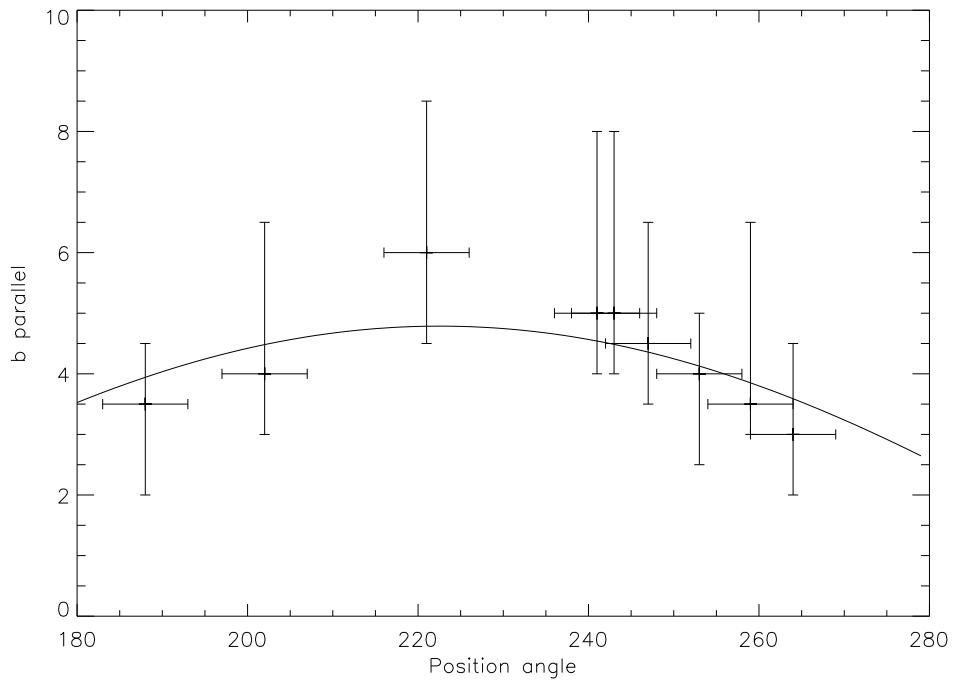
*Figure 5.10: The magnetic scaling factor b, as a function of position angle. The
curve shows the best-fit solution to Eq. 5.2.2.*

$225°\pm9°$ above. Therefore conclude that the magnetic field is oriented tangential to the apex.

The predicted magnetic field strength is ~3.4±0.5 mGauss at the apex. This value may be compared with magnetic fields derived from observations made by Norris (1984), (Chrysostomou et al. 1994) and Crutcher et al. (1999). They find that the magnetic field near IRc2 is ~3 mGauss (Norris 1984) and that north of IRc2 it is ~0.3 mGauss (Crutcher et al. 1999). Both of these are line-of-sight estimates. Chrysostomou et al. (1994) estimate the magnetic field strength by estimating the Alfvén velocity, v_A from the dispersion of the position angle of the polarization vectors. The Alfvén velocity is approximately equal to $b\times1.5$ km s^{-1}. Based on this they estimate that $b\sim10$ which is consistent with our results.

Density

We do not predict that the preshock density changes along the bow. This indicates that the medium here is not clumpy on scales of the size of this bow shock (~600 AU), or that the density variations in the medium are sufficiently small that they cannot be detected here.

Initial ortho/para ratio

The initial o/p ratio is in all segments equal to 3. In Kristensen et al. (2007a) the initial o/p ratio could not be determined although observations suggested it is lower than the high temperature equilibrium value of 3. If we lock the initial o/p ratio in our χ^2 analysis, we find that the value of χ^2 change by less than 5% no matter what the initial o/p ratio is. This implies that for our observations we cannot determine the initial o/p ratio.

5.2.3   Discussion of sources of error

For the above modelling there are four main sources of error. These sources are as follows:

- Geometrical effects: We ignore the inclination of the shock and the depth of emission.

- We do not consider photo-excitation by the massive O6 star, θ^1Ori C, located in the Trapezium at a projected distance of ~0.13pc (~27 000 AU).

- There may be a possible Mach disk located behind the apex of the bow. This is not included in our analysis.

- At the apex there may be an additional J-type shock component which is not spatially resolved in our observations.

Geometrical effects

The main assumption in constructing the 2D model is that the object is observed sufficiently edge-on that we can ignore the true inclination of the object with respect to the plane of the sky. As seen in Sect. 5.2.1 the actual inclination of the object is ∼40° with respect to the plane of the sky. Assuming that the width scales with $\sin i$, where i is the inclination angle, the width may be overestimated by ∼25%. This is about twice the observational uncertainty for the width in the strong v=1-0 S(1) line and smaller in the two other weaker lines.

If the width is smaller, then we would have overestimated our preshock density and underestimated the transverse magnetic field strength and shock velocity (Kristensen et al. 2007, in preparation). Based on observations, it is unlikely that the transverse magnetic field is higher (Norris 1984). The proper velocity of the object is ∼55 km s^{-1}, whereas we predict 49 km s^{-1}. For a shock with velocity 55 km s^{-1}, preshock density 5×10^5 cm^{-3} and magnetic scaling factor b=6.0, the FWHM of the local emission of the v=1-0 S(1) line is ∼100 AU below the observed width of ∼150 AU.

If the density is lowered to 10^5 cm^{-3}, the FWHM of the v=1-0 S(1) line is ∼400 AU, or more than twice the observed FWHM of the line. It is probably possible to fine tune the input parameters, but that would require a grid of shock models with a higher resolution than we used.

The PDR created by θ^1Ori C

As shown by Kristensen et al. (2003) the PDR generated by θ^1Ori C in the neighbouring Peak 2 (south-east of BN) has an effect of the order of 10–15% in bright objects. We reexamine this here for the shock analyzed in the present work. We compare our results with those of the "Meudon PDR code" (Le Petit et al. 2006).

For a density of 5×10^5 cm^{-3} and a radiation field of the order of 10^5 times the standard interstellar field (Draine 1978), the PDR models predict a brightness in v=1-0 S(1) more than an order of magnitude lower than observed. Even if the density is increased to 10^6 cm^{-3} it is impossible to reproduce the v=1-0 S(1) brightness. We therefore conclude that if there is a contribution from θ^1Ori C then it must be less than 10% of the v=1-0 S(1) brightness and we may ignore it. The v=1-0 S(0) brightness would be affected in a similar manner.

This is in agreement with the contribution estimated in Kristensen et al. (2003). It should be noted here that the uncertainty of the brightness is of the order of ∼3–10%, reddening apart. Lowering the brightness by ∼10% would
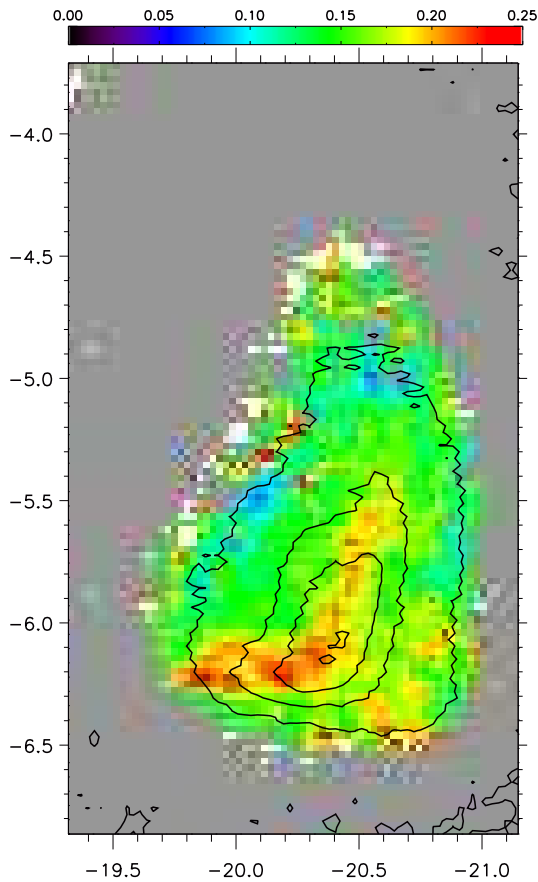
Figure 5.11: v=2-1 S(1) / v=1-0 S(1) line ratio in object 3. Co-ordinates are given with respect to TCC0016 and the colour bar is for the ratio. Contours are for v=1-0 S(1) absolute brightness. Contour levels are at 0.5, 1.0, 1.5 and 2.0×10^{-5} $W\,m^{-2}\,sr^{-1}$.

imply that we are overestimating the preshock density and shock velocity while underestimating the transverse magnetic field.

However, the v=2-1 S(1) brightness is usually more sensitive to the effects of a possible PDR. Again according to the "Meudon PDR code" (Le Petit et al. 2006) the v=2-1 S(1) / v=1-0 S(1) line ratio is ~0.2 for the above described initial conditions. In Fig. 5.11 we display this line ratio for our object. We see that the observed line ratio is in agreement with the PDR model predictions. However, as the absolute v=1-0 S(1) line brightness predicted is an order of magnitude lower than observed, so is the v=2-1 S(1) brightness. Therefore even in the v=2-1 S(1) line the PDR contribution is less than or equal to 10%, and we ignore it.

Existence of Mach disk

Behind the apex of the bow shock there is a small clump of brightly emitting gas. The distance between this clump and the apex is ~0″.3. It is at this location

that Nissen et al. (2007) observes a peak in radial velocity. The brightness is $\sim 1.5 \times 10^{-5}$ W m^{-2} sr^{-1} on average. This may be a Mach disk, but at present we do not have observational data with sufficient spatial resolution to support this. This qualitative effect is not included in the shock models. Thus we are possibly overestimating the width of the shock, particularly in the central parts (i.e. segments 3–6, see Fig. 5.5). The results would therefore be of the same order of magnitude as discussed previously in this section.

J-type shock component of the bow shock

We have assumed that we are observing a shock in steady-state. If there is a non steady-state component of the shock, this will show up as a J-type shock component (Chièze et al. 1998; Lesaffre et al. 2004). Non steady-state shocks are typically seen if the dynamical age of the shock is shorter than the steady-state age.

The projected distance between this object and the possible outflow source, radio source I (e.g. Menten & Reid 1995; Greenhill et al. 2004c; Nissen et al. 2007), is ~ 47 mpc (10^4 AU). At a velocity of ~ 50 km s^{-1} the dynamical age is $\gtrsim 1000$ yrs consistent with the dynamical age of the Orion bullets (Lee & Burton 2000; Doi et al. 2002). This may be compared to the steady-state timescale for a shock with preshock density 5×10^5 cm^{-3}, shock velocity 50 km s^{-1} and magnetic scaling factor b=6.0 which is ~ 120 yrs (see Sect. 2.2.2 for the definition of steady-state age).

Because the dynamical age is an order of mangitude greater than the steady-state timescale, we conclude that it is unlikely there is a non steady-state component of the shock. If the width of the shock is decreased (as discussed above), the time required to reach steady state is shorter, strengthening the argument that the shock is a steady-state shock.

5.2.4   Concluding remarks

We have analysed a single bow shock located in OMC1 in detail. One of the most important observational results is that we resolve the width of the shock, providing evidence that the shock is a C-type shock.

We have introduced a more sophisticated means of reproducing observations of bow shocks observed at high spatial resolution. This new method allows us in the example considered to predict a peak velocity of the bow shock which is in very good agreement with results from radial velocity and proper motion observations. Furthermore our predictions of the direction and strength of the magnetic field are consistent with independent estimates. These include observations which analyse the line-of-sight component of the magnetic field and the
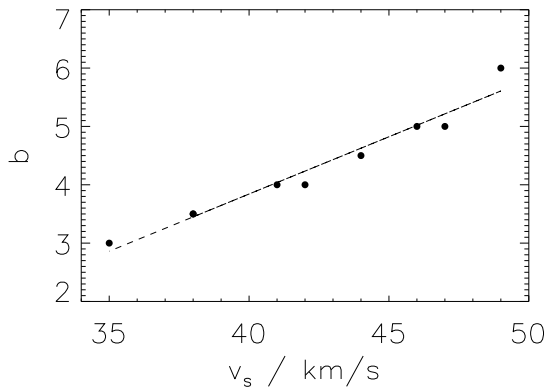
Figure 5.12: $b_\parallel$ as a function of $v_\perp$ for object 3. Each point shows results for a segment. The line shows the best fit straight line to the results.

total magnetic field as well as polarization observations of the region. Our prediction of how the magnetic field strength changes along the bow is in agreement with a simple geometrical model, where the apex is moving perpendicular to the magnetic field.

The data we have for most of the central part of OMC1 show that it would be possible to apply this new method on numerous objects which appear to be caused by shocks. The main requirement is that the shocks are moving close to the plane of the sky. Preliminary results from 3D modelling shows that this requirement is fulfilled when the angle with respect to the plane of the sky is less than 50° (Ravkilde et al. 2007, see below). Shocks moving along the line-of-sight are naturally not suitable candidates.

5.3   Comparison with 3D bow shock model - a first iteration

In this section we will use the best-fit results from the previous section as input parameters in the 3D model described in Sect. 2.3. We will also use the shape defined by the object. We do this as a first attempt to compare the 2D model with the 3D model. Later (currently a work in progress and not reported here) we intend to refine the 3D modelling to reproduce the observations.

5.3.1   Model input

We first of all assume that the preshock density is uniform and has a value of 5×10^5 cm^{-3} as suggested by the best-fit model (Table 5.2 and discussed in Sect. 5.2.2). We then assume that the magnetic field configuration is as discussed in Sect. 5.2.2. That is, we assume that the magnetic field is uniform and oriented
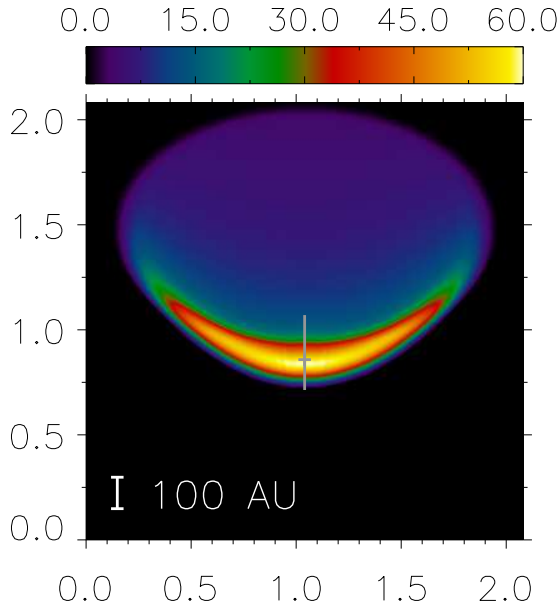
Figure 5.13: 3D model results for object 3 shown for the v=1-0 S(1) transition. The inclination with respect to the line of sight is 50°. The colour bar is in units of $10^{-5}\,W\,m^{-2}\,sr^{-1}$. Axes are in 10^{16} cm. The cross indicate the location of the apex.

tangential to the apex. We set the magnetic scaling factor to $b = 6.0$ at the apex and vary it with position angle as shown in Eqn. 5.2.2. We also keep the initial ortho/para ratio equal to 3 everywhere. We set the 2D shape of the bow to be the shape of the northern wing. It is given as (see also Eqn. 2.3.1):

$$z = 1.22 \times 10^{-3}\, r^2\, \text{AU}, \qquad\qquad (5.3.1)$$

where the vertex is the apex.

For this object the results show that $b_\parallel$ changes linearly with $v_\perp$ when moving along the bow, so that an increase in $b_\parallel$ by 1 leads to an increase in $v_\perp$ by ~6 km s^{-1}. This is shown in Fig. 5.12 for all 9 segments.

When doing the 3D modelling we have chosen to regrid our model results onto a cube with a pixel size of 4 AU. At the distance of OMC1 of 460 pc this corresponds to approximately one third of the pixel size in the observations (12.4 AU). The total size of the cube is (n_x, n_y, n_z)=(350,350,150) pixels=(1400,1400,600) AU.

5.3.2 Model results

Assuming that the inclination with respect to the plane of the sky is ~40° (Cunningham 2006; Nissen et al. 2007) we show the projected 3D bow shock in Fig. 5.13. In Table 5.3 we summarize the properties of the 3D model and compare them to observations. Here we only show results concerning the apex, that is

Table 5.3: Comparison of 3D model results and observations. We here show the observed properties of the apex, that is the point of maximum brightness and compare them to the 3D results also from the apex.

Property	Observation	3D model
Brightness, v=1-0 S(1) (10^{-5} W m^{-2} sr^{-1})	2.06±0.09	60.0
Brightness, v=1-0 S(0) (10^{-5} W m^{-2} sr^{-1})	0.75±0.06	12.7
Brightness, v=2-1 S(1) (10^{-5} W m^{-2} sr^{-1})	0.43±0.04	5.0
FWHM, v=1-0 S(1) (AU)	180±15	120
FWHM, v=1-0 S(0) (AU)	160±20	120
FWHM, v=2-1 S(1) (AU)	140±40	100

the point of peak brightness in the v=1-0 S(1) line. In the following we will go through the results from this modelling.

Inclination

In Fig. 5.14 we show the v=1-0 S(0) emission as a function of inclination angle, ψ between 90° (the shock is moving in the plane of the sky) and 10° (the shock is moving almost along the line of sight). Qualitatively the difference is very small for inclinations between 50° and 90°. The difference in peak brightness is ~18% between ψ=90° and 50°. Thus we show *a posteriori* that the dependence on inclination angle is sufficiently small, that we may consider that the shock is moving in the plane of the sky if the inclination angle is greater than 50°. It is important to note, that it is not a general conclusion, and we have only verified it for this particular 3D model.

Brightness

As can be seen from Table 5.3 the model is overestimating the brightness of the v=1-0 S(1) line by a factor of 30! For the other two lines the brightness is overestimated by a factor of 17 and 12, respectively. These high factors are somewhat surprising and it is of course interesting to understand the origin of this difference.

One of the assumptions of the 2D modelling was, that the depth (along the line of sight) is equal to the observed width (projected onto the plane of the sky). With the 3D models it is possible to verify this hypothesis. In order to quantify the depth, we will be using the number of points with T >1000 K as a measure. In general it is not possible to define a FWHM along the line of sight, as there may be a peak in emission both from the side of the shock facing us, and the side facing away from us. Moreover, in constructing the 3D model we
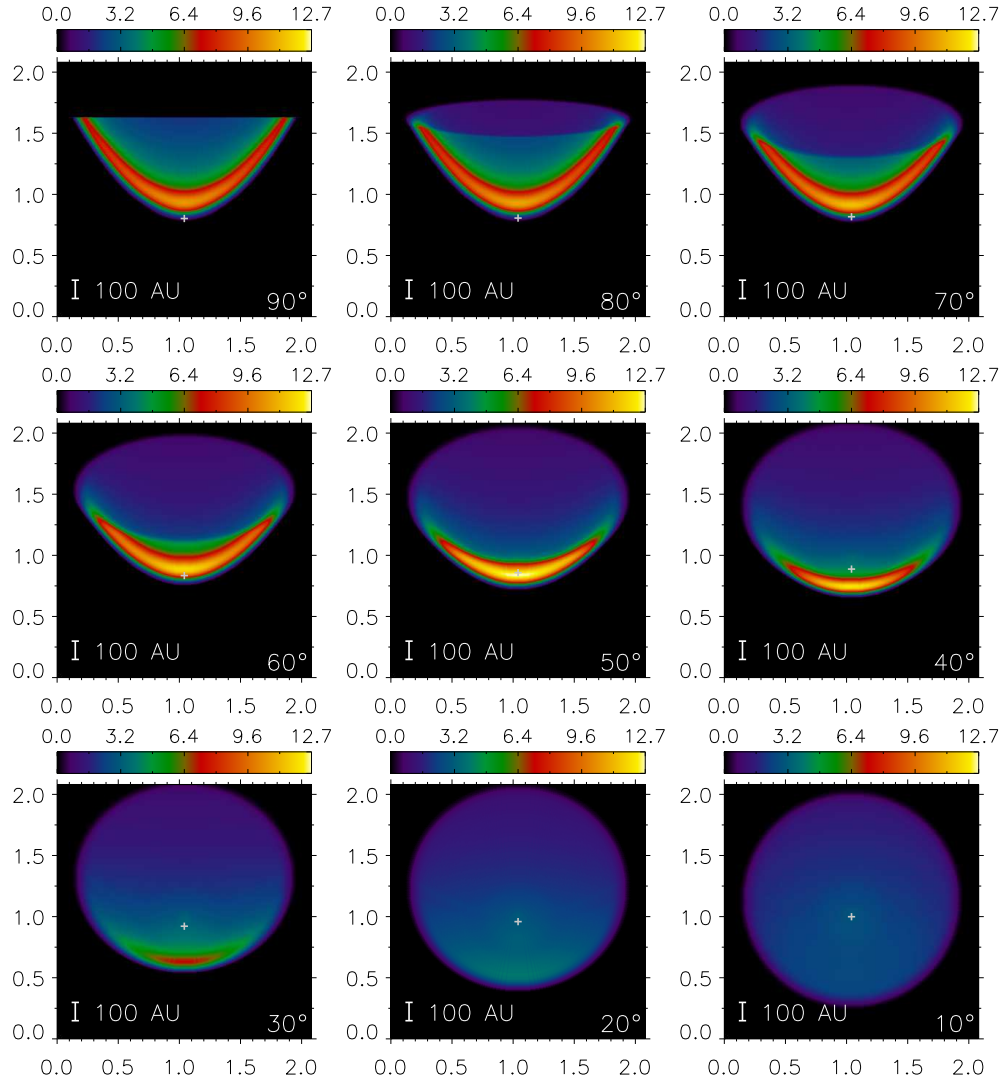
Figure 5.14: 3D model result as a function of inclination. We display H_2 v=1-0 S(0) emission. Axes are in units of 10^{16} cm, the colour bar is in units of 10^{-5} W m^{-2} sr^{-1}. The colour scale is kept constant for each figure. Inclination angles ψ are indicated in the lower left corner. The position of the projected apex is marked with a grey cross.

limited ourselves to points with $T > 1000$ K as it is at these temperatures H_2 is rovibrationally excited (see Sect. 2.3). In Fig. 5.15 we show the number of points as a function of spatial coordinates. In particular we find that the number of points with $T > 1000$ K is 231 at the apex corresponding to 918 AU. This
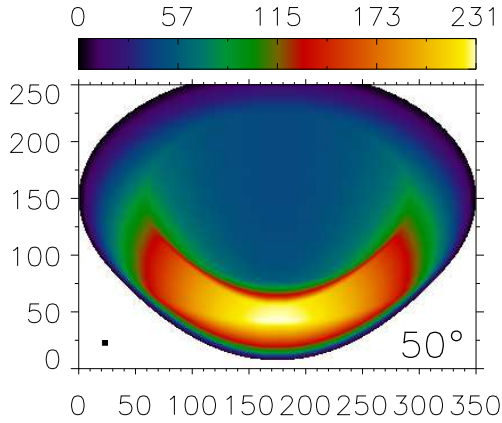
Figure 5.15: The number of points with T>1000 K for the bow shock model in Fig. 5.13. Axes are in pixels. The projection is smoothed by a 5×5 pixels moving boxcar average. The size of the boxcar is indicated by the small black square in the lower left corner. The colour bar represents the number of points with T>1000 K.

is ~5–6 times the observed FWHM, which is ~180–190 AU at the apex for the v=1-0 S(1) line and ~160–170 AU and ~140 AU for the v=1-0 S(0) and v=2-1 S(1) lines, respectively. Thus we are under-estimating the depth of the emitting gas by assuming that it is equal to the observed FWHM.

If we integrate the brightness over the entire length of the shock instead of the FWHM of the predicted local brightness profile, the model brightness would be increased since $I_{FWHM} < I_{total}$ where I_{FWHM} is the brightness integrated over the FWHM and I_{total} the total brightness. If we use I_{total} instead of I_{FWHM} the shock velocity and density would have been over-estimated, while the magnetic scaling factor would have been under-estimated.

To quantify this effect we made a new 3D model with the same shock velocity and transverse magnetic field strength, but a preshock density of 1×10^5 cm^{-3}. The new model predicts a peak brightness of ~1.0×10^{-5} W m^{-2} sr^{-1} for the v=1-0 S(1) H$_2$ line which is comparable to observations (~1.55×10^{-5} W m^{-2} sr^{-1}) but with a projected FWHM of ~450 AU.

We suspect that the reason the brightness in the original 3D model is 30 times higher than the observed value is due to insufficient resolution of the grid of models with respect to preshock density. As we have shown, we can lower the brightness substantially by reducing the preshock density. However, when doing so, we are increasing the projected FWHM. We now need to adjust the input parameters to reproduce observations and this is currently a work in progress.
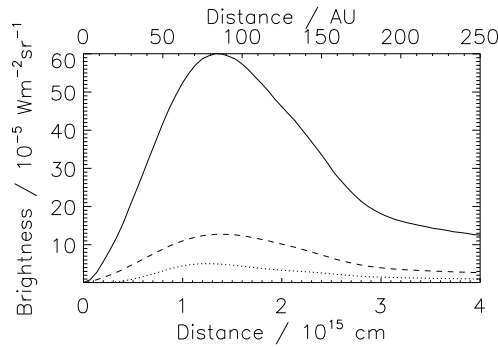
Figure 5.16: Brightness profiles relative to each other: v=1-0 S(1) (full line), v=1-0 S(0) (dashed line) and v=2-1 S(1) (dotted line). These brightness cuts are made along the grey line indicated in Fig. 5.13 going through the apex.

Width of the shock

Here we will discuss the predicted shock width from the 3D modelling. When discussing the shock width in this section, we will distinguish between the predicted width (the FWHM of the H_2 emission as would appear projected onto the plane sky) and the observed width (that is the observed FWHM). These widths are given in Table 5.3 for easy comparison.

The predicted brightness profiles at the apex are shown relative to each other in Fig. 5.16. These cuts have been made at the position indicated by the grey vertical line in Fig. 5.13. The prominent tail of the brightness profile reminds us, that we must be careful in blindly accepting the observed width as a solid parameter when fitting 1D models. This may be a major source of error if care is not taken to ensure that the overall shape of the brightness profiles are similar.

Mach Disk

As discussed above, we observe and resolve a small object directly behind the apex of the bow shock (Sect. 5.2.3). We speculated above that this may be a Mach disk. The projection maps of the initial 3D model of object 3 show a clear inability to reproduce this observed secondary object. This indicates that it is not a natural feature of a pure bow shock, but an independent object, thus supporting the conclusion that the observed object is a Mach disk. A future approach would be to include a Mach disk in the model and see if it is possible to reproduce this secondary object.

5.3.3   Sources of Error

There exists some sources of error in our model which we address below.

- The parameters for the present 3D model of object 3 was derived using the 2D cross section brightness profile fitting method discussed in the previ-

ous Sect. 5.2. Hence, any sources of error that apply to that technique of modelling are inherent in the current version of the 3D bow model. However, those parameters were only intended as initial guesses that we should not pick them in the blind, and as initial guesses they have worked well.

- The resolution of the grid of 1D models is found lacking with respect to preshock density n_H, consequently causing us to overestimate the brightnesses produced with the found FWHMs. It is probably possible to fine tune the parameters using a grid of higher resolution. However, calculating a grid with a resolution an order higher than the present would make the number of models in the grid reach ~1.5 million, requiring a vast computing time (more than ~20 years using present day computers). However it is of course possible to expand the grid locally around a possible solution to see if there are better solutions.

- We are only considering the emission where the temperature of the neutral species is higher than 1000 K. This is most significant for shocks with a high transverse magnetic field strength. However, the effect is to underestimate the brightness which we do not. We note here, that the effect would typically be much less than 1% at the orders of the parameters used for object 3 in Fig. 5.13.

- The emission through the volume of the bow shock as well as the Mach disk creates a prominent tail on the brightness profile implying that we may overestimate the FWHM. Therefore, the FWHM of the observed brightness profile should be seen as an upper limit.

5.3.4   Next iteration

To close in on the true parameters of object 3, the next step would be to examine in greater detail the importance of the number of points with T>1000 K. Furthermore it will be necessary to see how fast the brightness grows and the width decreases when going from a preshock density of 10^5 cm^{-3} to 5×10^5 cm^{-3}.

As this is done for object 3 treated here and possibly a few other bow shocks, we expect to be able to draw parallels from one case to the other growing further knowledge of the pros and cons of this technique. Ultimately we may be able to use it at as an interpretation tool in complex and violent areas such as most of the Orion Molecular Cloud or where, for example, 3D shock velocities are not available.
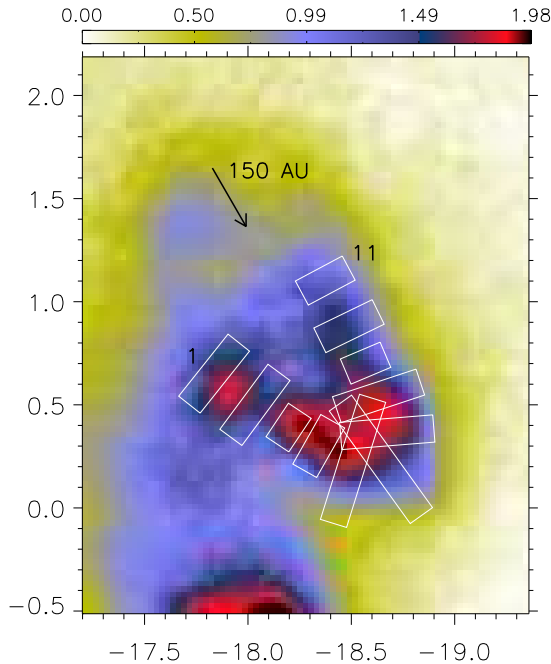
Figure 5.17: Continuum-subtracted image of object 1 shown in v=1-0 S(1) emission. Boxes show location and extent of the 11 segments. Segments 1 and 11 are marked for identification. The arrow has a position angle of 220° and a length corresponding to 150 AU. Coordinates are relative to TCC0016 and the colour bar is for brightness in units of 10^{-5} W m^{-2} sr^{-1}.

5.4   2D bow shock model of object 1

A similar analysis, but without the 3D modelling, was done for a different object[1]. Object 1 as it has been labelled in Fig. 4.4 is qualitatively different from object 3. The morphology is more clumpy and irregular but the position angle is almost the same, and it is found very close to object 3. The peak absolute brightness is similar with a brightness of $(1.98\pm0.09)\times10^{-5}$ W m^{-2} sr^{-1}. Object 1 is shown in Fig. 5.17 in v=1-0 S(1) emission.

Here we will briefly go through the results obtained for this object and the conclusions. We will follow the exact same procedure as in the previous section but will be more focused towards the results here.

5.4.1   Observational results

This object is slightly more extended than object 3 and so it is possible to cut it into 11 segments rather than 9. The object is very symmetrical and it was possible to fit a single parabolic curve to the shape of the bow. This gives a position angle of 220°±15°. From Cunningham (2006) the position angle is 243° and from Nissen et al. (2007) it is 239°. These two authors find a proper

---

[1]O. Venot, a 3rd year predoc student at the Université de Cergy-Pontoise, did this work in May and June 2007 under my supervision

Table 5.4: *Characteristics of the 11 segments of object 1 described in the text and displayed in Fig. 5.17. Brightness is given in units of 10^{-5} W m^{-2} sr^{-1} and FWHM perpendicular to the bow surface in units of AU. The uncertainties σ_{obs} given are 1σ.*

Seg.	p.a.	Brightness (10^{-5} W m^{-2} sr^{-1})			FWHM (AU)		
		1-0 S(1)	1-0 S(0)	2-1 S(1)	1-0 S(1)	1-0 S(0)	2-1 S(1)
1	142°	1.20±0.03	0.38±0.02	0.15±0.01	180±30	170±60	180±70
2	144°	1.33±0.04	0.40±0.02	0.16±0.02	180±20	80±40	20±50
3	142°	1.38±0.05	0.47±0.02	0.20±0.02	90±15	70±20	30±40
4	151°	1.44±0.05	0.58±0.02	0.25±0.02	130±15	100±20	20±40
5	163°	1.57±0.05	0.64±0.02	0.31±0.01	290±15	230±20	180±30
6	216°	1.31±0.04	0.52±0.02	0.26±0.01	310±15	140±20	160±30
7	274°	1.47±0.04	0.66±0.02	0.31±0.02	210±20	160±40	130±40
8	288°	1.46±0.03	0.53±0.02	0.27±0.01	200±25	80±50	110±50
9	293°	1.37±0.03	0.44±0.02	0.19±0.01	100±30	90±60	640±60
10	296°	1.35±0.03	0.50±0.02	0.18±0.01	140±30	120±60	160±60
11	298°	1.08±0.03	0.33±0.02	0.14±0.01	120±30	170±60	40±60

motion of 19 km s^{-1} and radial velocity of 18 km s^{-1} respectively, resulting in a 3D velocity of ~26 km s^{-1} and an angle with respect to the plane of the sky of 43°.

The observed constraints for each segment are listed in Table 5.4. They are as for object 3 the FWHM of the bow shock measured perpendicular to the bow surface and the brightness in v=1-0 S(1), v=1-0 S(0) and v=2-1 S(1) integrated over the FWHM.

We note here that because the opening angle of the shock is very narrow compared to the opening angle of object 3 it is not possible to measure directly the FWHM in segments 4 to 8. Therefore we measured the half width at half maximum (HFHM) and multiplied it by two.

5.4.2   2D model reproduction

We reproduce the results of each segment by the χ^2 method described above. Results are listed in Table 5.5. Even though results do not appear as continuous as for object 3, they do show the same order of magnitude in terms of input parameters. It is not surprising that the variations are more pronounced in this object as it is more clumpy in nature than object 3. In the following we will discuss what can be learned from the input parameters in much the same fashion as was done in Sect. 5.2.2.

Table 5.5: Input parameters of the models which best reproduce observations of object 1. Results (confidence intervals) are listed for each segment.

Seg.	Preshock density (cm^{-3})	Shock velocity ($\mathrm{km\,s}^{-1}$)	b	o/p_{ini}
1	5×10^5 (5×10^5–10^6)	45 (41–48)	5.5 (4.0–7.0)	3.00 (2.0–3.0)
2	10^6 (5×10^5–10^6)	34 (31–41)	3.5 (2.5–5.0)	3.00 (0.01–3.0)
3	10^6 (5×10^5–10^6)	33 (31–40)	3.0 (2.5–4.5)	3.00 (0.01–3.0)
4	5×10^5 (5×10^5–10^6)	47 (33–44)	3.5 (2.5–5.0)	3.00 (0.01–3.0)
5^a	5×10^5 (5×10^5–5×10^5)	50 (49–50)	6.5 (6.0–6.5)	3.00 (2.0–3.0)
6	5×10^5 (5×10^5–10^6)	44 (41–46)	4.5 (3.5–6.5)	3.00 (2.0–3.0)
7	5×10^5 (5×10^5–5×10^5)	42 (41–45)	3.5 (3.0–4.5)	3.00 (2.0–3.0)
8	10^6 (5×10^5–10^6)	36 (32–43)	4.0 (2.5–5.5)	3.00 (0.01–3.0)
9	5×10^5 (5×10^5–5×10^5)	46 (41–49)	5.5 (4.5–9.0)	2.00 (0.01–3.0)
10	5×10^5 (5×10^5–5×10^5)	44 (38–46)	4.5 (3.5–6.5)	3.00 (2.0–3.0)
11	5×10^5 (5×10^5–5×10^5)	43 (39–45)	5.0 (4.0–6.0)	3.00 (2.0–3.0)

[a] The velocity is at the upper boundary of our grid, and should only be seen as a lower limit.

Shock velocity

It is interesting to note that the velocity is much higher than measured by Cunningham (2006) and Nissen et al. (2007). However, as Cunningham notes, the uncertainty on the proper motion measurements is of the order of ~25 $\mathrm{km\,s}^{-1}$. If this is included, the 3D velocity is ~26±25 $\mathrm{km\,s}^{-1}$. The maximum velocity predicted here is greater than 50 $\mathrm{km\,s}^{-1}$. We also note that the range of velocities are very similar to the velocities in object 3. In Fig. 5.18 we show the distribution of shock velocities along the bow.

It is possible to estimate the position angle by using Eqn. 5.2.1 in Sect. 5.2.2. We find that the maximum velocity is ~43±4 $\mathrm{km\,s}^{-1}$. The position angle is 240°±18°. This is in agreement with the position angle determined above and the angle determined by Cunningham (2006) and Nissen et al. (2007).

Transverse magnetic field

The transverse magnetic field is higher than in object 3 but not significantly so. Here we find a maximum in Segment 5. However this segment may not be correctly reproduced as the velocity is at the upper limit of the grid. The absolute value of the transverse magnetic field strength is ~4.7 mGauss which is higher than estimated by Norris (1984).
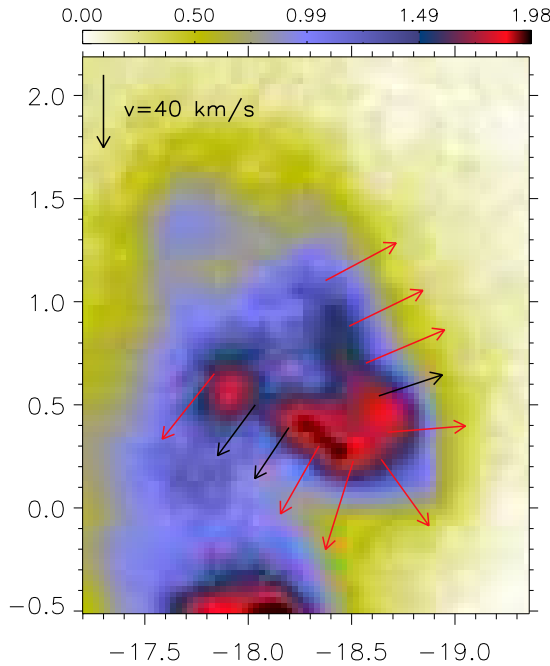
Figure 5.18: Velocity variations along the bow superposed on an image of object 1 as observed in v=1-0 S(1). Coordinates and colour bar are as in Fig. 5.17. The lengths of the arrows are scaled with velocity and the arrow in the top left corner has a length corresponding to 40 km s^{-1}. Red arrows indicate a preshock density of $5{\times}10^5$ cm^{-3} while black arrows represent 10^6 cm^{-3}.

Again it is possible to estimate the position angle of the magnetic field using Eqn. 5.2.2 in Sect. 5.2.2. However we do not simply use b when fitting. Instead we use $B = b \times \sqrt{n_H(\text{cm}^{-3})}$ μGauss since n_H is not constant. We find that the position angle of the transverse magnetic field is 113°±21°. This value almost fit the position angle of the shock which is ∼220° and 130° at right angles.

Density

In Fig. 5.18 we show the distribution of initial densities (red and black arrows). The distribution of the different densities does not show an apparent pattern. The average density is very similar to the density predicted for object 3, that is ∼5×10^5 cm^{-3}.

Initial ortho/para ratio

Again it is practically impossible to constrain the initial ortho/para ratio and it is equal to 3 everywhere except Segment 9, where it is 2. However, as for object 3, if the ortho/para ratio was locked, we find that it has little consequence for the final results.

Sources of error

Apart from the sources of error already discussed in Sect. 5.2.3, the main source is the clumpiness of object 1. As can be seen in Fig. 5.17 sometimes the segments are well aligned with individual knots, sometimes they are located on the edge of knots. The latter is the case for Segments 1 and 2. One method to overcome this could be to cut the shock into segments that are not of equal size and equally spaced. Instead the segments would cover knots in the shock. This has not been done yet but again higher spatial resolution observations would help us to better analyze this feature.

5.4.3   Conclusion

It is possible that differences in preshock density and magnetic field strength causes the shock to appear clumpy. This is also the conclusion we can draw from the model reproductions of observations. This object was more difficult to analyse than object 3 because of this clumpiness. This will almost certainly add another layer of uncertainty to the model reproductions, something we have chosen to ignore at present.

Nevertheless we do show that the method described in Sect. 5.2 is a robust method and does produce reliable results. We have not yet tried modelling this shock in 3D but that will certainly be a future project.

5.5   Conclusion and outlook

A lot of work remains to be done, both in terms of analysing existing observations, developing the 3D models further and planning follow-up observations. But we have shown here how it is possible to construct a 2D model where the results are in very good agreement with other independent observations. This same analysis will now be applied to other bow shocks found in our dataset.

So far we have only scratched the surface of 3D modelling. After the first iteration more work clearly needs to be done as the predicted surface brightness obviously is too high. It remains unclear whether the 2D modelling or the 3D modelling is the source of the problem. For this purpose it is probably necessary to greatly expand the grid of shock models to include more preshock densities. However for each density that is added ~3600 additional models needs to be run. Since it takes ~8 minutes to run a model, we are looking at a computing time of 20 days per additional density. A solution could be to write an optimization program that through an iterative process runs and compares models with observations by taking steps that becomes smaller and smaller.

A remaining question is also the nature of these bow shocks. The results from Sect. 4.4.3 suggest that they could be clumps overrun by the general outflow while here, it seems that they are caused by individually launched bullets. To verify the nature, it would be interesting to plot the dynamical age, that is, the distance from the outflow source divided by the 3D velocity as a function of distance to the outflow source. If the objects all have the same age, they are probably bullets launched by the same explosive event. If they show a large range of ages, with the older objects farther away, it would be more likely that they are clumps overrun by the outflow. Unfortunately Cunningham (2006) does not provide the appropriate data in his thesis, and it has so far not been possible to obtain the data.

We are planning to apply for follow-up observations with the Spitzer Space Telescope (85 cm mirror) using the InfraRed Spectrograph (IRS). It is important to do follow-up observations at other wavelengths probing the shocked gas at different temperatures. With the model predictions we are able to estimate the brightness in the pure rotational H_2 lines v=0-0 S(0)-S(7)[2] and find a typical brightness of the order of 10^{-6} W m^{-2} sr^{-1}. Although the spatial resolution is much smaller with Spitzer (between 1$.\!\!''$5 and 8$.\!\!''$3 depending on wavelength) it should be possible to isolate the objects and detect rotationally excited H_2. Another instrument that could be used for this purpose is the proposed satellite H2EX (Boulanger 2007). It is expected that H2EX will have a higher sensitivity and better spectral resolution than Spitzer. Furthermore it will operate as an integral field spectrometer. This could in principle be used to give us valuable information on the gas dynamics in complex star forming regions such as OMC1.

---

[2]This is work done by J. Goffart during a 2 month predoc position under my supervision. J. Goffart is a 3rd year student at the Université de Cergy-Pontoise

VLT/ISAAC observations of BHR71 and BHR137

In this chapter I will present observations of the two Bok globules, BHR 71 and BHR 137. Observations were performed in July 2002. I have not been involved in taking the observations, nor the initial data reduction. However the final steps of the data reduction (wavelength calibration, background subtraction, etc.) and the analysis are done by me.

In the case of OMC1 I have used spectroscopic imaging. In this Chapter I will focus more on long-slit spectroscopy. When observing isolated regions of star formation it may be desirable to use spectroscopy rather than narrow-band imaging. Narrow-band imaging is very suitable for a complex region like OMC1 but when the target is a single jet or shock as in many HH-objects, spectroscopy is better. In that case the disadvantages (lack of spatial information) are clearly outweighed by the advantages (large number of H_2 lines observable at the same time). In the present observations we detect between seven and nine H_2 lines in each object.

First I will describe the observations and data reduction. Then I will provide the results for different H_2 lines in different spatial regions. Finally I will interpret the results in terms of shock models before giving the concluding remarks.

6.1 Observations and data reduction

Observations were performed on the nights of July 12 and 14, 2002. Both sets of data were recorded using the Infrared Spectrometer and Array Camera (ISAAC; Moorwood et al. 1998) on the ESO VLT, UT1. Observations were centered on BHR71 IRS1 at $12^h01^m37\overset{s}{.}1$; $-65°08'54''$(J2000) and on BHR137 at $17^h21^m48^s$; $-44°08\overset{'}{.}8$ (J2000).

For both observations the long slit spectroscopic mode was used, using a slit-width of $2''$ and a spectral resolution of $\lambda/\delta\lambda$=200. The second order of the grating was used to gain access to the entire K-band (1.84–2.56 μm). The slit

length is 120″ with a pixel scale of 0.″146 per pixel. This corresponds to 29 AU at the distance of BHR71 (200 pc; Bourke et al. 1997) and 102 AU at the distance of BHR137 (700 pc; Bourke et al. 1995b). In the spectral direction, the pixel length is 7.03×10^{-4} μm/pixel. In the case of BHR137 the H-band was also observed (1.4–1.82 μm) where the pixel scale is 4.69×10^{-4} μm per pixel.

Observation of weak H_2 emission in the K-band is dominated by the problem of removing the sky background. This background consists at shorter wavelengths, up to ~2.2 μm, of emission from excited OH in the upper atmosphere, the so-called Meinel bands. At longer wavelengths, greater than ~2.4 μm, thermal emission from both the atmosphere and the instrument becomes obtrusive. The Meinel bands and thermal emission can be brighter by respectively two and three to four orders of magnitude than the signals for which we search. Moreover the Meinel bands are variable on a time-scale of minutes.

The tactics adopted were to record a spectrum on the object, and then nod the slit along its length, onto the sky and record again for the same time. The exposure time was chosen so as to take into account the rapid variability of the Meinel bands and also to avoid saturating the detector. For BHR71 the exposure time was 60 seconds while for BHR137 it was 100 seconds. In both cases the criteria listed above were satisfied.

BHR71 was observed four times at four slightly different slit positions. For the first three observations the slit was displaced 1″ with respect to the previous slit covering HH321A. The fourth slit was shifted 26″ to the west covering part of HH320A (see Fig. 6.1). Total exposure time for each spectrum was 1800 seconds. For BHR137 two spectra were recorded; one in the K-band and one in the H-band. Total exposure time for the K-band spectrum was 1800 seconds while it was 1200 seconds for the H-band. A finding chart for each set of observations are provided in Figs. 6.1 and 6.2, respectively where the position of the slits are shown.

For both sets of observations, imaging was also performed using the Short Wavelength Imaging mode (SWI) of ISAAC. Images were recorded using the K_s filter (2.03–2.29 μm; BHR 71 and 137) and NB213 and NB219 narrow-band filters (centered on 2.13 and 2.19 μm respectively; BHR 137 only). Here we do not present an analysis of the images. Here they are merely used as finding charts for our spectroscopic observations.

None of the observations were performed using adaptive optics, as this is not available. Thus the spatial resolution is seeing limited. In the case of BHR71 conditions were photometric and the seeing as measured from PSFs of stars in the field is ~0.″6. For observations of BHR137 the conditions were slightly worse resulting in a spatial resolution of ~0.″9.

Standard data reduction included dark subtraction, flat-fielding using twilight flats and sky-subtraction. This largely removed the OH Meinel bands and other
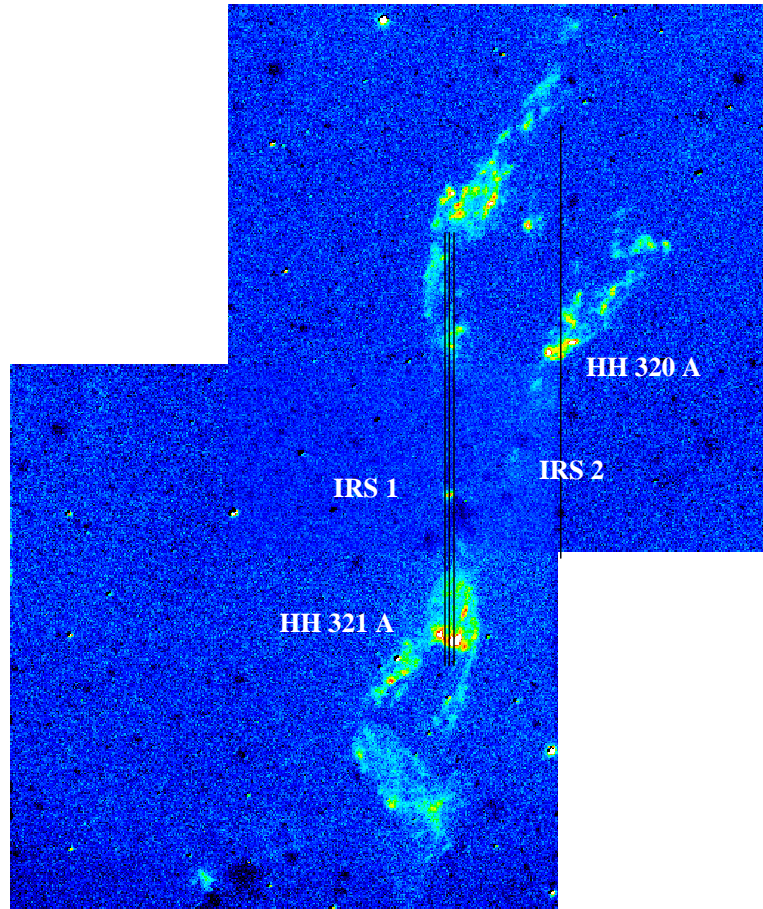
Figure 6.1: Finding chart for BHR71 showing continuum-subtracted H_2 emission from the v=1-0 S(1) line. The four different slit positions are marked with black lines. Each image measures $152''\times152''$ and North is up, East is left.

telluric features as well as thermal emission from the sky. In the case of BHR71 there were residual OH emission at about 10–15% of the peak H_2 intensity in all spectra. It is probably due to the rapid sky variation. To remove this, we identified a range of spatial positions within each slit with little or no H_2 emission, and subtracted it from the rest. This completely removed any residual OH emission.

For BHR137 photometric and spectral calibrations were performed each night with stars from the Hipparchos catalogue. For BHR71 no absolute calibration has been performed. To measure the line brightness we have fitted each spectral line with a Gaussian which is then integrated.
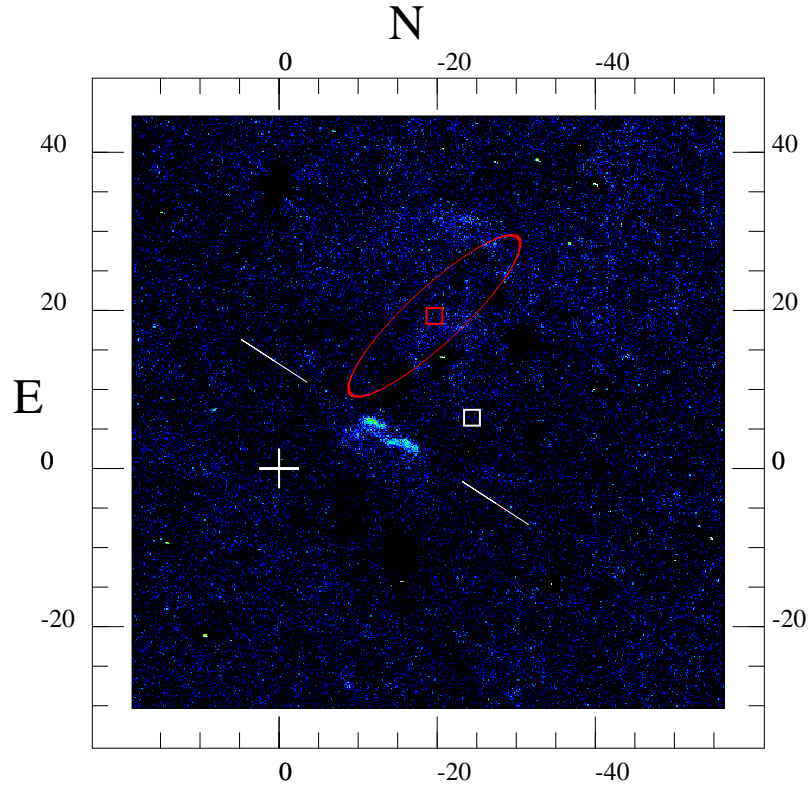
Figure 6.2: Finding chart for BHR137 showing continuum-subtracted H_2 emission from the v=1-0 S(1) line. The slit position is marked by the two white lines. The IRAS source is marked by the red rectangle and the error ellipse is shown. The white square shows the 1.3 mm-source (Reipurth et al. 1996). See also Fig. 1.13.

6.2 H_2 line results

In BHR71 we detect H_2 in four different places: HH321A, close to IRS 1, north of IRS 1 and HH320A (see Fig. 6.1). In the following we will refer to these knots of excitation as 1, 2, 3 and 4 respectively. In BHR137 we discover 2 knots of excited H_2 which we will refer to as A and B respectively (see Fig. 6.2). Results for BHR71 and BHR137 will be dealt with individually and compared later.

6.2.1 BHR71

In Fig. 6.3 we show a profile of v=1-0 S(1) emission through the centre slit. Here we identify three of the four knots of emission discussed above. In the
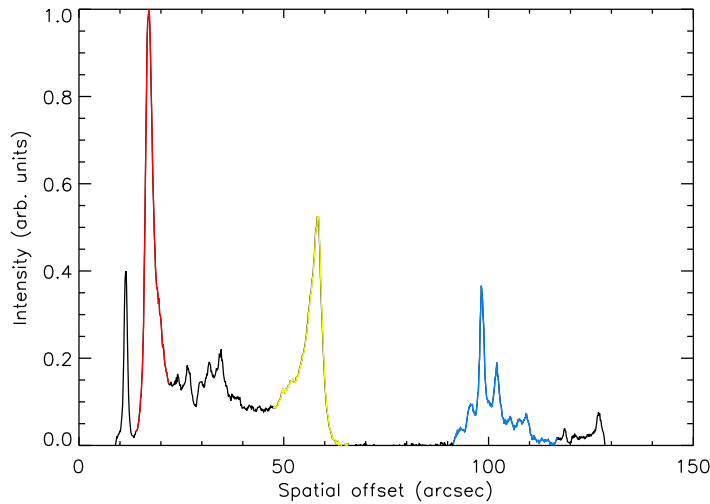
Figure 6.3: Spatial distribution of H$_2$ v=1-0 S(1) emission in BHR71 as observed through the centre slit in Fig. 6.1. In red is HH321A (knot 1), yellow shows emission associated with IRS 1 (knot 2) and in blue is emission located north of IRS 1 (knot 3). The abscissa is in arcseconds whith the zero point set arbitrarily. The ordinate is for v=1-0 S(1) emission in arbitrary units.

fourth slit we identify a single knot of H$_2$ emission coincident with HH320A (not shown here).

To improve the S/N ratio we integrate the emission over each knot. The resulting spectrum for knot 1 is shown in Fig. 6.4 where we detect thirteen H$_2$ lines. We do not consider the H$_2$ Q-branch longwards of 2.4 μm even though some of these lines are strong. In general the lines are blended. This is especially true for the v=1-0 Q(1) and Q(2) lines. Here we do not make an attempt to deblend the lines. Moreover the Q-lines may suffer from strong atmospheric absorption (Livingston & Wallace 1991).

The v=1-0 S(2) and S(3) lines and v=2-1 S(4) may also suffer from atmospheric absorption. However all of these lines are strong in our spectra. This implies that the absorption is probably not strong which is probably because the lines are Doppler-shifted out of atmospheric absorption features. Since it is difficult to quantify the amount of absorption—if any—we will consider the intensities from these lines as lower limits.

Because of the proximity of three of the slits, we choose to average the intensity for each knot. Results are shown in Table 6.1 where the intensities are given with respect to the v=1-0 S(1) line. Uncertainties quoted in this Table are
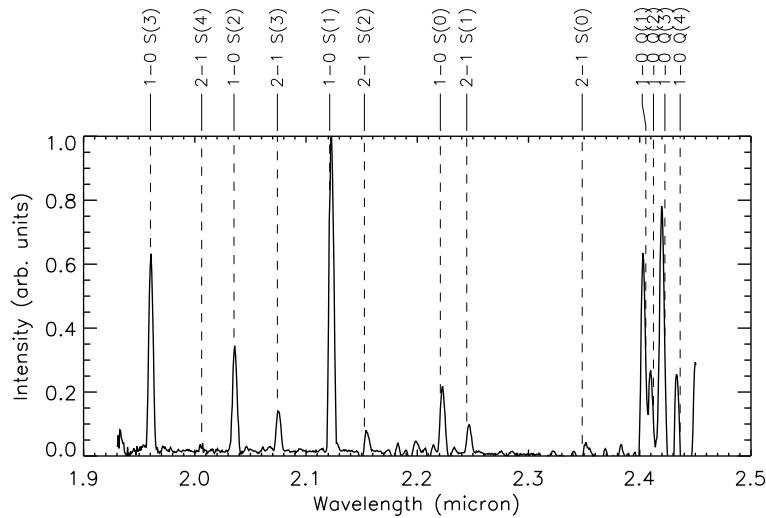
Figure 6.4: K-band spectrum of knot 1, BHR71. Detected H$_2$ lines are marked. Intensity is in arbitrary units.

1σ uncertainties.

In Fig. 6.5 we plot log(column density per sublevel) vs. the upper level energy in a socalled excitation or Boltzmann diagram. Any significant deviation of the ortho/para ratio from its statistical value of 3 would appear as a misalignment of the ortho and para data points in the Boltzmann diagrams. No such deviation is observed and we conclude that the ortho/para ratio is 3.

If the gas is excited at a single temperature, a straight line can be fitted through the data points. This is the case for the four knots we have observed. This is in contrast to the results of Giannini et al. (2004), where two temperatures are needed. However, they find that the second temperature is needed for energies higher than ~15 000 K (the v=3 and 4 upper levels) where we have no data points. The excitation temperatures they find for HH320A and HH321A (see Table 6.1) are significantly higher than our results. Our results are obtained by integrating over the entire region of each excitation knot. The same was done by Giannini et al. (2004, T. Giannini private communication). If we perform the same analysis, integrating the emission in the 5 pixels surrounding the peaks of HH320A and HH321A we find excitation temperatures of 2150±30 K and 2400±40 K respectively. In the case of HH321A there is now some agreement between the results, but for HH320A we find that the excitation temperature actually drops. The reason for this is unknown at present.

Table 6.1: Results for knots 1–4 in BHR71. All line intensities are given with respect to the v=1-0 S(1) intensity. The errors given are 1σ. A long line (—) indicates no detection. Finally we list the excitation temperature as obtained from the Boltzmann plots (see Fig. 6.5) with 1σ errors. For comparison we list the excitation temperature determined by Giannini et al. (2004).

Line	Knot 1 (HH321A)	Knot 2	Knot 3	Knot 4 (HH320A)
v=1-0 S(3)	0.69(±2.5%)	0.39(±24%)	0.77(±3.5%)	0.92(±3.0%)
v=2-1 S(4)	0.015(±26%)	—	0.062(±17%)	0.043(±20%)
v=1-0 S(2)	0.32(±2.9%)	0.25(±16%)	0.30(±3.5%)	0.35(±3.2%)
v=2-1 S(3)	0.11(±5.0%)	0.19(±18%)	0.094(±6.7%)	0.12(±6.0%)
v=1-0 S(1)	1.0	1.0	1.0	1.0
v=2-1 S(2)	0.053(±14%)	0.069(±52%)	0.026(±23%)	0.029(±15%)
v=1-0 S(0)	0.21(±4.9%)	0.30(±13%)	0.22(±3.0%)	0.21(±4.5%)
v=2-1 S(1)	0.090(±4.1%)	0.13(±30%)	0.12(±5.0%)	0.10(±2.9%)
v=2-1 S(0)	0.032(±26%)	0.065(±40%)	—	0.013(±22%)
T_{ex} (K), average	2200±30	2500±150	2190±30	2230±30
T_{ex} (K), peak	2400±40			2150±30
T_{ex} (K) Giannini et al.	2540±110			3140±140

6.2.2 BHR137

The first thing to be noticed is that the two excitation knots, A and B are less extended and much fainter than the excitation knots in BHR71. In Fig. 6.6 we show the spatial extent of the two knots as observed through the distribution of v=1-0 S(1) emission. As before, to improve the S/N ratio we integrate all the emission from each knot. The region over which we integrate is marked in Fig. 6.6. In Figs. 6.7 and 6.8 we show the resulting *K*- and *H*-band spectra of knot A, respectively. In total we detect ten H$_2$ lines, not counting the Q-branch and v=1-0 S(8) and S(9) even though they are marked on the figures. Furthermore we detect three [FeII] lines.

The observed line intensities are listed in Table 6.2. Here we list absolute as well as relative brightness to the v=1-0 S(1) line. Uncertainties listed are 1σ. In Fig. 6.9 we display Boltzmann diagrams for knots A and B.

We find no deviation from the equilibrium value of the ortho/para ratio of 3. We also find that it is possible to fit the data points in the Boltzmann diagram with a single line. As stated above, this may be because we are not probing
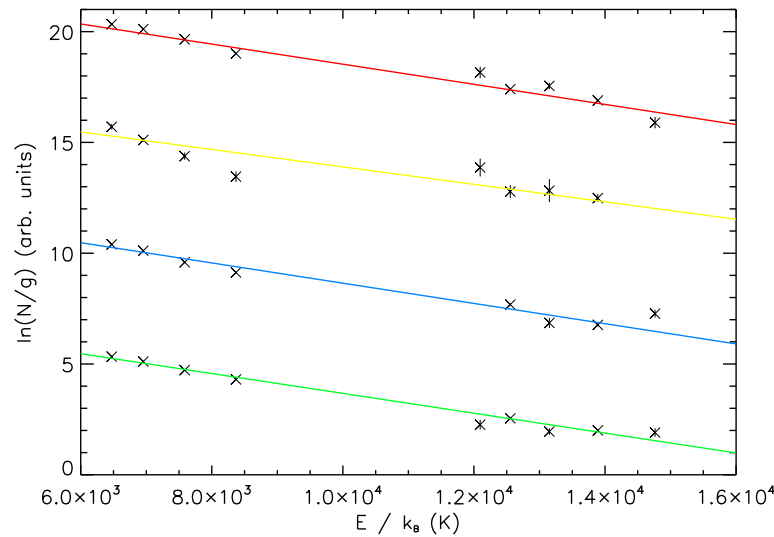
Figure 6.5: Boltzmann diagram for the four knots of emission identified. Red is knot 1 (HH321A), yellow is knot 2, blue is knot 3 and green is knot 4 (HH320A). 1σ error bars are shown as vertical lines. The lines show the best fit through the data. The corresponding excitation temperature is given in Table 6.1. Results have been displaced vertically by 5 so as to better show them.

the highly excited v≥3 gas. The excitation temperature of knots A and B is 1960±80 K and 1800±60 K respectively. This is the excitation temperature for the entire knots A and B. If we just focus on the peak of emission, the excitation temperature in knot A rises to 2180±110 K while it remains at 1800±70 K in knot B.

6.3   Interpretation and discussion

In the following we will be interpreting the emission from BHR71 and BHR137 in terms of shock models. As for OMC1 we will be using the results given in Chapter 2. It is possible that the PAH abundance is much lower than in OMC1. In cold dark clouds PAH emission features tend to disappear, which has been interpreted as the PAHs are adsorbing onto dust grains (e.g. Abergel et al. 2005, and references therein). Observations of PAH emission has not been made for these two particular clouds, and we adopt the PAH abundance of OMC1.

We will be using the relative H_2 line brightness as constraints in the case of BHR71 and the absolute H_2 and [FeII] line brightness for BHR137. We will
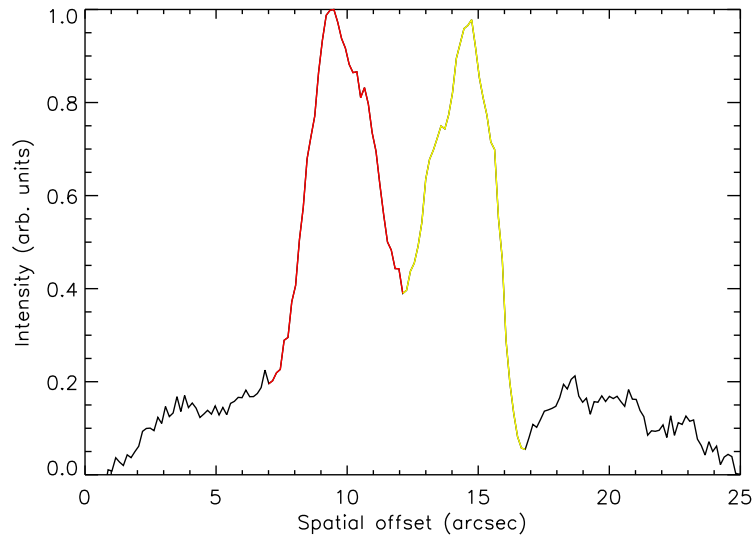
Figure 6.6: Spatial distribution of H₂ v=1-0 S(1) emission in BHR137. In red is knot A, yellow shows emission associated with knot B. The abscissa is in arcseconds. The zero point has been set arbitrarily. The ordinate is for v=1-0 S(1) emission in arbitrary units.

not be using the size as a constraint. The reason for this is, that even though the knots appear to be spatially resolved, we do not know their exact orientation with repsect to the slit position. The shock width is only a valid constraint when measured along the line of motion and the shock is moving close to the plane of the sky, as was done in the previous Chapter 5.

For both BHR71 and 137 we will begin with a short discussion of the interpretations that can be made just by looking at the results. Then we will perform a χ^2 analysis to determine the best fit models and discuss results.

6.3.1   BHR71

Giannini et al. (2004) detect no [FeII] emission from the outflow in BHR71. As they note, the visual extinction is low, ≤2 mag and so the non-detection is probably not due to extinction. Therefore the shock waves are most likely not dissociative (see Sect. 2.2.2), that is H_2 is not dissociated. Even though we are not considering the width as a constraint, from images of BHR71 (e.g. Fig. 6.1 or Bourke 2001) it appears that the shock width is resolved inside the slit, as it is oriented. If the width is resolved the shock is most likely not a pure J-type shock.
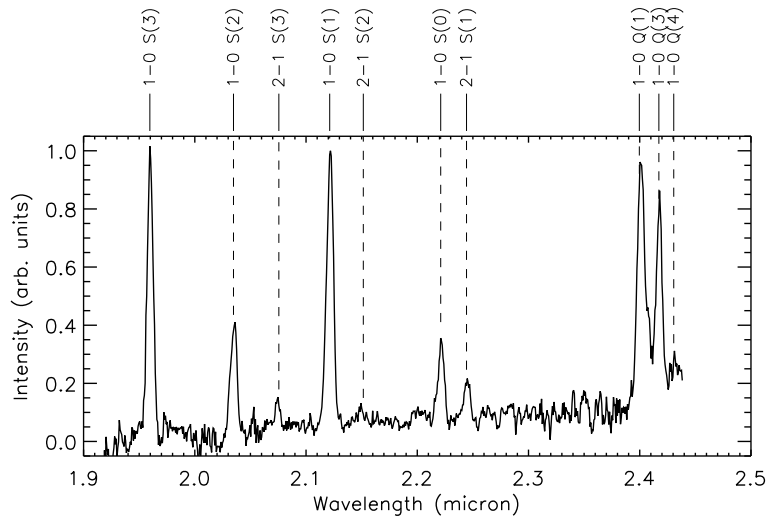
Figure 6.7: K-band spectrum of knot A, BHR137. Detected H_2 lines are marked. Intensity is in arbitrary units.
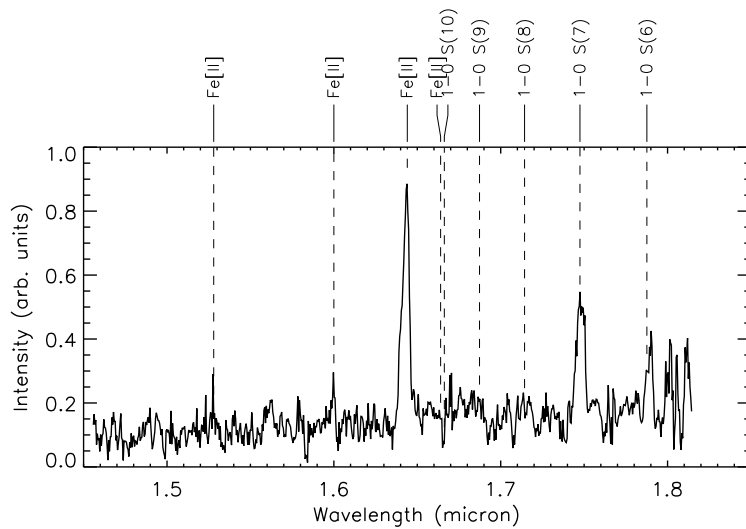
Figure 6.8: H-band spectrum of knot A, BHR137. We show the location of several H_2 and [FeII] lines. Intensity is in arbitrary units.

Table 6.2: Results for knots A and B in BHR137 in H- and K-band. Absolute brightness is given in units of 10^{-9} W m^{-2} sr^{-1}. Relative brightness is given with respect to the v=1-0 S(1) line. Errors given are 1σ, relative errors are given in percent. A long line (—) indicates no detection. Finally we list the excitation temperature as obtained from the Boltzmann plots (see Fig. 6.5) with 1σ errors.

	Absolute brightness		Relative brightness	
Line	Knot A	Knot B	Knot A	Knot B
v=1-0 S(3)	183±5	202±8	0.93(±4.1%)	0.94(±5.8%)
v=1-0 S(2)	83.7±4.6	78.0±4.3	0.43(±6.3%)	0.36(±7.0%)
v=2-1 S(3)	11.6±1.6	5.94±1.95	0.059(±13.9%)	0.028(±33.2%)
v=1-0 S(1)	197±6	215±9	1.0	1.0
v=2-1 S(2)	6.11±1.79	—	0.031(±29.4%)	—
v=1-0 S(0)	52.2±3.8	59.0±2.9	0.27(±7.8%)	0.28(±6.6%)
v=2-1 S(1)	29.2±2.8	24.0±3.5	0.15(±10.1%)	0.11(±15.1%)
v=1-0 Q(1)	203±16	261±25	1.03(±8.5%)	1.22(±10.7%)
v=1-0 Q(3)	79.5±10.3	102±13	0.40(±13.2%)	0.47(±13.8%)
v=1-0 Q(4)	31.2±14.4	62.1±27.7	0.16(±46.1%)	0.29(±44.7%)
[FeII] 1.534 μm	1.17±0.96	—	0.006(±81.8%)	—
[FeII] 1.600 μm	2.91±0.94	—	0.015(±32.4%)	—
[FeII] 1.644 μm	39.2±3.2	44.1±2.3	0.20(±8.6%)	0.206(±6.8
v=1-0 S(10)	1.97±0.96	—	0.010(±48.7%)	—
v=1-0 S(7)	26.7±2.6	25.7±1.3	0.136(±10.1%)	0.12(±6.8%)
v=1-0 S(6)	8.75±1.70	16.4±3.0	0.045(±19.7%)	0.076(±18.5%)
T_{ex} (K), aver.	1960±80	1800±60		
T_{ex} (K), peak	2180±110	1800±70		

It may be a J-type shock with a magnetic precursor as proposed by Giannini et al. (2004), this cannot be ruled out at this stage.

We perform the χ^2 analysis as described previously by calculating $\chi^2 = \frac{1}{n} \sum \frac{(X_{obs} - X_{mod})^2}{\sigma^2}$ for each model. The results for knots 1–3 are listed in Table 6.3. For all knots we find that the best-fit initial ortho/para ratio is 3.

From our analysis it appears that HH320A (knot 4) is quite different from the three other knots. It was not possible to determine a best fit model with any degree of confidence. The model in our grid that came closest was a J-type shock with b=0.1, n_H=10^7 cm^{-3} and v_s=19 km s^{-1}. The initial ortho/para ratio was 0.01. Unfortunately we have to exclude this model based on physical reasons. The preshock density is so high that model results are no longer to be
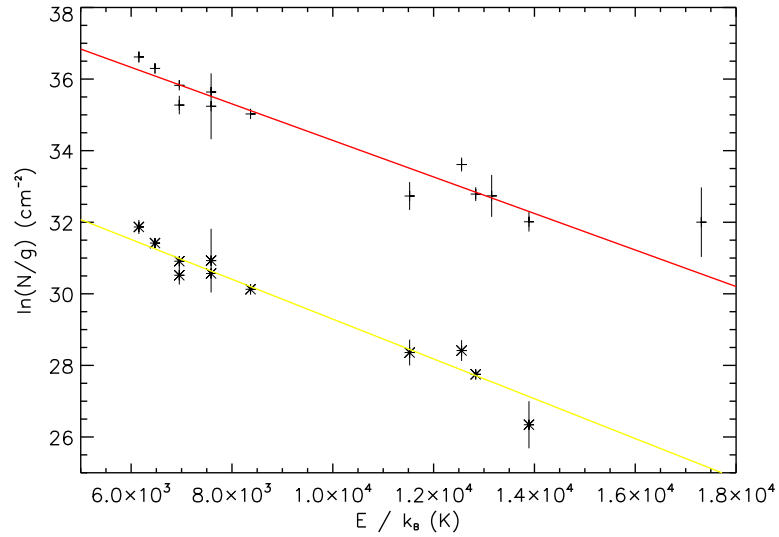
Figure 6.9: Boltzmann diagram for the two knots of emission identified. Red is knot A, yellow is knot B. Vertical lines show 1σ errors. The lines show the best fit through the data. The corresponding excitation temperature is given in Table 6.2. Results for knot B have been displaced vertically by 5.

Table 6.3: Best fit model results for knots 1–3 in BHR71. Confidence intervals are given in parentheses.

Shock Parameters	Knot 1 (HH321A)	Knot 2	Knot 3
n_H (cm^{-3})	5×10^4 (5×10^4–5×10^4)	5×10^6 (10^4–10^7)	5×10^4 (5×10^4–5×10^4)
v_s (km s^{-1})	32 (32–40)	18 (10–36)	36 (25–40)
b	7.0 (7.0–10.0)	5.5 (1.0–10.0)	8.5 (4.5–10.0)

trusted, as discussed in Sect. 2.1.1. If we are to reproduce the observations it is necessary to run J-type shock models with a magnetic precursor. We ran the same model as proposed by Giannini et al. (2004) with a preshock density of 10^4 cm^{-3}, shock velocity of 41 km s^{-1}, b equal to 1 and truncated the shock at 475 years. We confirm the predictions of Giannini et al. and conclude that a J-type shock with magnetic precursor reproduces observations much better. We have not calculated here a grid of J-type shocks with magnetic precursors and

Table 6.4: Best fit model results for knots A and B in BHR137. Confidence intervals are given in parentheses.

Shock Parameters	Knot A	Knot B
n_H (cm^{-3})	5×10^5 (10^5–5×10^5)	10^4 (10^4–10^4)
v_s (km s^{-1})	36 (36–49)	47 (47–47)
b	9.5 (9.5–10.0)	4.0 (4.0–4.0)

therefore we can not say whether there are models which reproduce observations even better. It is not possible to say whether such shocks would be better at reproducing the observations of the other knots.

For the other knots, it appears that knots 1 and 3 are similar in nature. This is not surprising as they are located on either side of the outflow source, and thus probably have a common point of origin. In both cases the magnetic field is very high, of the order of ~1.5–2.0 mGauss. We predict that the width of the H$_2$ emitting zone is ~1350 AU and 1700 in knot 1 and 3, respectively. The corresponding life times are ~250 years in both cases.

An interesting point is, that in both knots the maximum kinetic temperature is predicted to be ~800–850 K. This is lower than the threshold for efficient para- to ortho-H$_2$ conversion (see Sect. 2.2.2). But in both cases the initial ortho/para ratio is predicted to be 3, which is in agreement with both our observations and those of Giannini et al. (2004). This indicates that the preshock gas has probably been shocked before, which is expected from the maps of BHR71 found in e.g. Bourke (2001) and our Fig. 6.1. Here it is clear that HH321A is trailing behind HH321B. Thus HH321B has probably already shocked the ambient medium, and HH321A is propagating through the postshock gas of HH31B.

6.3.2   BHR137

In the case of BHR137 we detect [FeII] emission in both knots. This implies that at least part of the objects are subject to dissociative shocks (see Sect. 2.2.2). As in the case of BHR71 we can not at this stage say whether the shocks are pure J-type shocks or whether they are J-type shocks with magnetic precursors.

However the excitation temperature is quite low, in both knots it is below ~2000 K. This is not consistent with a pure J-type shock, where the excitation temperature is higher usually.

As before we do a χ^2 analysis on all lines, including the [FeII] lines. The best-fit models are listed in Table 6.4. All in all the results are not very satisfac-

tory as χ^2 is very large, and in the case of knot A, the value of b is at the edge of the grid. There is only one shock model that reproduces the observations of knot B at the 1σ-level. Furthermore, we did not expect the shocks to be purely C-type shocks with a high value of b. None of the shocks considered here are dissociative shocks. We tried redoing the χ^2 analysis without the [FeII] lines but results did not change.

We tried just looking at J-type shocks, but found that χ^2 increased by more than an order of magnitude. The conclusion is that we are probably seing a J-type shock with a magnetic precursor as in the case of BHR71, knot 4. The H_2 emission would primarily be generated in the magnetic precursor, whereas the [FeII] emission would be caused by the dissociative J-type shock.

To run a truncated C-type shock model, it is necessary to specify in the models when to truncate the C-type shock and let a J-type shock front develop. One method for estimating the truncation time is by calculating the dynamical age of the system. However in this case neither the shock velocity nor the distance to the outflow source are known. In fact the outflow source is not known, although it probably originates from either the BHR137 molecular core itself or the IRAS 17181–4405 source (see finding chart, Fig. 6.2). For the moment we do not pursue this any further.

6.4 Conclusion

We have here identified four knots of emission in the BHR71 outflow and two knots in the BHR137 outflow. This is the first time that pure H_2 emission has been detected from BHR137. For all knots we are able to fit a single excitation temperature to the observations. Excitation temperatures are in the range of ~1800–2500 K.

For knots 1–3 in BHR71 we are able to reproduce the observations with C-type shock models. We find that densities are of the order of 5×10^5 cm^{-3} and shock velocities are ~30–35 km s^{-1}. For knot 4 (HH320A) we confirm the results of Giannini et al. (2004) that the shock is a J-type shock with a magnetic precursor.

For knots A and B in the BHR137 outflow we are not able to reproduce observations satisfactory with neither pure C- nor pure J-type shock models. The shocks are probably truncated C-type shocks as in the case of knot 4 in BHR71. This is supported by the fact that we observe [FeII] emission which is typically observed in dissociative J-type shocks. However the H_2 emission appears to be generated in a soft C-type shock, which explains the low excitation temperatures. We conclude that the shock causing the emission in BHR137 is probably a J-type shock with a magnetic precursor.

Observations of N159-5, VLT/NACO

In this Chapter I will describe observations performed in October 2004 of the massive star forming region N159-5 in the Large Magellanic Cloud. Observations were made using the spectral capabilities of NACO on the ESO-VLT, UT4. I have not been involved in taking the data, nor the initial data reduction. My work was centered on reducing the K-band part of the spectra and extracting information on the H_2 emission lines found in the spectra and the analysis thereof. Furthermore I have been responsable for the proposed morphology of the object. This also makes up my contribution to Publication III, Testor et al. (2007).

First I will describe the observations and data reduction. Then I will describe how I have extracted the H_2 line brightness before interpreting the results. Finally I will compare the observations of this active massive star forming region with another massive star forming region, OMC1.

7.1   Observations and data reduction

Long-slit K- and H-band spectra of N159-5 were obtained on the night of October 10, 2004 using the ESO-VLT, UT4 equipped with the NACO adaptive optics system and infrared camera. Furthermore K_s band images of N159-5 were obtained on the nights of October 8 and December 4, 2004. For spectroscopy the S54 camera mode was used, whereas for imaging both the S54 and S27 camera modes were used. The resulting pixel scales are 52.74 mas/pixel and 26.37 mas/pixel respectively. This corresponds to 13 mpc and 6.6 mpc at the adopted distance of 51 kpc to N159-5 (Cole 1998).

The object itself was used as a reference object for locking the AO system. The magnitude is $K_s = 14.30$ mag (Meynadier et al. 2004). The atmospheric conditions were photometric and the seeing in the visible was at $\sim 0''\!.8$ for all observations. With the AO correction the resulting spatial resolution is of the order of $\sim 0''\!.11$–$0''\!.22$. In Fig. 7.1 we provide a finding chart of the region obtained from our K_s band imaging.
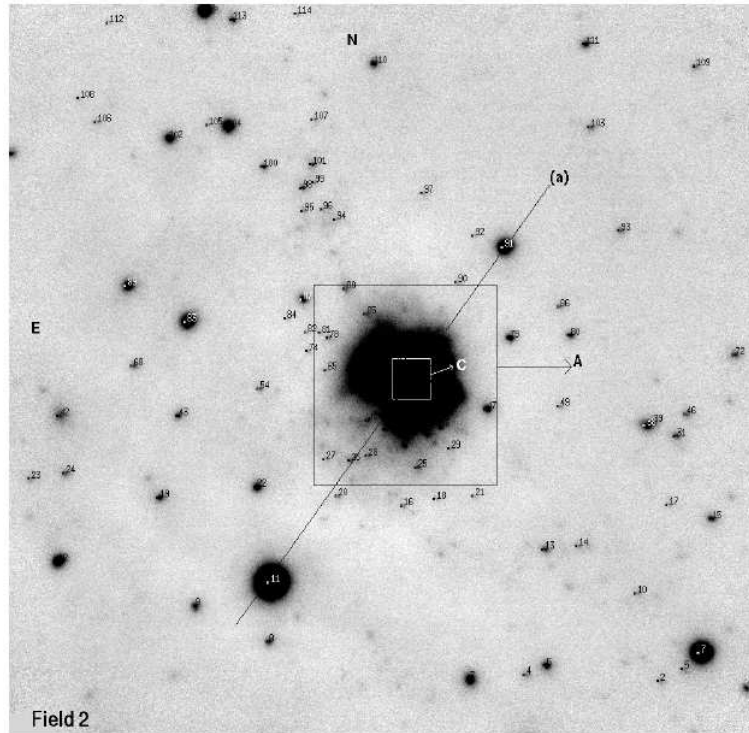
Figure 7.1: Finding chart for N159-5 showing K_s band emission obtained with the S27 camera. Stars detected are marked with numbers. The inset A ($6.''6 \times 6.''$) contains the HEB N159-5. The small inset C ($1.''34 \times 1.''34$) contains the central star #2-55. The location of the slit (a) used in the spectroscopic mode is indicated by a solid line. Total field size is $26.''9 \times 23.''8$ corresponding to 7 pc$\times$6 pc.

For spectroscopy the SHK mode was used. Thus the wavelength range covered is 1.3–2.6 μm. A slit width of 176 mas was chosen. The position angle of the slit is 130.3° and is displayed on Fig. 7.1. The spectral resolution is ~500. As before the pixel scale in the spatial direction is 52.74 mas/pixel whereas in the wavelength direction it is 1.94 nm/pixel. A total of twenty exposures were taken, each with an integration time of 200 seconds. The exposure time was chosen so as to take into account the sky background, in particular OH emission and thermal emission as discussed previously in Sect. 6.1. A star with similar airmass was observed in order to remove telluric absorption features. No absolute calibration has been performed.

Data reduction of the spectra were performed in the standard way, and consists of dark subtraction and flat-fielding followed by sky subtraction. We also smoothed the image in the spatial direction by applying a boxcar of width 11
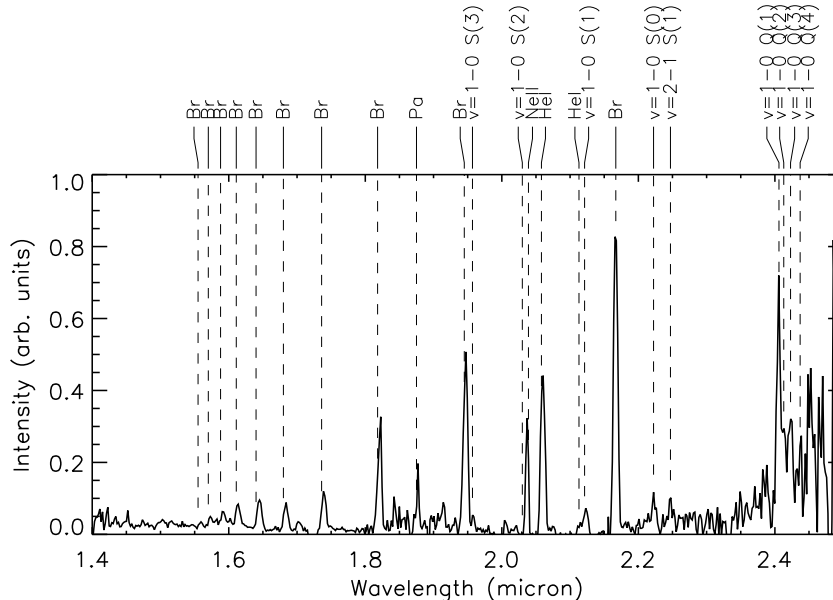
Figure 7.2: Example of H- and K-band spectrum of N159-5. Units of intensity are arbitrary. Identified lines are marked. Br indicate the Brackett series and Pa is Paschenα.

pixels. This degraded the spatial resolution to 0.''35. We show an example of such a spectrum in Fig. 7.2.

7.2   H$_2$ line results

The first thing to do is find the spatial distribution of v=1-0 S(1) emission as was done for BHR71 and BHR137. The distribution is shown in Fig. 7.3 with respect to star #2-55 located at 05^{h}40^{m}4^s.45; −69°44'37.''42, (J2000). Star #2-55 is thought to be one of the main exciting sources (see below, Sect. 7.3). Variations in H$_2$ emission is also present in Krabbe et al. (1991), who imaged the region in the H$_2$ v=1-0 S(1) line at a subarcsecond spatial resolution.

We identify four regions of H$_2$ emission: North-west of star #2-11 (05^{h}40^{m}5^s.38; −69°44'43.''82; J2000), South-east and North-west of star #2-55 and South-east of star #2-91 (05^{h}40^{m}3^s.80; −69°44'33.''00; J2000). We name these regions 11NW, 55SE, 55NW and 91SE respectively. As before we integrate over all emission in each zone of emission to improve the signal-to-noise ratio. In Fig. 7.2 we show the integrated spectrum of zone 55NW as an illustra-
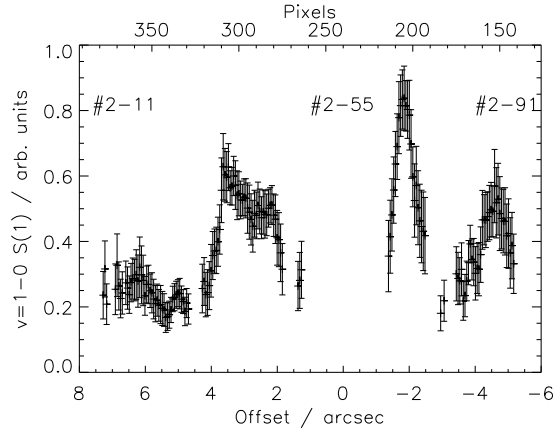
Figure 7.3: Spatial distribution of H_2 v=1-0 S(1) emission. Coordinates are given with respect to star #2-55. Error bars are 1σ. Data points with more than 50% relative error have been rejected.

tive example. This spectrum has been integrated over 30 pixels. The widths of the four zones are 0.35 pc, 0.60 pc, 0.20 pc and 0.40 pc respectively.

We note that the spectrum shown in Fig. 7.2 is dominated by atomic and ionic line emission and very few H_2 lines are detected. This is typical for an HII region. The H_2 lines that we do detect are the v=1-0 S(1), v=1-0 S(0) and v=2-1 S(1) lines. The v=1-0 S(2) and v=1-0 S(3) lines are also detected, but they are so close to strong atomic lines (Brδ and HeI, respectively) that we cannot determine their intensity. Furthermore the H_2 Q-branch is discovered, but the individual lines are very blended.

The v=1-0 S(1) line is also blended with a HeI line. In order to obtain line intensities we have fitted gaussian functions to each of the two lines and integrated the result. We have then subtracted the gaussian fit from each line to ensure that we have reproduced the line intensity.

None of the lines are atmospherically absorbed. We have adopted a V_{lsr} of 235 km s^{-1} (Johansson et al. 1998) and this does not Doppler-shift any of the lines into significant absorption features (Livingston & Wallace 1991).

In Table 7.1 we list the intensities of the three H_2 lines. Only around star #2-55 do we detect all three lines although the v=2-1 S(1) line profile is ~50% broader in 55SE than other line profiles. Typically the FWHM of the line profiles in this region is ~3 pixels whereas the FWHM of the v=2-1 S(1) line is ~4 pixels. Therefore there may be some contribution from another line or a bad pixel which we have not successfully removed. Inspecting the spectrum by hand did not reveal anything unusual.

Table 7.1: Integrated emission from the four zones 11NW, 55SE, 55NW and 91SE identified in Fig. 7.3. Errors are 1σ. Brightness is given with respect to the v=1-0 S(1) line. A long line (—) indicates no detection.

Line	λ (μm)	11NW	55SE	55NW	91SE
v=1-0 S(1)	2.121	1.00	1.00	1.00	1.00
v=1-0 S(0)	2.223	0.87±0.35	0.86±0.26	0.82±0.32	—
v=2-1 S(1)	2.247	—	0.98±0.29[a]	0.55±0.47	0.64±0.27

[a] This line profile is significantly broader than other line profiles, and this value should only be taken as an upper limit.

7.3 Exciting source

This section is a shortened version of Sect. 3.3 in Testor et al. (2007) where the nature of the ionizing source in N159-5 is discussed. I have not been involved in this work at all, but I refer to it for completeness and because it is important for our analysis of the H$_2$ emission in the following section.

From the spectrum of #2-55 a Brγ/HeI(2.112 μm) line ratio of ~0.04 is found. According to Hanson et al. (2002) this indicates that the HII region could be created by a single O7V star or hotter. The HeII(2.185 μm) absorption line is not detected. Neither is the NIII(2.115 μm) line. This implies that the spectral type of the star is later than O7/O8 (Bik et al. 2005). Star #2-55 is therefore classified as type O8V.

The radio spectral type of the ionizing source is classified as O4 or O5 (Martín-Hernández et al. 2005; Indebetouw et al. 2004, respectively). This is hotter than the spectral type of #2-55 and the conclusion is that more than one star is responsible for the ionization. When integrating emission over the stars #2-66, 71 and 75 a Brγ/HeI(2.112 μm) line ratio of ~0.035 is measured. This strengthens the conclusion that there are other massive stars which contribute to the ionization (Hanson et al. 2002).

7.4 Interpretation and discussion

In the following we will briefly go through what can be learned from the observed line emissions in terms of shock- and PDR-excitation. For PDRs we will be using the "Meudon PDR code" (Le Petit et al. 2006) and for shock models we will be using the one described in (Flower & Pineau des Forêts 2003) and Chapter 2.

In the following we briefly summarize what can be learnt from the observed line ratios, independent of models:

- The v=1-0 S(0) emission is ~0.85 in the three regions where it is detected, which is comparable to the v=1-0 S(1) emission. This indicates that the para-H$_2$ line v=1-0 S(0) is stronger than what would be expected based on pure spin statistics where a value closer to ~0.2 would be expected (see Sect. 4.1). This under-population of the ortho-state v=1, J=3 indicates that the ortho/para ratio is probably lower than the high temperature equilibrium value of 3.

- The v=2-1 S(1) emission shows a value of ~0.6 typical of PDRs (Le Petit et al. 2006). The resulting excitation temperature is ~6700 K (see Eqn. 5.1.2). This value is difficult to model with shock models (see below) indicating that at least the three regions where v=2-1 S(1) emission is detected are PDRs.

The excitation mechanism is very likely a PDR and not shocks for the following reasons: The width of each region is very large, indicating that if the excitation mechanism was a shock then it would have to be a magnetic C-type shock rather than a non-magnetic J-type shock. However to create widths of the order of 0.5 pc it is necessary to have a high magnetic field or very low preshock density. In shock models the magnetic field is assumed to be frozen into the preshock gas at a flux density of $b \times [n_H(\mathrm{cm}^{-3})]^{1/2}$ μGauss. If a C-type shock were to be responsible for the observed width b would have to be greater than 10. This would however produce low values of the relative brightness of v=2-1 S(1) (<0.2). The relative v=1-0 S(0) brightness predicted by the models would be lower than 0.3. None of these predictions are in agreement with observations.

The relative brightness of v=2-1 S(1) has classically been used to discriminate between shocks and PDRs. Here we find that the relative brightness is ~0.6 which is easily reproduced by PDR models (Le Petit et al. 2006). The main obstacle of fitting the observed brightness with PDR models is the high relative brightness of the v=1-0 S(0) para line. This could be explained by a value of the ortho/para ratio being lower than the high temperature equilibrium value of 3. Low ortho/para ratios are not uncommon in PDRs and have been observed previously (e.g. Chrysostomou et al. 1993; Habart et al. 2003).

Using the relative brightness of v=2-1 S(1) it may be possible to estimate the density using the "Meudon PDR Model" (Le Petit et al. 2006). The best fit models have a density of $\lesssim 10^5$ cm^{-3} independent of the incident radiation field. Without further observational constraints it is not possible to limit the density further. This may be compared with the density found in for example N88, another HEB in the SMC. Here it was found from observations of several H$_2$

lines that the density is 10^3 cm^{-3} (Testor et al. 2005). We cannot rule out that the density in N159-5 is different from 10^3 cm^{-3}.

With the PDR model we may predict that the v=1-0 S(1) absolute brightness is less than ~2.5×10^{-8} W m^{-2} sr^{-1}, again independent of incident radiation field. In N88 the absolute v=1-0 S(1) brightness is 6.4×10^{-8} W m^{-2} sr^{-1} (Testor et al. 2005). If this is compared to the PDR models the density should be of the order of a few times 10^5 cm^{-3}, although the authors argue that it must be several orders of magnitude lower. However their argument is based primarily on line ratios and they do not use the absolute brightness very much.

If the H$_2$ data in Testor et al. (2005) are re-analysed in the frame of the "Meudon PDR code", I find that the density is indeed a few times 10^5 cm^{-3}. This result is consistent with the absolute v=1-0 S(1) brightness and the line ratio of v=1-0 S(1) and the following lines: v=1-0 S(3), v=1-0 S(2), v=2-1 S(3), v=2-1 S(2) and v=2-1 S(1). As for object N159-5 it is not possible to reproduce the v=1-0 S(0) / v=1-0 S(1) line ratio. The conclusion is therefore, that the density in N88 has probably been underestimated, at least if one is to trust the results from the "Meudon PDR model".

7.5 Morphological model and comparison with galactic objects

N159-5 have been observed by the Hubble Space Telescope in the Hα line by Heydari-Malayeri et al. (1999). In Fig. 7.4 we show the Hα emission along with K$_s$ emission in a colour-composite image. On this image we also show 3 cm radio contours from Indebetouw et al. (2004). Hα emission is seen in two wings. For this reason the nebula is sometimes referred to as the "Papillon" (butterfly) nebula. The overall diameter is of the order of ~5″ corresponding to ~1.3 pc.

In the K_s band the eastern wing is all but invisible and only the western wing is prominent. The central star #2-55 is very faint in Hα but in K_s it is one of the brightest stars. In the western wing we discover a very compact embedded stellar cluster, which is illustrated in Fig. 7.1 by Box A.

The 3 cm continuum emmision (Indebetouw et al. 2004) is located on top of the western emission wing. We find that the peak emission of Brγ and HeI(2.113 μm) lines are superposed on the position of the peak of the radio emission, characteristic of HII regions.

The above mentioned properties are very similar to the galactic object SH2 269 (Sharpless 1959) located at a distance of ~2 kpc (Heydari-Malayeri et al. 1982). The size of SH2 269 and N159-5 are similar (~1.2 pc) and SH2 269
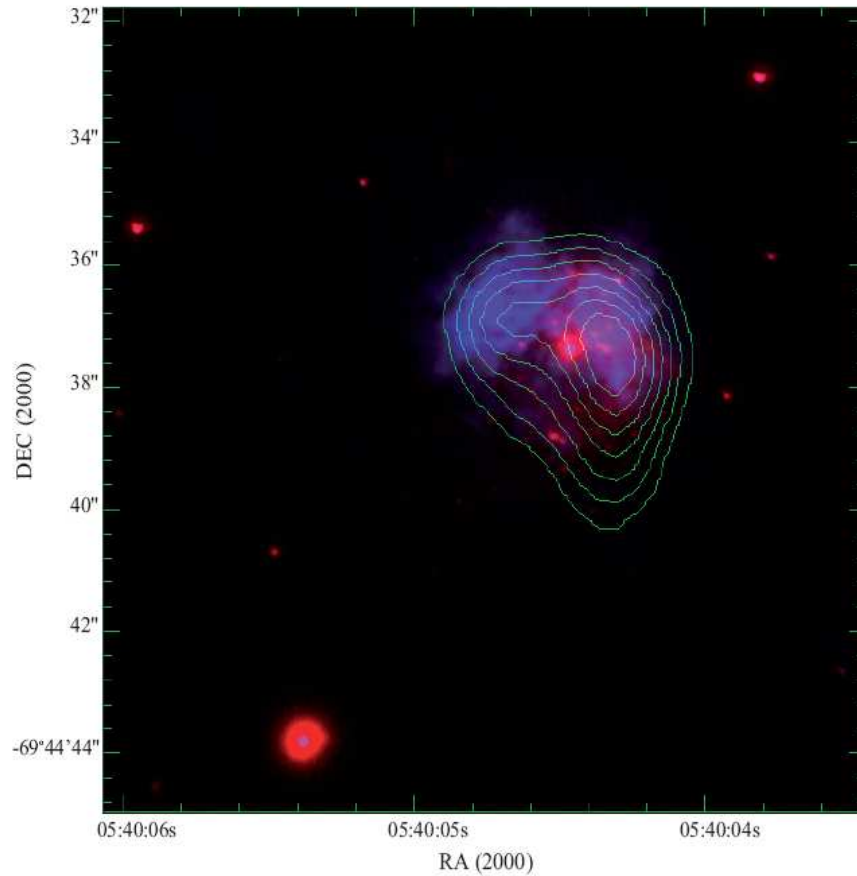
Figure 7.4: Colour-composite image of N159-5. Hα is shown in red and K_s emission is shown in blue. Overlaid are 3 cm radio contours (Indebetouw et al. 2004). The size of the field is $13''.2 \times 13''.2$ or ~3.3×3.3 pc.

also consists of two lobes of Hα emission (Heydari-Malayeri et al. 1982). It also contains an embedded cluster observed at NIR wavelengths (Eiroa & Casali 1995). The stellar density is higher in the western wing (Eiroa & Casali 1995; Jiang et al. 2003). They are also very similar to OMC1, which we will discuss in more detail in the following.

We propose the following model of the N159-5 region. Overall the structure is comparable to the Orion region (O'Dell 2001), where young OB stars (in OMC1 the Trapezium cluster) form at the edge of the molecular cloud. The massive stars irradiate the parent molecular cloud creating the 'veil' or 'lid' of ionized material in front of the molecular cloud. The surface of the underlying molecular cloud will be lit up by the massive stars and a blister of ionized gas

will be created.

The stars that are currently forming inside the molecular cloud are all deeply embedded and only observable in the mid infrared or at longer wavelengths (Beuther et al. 2004). In the Orion nebula this is observed in a face-on geometry.

We therefore propose that the N159-5 region is similar to the Orion Nebula with the main difference being, that we are seing the nebula in an edge-on geometry, compared to Orion. In this scenario the eastern lobe of Hα emission (no infrared counterpart) would correspond to the Orion lid, and the western lobe is the molecular cloud itself. We also note that for such a distant object it is not possible to resolve the knots of shocked gas that we are observing in OMC1.

This also matches our spectroscopic data in which the slit pass through the central exciting source of the nebula at a position angle of 130.3°. The brightest part of the PDR is seen just NW of star #2-55, while the PDR SE of star #2-55 is more elongated and not as bright. This would be true if the PDR to the SE is less dense than that to the NW given that they are both exposed to the same radiation field.

7.6 Conclusion

We have isolated H_2 emission from this object over almost the entire length of the slit. The emission may readily be reproduced by PDR models whereas shock models prove inadequate. We find that to reproduce the observed v=2-1 S(1) / v=1-0 S(1) line emission the density should be less than 10^5 cm^{-3} independent of the incident radiation field. It is necessary to have further observational constraints in order to determine the density more accurately.

We also propose that the nature of this object is very similar to OMC1, only it is observed in a different geometry. Here we would be observing it edge-on compared to the face-on geometry of OMC1. Since this object is ~100 times more distant than OMC1 we do not resolve any individual shocks but only see the large scale structure.

Clearly more work needs to be done on this object. This includes obtaining spectra that are absolutely calibrated and preferrably at longer exposure times to obtain more H_2 lines.

Conclusions and outlook

The work performed during this thesis has served two purposes: First of all it has served to quantify physical conditions in active star forming region, second of all it has served to better understand the excitation mechanisms in star forming regions, in particular interstellar shock waves. In this Chapter I will briefly recapitulate the results and conclusions of the thesis, and I will give an outline of where to go from here.

8.1   Conclusions

8.1.1   Shock models

To analyse observations and gain a better understanding of shock physics, a large grid of shock models was run. Through analysis of this grid it is possible to make a number of predictions such as the width of shocks, the ortho/para ratio in shocks as a function of shock temperature, [FeII] emission is a clear indicator of a dissociative shock, etc. Model results and predictions are being prepared for publication now and will be a valuable tool when interpreting observations.

We have implemented methods for validating model results, both by testing if results are un-physical or if results show large discrepancies with respect to neighbouring results. It is quite possible that we have not detected all possible criteria for filtering model results yet.

Model result extraction and result verification are now automated processes. Running a large grid is therefore only a question of computer time. In the future it will still be necessary to run grids, both as the model is updated, but also to improve the resolution locally in the existing grid.

The model results should not be seen as the absolute and final truth. There are several shortcomings to the model, some of which are relatively straight-forward to solve, while others are not ready to be implemented yet. Of the latter, the 1D geometry is one the most important shortcomings.

8.1.2   OMC1

Most of the work I have done during my three years has been centered on OMC1. Therefore I will here provide a more detailed summary, focusing first on the differences between the two sets of observations from the CFHT and VLT. I will then go through some of the more important results from the two datasets before commenting on the development that has taken place in this thesis from 1D shock models to 2D and 3D models.

Two datasets — two results

There are differences between the absolute brightness of the v=1-0 S(1) line in the two datasets, but as it turned out, these differences may be attributed to differences in spatial resolution. The spatial resolution in the CFHT data is $\sim0\rlap{.}''40$ while it is $\sim0\rlap{.}''15$ in the VLT data.

However, the two datasets are not in agreement with eachother with respect to the ratio between the two lines v=1-0 S(1) and v=1-0 S(0), R_{10}. In particular the ratio in region West is two times higher in the VLT data than in the CFHT data, although when plotting the absolute v=1-0 S(1) brightness as a function of R_{10} the appearance is qualitatively similar in the two sets of observations. In region North the appearance is not similar and neither is the range of ratios covered. Part of this is due to the fact that the location of region North in the CFHT data is not the same as in the VLT data, but this cannot be the entire explanation.

At a first glance it would seem evident that the VLT data are more accurate than the CFHT data due to a higher spatial resolution and a higher sensitivity. But as was shown, there are also some problems with the line ratio R_{10} in the VLT data. At the moment I have not found the reason for these differences, and I hesitate in concluding that one dataset is more correct than the other.

The fact remains that the VLT data have a better spatial resolution and higher sensitivity. Therefore it is likely that there is a problem with the CFHT data, but without a more detailed analysis it is not possible to quantify at the moment.

Analysis of large scales using the CFHT data

For OMC1 we performed an analysis of the large scale structures. This was done based on the CFHT data of the v=1-0 S(1) and v=1-0 S(0) H_2 rovibrational transitions. We identified four classes of emission associated with three different spatial regions of OMC1. For each of these classes we identified a range of possible shock velocities, preshock densities and initial ortho/para ratios for two different values of the magnetic scaling factor, b. Shock velocities are in the range of $10-40\,\mathrm{km\,s^{-1}}$. We showed that the preshock density is high, on average

between 10^5–10^7 cm^{-3}. We showed that at if a scale size of ~1000 AU was adopted as the typical size of objects, then their mass is below the Jeans mass. This would imply that the outflow in the BN-KL nebula is not generating a new wave of star formation through compression of the ambient medium.

Analysis of individual objects observed by the VLT

The VLT observations of the v=1-0 S(0), v=1-0 S(1) and v=2-1 S(1) H$_2$ transitions have a spatial resolution 0″.15, that is a factor of 3−4 better than the CFHT data. With these data it is possible to resolve the shock width of individual bow shocks south-west of BN providing a very strong argument that shocks here are C-type shocks rather than J-type shocks.

We have developped a new method for reproducing observations of individual bow shocks, by cutting the bow shock into a number of quasi-plane parallel shocks, something which has not been done before. This method is not only applicable to bow shocks but to almost any type of shock, as long as the shock is moving relatively close to the plane of the sky and appears filamentary. By way of example, we have chosen one object in OMC1 where we apply this method. The object was chosen because of a well-defined bow-shaped morphology and because it is relatively isolated. Unfortunately the object is not moving in the plane of the sky, but at an angle of ~40°. It was not possible to find an object that showed both a well-defined morphology and moving in the plane of the sky.

For the analysis of this object we use the shock width as an observational constraints on models, something which has not been done before. The models reproducing the observations predict the shock velocity. This is very close to the measured object velocity, which could indicate that the shocks are caused by bullets moving into the ambient medium. Further evidence is needed before making this conclusion. One way of determining if this is true could be to plot the dynamical age of objects in this region as a function of distance to the launching object. If the age is constant, then it would imply that the objects are launched at the same time and are most likely bullets. To prove this hypothesis it is necessary to analyse the radial velocity data from Nissen et al. (2007) and the proper motion data from Cunningham (2006), which have not been made publically available yet, and which he has not provided us with.

We have developped a 3D bow shock model. We have used the best-fit parameters of our 2D modelling as input parameters for this 3D model, but unfortunately the 3D model, with this particular set of input parameters, do not reproduce observations well. More iterations are clearly needed.

Model development

As this work has developped from first analysing large scale properties of OMC1 to analysing individual objects observed at high spatial resolution, so the methods of analysis have also developped. Beginning with the standard 1D model the methods for reproducing observations have become more and more sophisticated. The first is the development of the 2D model where we cut a bow shock in segments and assume that each segment may be reproduced by a 1D model. We have validated *a posteori* that this method may be used if the shock is moving relatively close to the plane of the sky, i.e. within ~50°.

We have developed a 3D model and we are currently trying to reproduce observations of our example bow shock with this model. So far only the first iteration has been made, and more work is surely needed.

In general 1D models are best at reproducing large scale observations where the geometry is not well-defined or if a shock is moving along the line of sight. 2D models excel in reproducing shocks where the structure is more filamentary and where the shock is moving close to the plane of the sky. If the object is a bow shock then the 3D model is better suited. This is true even if the bow shock is moving close to the plane of the sky since line-of-sight effects are implicitly taken into account. As shown here, for a bow shock moving close to the plane of the sky, it can be a good idea to start with a 2D model and let the model results provide an initial guess for the bow parameters. Later it is then necessary to refine this guess.

8.1.3   BHR71 and BHR137

The outflows from the two Bok globules BHR71 and BHR137 proved more difficult to model than the objects in OMC1. In the case of BHR71 we were able to reproduce observations and predict preshock densities of 5×10^4 cm^{-3} and shock velocities of the order of 30-40 km s^{-1}. The magnetic field is very strong with a value of 1.5-2.0 mGauss. For BHR137 it was not possible to reproduce observations with steady state shock models. H_2 emission tend to favour a C-type component of the shock while [FeII] emission clearly favours a J-type component. This is consistent truncated C-type shock, which is not included in the grid of models.

8.1.4   N159-5

For the extra-galactic compact HII region and high excitation blob, N159-5 in LMC, we conclude that shocks are not the main excitation mechanism. Instead H_2 emission is generated by a powerful PDR generated by one or more O-stars.

We determine that the density is of the order of or less than 10^5 cm^{-3} almost independent of the incident radiation field. It is possible that some of the emission is generated by shocks, but at the distance of N159-5 it is not possible to resolve individual shocks. Finally we propose that the object is comparable to OMC1.

8.2   Outlook

In many ways this thesis has only begun to show the way for future work. With respect to OMC1 this includes 2D modelling in a systematic way of more objects, both bow shaped but also of more irregular morphology. With the high spatial resolution VLT data it should be possible to model individual shock waves at higher precision than before and in this way it will be possible to map, for example, the preshock density as obtained from this modelling.

Regarding 3D bow shock models it is necessary to further refine the modelling of bow shocks. One way of doing this is to let a computer algorithm optimize the results and do the refinement automatically. This work has not begun yet.

So far observations have been made of hot, rovibrationally excited H$_2$. To completement these observations it would be desirable to observe warm, rotationally excited H$_2$ by using the Spitzer Space Telescope. Other molecular shock tracers, such as SiO, would also complement these observations. Another approach would be to do integral field spectroscopy in the NIR of a number of bow shocks. This can be done using e.g. Sinfoni at the ESO-VLT. The advantage would be a relatively high spatial resolution and full spectral coverage in each spatial pixel.

To improve modelling of BHR71 and BHR137 it will be necessary to complement the grid of shock models with models of non-steady state shocks, or truncated C-type shocks. It is not feasible to run a grid of these shocks, as adding another free input parameter would dramatically increase computation time. However it should be possible to use the preshock condition estimates of steady state J- and C-type shock modelling to obtain a first guess, and then proceed with more iterations from there.

A

Legends for figures

For most of the Chapters I have tried to keep the legends of the figures consistent throughout, and here I provide a list of these legends.

Chapter 2

Preshock density:
10^4 cm^{-3}: Red
10^5 cm^{-3}: Blue
10^6 cm^{-3}: Green
10^7 cm^{-3}: Yellow

Chapter 5

v=1-0 S(1) emission: Black
v=1-0 S(0) emission: Red
v=2-1 S(1) emission: Blue

Chapter 6

BHR71:
Knot 1: Red
Knot 2: Yellow
Knot 3: Blue
Knot 4: Green

BHR137:
Knot A: Red
Knot B: Yellow

Model input and outputs

In the following we list some of the input and output from the model. We have chosen a C-type shock with velocity $10\,\mathrm{km\,s^{-1}}$, preshock density $10^4\,\mathrm{cm^{-3}}$, b=1.0 and initial ortho/para ratio of 3.0 as arepresentative shock.

- We show the input file used to generate this shock. Here a numner of physical parameters are defined as described in Chapter 2.

- In Table B.1 we list the species found in the model along with the initial abundances for the representative model.

- Then we list the 1040 chemical reactions used in the model.

- In Table B.2 we list the different fine-structure and meta-stable transitions that are recorded in the model. These include primarily [FeII] fine-structure lines.

- The recorded H_2 line brightness are listed in Table B.3 sorted by wavelength band. H_2 lines are recorded for each of the J-, H- and K-bands in the near-infrared part of the spectrum and the wavelength range observed by the Spitzer Space Telescope.

An example of the input file used to generate a C-type shock with shock velocity $10\,\mathrm{km\,s^{-1}}$, preshock density $10^4\,\mathrm{cm^{-3}}$, b=1.0 and initial ortho/para ratio of 3.0

```
!---- shock parameters -----------------------------------------------
C                        ! shock type : 'C' or 'J', Steady state : 'S'
3                        ! Nfluids : 1, 2 ou 3
1.0                      ! Bbeta -> Bfield = Bbeta * sqrt(nH)
10                       ! Vs -> shock speed (km/s)
1.0e3                    ! Vn - Vi initial (cm s-1)
3.0                      ! op_H2 -> initial H2 ortho/para ratio (999.9 -> ETL)
10.0                     ! T(n,i,e) -> initial gas temperature (K)
1.0D4                    ! nH_init -> initial value for n(H)+2.0 n(H2)+n(H+)(cm-3)
15                       ! Tgrains -> initial grain temperature (K)
0                        ! Cool_KN -> 1: Kaufman & Neufeld cooling
!---- environment ----------------------------------------
5.0D-17                  ! Zeta -> cosmic ray ionization rate (s-1)
0.D0                     ! RAD  -> flux radiation (multiplicative factor)
0.D0                     ! Av   -> initial extinction (magnitudes)
!---- numerical parameters -------------------------------
10000                    ! Nstep_max   -> max number of integration steps
5                        ! Nstep_w -> number of steps between 2 outputs
100                      ! NH2_lev -> Number of H2 levels included
150                      ! NH2_lines_out -> Max number of H2 lines in output file
BOTH                     ! H_H2_flag -> H-H2 collisions : DRF, MM or BOTH
1                        ! iforH2 -> Formation on grain model (1, 2, 3, 4)
2                        ! ikinH2 -> Kinetic energy of H2 newly formed (1, 2)
1.0D11                   ! XLL -> caracteristic viscous length (cm)
1.00D-7                  ! Eps_V -> precision of computation
1.00D8                   ! timeJ -> shock age (years)
1.00D8                   ! duration_max -> max. shock duration (years)
1                        ! Force_I_C -> 1: Force Ion Conservation
!---- output specifications ------------------------------
FD                       ! species: 'AD' (cm-3), 'CD' (cm-2) or 'FD' (n(x)/nH)
AD                       ! H2 levels: 'AD' (cm-3), 'CD' (cm-2) or 'ln(N/g)'
integrated               ! H2 lines: 'local' (erg/s/cm3) or 'integrated' (erg/s/cm2/sr)
!---------------------------------------------------------

  INTEGER             :: iforH2 = 1  ! Flag : H2 formation on grains
                                     !   0: 1/3 of 4.4781 eV in internal energy
                                     !      (=> 17249 K) (Allen, 1999)
                                     !   1: Proportional to Boltzman Distrib
                                     !      at 17249 K
                                     !   2: Dissociation limit: v = 14, J = 0,1
                                     !      (4.4781 eV)
                                     !   3: v = 6, J = 0,1
                                     !   4: fraction = relative populations at t,
                                     !      initialised as H2_lev%density
                                     !      and changed during integration
  INTEGER             :: ikinH2 = 2  ! Flag : H2 formation energy released
                                     !            kinetic energy
                                     !   1: 0.5 * (4.4781 - internal)
                                     !   2: Inf(1.4927 eV, 4.4781 - internal)
```

Table B.1: Initial species abundances in a C-type shock model with $v_s=10\,km\,s^{-1}$, $n_H=10^4\,cm^{-3}$, $b=1.0$ and initial ortho/para ratio equal to 3.0. Numbers in parentheses are powers of 10. One asterisk (*) indicates that the species is found in the grain mantle, two asterisks (**) that it is found in the grain core.

	Species	Abundance		Species	Abundance		Species	Abundance
1	H	1.45(+00)	47	Mg	1.00(-12)	93	N^+	9.84(-07)
2	H_2	5.00(+03)	48	Fe	1.46(-03)	94	NH^+	1.79(-10)
3	He	1.00(+03)	49	$C_{54}H_{18}$	9.71(-03)	95	NH_2^+	6.69(-09)
4	C	6.94(-03)	50	C_6	1.00(-12)	96	NH_3^+	1.48(-06)
5	CH	1.04(-04)	51	C_{60}	6.14(-07)	97	NH_4^+	8.84(-06)
6	CH_2	4.00(-04)	52	H_2O^*	1.03(+00)	98	CN^+	1.62(-11)
7	CH_3	3.73(-06)	53	CO^*	8.27(-02)	99	C_2N^+	6.51(-07)
8	CH_4	1.48(-04)	54	CO_2^*	1.34(-01)	100	HCN^+	3.53(-10)
9	O	2.24(-01)	55	CH_4^*	1.55(-02)	101	H_2CN^+	1.38(-05)
10	O_2	9.78(-02)	56	NH_3^*	1.55(-01)	102	H_2NC^+	1.49(-07)
11	OH	1.23(-03)	57	CH_3OH^*	1.86(-01)	103	N_2^+	1.72(-10)
12	H_2O	5.58(-03)	58	H_2CO^*	6.20(-02)	104	N_2H^+	1.40(-05)
13	CO	8.12(-01)	59	HCO_2H^*	7.24(-02)	105	NO^+	8.01(-07)
14	CO_2	2.97(-04)	60	OCS^*	2.07(-03)	106	HNO^+	8.09(-08)
15	C_2	3.88(-05)	61	H_2S^*	3.72(-03)	107	S^+	3.01(-04)
16	C_2H	1.28(-05)	62	O^{**}	1.40(+00)	108	SH^+	5.14(-05)
17	C_2H_2	1.02(-06)	63	Si^{**}	3.37(-01)	109	H_2S^+	1.56(-07)
18	C_3	7.25(-10)	64	Mg^{**}	3.70(-01)	110	H_3S^+	4.20(-07)
19	C_3H	5.40(-09)	65	Fe^{**}	3.23(-01)	111	CS^+	2.42(-10)
20	C_3H_2	4.44(-08)	66	C^{**}	1.63(+00)	112	HCS^+	1.03(-06)
21	CH_3OH	1.00(-12)	67	H^+	4.78(-05)	113	SO^+	1.38(-05)
22	H_2CO	1.00(-12)	68	H_2^+	2.29(-08)	114	HSO^+	1.09(-07)
23	HCO_2H	1.00(-12)	69	H_3^+	8.51(-05)	115	HSO_2^+	5.84(-08)
24	N	1.06(-01)	70	He^+	8.79(-06)	116	$HOCS^+$	6.10(-10)
25	NH	1.11(-03)	71	C^+	2.23(-05)	117	Si^+	6.74(-15)
26	NH_2	1.73(-02)	72	CH^+	3.95(-10)	118	SiH^+	3.13(-17)
27	NH_3	5.31(-03)	73	CH_2^+	7.09(-10)	119	SiH_2^+	1.02(-17)
28	CN	1.63(-03)	74	CH_3^+	2.78(-06)	120	SiH_3^+	4.33(-20)
29	HCN	1.98(-03)	75	CH_4^+	5.68(-11)	121	SiH_4^+	1.00(-20)
30	HNC	2.65(-03)	76	CH_5^+	5.32(-08)	122	SiH_5^+	1.00(-20)
31	N_2	2.51(-01)	77	O^+	8.37(-10)	123	SiO^+	1.45(-18)
32	NO	6.52(-04)	78	O_2^+	8.82(-06)	124	$SiOH^+$	1.28(-14)
33	S	1.45(-01)	79	OH^+	3.48(-09)	125	Fe^+	3.57(-06)
34	SH	2.02(-04)	80	H_2O^+	4.80(-09)	126	$C_{54}H_{18}^+$	5.41(-06)
35	H_2S	1.51(-04)	81	H_3O^+	1.02(-05)	127	C_{60}^+	4.12(-08)
36	CS	8.60(-04)	82	CO^+	2.14(-10)	128	C_{54}^+	1.00(-12)
37	SO	1.42(-04)	83	HCO^+	1.49(-04)	129	$C_{54}H_{18}^-$	2.90(-04)
38	SO_2	1.87(-04)	84	HCO_2^+	1.46(-07)	130	C_{60}^-	5.50(-08)
39	OCS	1.80(-07)	85	C_2^+	1.09(-12)	131	C_{54}^-	1.00(-12)
40	Si	1.94(-13)	86	C_2H^+	1.56(-12)	132	e^-	
41	SiH	5.61(-17)	87	$C_2H_2^+$	3.21(-08)	133	Grain	
42	SiH_2	3.45(-19)	88	$C_2H_3^+$	7.25(-09)	134	Photon	
43	SiH_3	1.00(-20)	89	C_3^+	1.91(-13)	135	CRP	
44	SiH_4	1.00(-20)	90	C_3H^+	1.52(-11)	136	Sec. Photon	
45	SiO	1.44(-11)	91	$C_3H_2^+$	1.21(-11)			
46	SiO_2	4.28(-13)	92	$C_3H_3^+$	6.61(-10)			

The chemical reactions taken into account in the model. R is for reactants and P is for products. In general the reaction rate is calculated as `gamma*EXP(-beta/T)*(T/300)**alpha`

```
!      R1      R2      P1      P2      P3      P4      gamma    alpha    beta
! ----------------------------------------------------------------------------
       H      +H      =H2                                   8.14D-17  0.5
IONIZ  H      +ELECTR =H+      ELECTR  ELECTR                9.20D-10  0.5    157890.0
IONIZ  H2     +ELECTR =H2+     ELECTR  ELECTR                1.40D-09  0.5    179160.0
IONIZ  H      +H+     =H+      H+      ELECTR                1.30D-13  0.5    157890.0
IONIZ  H      +H3+    =H3+     H+      ELECTR                1.30D-13  0.5    157890.0
IONIZ  H      +He+    =He+     H+      ELECTR                1.30D-13  0.5    157890.0
IONIZ  H      +H3O+   =H3O+    H+      ELECTR                1.30D-13  0.5    157890.0
IONIZ  H      +H3S+   =H3S+    H+      ELECTR                1.30D-13  0.5    157890.0
IONIZ  H      +HCO+   =HCO+    H+      ELECTR                1.30D-13  0.5    157890.0
IONIZ  H      +Fe+    =Fe+     H+      ELECTR                1.30D-13  0.5    157890.0
IONIZ  H      +NH3+   =NH3+    H+      ELECTR                1.30D-13  0.5    157890.0
IONIZ  H      +NH4+   =NH4+    H+      ELECTR                1.30D-13  0.5    157890.0
IONIZ  H      +S+     =S+      H+      ELECTR                1.30D-13  0.5    157890.0
IONIZ  H      +SiOH+  =SiOH+   H+      ELECTR                1.30D-13  0.5    157890.0
IONIZ  H      +O2+    =O2+     H+      ELECTR                1.30D-13  0.5    157890.0
IONIZ  H2     +H+     =H+      H2+     ELECTR                1.10D-13  0.5    179160.0
IONIZ  H2     +H3+    =H3+     H2+     ELECTR                1.10D-13  0.5    179160.0
IONIZ  H2     +He+    =He+     H2+     ELECTR                1.10D-13  0.5    179160.0
IONIZ  H2     +H3O+   =H3O+    H2+     ELECTR                1.10D-13  0.5    179160.0
IONIZ  H2     +H3S+   =H3S+    H2+     ELECTR                1.10D-13  0.5    179160.0
IONIZ  H2     +HCO+   =HCO+    H2+     ELECTR                1.10D-13  0.5    179160.0
IONIZ  H2     +Fe+    =Fe+     H2+     ELECTR                1.10D-13  0.5    179160.0
IONIZ  H2     +NH3+   =NH3+    H2+     ELECTR                1.10D-13  0.5    179160.0
IONIZ  H2     +NH4+   =NH4+    H2+     ELECTR                1.10D-13  0.5    179160.0
IONIZ  H2     +S+     =S+      H2+     ELECTR                1.10D-13  0.5    179160.0
IONIZ  H2     +SiOH+  =SiOH+   H2+     ELECTR                1.10D-13  0.5    179160.0
IONIZ  H2     +O2+    =O2+     H2+     ELECTR                1.10D-13  0.5    179160.0
IONIZ  He     +H+     =H+      He+     ELECTR                1.10D-13  0.5    285328.0
IONIZ  He     +H3+    =H3+     He+     ELECTR                1.10D-13  0.5    285328.0
IONIZ  He     +He+    =He+     He+     ELECTR                1.10D-13  0.5    285328.0
IONIZ  He     +H3O+   =H3O+    He+     ELECTR                1.10D-13  0.5    285328.0
IONIZ  He     +H3S+   =H3S+    He+     ELECTR                1.10D-13  0.5    285328.0
IONIZ  He     +HCO+   =HCO+    He+     ELECTR                1.10D-13  0.5    285328.0
IONIZ  He     +Fe+    =Fe+     He+     ELECTR                1.10D-13  0.5    285328.0
IONIZ  He     +NH3+   =NH3+    He+     ELECTR                1.10D-13  0.5    285328.0
IONIZ  He     +NH4+   =NH4+    He+     ELECTR                1.10D-13  0.5    285328.0
IONIZ  He     +S+     =S+      He+     ELECTR                1.10D-13  0.5    285328.0
IONIZ  He     +SiOH+  =SiOH+   He+     ELECTR                1.10D-13  0.5    285328.0
IONIZ  He     +O2+    =O2+     He+     ELECTR                1.10D-13  0.5    285328.0
DISSO  H2     +ELECTR =ELECTR  H       H                     2.00D-09  0.5    116300.0
DISSO  H2     +H      =H       H       H                     1.00D-10  0.0     52000.0
DISSO  H2     +He     =He      H       H                     1.00D-11  0.0     52000.0
DISSO  H2     +H2     =H2      H       H                     1.25D-11  0.0     52000.0
DISSO  H2     +H+     =H+      H       H                     3.00D-11  0.5     52000.0
DISSO  H2     +H3+    =H3+     H       H                     3.00D-11  0.5     52000.0
DISSO  H2     +He+    =He+     H       H                     3.00D-11  0.5     52000.0
DISSO  H2     +H3O+   =H3O+    H       H                     3.00D-11  0.5     52000.0
DISSO  H2     +H3S+   =H3S+    H       H                     3.00D-11  0.5     52000.0
DISSO  H2     +HCO+   =HCO+    H       H                     3.00D-11  0.5     52000.0
DISSO  H2     +Fe+    =Fe+     H       H                     3.00D-11  0.5     52000.0
DISSO  H2     +NH3+   =NH3+    H       H                     3.00D-11  0.5     52000.0
DISSO  H2     +NH4+   =NH4+    H       H                     3.00D-11  0.5     52000.0
DISSO  H2     +S+     =S+      H       H                     3.00D-11  0.5     52000.0
DISSO  H2     +SiOH+  =SiOH+   H       H                     3.00D-11  0.5     52000.0
DISSO  H2     +O2+    =O2+     H       H                     3.00D-11  0.5     52000.0
       C54H18 +ELECTR =C54H18- PHOTON                        1.00D-07  0.00        0.0
```

```
C54H18++ELECTR =C54H18   PHOTON                    3.30D-06  -.50      0.0
C54H18++C54H18-=C54H18   C54H18                     3.00D-09  -.50      0.0
C54H18-+H+     =C54H18   H                          7.50D-08  -.50      0.0
C54H18-+H3+    =C54H18   H2       H                 2.20D-08  -.50      0.0
C54H18-+H3+    =C54H18   H        H        H        2.20D-08  -.50      0.0
C54H18-+He+    =C54H18   He                         3.80D-08  -.50      0.0
C54H18-+C+     =C54H18   C                          2.20D-08  -.50      0.0
C54H18-+H3O+   =C54H18   H2O      H                 1.70D-08  -.50      0.0
C54H18-+H3S+   =C54H18   H2S      H                 1.30D-08  -.50      0.0
C54H18-+NH4+   =C54H18   NH3      H                 1.80D-08  -.50      0.0
C54H18-+HCO+   =C54H18   CO       H                 1.40D-08  -.50      0.0
C54H18-+HCS+   =C54H18   CS       H                 1.10D-08  -.50      0.0
C54H18-+Si+    =C54H18   Si                         1.40D-08  -.50      0.0
C54H18-+Fe+    =C54H18   Fe                         1.00D-08  -.50      0.0
C54H18-+S+     =C54H18   S                          1.30D-08  -.50      0.0
C54H18 +H+     =C54H18+  H                          4.40D-09  0.00      0.0
C54H18 +H3+    =C54H18+  H2       H                 1.30D-09  0.00      0.0
C54H18 +H3+    =C54H18+  H        H        H        1.30D-09  0.00      0.0
C54H18 +He+    =C54H18+  He                         2.20D-09  0.00      0.0
C54H18 +C+     =C54H18+  C                          1.30D-09  0.00      0.0
C54H18 +H3O+   =C54H18+  H2O      H                 1.00D-09  0.00      0.0
C54H18 +H3S+   =C54H18+  H2S      H                 7.40D-10  0.00      0.0
C54H18 +NH4+   =C54H18+  NH3      H                 1.00D-09  0.00      0.0
C54H18 +HCO+   =C54H18+  CO       H                 8.20D-10  0.00      0.0
C54H18 +HCS+   =C54H18+  CS       H                 6.50D-10  0.00      0.0
C54H18 +Si+    =C54H18+  Si                         8.30D-10  0.00      0.0
C54H18 +Fe+    =C54H18+  Fe                         5.90D-10  0.00      0.0
C54H18 +S+     =C54H18+  S                          7.80D-10  0.00      0.0
C54H18-+H      =C54H18   H        ELECTR            3.30D-09  0.00   5500.0
C54H18-+C      =C54H18   C        ELECTR            9.60D-10  0.00   5500.0
C54H18-+CH     =C54H18   CH       ELECTR            9.60D-10  0.00   5500.0
C54H18-+O      =C54H18   O        ELECTR            8.30D-10  0.00   5500.0
C54H18-+OH     =C54H18   OH       ELECTR            8.30D-10  0.00   5500.0
C54H18 +SECPHO =C54H18+  ELECTR                     2.00D+04  0.00 140000.0
C54H18-+SECPHO =C54H18   ELECTR                     2.00D+04  0.00 140000.0
C60    +ELECTR =C60-     PHOTON                     6.900D-5  0.50      0.0
C60-   +H+     =C60      H                          1.60D-06  0.50      0.0
C60-   +H3+    =C60      H2       H                 4.61D-07  0.50      0.0
C60-   +H3+    =C60      H        H        H        4.61D-07  0.50      0.0
C60-   +He+    =C60      He                         8.00D-07  0.50      0.0
C60-   +C+     =C60      C                          4.61D-07  0.50      0.0
C60-   +H3O+   =C60      H2O      H                 3.66D-07  0.50      0.0
C60-   +H3S+   =C60      H2S      H                 2.70D-07  0.50      0.0
C60-   +NH4+   =C60      NH3      H                 3.76D-07  0.50      0.0
C60-   +HCO+   =C60      CO       H                 2.96D-07  0.50      0.0
C60-   +HCS+   =C60      CS       H                 2.38D-07  0.50      0.0
C60-   +Si+    =C60      Si                         3.01D-07  0.50      0.0
C60-   +Fe+    =C60      Fe                         2.13D-07  0.50      0.0
C60-   +S+     =C60      S                          2.82D-07  0.50      0.0
C60    +H+     =C60+     H                          1.60D-06  0.50      0.0
C60    +H3+    =C60+     H2       H                 4.61D-07  0.50      0.0
C60    +H3+    =C60+     H        H        H        4.61D-07  0.50      0.0
C60    +He+    =C60+     He                         8.00D-07  0.50      0.0
C60    +C+     =C60+     C                          4.61D-07  0.50      0.0
C60    +H3O+   =C60+     H2O      H                 3.66D-07  0.50      0.0
C60    +H3S+   =C60+     H2S      H                 2.70D-07  0.50      0.0
C60    +NH4+   =C60+     NH3      H                 3.76D-07  0.50      0.0
C60    +HCO+   =C60+     CO       H                 2.96D-07  0.50      0.0
C60    +HCS+   =C60+     CS       H                 2.38D-07  0.50      0.0
C60    +Si+    =C60+     Si                         3.01D-07  0.50      0.0
C60    +Fe+    =C60+     Fe                         2.13D-07  0.50      0.0
C60    +S+     =C60+     S                          2.82D-07  0.50      0.0
```

```
        C60+    +ELECTR =C60     PHOTON                  6.900D-5  0.50      0.0
        C60     +SECPHO =C60+    ELECTR                  0.63D+08  0.00 140000.0
        C60-    +SECPHO =C60     ELECTR                  0.41D+09  0.00 140000.0
SHATT   C60-    +C60    =C60     C54-       C6           7.000D-7  0.50 200000.0
SHATT   C60+    +C60    =C60     C54+       C6           7.000D-7  0.50 200000.0
        H       +CRP    =H+      ELECTR                  4.60D-01  0.00      0.0
        He      +CRP    =He+     ELECTR                  5.00D-01  0.00      0.0
        H2      +CRP    =H+      H          ELECTR       4.00D-02  0.00      0.0
        H2      +CRP    =H       H                       1.50D+00  0.00      0.0
        H2      +CRP    =H2+     ELECTR                  9.60D-01  0.00      0.0
        C       +CRP    =C+      ELECTR                  1.80D+00  0.00      0.0
        O       +CRP    =O+      ELECTR                  2.80D+00  0.00      0.0
        C       +SECPHO =C+      ELECTR                  1.02D+03  0.00 140000.0
        CH      +SECPHO =C       H                       1.46D+03  0.00 140000.0
        CH4     +SECPHO =CH3     H                       4.68D+03  0.00 140000.0
        CH+     +SECPHO =C       H+                      3.52D+02  0.00 140000.0
        OH      +SECPHO =O       H                       1.02D+03  0.00 140000.0
        H2O     +SECPHO =OH      H                       1.94D+03  0.00 140000.0
        O2      +SECPHO =O2+     ELECTR                  2.34D+02  0.00 140000.0
        O2      +SECPHO =O       O                       1.50D+03  0.00 140000.0
        CO2     +SECPHO =CO      O                       3.42D+03  0.00 140000.0
        C2      +SECPHO =C       C                       4.74D+02  0.00 140000.0
        C2H     +SECPHO =C2      H                       8.16D+03  0.00 140000.0
        C2H2    +SECPHO =C2H     H                       1.03D+04  0.00 140000.0
        C2H2    +SECPHO =C2H2+   ELECTR                  2.62D+03  0.00 140000.0
        C3      +SECPHO =C2      C                       2.24D+03  0.00 140000.0
        C3H     +SECPHO =C3      H                       8.16D+03  0.00 140000.0
        C3H2    +SECPHO =C3H     H                       8.16D+03  0.00 140000.0
        CO      +SECPHO =C       O                       6.80D+02  1.20 140000.0
        O       +H2     =OH      H                       1.55D-13  2.80   2980.0
        CO      +H      =OH      C                       1.10D-10  0.50  77700.0
        O2      +H      =OH      O                       1.63D-09  -.90   8750.0
        OH      +H      =O       H2                      7.00D-14  2.80   1950.0
        OH      +H2     =H2O     H                       9.54D-13  2.00   1490.0
        H2O     +H      =OH      H2                      5.24D-12  1.90   9265.0
        C       +H2     =CH      H                       1.16D-09  0.50  14100.0
        C       +H      =CH      PHOTON                  1.00D-17  0.00      0.0
        CH      +H2     =CH2     H                       2.38D-10  0.00   1760.0
        CH2     +H2     =CH3     H                       5.18D-11  0.17   6400.0
        CH3     +H2     =CH4     H                       3.00D-10  0.00   5460.0
        C2      +H2     =C2H     H                       1.60D-10  0.00   1419.0
        C2H     +H2     =C2H2    H                       1.14D-11  0.00    950.0
        CH      +H      =C       H2                      1.16D-09  0.50   2200.0
        CH2     +H      =CH      H2                      4.70D-10  0.00    370.0
        CH3     +H      =CH2     H2                      5.18D-11  0.17   5600.0
        CH4     +H      =CH3     H2                      3.00D-10  0.00   6560.0
        O2      +C      =CO      O                       3.30D-11  0.50      0.0
        OH      +CO     =CO2     H                       4.40D-13 -1.15    390.0
        OH      +C      =CO      H                       3.10D-11  -.36      0.0
        OH      +O      =O2      H                       3.10D-11  -.36      0.0
        CH      +O      =HCO+    ELECTR                  2.40D-14  0.50      0.0
        CH      +O      =CO      H                       9.50D-11  0.50      0.0
        CH2     +O      =CO      H          H            2.00D-11  0.50      0.0
        CH3     +O      =CO      H2         H            1.80D-10  0.50      0.0
        C2      +O      =CO      C                       5.00D-11  0.50      0.0
        C2H     +O      =CO      CH                      1.00D-10  0.00    250.0
        C3      +O      =CO      C2                      5.00D-11  0.50      0.0
        C3H     +O      =C2H     CO                      5.00D-11  0.50      0.0
        C3H2    +O      =C2H2    CO                      5.00D-11  0.50      0.0
        C+      +H      =CH+     PHOTON                  7.00D-17  0.00      0.0
        C+      +H2     =CH2+    PHOTON                  5.00D-16  0.00      0.0
        C+      +H2     =CH+     H                       1.50D-10  0.00   4640.0
```

```
CH+     +H      =C+     H2              1.50D-10  0.00      0.0
CH+     +H2     =CH2+   H               1.20D-09  0.00      0.0
CH2+    +H      =CH+    H2              1.20D-09  0.00   2700.0
CH2+    +H2     =CH3+   H               7.00D-10  0.00      0.0
CH3+    +H      =CH2+   H2              7.00D-10  0.00  10560.0
CH3+    +H2     =CH5+   PHOTON          6.00D-15  0.00      0.0
CH3+    +H2     =CH4+   H               2.00D-10  0.00  32500.0
CH4+    +H      =CH3+   H2              2.00D-10  0.00      0.0
CH4+    +H2     =CH5+   H               4.00D-11  0.00      0.0
CH5+    +H      =CH4+   H2              4.00D-11  0.00   2200.0
H+      +ELECTR =H      PHOTON          2.90D-12  -.74      0.0
H2+     +ELECTR =H      H               1.60D-08  -.43      0.0
He+     +ELECTR =He     PHOTON          4.50D-12  -.67      0.0
H3+     +ELECTR =H2     H               1.50D-07  -.50      0.0
C+      +ELECTR =C      PHOTON          4.40D-12  -.61      0.0
CH+     +ELECTR =C      H               1.50D-07  -.42      0.0
CH2+    +ELECTR =C      H2              1.25D-07  -.50      0.0
CH2+    +ELECTR =CH     H               1.25D-07  -.50      0.0
CH3+    +ELECTR =CH2    H               1.75D-07  -.50      0.0
CH3+    +ELECTR =CH     H2              1.75D-07  -.50      0.0
CH4+    +ELECTR =CH3    H               3.00D-07  -.50
CH4+    +ELECTR =CH2    H       H       3.00D-07  -.50
CH5+    +ELECTR =CH     H2      H2      8.75D-08  -.30      0.0
CH5+    +ELECTR =CH2    H2      H       8.75D-08  -.30      0.0
CH5+    +ELECTR =CH3    H2              8.75D-08  -.30      0.0
CH5+    +ELECTR =CH4    H               8.75D-08  -.30      0.0
H+      +H2     =H2+    H               6.40D-10  0.00  21300.0
H2+     +H      =H+     H2              6.40D-10  0.00      0.0
H2+     +H2     =H3+    H               2.10D-09  0.00      0.0
H3+     +H      =H2+    H2              2.10D-09  0.00  20000.0
H+      +O      =O+     H               6.00D-10  0.00    227.0
H+      +OH     =OH+    H               2.10D-09  0.00      0.0
H+      +O2     =O2+    H               1.20D-09  0.00      0.0
H+      +H2O    =H2O+   H               8.20D-09  0.00      0.0
H+      +CH     =CH+    H               1.90D-09  0.00      0.0
H+      +CH2    =CH+    H2              1.40D-09  0.00      0.0
H+      +CH2    =CH2+   H               1.40D-09  0.00      0.0
H+      +CH3    =CH3+   H               3.40D-09  0.00      0.0
H+      +CH4    =CH3+   H2              2.28D-09  0.00      0.0
H+      +CH4    =CH4+   H               1.52D-09  0.00      0.0
H+      +CO2    =HCO+   O               4.20D-09  0.00      0.0
H2+     +C      =CH+    H               2.40D-09  0.00      0.0
H2+     +O      =OH+    H               1.50D-09  0.00      0.0
H2+     +CO     =HCO+   H               2.16D-09  0.00      0.0
H2+     +CO     =CO+    H2              6.44D-10  0.00      0.0
H2+     +OH     =OH+    H2              7.60D-10  0.00      0.0
H2+     +H2O    =H2O+   H2              3.90D-09  0.00      0.0
H2+     +H2O    =H3O+   H               3.40D-09  0.00      0.0
H2+     +CH     =CH+    H2              7.10D-10  0.00      0.0
H2+     +CH     =CH2+   H               7.10D-10  0.00      0.0
H2+     +CH2    =CH3+   H               1.00D-09  0.00      0.0
H2+     +CH2    =CH2+   H2              1.00D-09  0.00      0.0
H3+     +O      =OH+    H2              8.00D-10  0.00      0.0
H3+     +OH     =H2O+   H2              1.30D-09  0.00      0.0
H3+     +CO     =HCO+   H2              1.70D-09  0.00      0.0
H3+     +CO2    =HCO2+  H2              2.00D-09  0.00      0.0
H3+     +H2O    =H3O+   H2              4.30D-09  0.00      0.0
H3+     +C      =CH+    H2              2.00D-09  0.00      0.0
H3+     +CH     =CH2+   H2              1.20D-09  0.00      0.0
H3+     +CH2    =CH3+   H2              1.70D-09  0.00      0.0
H3+     +CH3    =CH4+   H2              2.10D-09  0.00      0.0
H3+     +CH4    =CH5+   H2              1.90D-09  0.00      0.0
```

He+	+H2	=H+	H	He		1.10D-13	-.24	0.0
He+	+OH	=OH+	He			5.50D-10	0.00	0.0
He+	+OH	=O+	H	He		5.50D-10	0.00	0.0
He+	+H2O	=OH+	H	He		2.30D-10	-.94	0.0
He+	+H2O	=H2O+	He			4.86D-11	-.94	0.0
He+	+H2O	=H+	OH	He		1.64D-10	-.94	0.0
He+	+CO	=C+	O	He		1.50D-09	0.00	0.0
He+	+O2	=O+	O	He		1.00D-09	0.00	0.0
He+	+CO2	=CO+	O	He		7.70D-10	0.00	0.0
He+	+CO2	=O+	CO	He		1.80D-10	0.00	0.0
He+	+CO2	=C+	O2	He		4.00D-11	0.00	0.0
He+	+CH	=C+	H	He		1.10D-09	0.00	0.0
He+	+CH2	=C+	H2	He		7.50D-10	0.00	0.0
He+	+CH2	=CH+	H	He		7.50D-10	0.00	0.0
He+	+CH3	=CH+	H2	He		9.00D-10	0.00	0.0
He+	+CH3	=CH2+	H	He		9.00D-10	0.00	0.0
He+	+CH4	=H+	CH3	He		4.00D-10	0.00	0.0
He+	+CH4	=CH+	H2	H	He	2.56D-10	0.00	0.0
He+	+CH4	=CH2+	H2	He		8.48D-10	0.00	0.0
He+	+CH4	=CH3+	H	He		8.00D-11	0.00	0.0
He+	+CH4	=CH4+	He			1.60D-11	0.00	0.0
C+	+OH	=CO+	H			8.00D-10	0.00	0.0
C+	+OH	=H+	CO			8.00D-10	0.00	0.0
C+	+H2O	=HCO+	H			2.43D-09	-.63	0.0
C+	+O2	=O+	CO			5.15D-10	0.00	0.0
C+	+O2	=CO+	O			3.15D-10	0.00	0.0
C+	+CO2	=CO+	CO			1.10D-09	0.00	0.0
C+	+CH	=C2+	H			3.80D-10	0.00	0.0
C+	+CH	=CH+	C			3.80D-10	0.00	0.0
C+	+CH2	=CH2+	C			5.20D-10	0.00	0.0
C+	+CH2	=C2H+	H			5.20D-10	0.00	0.0
C+	+CH4	=C2H2+	H2			3.25D-10	0.00	0.0
C+	+CH4	=C2H3+	H			9.75D-10	0.00	0.0
O+	+H	=H+	O			6.00D-10	0.00	0.0
O+	+H2	=OH+	H			1.20D-09	0.00	0.0
O2+	+C	=CO+	O			5.20D-11	0.00	0.0
O2+	+C	=C+	O2			5.20D-11	0.00	0.0
OH+	+H2	=H2O+	H			1.01D-09	0.00	0.0
H2O+	+H2	=H3O+	H			8.30D-10	0.00	0.0
H3O+	+H	=H2O+	H2			6.10D-10	0.00	20500.0
H3O+	+C	=HCO+	H2			1.00D-11	0.00	0.0
H3O+	+CH	=CH2+	H2O			6.80D-10	0.00	0.0
H3O+	+CH2	=CH3+	H2O			9.40D-10	0.00	0.0
O+	+ELECTR	=O	PHOTON			3.40D-12	-.64	0.0
O2+	+ELECTR	=O	O			1.95D-07	-.70	0.0
OH+	+ELECTR	=O	H			3.75D-08	-.50	0.0
H2O+	+ELECTR	=OH	H			3.15D-07	-.50	0.0
H3O+	+ELECTR	=OH	H2			8.45D-07	-.50	0.0
H3O+	+ELECTR	=H2O	H			4.55D-07	-.50	0.0
CH3+	+O	=HCO+	H2			3.10D-10	0.00	0.0
CH3+	+O	=H3+	CO			1.30D-11	0.00	0.0
CH5+	+O	=H3O+	CH2			2.16D-10	0.00	0.0
CH5+	+CO	=HCO+	CH4			9.90D-10	0.00	0.0
CH5+	+H2O	=H3O+	CH4			3.70D-09	0.00	0.0
CO+	+H2	=HCO+	H			1.30D-09	0.00	0.0
CO+	+H	=H+	CO			7.50D-10	0.00	0.0
HCO+	+H	=CO+	H2			1.30D-09	0.00	24500.0
HCO+	+C	=CH+	CO			1.10D-09	0.00	0.0
HCO+	+CH	=CH2+	CO			6.30D-10	0.00	0.0
HCO+	+CH2	=CH3+	CO			8.60D-10	0.00	0.0
HCO+	+CH3	=CH4+	CO			1.40D-09	0.00	9060.0
HCO+	+CH4	=CH5+	CO			9.90D-10	0.00	4920.0

```
HCO+    +H2O    =H3O+    CO              2.50D-09  0.00     0.0
HCO+    +O2     =HCO2+   O               1.00D-09  0.00  1450.0
HCO2+   +O      =HCO+    O2              1.00D-09  0.00     0.0
HCO+    +OH     =HCO2+   H               1.00D-09  0.00     0.0
HCO2+   +H      =HCO+    OH              1.00D-09  0.00  7500.0
HCO2+   +CO     =HCO+    CO2             1.00D-09  0.00     0.0
HCO+    +CO2    =HCO2+   CO              1.00D-09  0.00  5000.0
HCO2+   +CH4    =CH5+    CO2             7.80D-10  0.00     0.0
CO+     +ELECTR =C       O               1.00D-07  -.46     0.0
HCO+    +ELECTR =CO      H               2.40D-07  -.69     0.0
HCO2+   +ELECTR =CO2     H               2.24D-07  -.50     0.0
HCO2+   +ELECTR =CO      OH              1.16D-07  -.50     0.0
C2+     +H2     =C2H+    H               1.40D-09  0.00     0.0
C2+     +H2     =H+      C2H             1.50D-09  0.00  1260.0
C2H+    +H2     =C2H2+   H               1.70D-09  0.00     0.0
C2H2+   +H2     =C2H3+   H               5.00D-10  0.00   800.0
C2+     +ELECTR =C       C               3.00D-07  -.50     0.0
C2H+    +ELECTR =C2      H               1.35D-07  -.50     0.0
C2H+    +ELECTR =CH      C               1.35D-07  -.50     0.0
C2H2+   +ELECTR =C2H     H               1.50D-07  -.50     0.0
C2H2+   +ELECTR =CH      CH              1.50D-07  -.50     0.0
C2H3+   +ELECTR =C2H     H2              1.35D-07  -.50     0.0
C2H3+   +ELECTR =CH2     CH              1.35D-07  -.50     0.0
C2H3+   +ELECTR =C2H2    H               3.00D-08  -.50     0.0
C3+     +H2     =C3H+    H               3.00D-10  0.00     0.0
C3H+    +H2     =C3H2+   H               1.00D-09  0.00   500.0
C3H+    +H2     =C3H3+   PHOTON          3.00D-13  -1.0     0.0
C3H2+   +H2     =C3H3+   H               1.00D-10  0.00  2000.0
C3+     +ELECTR =C2      C               3.00D-07  -.50     0.0
C3H+    +ELECTR =C2      CH              1.50D-07  -.50     0.0
C3H+    +ELECTR =C2H     C               1.50D-07  -.50     0.0
C3H2+   +ELECTR =C3H     H               1.50D-07  -.50     0.0
C3H2+   +ELECTR =C2H     CH              1.50D-07  -.50     0.0
C3H3+   +ELECTR =C3H2    H               1.50D-07  -.50     0.0
C3H3+   +ELECTR =C2H2    CH              1.50D-07  -.50     0.0
H+      +C2     =C2+     H               3.10D-09  0.00     0.0
H+      +C2H    =C2+     H2              1.50D-09  0.00     0.0
H+      +C2H    =C2H+    H               1.50D-09  0.00     0.0
H+      +C2H2   =C2H+    H2              2.00D-09  0.00     0.0
H+      +C2H2   =C2H2+   H               2.00D-09  0.00     0.0
H+      +C3H    =C3+     H2              2.00D-09  0.00     0.0
H+      +C3H    =C3H+    H               2.00D-09  0.00     0.0
H+      +C3H2   =C3H+    H2              2.00D-09  0.00     0.0
H+      +C3H2   =C3H2+   H               2.00D-09  0.00     0.0
He+     +C2H    =C+      CH      He      5.10D-10  0.00     0.0
He+     +C2H    =CH+     C       He      5.10D-10  0.00     0.0
He+     +C2H    =C2+     H       He      5.10D-10  0.00     0.0
He+     +C2H2   =CH+     CH      He      7.70D-10  0.00     0.0
He+     +C2H2   =C2+     H2      He      1.61D-09  0.00     0.0
He+     +C2H2   =C2H+    H       He      8.75D-10  0.00     0.0
He+     +C2H2   =C2H2+   He              2.45D-10  0.00     0.0
He+     +C3H    =C3+     H       He      2.00D-09  0.00     0.0
He+     +C3H2   =C3H+    H       He      1.00D-09  0.00     0.0
He+     +C3H2   =C3+     H2      He      1.00D-09  0.00     0.0
H3+     +C2H    =C2H2+   H2              1.70D-09  0.00     0.0
H3+     +C2H2   =C2H3+   H2              2.90D-09  0.00     0.0
H3+     +C3H    =C3H2+   H2              2.00D-09  0.00     0.0
H3+     +C3H2   =C3H3+   H2              2.00D-09  0.00     0.0
C+      +C2H    =C3+     H               1.00D-09  0.00     0.0
C+      +C2H2   =C3H+    H               2.20D-09  0.00     0.0
HCO+    +C2H    =C2H2+   CO              7.80D-10  0.00     0.0
HCO+    +C2H2   =C2H3+   CO              1.36D-09  0.00     0.0
```

HCO+	+C3H	=C3H2+	CO		1.40D-09	0.00	0.0
HCO+	+C3H2	=C3H3+	CO		1.40D-09	0.00	0.0
H3O+	+C2H	=C2H2+	H2O		2.20D-10	0.00	4100.0
H3O+	+C2H2	=C2H3+	H2O		1.00D-09	0.00	7330.0
H3O+	+C3H	=C3H2+	H2O		2.00D-09	0.00	0.0
H3O+	+C3H2	=C3H3+	H2O		3.00D-09	0.00	0.0
C2H2+	+H2O	=H3O+	C2H		2.20D-10	0.00	0.0
C2H3+	+H2O	=H3O+	C2H2		1.11D-09	0.00	0.0
C3H+	+H2O	=HCO+	C2H2		2.48D-10	0.00	0.0
C3H+	+H2O	=C2H3+	CO		2.02D-10	0.00	0.0
H+	+Fe	=Fe+	H		7.40D-09	0.00	0.0
H3+	+Fe	=Fe+	H2	H	4.90D-09	0.00	0.0
C+	+Fe	=Fe+	C		2.60D-09	0.00	0.0
HCO+	+Fe	=Fe+	CO	H	1.90D-09	0.00	0.0
H3O+	+Fe	=Fe+	H2O	H	3.10D-09	0.00	0.0
O2+	+Fe	=Fe+	O2		1.10D-09	0.00	0.0
Fe+	+ELECTR	=Fe	PHOTON		3.70D-12	-.65	0.0
N	CRP	N+	ELECTR		2.10E+00	0.00	0.0
CN	+SECPHO	=C	N		2.12D+04	0.00	140000.0
HCN	+SECPHO	=CN	H		6.23D+03	0.00	140000.0
HNC	+SECPHO	=CN	H		6.23D+03	0.00	140000.0
NH2	+SECPHO	=NH	H		1.60D+02	0.00	140000.0
NH2	+SECPHO	=NH2+	ELECTR		1.30D+03	0.00	140000.0
NH3	+SECPHO	=NH2	H		2.63D+03	0.00	140000.0
NH3	+SECPHO	=NH	H2		1.08D+03	0.00	140000.0
NH3	+SECPHO	=NH3+	ELECTR		1.15D+03	0.00	140000.0
NO	+SECPHO	=N	O		9.64D+02	0.00	140000.0
NO	+SECPHO	=NO+	ELECTR		9.88D+02	0.00	140000.0
N	H2	NH	H		8.66D-10	0.50	14600.0
NH	H2	NH2	H		5.25D-12	0.79	6700.0
NH2	H2	NH3	H		6.22D-11	0.50	6300.0
CN	H2	HCN	H		3.53D-13	3.31	756.0
NH	H	N	H2		8.66D-10	0.50	2400.0
NH2	H	NH	H2		5.25D-12	0.79	2200.0
NH3	H	NH2	H2		6.22D-11	0.50	5700.0
NH	O	OH	N		2.90D-11	0.50	0.0
NH2	O	NH	OH		3.50D-12	0.50	0.0
NH3	O	NH2	OH		2.50D-12	0.00	3020.0
CN	O	CO	N		1.80D-11	0.50	50.0
NH3	OH	NH2	H2O		2.30D-12	0.00	800.0
NH	C	CN	H		1.10D-10	0.50	0.0
CH	N	CN	H		2.10D-11	0.00	0.0
CN	N	N2	C		7.30D-10	0.00	4500.0
NH	N	N2	H		5.00D-11	0.50	0.0
OH	N	NO	H		5.30D-11	0.00	50.0
O2	N	NO	O		3.30D-12	1.00	3150.0
NO	C	CN	O		1.10D-10	0.50	0.0
NO	N	N2	O		3.40D-11	0.00	50.0
NO	O	O2	N		7.50D-13	1.00	16000.0
HNC	H	HCN	H		1.00D-10	0.50	200.0
HNC	O	CO	NH		2.00D-10	0.50	200.0
HNC	OH	H2O	CN		2.00D-10	0.50	200.0
HNC	O2	CO2	NH		2.00D-11	0.50	2000.0
NH2	C	HNC	H		2.00D-11	0.50	0.0
CH2	N	HCN	H		2.00D-11	0.50	0.0
CH3	N	HCN	H2		2.00D-11	0.50	0.0
CH5+	HNC	C2H3+	NH3		1.00D-09	0.00	0.0
CH5+	HCN	C2H3+	NH3		1.00D-09	0.00	5120.0
N+	H2	NH+	H		8.40D-10	0.00	168.5
NH+	H2	NH2+	H		1.27D-09	0.00	0.0
NH+	H2	H3+	N		2.25D-10	0.00	0.0
NH2+	H2	NH3+	H		2.70D-10	0.00	0.0

NH3+	H2	NH4+	H		2.40D-12	0.00	0.0
NH+	H	N+	H2		6.52D-10	0.00	0.0
NH2+	H	NH+	H2		1.27D-09	0.00	24000.0
NH3+	H	NH2+	H2		2.25D-10	0.00	12800.0
NH4+	H	NH3+	H2		1.00D-09	0.00	11000.0
CN+	H2	HCN+	H		1.00D-09	0.00	0.0
HCN+	H	CN+	H2		1.00D-09	0.00	15800.0
HCN+	H2	H2CN+	H		9.80D-10	0.00	0.0
H2CN+	H	HCN+	H2		9.80D-10	0.00	34400.0
N2+	H2	N2H+	H		2.00D-09	0.24	0.0
N2H+	H	N2+	H2		2.10D-09	0.00	30300.0
N2H+	H2	H3+	N2		1.80D-09	0.00	8300.0
H+	HNC	H+	HCN		1.00D-09	0.00	0.0
H+	HCN	H+	HNC		1.00D-09	0.00	7850.0
H+	NH	NH+	H		2.10D-09	0.00	0.0
H+	NH2	NH2+	H		2.90D-09	0.00	0.0
H+	NH3	NH3+	H		5.20D-09	0.00	0.0
H+	CN	CN+	H		2.10D-09	0.00	6150.0
H+	HCN	HCN+	H		1.10D-08	0.00	0.0
H+	NO	NO+	H		1.90D-09	0.00	0.0
He+	NH	N+	H	He	1.10D-09	0.00	0.0
He+	NH2	NH+	H	He	8.00D-10	0.00	0.0
He+	NH2	N+	H2	He	8.00D-10	0.00	0.0
He+	NH3	NH3+	He		2.64D-10	0.00	0.0
He+	NH3	NH2+	H	He	1.76D-09	0.00	0.0
He+	NH3	NH+	H2	He	1.76D-10	0.00	0.0
He+	CN	C+	N	He	8.80D-10	0.00	0.0
He+	CN	N+	C	He	8.80D-10	0.00	0.0
He+	HCN	CN+	H	He	1.46D-09	0.00	0.0
He+	HCN	CH+	N	He	6.20D-10	0.00	0.0
He+	HCN	C+	NH	He	7.75D-10	0.00	0.0
He+	HCN	N+	CH	He	2.48D-10	0.00	0.0
He+	HNC	CN+	H	He	1.55D-09	0.00	0.0
He+	HNC	C+	NH	He	1.55D-09	0.00	0.0
He+	N2	N+	N	He	7.92D-10	0.00	0.0
He+	N2	N2+	He		4.08D-10	0.00	0.0
He+	NO	N+	O	He	1.38D-09	0.00	0.0
He+	NO	O+	N	He	2.24D-10	0.00	0.0
H3+	NH	NH2+	H2		1.30D-09	0.00	0.0
H3+	NH2	NH3+	H2		1.80D-09	0.00	0.0
H3+	NH3	NH4+	H2		9.10D-09	0.00	0.0
H3+	N	NH2+	H		4.50D-10	0.00	0.0
H3+	CN	HCN+	H2		1.00D-09	0.00	0.0
H3+	CN	H2CN+	H		1.00D-09	0.00	0.0
H3+	HCN	H2CN+	H2		9.50D-09	0.00	0.0
H3+	HNC	H2CN+	H2		9.50D-09	0.00	0.0
H3+	N2	N2H+	H2		1.30D-09	0.00	0.0
H3+	NO	HNO+	H2		1.10D-09	0.00	0.0
H3O+	NH3	NH4+	H2O		2.20D-09	0.00	0.0
H3O+	CN	H2CN+	OH		4.50D-09	0.00	0.0
H3O+	HCN	H2CN+	H2O		4.50D-09	0.00	0.0
H2CN+	H2O	H3O+	HCN		4.50D-09	0.00	2460.0
H3O+	HNC	H2CN+	H2O		4.50D-09	0.00	0.0
H2CN+	H2O	H3O+	HNC		4.50D-09	0.00	10300.0
HCO+	NH	NH2+	CO		6.40D-10	0.00	0.0
NH2+	CO	HCO+	NH		6.40D-10	0.00	6100.0
HCO+	NH2	NH3+	CO		8.90D-10	0.00	0.0
HCO+	NH3	NH4+	CO		1.90D-09	0.00	0.0
HCO+	HCN	H2CN+	CO		3.70D-09	0.00	0.0
HCO+	HNC	H2CN+	CO		3.70D-09	0.00	0.0
HCO2+	NO	HNO+	CO2		1.00D-10	0.00	0.0
C+	NH	CN+	H		7.80D-10	0.00	0.0

```
C+      NH2     HCN+    H                    1.10D-09   0.00      0.0
C+      NH3     NH3+    C                    5.29D-10   0.00      0.0
C+      NH3     H2NC+   H                    7.80D-10   0.00      0.0
C+      NH3     H2CN+   H                    7.80D-10   0.00      0.0
C+      NH3     HCN+    H2                   2.08D-10   0.00      0.0
C+      HCN     C2N+    H                    3.40D-09   0.00      0.0
C+      HNC     C2N+    H                    3.40D-09   0.00      0.0
C+      NO      NO+     C                    3.40D-09   0.00      0.0
C+      NO      N+      CO                   9.02D-10   0.00      0.0
N+      CO      C+      NO                   9.02D-10   0.00   15400.0
O2+     N       NO+     O                    7.84D-11   0.00      0.0
O2+     NH3     NH3+    O2                   2.00D-09   0.00      0.0
O2+     NO      NO+     O2                   4.40D-10   0.00      0.0
CH2+    N       HCN+    H                    9.40D-10   0.00      0.0
C2H+    N       C2N+    H                    8.30D-10   0.00      0.0
CH3+    N       HCN+    H2                   6.70D-11   0.00      0.0
CH3+    N       H2CN+   H                    6.70D-11   0.00      0.0
C2H2+   N       CH+     HCN                  2.50D-11   0.00      0.0
C2H2+   N       CH+     HNC                  2.50D-11   0.00   2600.0
C2H2+   N       C2N+    H2                   2.25D-10   0.00      0.0
N+      O2      O2+     N                    2.81D-10   0.00      0.0
N+      O2      NO+     O                    2.37D-10   0.00      0.0
N+      O2      O+      NO                   3.30D-11   0.00      0.0
N+      CO      CO+     N                    8.25D-10   0.00      0.0
N+      CO      NO+     C                    1.46D-10   0.00      0.0
N+      NO      NO+     N                    4.51D-10   0.00      0.0
N+      NO      N2+     O                    7.95D-11   0.00      0.0
NH3+    H2O     NH4+    OH                   2.50D-10   0.00      0.0
NH4+    OH      NH3+    H2O                  2.50D-10   0.00   3400.0
N2H+    O       OH+     N2                   1.40D-10   0.00   3400.0
N2H+    H2O     H3O+    N2                   2.60D-09   0.00      0.0
N2H+    CO      HCO+    N2                   8.80D-10   0.00      0.0
HCO+    N2      N2H+    CO                   8.80D-10   0.00  11200.0
N2H+    CO2     HCO2+   N2                   1.40D-09   0.00      0.0
HCO2+   N2      N2H+    CO2                  1.40D-09   0.00   6400.0
N2H+    NH3     NH4+    N2                   2.30D-09   0.00      0.0
NH4+    N2      N2H+    NH3                  2.30D-09   0.00  44000.0
N2H+    NO      HNO+    N2                   3.40D-10   0.00      0.0
C2N+    NH3     N2H+    C2H2                 1.90D-10   0.00      0.0
C2N+    NH3     H2CN+   HCN                  1.70D-09   0.00      0.0
HNO+    C       CH+     NO                   1.00D-09   0.00      0.0
HNO+    CO      HCO+    NO                   1.00D-10   0.00      0.0
HNO+    CO2     HCO2+   NO                   1.00D-10   0.00      0.0
HNO+    OH      H2O+    NO                   6.20D-10   0.00      0.0
HNO+    H2O     H3O+    NO                   2.30D-09   0.00      0.0
NO+     Fe      Fe+     NO                   1.00D-09   0.00      0.0
N+      ELECTR  N       PHOTON               3.80D-12  -0.62      0.0
NH+     ELECTR  N       H                    2.00D-07  -0.50      0.0
NH2+    ELECTR  NH      H                    1.50D-07  -0.50      0.0
NH2+    ELECTR  N       H        H           1.50D-07  -0.50      0.0
NH3+    ELECTR  NH2     H                    3.00D-07  -0.50      0.0
NH4+    ELECTR  NH2     H2                   7.60D-07  -0.50      0.0
NH4+    ELECTR  NH3     H                    7.60D-07  -0.50      0.0
CN+     ELECTR  C       N                    1.80D-07  -0.50      0.0
C2N+    ELECTR  C2      N                    1.00D-07  -0.50      0.0
C2N+    ELECTR  CN      C                    2.00D-07  -0.50      0.0
HCN+    ELECTR  CN      H                    1.50D-07  -0.50      0.0
HCN+    ELECTR  CH      N                    1.50D-07  -0.50      0.0
N2+     ELECTR  N       N                    3.60D-08  -0.42      0.0
N2H+    ELECTR  N2      H                    1.70D-07  -1.00      0.0
H2CN+   ELECTR  HCN     H                    1.75D-07  -0.50      0.0
H2CN+   ELECTR  HNC     H                    1.75D-07  -0.50      0.0
```

H2NC+	ELECTR	HNC	H	1.75D-07	-0.50	0.0
H2NC+	ELECTR	NH2	C	1.75D-07	-0.50	0.0
NO+	ELECTR	N	O	4.30D-07	-0.37	0.0
HNO+	ELECTR	NO	H	3.00D-07	-0.50	0.0
SO	+SECPHO	=S	O	9.64D+02	0.00	140000.0
CS	+SECPHO	=S	C	2.12D+04	0.00	140000.0
SH	+SECPHO	=S	H	1.46D+03	0.00	140000.0
OCS	+SECPHO	=CO	S	1.07D+04	0.00	140000.0
H2S	+SECPHO	=S	H2	1.03D+04	0.00	140000.0
H2S	+SECPHO	=H2S+	ELECTR	3.39D+03	0.00	140000.0
SO2	+SECPHO	=SO	O	1.77D+03	0.00	140000.0
S	+H2	=SH	H	1.04D-10	.132	9620.0
SH	+H2	=H2S	H	6.41D-12	.087	8050.0
SH	+H	=S	H2	2.50D-11	0.00	0.0
H2S	+H	=SH	H2	1.29D-11	0.00	860.0
SO	+H	=OH	S	5.90D-10	-.31	11100.0
SO2	+H	=SO	OH	9.25D-09	-.74	14700.0
OCS	+H	=SH	CO	1.70D-11	0.00	2000.0
SH	+O	=SO	H	1.60D-10	0.00	100.0
SH	+O	=OH	S	1.70D-11	0.67	950.0
H2S	+O	=SH	OH	1.40D-11	0.00	1920.0
H2S	+OH	=SH	H2O	6.30D-12	0.00	80.0
CS	+O	=CO	S	2.70D-10	0.00	760.0
CS	+OH	=OCS	H	1.55D-13	1.12	800.0
S	+O2	=SO	O	5.19D-12	0.00	265.0
SO	+O	=S	O2	6.60D-13	0.00	2760.0
SO	+O2	=SO2	O	1.40D-12	0.00	2820.0
SO	+OH	=SO2	H	1.96D-10	-.17	0.0
SO	+N	=NO	S	1.73D-11	0.50	750.0
SO	+C	=CO	S	7.20D-11	0.00	0.0
SO	+C	=CS	O	1.70D-10	0.00	0.0
SO2	+O	=SO	O2	9.27D-11	-.46	9140.0
OCS	+O	=SO	CO	2.60D-11	0.00	2250.0
CH	+S	=CS	H	1.10D-12	0.00	0.0
CH	+S	=SH	C	1.73D-11	0.50	4000.0
OH	+S	=SO	H	1.00D-10	0.00	100.0
SH	+C	=CS	H	2.00D-11	0.00	0.0
SH	+C	=CH	S	1.20D-11	0.58	5880.0
SH	+CO	=OCS	H	5.95D-14	1.12	8330.0
S+	+H2	=SH+	H	2.20D-10	0.00	9860.0
SH+	+H2	=H2S+	H	1.90D-10	0.00	8500.0
SH+	+H2	=H3S+	PHOTON	1.00D-15	0.00	0.0
H2S+	+H2	=H3S+	H	1.40D-11	0.00	2300.0
CS+	+H2	=HCS+	H	4.80D-10	0.00	0.0
SH+	+H	=S+	H2	1.10D-10	0.00	0.0
H2S+	+H	=SH+	H2	2.00D-10	0.00	0.0
H3S+	+H	=H2S+	H2	6.00D-11	0.00	0.0
SO+	+H	=S+	OH	6.10D-10	0.00	11385.0
H+	+S	=S+	H	1.00D-15	0.00	0.0
H+	+SH	=SH+	H	1.60D-09	0.00	0.0
H+	+SH	=S+	H2	1.60D-09	0.00	0.0
H+	+H2S	=H2S+	H	7.60D-09	0.00	0.0
H+	+CS	=CS+	H	4.90D-09	0.00	0.0
H+	+SO	=SO+	H	3.20D-09	0.00	0.0
H+	+OCS	=SH+	CO	5.90D-09	0.00	0.0
H3+	+S	=SH+	H2	2.60D-09	0.00	0.0
H3+	+SH	=H2S+	H2	1.90D-09	0.00	0.0
H3+	+H2S	=H3S+	H2	3.70D-09	0.00	0.0
H3+	+CS	=HCS+	H2	2.90D-09	0.00	0.0
H3+	+SO	=HSO+	H2	1.90D-09	0.00	0.0
H3+	+SO2	=HSO2+	H2	1.30D-09	0.00	0.0
H3+	+OCS	=HOCS+	H2	1.90D-09	0.00	0.0

He+	+SH	=S+	H	He	1.70D-09	0.00	0.0
He+	+H2S	=S+	H2	He	3.60D-09	0.00	0.0
He+	+H2S	=SH+	H	He	4.80D-10	0.00	0.0
He+	+H2S	=H2S+	He		3.10D-10	0.00	0.0
He+	+CS	=C+	S	He	1.30D-09	0.00	0.0
He+	+CS	=S+	C	He	1.30D-09	0.00	0.0
He+	+SO	=O+	S	He	8.30D-10	0.00	0.0
He+	+SO	=S+	O	He	8.30D-10	0.00	0.0
He+	+OCS	=CS+	O	He	7.60D-10	0.00	0.0
He+	+OCS	=S+	CO	He	7.60D-10	0.00	0.0
He+	+OCS	=CO+	S	He	7.60D-10	0.00	0.0
He+	+OCS	=O+	CS	He	7.60D-11	0.00	0.0
He+	+SO2	=S+	O2	He	8.60D-10	0.00	0.0
He+	+SO2	=SO+	O	He	3.44D-09	0.00	0.0
C+	+S	=S+	C		1.50D-09	0.00	0.0
C+	+SH	=CS+	H		1.10D-09	0.00	0.0
C+	+H2S	=HCS+	H		1.28D-09	0.00	0.0
C+	+H2S	=H2S+	C		4.25D-10	0.00	0.0
C+	+CS	=CS+	C		1.60D-09	0.00	700.0
C+	+SO	=S+	CO		2.60D-10	0.00	0.0
C+	+SO	=CS+	O		2.60D-10	0.00	0.0
C+	+SO	=SO+	C		2.60D-10	0.00	0.0
C+	+SO	=CO+	S		2.60D-10	0.00	0.0
C+	+OCS	=CS+	CO		1.60D-09	0.00	0.0
C+	+SO2	=SO+	CO		2.30D-09	0.00	0.0
CH+	+S	=S+	CH		4.70D-10	0.00	0.0
CH+	+S	=SH+	C		4.70D-10	0.00	0.0
CH+	+S	=CS+	H		4.70D-10	0.00	0.0
CH+	+SO	=OH+	CS		1.00D-09	0.00	0.0
CH+	+SO	=SH+	CO		1.00D-09	0.00	0.0
CH3+	+S	=HCS+	H2		1.40D-09	0.00	0.0
CH3+	+SO	=HOCS+	H2		9.50D-10	0.00	0.0
CH5+	+S	=SH+	CH4		1.30D-09	0.00	0.0
H3O+	+S	=SH+	H2O		3.20D-10	0.00	4930.0
H3O+	+H2S	=H3S+	H2O		1.90D-09	0.00	0.0
HCO+	+S	=SH+	CO		3.30D-10	0.00	0.0
HCO+	+SH	=H2S+	CO		8.20D-10	0.00	0.0
HCO+	+CS	=HCS+	CO		1.20D-09	0.00	0.0
HCO+	+SO	=HSO+	CO		7.50D-10	0.00	0.0
HCO+	+H2S	=H3S+	CO		1.60D-09	0.00	0.0
HCO+	+OCS	=HOCS+	CO		1.10D-09	0.00	0.0
O2+	+S	=SO+	O		5.40D-10	0.00	0.0
O2+	+S	=S+	O2		5.40D-10	0.00	0.0
O2+	+H2S	=H2S+	O2		1.40D-09	0.00	0.0
S+	+CH	=CS+	H		6.20D-10	0.00	0.0
S+	+CH2	=HCS+	H		1.00D-11	0.00	0.0
S+	+OH	=SO+	H		6.10D-10	0.00	0.0
S+	+OH	=SH+	O		2.90D-10	0.00	8820.0
S+	+SH	=SH+	S		9.70D-10	0.00	350.0
S+	+NO	=NO+	S		3.20D-10	0.00	0.0
S+	+NH3	=NH3+	S		1.60D-09	0.00	0.0
S+	+O2	=SO+	O		2.30D-11	0.00	0.0
NH3+	+H2S	=NH4+	SH		6.00D-10	0.00	0.0
HNO+	+S	=SH+	NO		1.10D-09	0.00	0.0
N2H+	+S	=SH+	N2		1.10D-09	0.00	0.0
SH+	+O	=SO+	H		2.90D-10	0.00	0.0
SH+	+O	=S+	OH		2.90D-10	0.00	0.0
SH+	+S	=S+	SH		9.70D-10	0.00	0.0
SH+	+C	=CS+	H		9.90D-10	0.00	0.0
SH+	+CH	=CH2+	S		5.80D-10	0.00	0.0
SH+	+OH	=H2S+	O		3.10D-10	0.00	7500.0
SH+	+OH	=H2O+	S		4.30D-10	0.00	9200.0

```
SH+    +H2O   =H3O+  S                6.30D-10  0.00      0.0
SH+    +H2S   =H2S+  SH               5.00D-10  0.00   1000.0
SH+    +H2S   =H3S+  S                5.00D-10  0.00      0.0
SH+    +NO    =NO+   SH               3.30D-10  0.00      0.0
SH+    +NH3   =NH3+  SH               5.25D-10  0.00      0.0
SH+    +NH3   =NH4+  S                9.75D-10  0.00      0.0
H2S+   +O     =SH+   OH               3.10D-10  0.00      0.0
H2S+   +O     =SO+   H2               3.10D-10  0.00      0.0
H2S+   +C     =HCS+  H                1.00D-09  0.00      0.0
H2S+   +S     =S+    H2S              1.10D-09  0.00      0.0
H2S+   +SH    =SH+   H2S              5.00D-10  0.00      0.0
H2S+   +NO    =NO+   H2S              3.70D-10  0.00      0.0
H2S+   +H2O   =H3O+  SH               8.10D-10  0.00      0.0
H2S+   +NH3   =NH4+  SH               1.36D-09  0.00      0.0
H2S+   +NH3   =NH3+  H2S              3.40D-10  0.00      0.0
H3S+   +NH3   =NH4+  H2S              1.90D-09  0.00      0.0
H3S+   +HCN   =H2CN+ H2S              1.90D-09  0.00      0.0
HCS+   +O     =HCO+  S                1.00D-09  0.00      0.0
SO+    +NH3   =NH3+  SO               1.30D-09  0.00      0.0
S+     +Fe    =Fe+   S                1.80D-10  0.00      0.0
SH+    +Fe    =Fe+   SH               1.60D-09  0.00      0.0
SO+    +Fe    =Fe+   SO               1.60D-09  0.00      0.0
H2S+   +Fe    =Fe+   H2S              1.80D-09  0.00      0.0
S+     +ELECTR =S    PHOTON           3.90D-12  -.63      0.0
SH+    +ELECTR =S    H                2.00D-07  -.50      0.0
H2S+   +ELECTR =SH   H                1.50D-07  -.50      0.0
H2S+   +ELECTR =S    H      H         1.50D-07  -.50      0.0
H2S+   +ELECTR =H2S  PHOTON           1.10D-10  -.70      0.0
H3S+   +ELECTR =H2S  H                3.00D-07  -.50      0.0
H3S+   +ELECTR =SH   H2               1.00D-07  -.50      0.0
CS+    +ELECTR =C    S                2.00D-07  -.50      0.0
HCS+   +ELECTR =CS   H                7.00D-07  -.50      0.0
SO+    +ELECTR =S    O                2.00D-07  -.50      0.0
HSO+   +ELECTR =SO   H                2.00D-07  -.50      0.0
HSO2+   ELECTR  SO   H      O         1.00E-07  -.50      0.0
HSO2+   ELECTR  SO   OH               1.00E-07  -.50      0.0
HOCS+  +ELECTR =OH   CS               2.00D-07  -.50      0.0
HOCS+  +ELECTR =OCS  H                2.00D-07  -.50      0.0
Si     +SECPHO =Si+  ELECTR           3.00D+03  0.00 140000.0
SiO    +SECPHO =Si   O                3.00D+03  0.00 140000.0
SiO2   +SECPHO =SiO  O                3.00D+03  0.00 140000.0
SiH    +SECPHO =Si   H                1.46D+03  0.00 140000.0
SiH4   +SECPHO =SiH3 H                4.68D+03  0.00 140000.0
SiH4    H       SiH3 H2               2.60D-11  0.00   1400.0
SiH3    H       SiH2 H2               2.00D-11  0.00      0.0
SiH2    H       SiH  H2               2.00D-11  0.00      0.0
SiH     H       Si   H2               2.00D-11  0.00      0.0
SiH2    O2      SiO  H2O              7.50D-12  0.00      0.0
SiH     O2      SiO  OH               1.70D-10  0.00      0.0
SiH2    O       SiO  H      H         5.00D-11  0.50      0.0
SiH     O       SiO  H                4.00D-11  0.50      0.0
Si      O2      SiO  O                2.70D-10  0.00    111.0
Si      OH      SiO  H                1.00D-10  0.00    111.0
SiO     OH      SiO2 H                1.00D-12  -0.70     0.0
Si+     H2      SiH2+ PHOTON          3.00D-18  0.00      0.0
SiH+    H2      SiH3+ PHOTON          3.00D-17  -1.00     0.0
SiH3+   H2      SiH5+ PHOTON          1.00D-18  -0.50     0.0
Si+     H2      SiH+  H               1.50D-10  0.00  14310.0
SiH+    H2      SiH2+ H               1.20D-09  0.00  28250.0
SiH2+   H2      SiH3+ H               7.00D-10  0.00   6335.0
SiH3+   H2      SiH4+ H               2.00D-10  0.00  47390.0
SiH4+   H2      SiH5+ H               1.00D-09  0.00      0.0
```

SiH+	H	Si+	H2		1.90D-09	0.00	0.0
SiH2+	H	SiH+	H2		1.20D-09	0.00	0.0
SiH3+	H	SiH2+	H2		7.00D-10	0.00	0.0
SiH4+	H	SiH3+	H2		2.00D-10	0.00	0.0
SiH5+	H	SiH4+	H2		4.00D-11	0.00	4470.0
SiO+	H2	SiOH+	H		3.20D-10	0.00	0.0
H+	Si	Si+	H		9.90E-10	0.00	0.0
H+	SiH	SiH+	H		1.70E-09	0.00	0.0
H+	SiH	Si+	H2		1.70E-09	0.00	0.0
H+	SiH2	SiH2+	H		1.50E-09	0.00	0.0
H+	SiH2	SiH+	H2		1.50E-09	0.00	0.0
H+	SiH3	SiH3+	H		1.50E-09	0.00	0.0
H+	SiH3	SiH2+	H2		1.50E-09	0.00	0.0
H+	SiH4	SiH4+	H		1.50E-09	0.00	0.0
H+	SiH4	SiH3+	H2		1.50E-09	0.00	0.0
H+	SiO	SiO+	H		3.30E-09	0.00	0.0
He+	Si	Si+	He		3.30E-09	0.00	0.0
He+	SiH	Si+	H	He	1.80E-09	0.00	0.0
He+	SiH2	SiH+	H	He	1.00E-09	0.00	0.0
He+	SiH2	Si+	H2	He	1.00E-09	0.00	0.0
He+	SiH3	SiH2+	H	He	1.00E-09	0.00	0.0
He+	SiH3	SiH+	H2	He	1.00E-09	0.00	0.0
He+	SiH4	SiH3+	H	He	1.00E-09	0.00	0.0
He+	SiH4	SiH2+	H2	He	1.00E-09	0.00	0.0
He+	SiO	Si+	O	He	8.60E-10	0.00	0.0
He+	SiO	O+	Si	He	8.60E-10	0.00	0.0
He+	SiO2	SiO+	O	He	5.00E-10	0.00	0.0
He+	SiO2	Si+	O2	He	5.00E-10	0.00	0.0
C+	Si	Si+	C		2.10E-09	0.00	0.0
C+	SiH2	SiH2+	C		1.00E-09	0.00	0.0
C+	SiH3	SiH3+	C		1.00E-09	0.00	0.0
C+	SiO	Si+	CO		5.40E-10	0.00	0.0
C+	SiO2	SiO+	CO		1.00E-09	-0.60	0.0
S+	Si	Si+	S		1.60E-09	0.00	0.0
S+	SiH	SiH+	S		4.20E-10	0.00	0.0
H3+	Si	SiH+	H2		2.00E-09	0.00	0.0
H3+	SiH	SiH2+	H2		2.00E-09	0.00	0.0
H3+	Si	SiH2+	H		1.70E-09	0.00	0.0
H3+	SiH2	SiH3+	H2		2.00E-09	0.00	0.0
H3+	SiH3	SiH4+	H2		2.00E-09	0.00	0.0
H3+	SiH4	SiH5+	H2		2.00E-09	0.00	0.0
H3+	SiO	SiOH+	H2		2.00E-09	0.00	0.0
H3O+	Si	SiH+	H2O		1.80E-09	0.00	0.0
H3O+	SiH	SiH2+	H2O		9.70E-10	0.00	0.0
H3O+	SiH2	SiH3+	H2O		2.00E-09	0.00	0.0
H3O+	SiO	SiOH+	H2O		2.00E-09	0.00	0.0
HCO+	Si	SiH+	CO		1.60E-09	0.00	0.0
HCO+	SiH	SiH2+	CO		8.70E-10	0.00	0.0
HCO+	SiH2	SiH3+	CO		2.00E-09	0.00	0.0
HCO+	SiH4	SiH5+	CO		1.40E-09	0.00	0.0
HCO+	SiO	SiOH+	CO		7.90E-10	0.00	0.0
Si+	OH	SiO+	H		6.30E-10	0.00	0.0
Si+	H2O	SiOH+	H		2.30E-10	-0.60	0.0
Si+	O2	SiO+	O		1.00E-13	0.00	0.0
SiH+	O	SiO+	H		4.00E-10	0.00	0.0
SiH+	NH3	NH4+	Si		1.00E-09	0.00	0.0
SiH+	H2O	H3O+	Si		8.00E-10	0.00	0.0
SiH2+	O	SiOH+	H		6.30E-10	0.00	0.0
SiH2+	O2	SiOH+	OH		2.40E-11	0.00	0.0
SiH3+	O	SiOH+	H2		2.00E-10	0.00	0.0
SiH4+	H2O	H3O+	SiH3		2.00E-09	0.00	0.0
SiH4+	CO	HCO+	SiH3		1.00E-09	0.00	0.0

```
            SiH5+   H2O     H3O+    SiH4                    2.00E-09  0.00     0.0
            Si+     ELECTR  Si      PHOTON                  4.90E-12 -0.60     0.0
            SiH+    ELECTR  Si      H                       2.00E-07 -0.50     0.0
            SiH2+   ELECTR  Si      H       H               2.00E-07 -0.50     0.0
            SiH2+   ELECTR  SiH     H                       1.50E-07 -0.50     0.0
            SiH2+   ELECTR  Si      H2                      1.50E-07 -0.50     0.0
            SiH3+   ELECTR  SiH2    H                       1.50E-07 -0.50     0.0
            SiH3+   ELECTR  SiH     H2                      1.50E-07 -0.50     0.0
            SiH4+   ELECTR  SiH3    H                       1.50E-07 -0.50     0.0
            SiH4+   ELECTR  SiH2    H2                      1.50E-07 -0.50     0.0
            SiH5+   ELECTR  SiH4    H                       1.50E-07 -0.50     0.0
            SiH5+   ELECTR  SiH3    H2                      1.50E-07 -0.50     0.0
            SiO+    ELECTR  Si      O                       2.00E-07 -0.50     0.0
            SiOH+   ELECTR  SiO     H                       1.50E-07 -0.50     0.0
            SiOH+   ELECTR  Si      OH                      1.50E-07 -0.50     0.0
EROSI Mg**   +He    =GRAIN  He      Mg                      1.221D-2  73.0   41.187
EROSI Fe**   +He    =GRAIN  He      Fe                      1.151D-2  73.0   40.976
EROSI Si**   +He    =GRAIN  He      Si                      1.224D-2  73.0   42.175
EROSI C**    +He    =GRAIN  He      C                       1.224D-2  73.0   42.175
EROSI O**    +He    =GRAIN  He      O                       5.348D-2  73.0   36.030
EROSI Mg**   +C     =GRAIN  C       Mg                      2.935D-2  48.0   36.740
EROSI Fe**   +C     =GRAIN  C       Fe                      2.386D-2  47.0   42.794
EROSI Si**   +C     =GRAIN  C       Si                      2.698D-2  48.0   36.502
EROSI C**    +C     =GRAIN  C       C                       2.698D-2  48.0   36.502
EROSI O**    +C     =GRAIN  C       O                       1.054D-1  48.0   30.812
EROSI Mg**   +N     =GRAIN  N       Mg                      2.935D-2  48.0   36.740
EROSI Fe**   +N     =GRAIN  N       Fe                      2.386D-2  47.0   42.794
EROSI Si**   +N     =GRAIN  N       Si                      2.698D-2  48.0   36.502
EROSI C**    +N     =GRAIN  N       C                       2.698D-2  48.0   36.502
EROSI O**    +N     =GRAIN  N       O                       1.054D-1  48.0   30.812
EROSI Mg**   +O     =GRAIN  O       Mg                      2.884D-2  48.0   30.238
EROSI Fe**   +O     =GRAIN  O       Fe                      4.116D-2  44.0   59.438
EROSI Si**   +O     =GRAIN  O       Si                      3.373D-2  47.0   37.810
EROSI C**    +O     =GRAIN  O       C                       3.373D-2  47.0   37.810
EROSI O**    +O     =GRAIN  O       O                       1.006D-1  47.0   31.588
EROSI Mg**   +H2O   =GRAIN  H2O     Mg                      2.884D-2  48.0   30.238
EROSI Fe**   +H2O   =GRAIN  H2O     Fe                      4.116D-2  44.0   59.438
EROSI Si**   +H2O   =GRAIN  H2O     Si                      3.373D-2  47.0   37.810
EROSI C**    +H2O   =GRAIN  H2O     C                       3.373D-2  47.0   37.810
EROSI O**    +H2O   =GRAIN  H2O     O                       1.006D-1  47.0   31.588
EROSI Mg**   +N2    =GRAIN  N2      Mg                      2.093D-2  48.0   27.730
EROSI Fe**   +N2    =GRAIN  N2      Fe                      4.324D-2  47.0   42.335
EROSI Si**   +N2    =GRAIN  N2      Si                      2.217D-2  47.0   28.013
EROSI C**    +N2    =GRAIN  N2      C                       2.217D-2  47.0   28.013
EROSI O**    +N2    =GRAIN  N2      O                       1.149D-1  46.0   46.018
EROSI Mg**   +CO    =GRAIN  CO      Mg                      2.093D-2  48.0   27.730
EROSI Fe**   +CO    =GRAIN  CO      Fe                      4.324D-2  47.0   42.335
EROSI Si**   +CO    =GRAIN  CO      Si                      2.217D-2  47.0   28.013
EROSI C**    +CO    =GRAIN  CO      C                       2.217D-2  47.0   28.013
EROSI O**    +CO    =GRAIN  CO      O                       1.149D-1  46.0   46.018
EROSI Mg**   +O2    =GRAIN  O2      Mg                      2.093D-2  48.0   27.730
EROSI Fe**   +O2    =GRAIN  O2      Fe                      4.324D-2  47.0   42.335
EROSI Si**   +O2    =GRAIN  O2      Si                      2.217D-2  47.0   28.013
EROSI C**    +O2    =GRAIN  O2      C                       2.217D-2  47.0   28.013
EROSI O**    +O2    =GRAIN  O2      O                       1.149D-1  46.0   46.018
ADSOR C      +GRAIN =CH4*                                   1.00D+00         102.
ADSOR CH     +GRAIN =CH4*                                   1.00D+00         102.
ADSOR CH2    +GRAIN =CH4*                                   1.00D+00         102.
ADSOR CH3    +GRAIN =CH4*                                   1.00D+00         102.
ADSOR CH4    +GRAIN =CH4*                                   1.00D+00         102.
ADSOR O      +GRAIN =H2O*                                   1.00D+00         102.
ADSOR OH     +GRAIN =H2O*                                   1.00D+00         102.
```

```
ADSOR H2O    +GRAIN  =H2O*                            1.00D+00        102.
ADSOR CO     +GRAIN  =CO*                             1.00D+00        102.
ADSOR CO2    +GRAIN  =CO2*                            1.00D+00        102.
ADSOR C2     +GRAIN  =CH4*   CH4*                     1.00D+00        102.
ADSOR C2H    +GRAIN  =CH4*   CH4*                     1.00D+00        102.
ADSOR C2H2   +GRAIN  =CH4*   CH4*                     1.00D+00        102.
ADSOR C3     +GRAIN  =CH4*   CH4*    CH4*             1.00D+00        102.
ADSOR C3H    +GRAIN  =CH4*   CH4*    CH4*             1.00D+00        102.
ADSOR C3H2   +GRAIN  =CH4*   CH4*    CH4*             1.00D+00        102.
ADSOR NH     +GRAIN  =NH3*                            1.00D+00        102.
ADSOR NH2    +GRAIN  =NH3*                            1.00D+00        102.
ADSOR NH3    +GRAIN  =NH3*                            1.00D+00        102.
ADSOR CN     +GRAIN  =CH4*   NH3*                     1.00D+00        102.
ADSOR HCN    +GRAIN  =CH4*   NH3*                     1.00D+00        102.
ADSOR HNC    +GRAIN  =CH4*   NH3*                     1.00D+00        102.
ADSOR NO     +GRAIN  =H2O*   NH3*                     1.00D+00        102.
ADSOR OCS    +GRAIN  =OCS*                            1.00D+00        102.
ADSOR S      +GRAIN  =H2S*                            1.00D+00        102.
ADSOR SH     +GRAIN  =H2S*                            1.00D+00        102.
ADSOR H2S    +GRAIN  =H2S*                            1.00D+00        102.
ADSOR CS     +GRAIN  =CH4*   H2S*                     1.00D+00        102.
ADSOR SO     +GRAIN  =H2O*   H2S*                     1.00D+00        102.
SPUTT CH4*   +H      =CH4    H       GRAIN    4.00D-05  0.00   2000.0
SPUTT CH4*   +H2     =CH4    H2      GRAIN    1.00D-04  0.00   2000.0
SPUTT CH4*   +He     =CH4    He      GRAIN    8.00D-04  0.00   2000.0
SPUTT H2O*   +H      =H2O    H       GRAIN    4.00D-05  0.00   6000.0
SPUTT H2O*   +H2     =H2O    H2      GRAIN    1.00D-04  0.00   6000.0
SPUTT H2O*   +He     =H2O    He      GRAIN    8.00D-04  0.00   6000.0
SPUTT CO*    +H      =CO     H       GRAIN    4.00D-05  0.00   1900.0
SPUTT CO*    +H2     =CO     H2      GRAIN    1.00D-04  0.00   1900.0
SPUTT CO*    +He     =CO     He      GRAIN    8.00D-04  0.00   1900.0
SPUTT CO2*   +H      =CO2    H       GRAIN    4.00D-05  0.00   3100.0
SPUTT CO2*   +H2     =CO2    H2      GRAIN    1.00D-04  0.00   3100.0
SPUTT CO2*   +He     =CO2    He      GRAIN    8.00D-04  0.00   3100.0
SPUTT NH3*   +H      =NH3    H       GRAIN    4.00D-05  0.00   3600.0
SPUTT NH3*   +H2     =NH3    H2      GRAIN    1.00D-04  0.00   3600.0
SPUTT NH3*   +He     =NH3    He      GRAIN    8.00D-04  0.00   3600.0
SPUTT CH3OH* +H      =CH3OH  H       GRAIN    4.00D-05  0.00   6000.0
SPUTT CH3OH* +H2     =CH3OH  H2      GRAIN    1.00D-04  0.00   6000.0
SPUTT CH3OH* +He     =CH3OH  He      GRAIN    8.00D-04  0.00   6000.0
SPUTT H2CO*  +H      =H2CO   H       GRAIN    4.00D-05  0.00   6000.0
SPUTT H2CO*  +H2     =H2CO   H2      GRAIN    1.00D-04  0.00   6000.0
SPUTT H2CO*  +He     =H2CO   He      GRAIN    8.00D-04  0.00   6000.0
SPUTT HCO2H* +H      =HCO2H  H       GRAIN    4.00D-05  0.00   6000.0
SPUTT HCO2H* +H2     =HCO2H  H2      GRAIN    1.00D-04  0.00   6000.0
SPUTT HCO2H* +He     =HCO2H  He      GRAIN    8.00D-04  0.00   6000.0
SPUTT OCS*   +H      =OCS    H       GRAIN    4.00D-05  0.00   6000.0
SPUTT OCS*   +H2     =OCS    H2      GRAIN    1.00D-04  0.00   6000.0
SPUTT OCS*   +He     =OCS    He      GRAIN    8.00D-04  0.00   6000.0
SPUTT H2S*   +H      =H2S    H       GRAIN    4.00D-05  0.00   6000.0
SPUTT H2S*   +H2     =H2S    H2      GRAIN    1.00D-04  0.00   6000.0
SPUTT H2S*   +He     =H2S    He      GRAIN    8.00D-04  0.00   6000.0
DESOR CH4*   +CRP    =CH4    GRAIN            7.00D+01  0.00      0.0
DESOR H2O*   +CRP    =H2O    GRAIN            7.00D+01  0.00      0.0
DESOR CO*    +CRP    =CO     GRAIN            7.00D+01  0.00      0.0
DESOR CO2*   +CRP    =CO2    GRAIN            7.00D+01  0.00      0.0
DESOR NH3*   +CRP    =NH3    GRAIN            7.00D+01  0.00      0.0
DESOR CH3OH* +CRP    =CH3OH  GRAIN            7.00D+01  0.00      0.0
DESOR H2CO*  +CRP    =H2CO   GRAIN            7.00D+01  0.00      0.0
DESOR HCO2H* +CRP    =HCO2H  GRAIN            7.00D+01  0.00      0.0
DESOR OCS*   +CRP    =OCS    GRAIN            7.00D+01  0.00      0.0
DESOR H2S*   +CRP    =H2S    GRAIN            7.00D+01  0.00      0.0
```

Table B.2: FeII, fine-structure and meta-stable lines recorded in the models.

[FeII] λ (μm)	Fine-structure	λ (μm)	Meta-stable	λ (Å)
1.248	C^+	158	C^+	2324.7
1.257	Si^+	34.8	C^+	2323.5
1.271	C	609.8	C^+	2328.1
1.279	C	370.4	C^+	2326.9
1.295	Si	129.7	C^+	2325.4
1.298	Si	68.5	C	9850
1.321	O	63.2	C	9824
1.328	O	145.3	O	6300
1.534	N^+	205.3	O	6363
1.600	N^+	121.8	S^+	6731
1.644			S^+	6716
1.664			N^+	6527
1.677			N^+	6548
1.711			N^+	6583
1.745			N	5200
1.798			N	5197
1.800				
1.810				
17.936				
25.988				
35.777				

Table B.3: 61 H_2 lines already recorded from the grid of shock models sorted by wavelength. All wavelengths are given in μm.

J-band (1.0-1.3 μm)		H-band (1.4-1.8 μm)		K-band (2.0-2.5 μm)		Spitzer (5.0-30.0 μm)	
λ	Trans.	λ	Trans.	λ	Trans.	λ	Trans.
1.064	2-0 S(7)	1.418	3-1 O(3)	1.957	1-0 S(3)	4.953	1-1 S(9)
1.073	2-0 S(6)	1.432	2-0 O(5)	2.003	2-1 S(4)	5.052	0-0 S(8)
1.085	2-0 S(5)	1.467	3-1 O(4)	2.033	1-0 S(3)	5.510	0-0 S(7)
1.100	2-0 S(4)	1.487	2-0 O(6)	2.073	2-1 S(3)	5.809	1-1 S(7)
1.117	2-0 S(3)	1.522	3-1 O(5)	2.121	1-0 S(1)	6.107	0-0 S(6)
1.138	2-0 S(2)	1.687	1-0 S(9)	2.154	2-1 S(2)	6.908	0-0 S(5)
1.162	2-0 S(1)	1.714	1-0 S(8)	2.223	1-0 S(0)	8.023	0-0 S(4)
1.189	2-0 S(0)	1.748	1-0 S(7)	2.247	2-1 S(1)	9.662	0-0 S(3)
1.233	3-1 S(1)	1.788	1-0 S(6)	2.355	2-1 S(0)	12.28	0-0 S(2)
1.238	2-0 Q(1)	1.835	1-0 S(5)	2.386	3-2 S(1)	17.03	0-0 S(1)
1.242	2-0 Q(2)			2.406	1-0 Q(1)	28.21	0-0 S(0)
1.247	2-0 Q(3)			2.413	1-0 Q(2)		
1.254	2-0 Q(4)			2.423	1-0 Q(3)		
1.262	3-1 S(0)			2.437	1-0 Q(4)		
1.263	2-0 Q(5)			2.454	1-0 Q(5)		
1.274	2-0 Q(6)			2.475	1-0 Q(6)		
1.287	2-0 Q(7)			2.499	1-0 Q(7)		
1.293	2-0 O(2)			2.501	3-2 S(0)		
1.314	3-1 Q(1)						
1.318	2-0 Q(9)						
1.318	3-1 Q(2)						
1.335	2-0 O(3)						

Model results for classes A1, A2, B and C and objects 1, 2 and 3

In the following we present the results of the models that fit observations at the 3σ level. The observational constraints for these models are listed in tables 4.1 and 4.2.

Table C.1: *Best fit models at the 3σ limit for class A1, A2, B and C for b=1.0 and b=5.0. If it was not possible to match observations with models at the 3σ limit, we have left a horizontal line (—).*

	o/p_{ini}=0.01	o/p_{ini}=1.0	o/p_{ini}=2.0	o/p_{ini}=3.0
Class A1, b=1.0				
Preshock density / cm^{-3}	5.0×10^4–4.0×10^5	5.0×10^4–5.0×10^6	1.0×10^5–1.1×10^7	1.0×10^6–1.1×10^7
v_s / km s^{-1}	22–41	11–40	15–34	10–17
Postshock density / cm^{-3}	1.6×10^6–6.6×10^6	1.5×10^6–4.0×10^7	2.6×10^6–1.2×10^8	1.3×10^7–8.0×10^7
Width / AU	50–210	5–220	2–130	3–20
o/p_{int}	1.1–2.3	1.3–2.7	2.4–2.8	3.0
ϕ_{10}	0.8–2.2	1.1–2.4	2.4–2.5	2.4–2.7
Class A2, b=1.0				
Preshock density / cm^{-3}	5.0×10^4–2.5×10^5	5.4×10^4–6.0×10^5	5.4×10^4–1.3×10^7	1.0×10^6–1.4×10^7
v_s / km s^{-1}	28–43	21–43	15–43	10–19
Postshock density / cm^{-3}	1.6×10^6–5.3×10^6	1.6×10^6–9.5×10^6	1.6×10^6–1.4×10^8	1.4×10^7–1.0×10^8
Width / AU	60–200	30–200	2–200	2–20
o/p_{int}	1.5–2.4	1.9—2.8	2.4–2.9	3.0
ϕ_{10}	1.4–2.3	1.5–2.4	2.4–2.5	2.4–2.8
Class B, b=1.0				
Preshock density / cm^{-3}	1.0×10^5–6.0×10^5	1.0×10^5–4.6×10^6	1.0×10^5–1.2×10^7	1.0×10^6–1.1×10^7
v_s / km s^{-1}	22–36	12–36	15–36	10–18
Postshock density / cm^{-3}	2.7×10^6–9.9×10^6	2.7×10^6–4.0×10^7	2.7×10^6–1.3×10^8	1.3×10^7–1.5×10^8
Width / AU	30–130	6–130	2–130	2–20
o/p_{int}	1.0–1.9	1.4–2.6	2.4–2.9	3.0
ϕ_{10}	0.9–2.0	1.1–2.4	2.4–2.5	2.4–2.8
Class C, b=1.0				
Preshock density / cm^{-3}	2.5×10^5–4.0×10^5	3.0×10^5–4.5×10^6	2.5×10^5–1.5×10^7	1.0×10^6–1.5×10^7
v_s / km s^{-1}	25–28	12–27	15–28	10–19
Postshock density / cm^{-3}	5.3×10^6–7.5×10^6	6.1×10^6–4.0×10^7	5.3×10^6–1.7×10^8	1.4×10^7–1.1×10^8
Width / AU	40–60	6–60	2–60	2–20
o/p_{int}	1.3–1.5	1.4–2.3	2.4–2.7	3.0
ϕ_{10}	1.3–1.6	1.1–2.2	2.4–2.6	2.4–2.8
Class A1, b=5.0				
Preshock density / cm^{-3}	1.5×10^5–3.5×10^5	2.0×10^5–5.0×10^6	2.0×10^5–5.0×10^6	2.5×10^5–5.0×10^6
v_s / km s^{-1}	36–43	21–40	21–40	21–38
Postshock density / cm^{-3}	9.3×10^5–1.8×10^6	1.1×10^6–1.4×10^7	1.1×10^6–1.4×10^7	1.4×10^6–1.4×10^7
Width / AU	280–540	30–440	30–440	40–370
o/p_{int}	0.6–0.8	1.2–1.8	2.1–2.5	3.0
ϕ_{10}	1.1–1.9	1.0–2.1	1.7–2.2	2.3–2.4
Class A2, b=5.0				
Preshock density / cm^{-3}	—	2.5×10^5–4.0×10^5	2.5×10^5–4.5×10^6	1.5×10^5–4.5×10^6
v_s / km s^{-1}	—	36–40	22–40	21–40
Postshock density / cm^{-3}	—	1.4×10^6–2.0×10^6	1.4×10^6–1.3×10^7	8.6×10^6–1.3×10^7
Width / AU	—	250–360	40–360	40–70
o/p_{int}	—	1.7–1.8	2.2–2.5	3.0
ϕ_{10}	—	1.9–2.1	1.8–2.3	2.2–2.3
Class B, b=5.0				
Preshock density / cm^{-3}	—	5.5×10^5–4.5×10^6	5.5×10^5–5.0×10^6	5.5×10^5–5.0×10^6
v_s / km s^{-1}	—	22–34	22–33	21–33
Postshock density / cm^{-3}	—	2.6×10^6–1.3×10^7	2.6×10^6–1.5×10^7	2.6×10^6–1.4×10^7
Width / AU	—	40–200	40–200	40–200
o/p_{int}	—	1.3–1.5	2.2–2.3	3.0
ϕ_{10}	—	1.1–1.5	1.8–2.1	2.3–2.7
Class C, b=5.0				
Preshock density / cm^{-3}	—	—	—	—
v_s / km s^{-1}	—	—	—	—
Postshock density / cm^{-3}	—	—	—	—
Width / AU	—	—	—	—
o/p_{int}	—	—	—	—
ϕ_{10}	—	—	—	—

Table C.2: *Best fit C-type shock models at the 3σ limit for objects 1, 2 and 3 identified in table 4.2 and Fig. 4.5. If it was not possible to match observations with models at the 3σ limit, we have left a horizontal line (—).*

	$o/p_{ini}=0.01$	$o/p_{ini}=1.0$	$o/p_{ini}=2.0$	$o/p_{ini}=3.0$
Object 1, $b=1.0$				
Preshock density / cm^{-3}	—	6.0×10^5–5.0×10^6	6.0×10^5–1.5×10^6	1.0×10^6–1.35×10^6
v_s / $km\,s^{-1}$	—	16–21	16–20	16–18
Postshock density / cm^{-3}	—	9.5×10^6–6.0×10^7	9.0×10^6–1.8×10^7	1.3×10^7–1.6×10^7
Width / AU	—	5–30	20–30	10–20
o/p_{int}	—	1.6–1.9	2.3–2.4	3.0
ϕ_{10}	—	1.5–1.6	2.0–2.1	2.7–2.8
Object 2, $b=1.0$				
Preshock density / cm^{-3}	5.0×10^4–1.0×10^5	5.0×10^4–1.0×10^5	5.0×10^4–1.0×10^5	5.0×10^4–1.0×10^5
v_s / $km\,s^{-1}$	34–41	34–40	35–40	34–40
Postshock density / cm^{-3}	1.6×10^6–2.6×10^6	1.5×10^6–2.6×10^6	1.5×10^6–2.7×10^6	1.5×10^6–2.6×10^6
Width / AU	130–210	130–220	130–220	130–220
o/p_{int}	1.9–2.3	2.5–2.7	2.8–2.9	3.0
ϕ_{10}	1.8–2.2	2.3–2.4	2.4–2.5	2.5–2.6
Object 3, $b=1.0$				
Preshock density / cm^{-3}	7.0×10^4–1.2×10^5	5.0×10^4–1.0×10^5	5.0×10^4–1.0×10^5	5.0×10^4–1.0×10^5
v_s / $km\,s^{-1}$	33–37	34–38	34–38	34–38
Postshock density / cm^{-3}	2.0×10^6–3.0×10^6	1.4×10^6–2.6×10^6	1.4×10^6–2.6×10^6	1.4×10^6–2.6×10^6
Width / AU	120–170	130–230	130–230	130–230
o/p_{int}	1.9–2.2	2.5–2.7	2.8–2.9	3.0
ϕ_{10}	1.8–2.0	2.3–2.4	2.4–2.5	2.5–2.6
Object 1, $b=5.0$				
Preshock density / cm^{-3}	—	—	—	—
v_s / $km\,s^{-1}$	—	—	—	—
Postshock density / cm^{-3}	—	—	—	—
Width / AU	—	—	—	—
o/p_{int}	—	—	—	—
ϕ_{10}	—	—	—	—
Object 2, $b=5.0$				
Preshock density / cm^{-3}	2.5×10^5–4.5×10^5	2.5×10^5–5.0×10^5	2.0×10^5–5.0×10^5	2.0×10^5–5.0×10^5
v_s / $km\,s^{-1}$	36–40	34–40	34–40	34–40
Postshock density / cm^{-3}	1.4×10^6–2.3×10^6	1.4×10^6–2.4×10^6	1.1×10^6–2.4×10^6	1.1×10^6–2.4×10^6
Width / AU	220–360	210–360	210–440	210–440
o/p_{int}	0.6–0.7	1.5–1.8	2.3–2.5	3.0
ϕ_{10}	1.2–1.7	1.4–2.1	2.1–2.2	2.3–2.7
Object 3, $b=5.0$				
Preshock density / cm^{-3}	2.5×10^5–4.5×10^5	2.5×10^5–5.5×10^5	2.5×10^5–5.0×10^5	2.5×10^5–4.5×10^5
v_s / $km\,s^{-1}$	35–38	33–38	33–38	34–38
Postshock density / cm^{-3}	1.4×10^6–2.2×10^6	1.4×10^6–2.6×10^6	1.4×10^6–2.3×10^6	1.4×10^6–2.2×10^6
Width / AU	230–370	200–370	210–370	240–370
o/p_{int}	0.5–0.7	1.4–1.7	2.3–2.5	3.0
ϕ_{10}	0.8–1.5	1.3–2.0	2.1–2.2	2.4–2.7

D

Publications

Here I provide the first page of publications I, II and III.

Astronomy
&
Astrophysics

Excitation conditions in the Orion molecular cloud obtained from observations of ortho- and para-lines of H₂[★,★★]

L. E. Kristensen[1], T. L. Ravkilde[2], D. Field[2,★★★], J. L. Lemaire[1,★★★], and G. Pineau des Forêts[3,1]

[1] Observatoire de Paris & Université de Cergy-Pontoise, LERMA, UMR 8112 du CNRS, 92195 Meudon Cedex, France
    e-mail: `lars.kristensen@u-cergy.fr`
[2] Department of Physics and Astronomy, University of Aarhus, 8000 Aarhus C, Denmark
[3] Institut d'Astrophysique Spatiale, UMR 8617 du CNRS, Université de Paris Sud, 91405 Orsay, France

ABSTRACT

Aims. We seek to study excitation mechanisms in the inner region of the Orion Molecular Cloud by comparing observations of ortho- and para-lines of H₂ with theoretical models of slow shocks and photodissociation regions.
Methods. K-band observations of H₂ obtained with the Canada-France-Hawaii 3.6 m telescope using the PUEO adaptive optics system are reported. Data were centered on the Becklin-Neugebauer object northwest of the Trapezium stars. Narrow-band filters were used to isolate emission from the $v = 1$–0 S(1) ortho- and $v = 1$–0 S(0) para-lines at a spatial resolution of 0.″45 (∼200 AU). We are able to combine their intensity to obtain the column densities of rovibrationally excited ortho and para H₂ levels of the molecular gas at high spatial resolution.
Results. The resulting line ratios show variations between 2 and the statistical equilibrium value of 6. We find 4 different classes of emission, characterised by the ratio of the $v = 1$–0 S(1) and S(0) line brightness and the absolute line brightness. Shock models are used to estimate the physical properties of pre-shock density and shock velocity for these 4 classes. We find that the pre-shock density is in the range of 10^5–10^7 cm^{-3} and shock velocities lie between 10 and 40 km s^{-1}. Studies of individual objects, using additional constraints of shock velocity and width, allow quite precise physical conditions to be specified in three prominent bow shocks, one with a shock speed of 18 ± 2 km s^{-1} and pre-shock density $1 \pm 0.5 \times 10^6$ cm^{-3} (3σ) and two with shock speeds of ∼36 ± 2 km s^{-1} and pre-shock densities of $7.5 \pm 2.5 \times 10^4$ cm^{-3}.

Key words. ISM: individual objects: OMC1 – ISM: kinematics and dynamics – ISM: molecules – shock waves – ISM: lines and bands

1. Introduction

The aim of this work is to study the nature of shocks in the inner region of the Orion Molecular Cloud (OMC1) using H₂ NIR emission within a radius of ∼30″ of the BN-IRc2 complex. OMC1, $D = 460$ pc (Bally et al. 2000), is the closest active massive star forming region. Among the wealth of information available reference is only included here to those data and theoretical models which have a direct bearing on H₂ emission in shocks. For general reviews of the Orion region, the reader is referred to O'Dell (2001) and Ferland (2001).

OMC1 and its immediate surroundings form a nursery of OB stars, both exposed, as in the Trapezium, and buried deep within dusty gas (Menten & Reid 1995; Gezari et al. 1998; Beuther et al. 2004). Spatially associated with these massive stars is a cluster of young low mass stars formed in the last 10^6 years (Hillenbrand 1997). It has long been suggested that outflows from young OB stars may trigger star formation

(Elmegreen & Lada 1977). This may serve to explain the general observation that the great majority of low mass stars form in clusters, many with OB associations. How this trigger may operate remains unclear. The present work seeks in a modest way to shed more light on this issue by characterizing shocks associated with OB stars in more detail than has previously been achieved, using both observation and theory.

The gas in OMC1 displays very many flows, varying in velocity between a few km s^{-1} (Chrysostomou et al. 1997; Gustafsson et al. 2003; Gustafsson 2006; Nissen et al. 2007) to several hundred km s^{-1}, the latter represented by the well-known fingers and bullets (eg. Allen & Burton 1993). The origin of the flows is threefold arising from outflows from OB stars, which permeate the entire region of OMC1 (Allen & Burton 1993; Stone et al. 1995; McCaughrean & Mac Low 1997; Doi et al. 2002; O'Dell & Doi 2003), local flows arising from outflows from low mass protostellar objects buried within OMC1 (Gustafsson et al. 2003; Nissen et al. 2007), and supersonic turbulence (Gustafsson et al. 2006a,b). Flows in the inner zone generate slow shocks, graphically illustrated in Gustafsson et al. (2003) & Nissen et al. (2007), with a detailed morphology given by K-band IR images of the $v = 1$–0 S(1) line at 2.121 μm (McCaughrean & Mac Low 1997; Schild et al. 1997; Chen et al. 1998; Stolovy et al. 1998; Schultz et al. 1999; Vannier et al. 2001; Gustafsson et al. 2003; Kristensen et al. 2003; Lacombe et al. 2004). Lacombe et al. (2004), using the NACO adaptive

---

★ Based on observations obtained at the Canada-France-Hawaii Telescope (CFHT) which is operated by the National Research Council of Canada, the Institut National des Sciences de l'Univers of the Centre National de la Recherche Scientifique of France, and the University of Hawaii.

★★ Appendix A is only available in electronic form at `http://www.aanda.org`

★★★ Visiting astronomer at the Canada-France-Hawaii Telescope, Mauna Kea, Hawaii.

Observational 2D model of H_2 emission from a bow shock in the Orion Molecular Cloud*

L. E. Kristensen[1], T. L. Ravkilde[2], G. Pineau des Forêts[1,3], S. Cabrit[1], D. Field[2], M. Gustafsson[4], S. Diana[1], and J. L. Lemaire[1]

[1] Observatoire de Paris & Université de Cergy-Pontoise, LERMA, UMR 8112 du CNRS, 92195 Meudon Cedex, France
   e-mail: `lars.kristensen@u-cergy.fr`
[2] Department of Physics and Astronomy, University of Aarhus, 8000 Aarhus C, Denmark
[3] Institut d'Astrophysique Spatiale, UMR 8617 du CNRS, Université de Paris Sud, 91405 Orsay, France
[4] Max Planck Institut für Astronomie, D-69117 Heidelberg, Germany

Abstract

Aims. We present a new method for reproducing high spatial resolution observations of bow shocks by using 1D plane parallel shock models. As an example we analyse one bow shock located in the Orion Molecular Cloud (OMC1).
Methods. We use high spatial resolution near-infrared observations of H_2 rovibrational emission to constrain shock models. These observations have been made at the ESO-VLT using a combination of the NACO adaptive optics system and infrared camera array and the Fabry-Perot interferometer. Three rovibrational H_2 lines have been observed: v=1-0 S(1) at 2.12μm, v=1-0 S(0) at 2.23μm and v=2-1 S(1) at 2.25μm. The spatial resolution is 0''.15~70 AU. We analyse a single bow shock located in our field, featuring a very well defined morphology and high brightness.
Results. One dimensional shock models are combined to estimate the physical properties of pre-shock density, shock velocity and transverse magnetic field strength along the bow shock. We find that the pre-shock density is constant at ~5×10^5 cm^{-3} and shock velocities lie between ~35 km s^{-1} in the wings of the shock and ~50 km s^{-1} at the apex. We also find that the transverse magnetic field is stronger at the apex and weaker further down the wings varying between ~2 and 4 mGauss. Predictions of shock velocity and magnetic field strength agree with previous independent observations.

Key words. ISM: individual objects: OMC1 – ISM: kinematics and dynamics – ISM: molecules – Shock waves – ISM: lines and bands

1. Introduction

With this work we present a new method for analysing bow shocks caused by outflows. These shocks may originate from a multitude of objects ranging from young stellar objects (YSOs), planetary nebulae, supernova explosions, neutron stars to active galactic nuclei. In this paper we will limit our focus to jets and outflows from YSOs.

Although jets and outflows from YSOs are not a natural consequence of any unified theoretical model of star formation, observations show that they are an integral part of star formation. Jets and outflows play an important role both in the formation of individual stars, but also in inducing new generations of stars (e.g. Elmegreen & Lada 1977; Vannier et al. 2001). Therefore by observing and modelling shocks it is possible to gain significant insight into the physical conditions found in

star forming regions (see e.g. Smith et al. 2003; Giannini et al. 2006; Neufeld et al. 2006; Kristensen et al. 2007, for recent results) providing new constraints for models of clustered star formation.

The Orion Molecular Cloud (OMC1) is the closest site of active massive star formation located at a distance of ~440pc (Hirota et al. 2007). Here more than 1000 stars have formed around the Trapezium OB association within the last 1 Myr (Hillenbrand et al. 1998). On the surface of OMC1 an outflow was launched approximately centered on the Becklin-Neugebauer object (BN, a B3 star; Gezari et al. 1998). This resulted in the launch of more than 50 so-called "fingers". At the apex of each finger a fast moving "bullet" is found (Axon & Taylor 1984; Doi et al. 2002), a dissociative shock which is observed in [FeII] emission with H_2 emission trailing behind in prominent bow shocks (Allen & Burton 1993). The fingers are mostly found to the North-West of BN and shock velocities are measured from proper motions to be several hundred km s^{-1}

Astronomy
&
Astrophysics

VLT/NACO near-infrared imaging and spectroscopy of N159-5 in the LMC HII complex N159[*],[**]

G. Testor[1], J. L. Lemaire[2], L. E. Kristensen[2], D. Field[3], and S. Diana[2]

[1] LUTH, UMR 8102 du CNRS, Observatoire de Paris, 92195 Meudon, France
    e-mail: `gerard.testor@obspm.fr`
[2] LERMA, UMR 8112 du CNRS, Observatoire de Paris, 92195 Meudon, and Université de Cergy-Pontoise, 95031 Cergy Cedex, France
    e-mail: `jean-louis.lemaire@obspm.fr`
[3] Department of Physics and Astronomy, Århus University, 8000 Århus C, Denmark
    e-mail: `dfield@phys.au.dk`

ABSTRACT

We present high-resolution near-infrared imaging of the compact HII region N159-5 and its immediate environment in the giant-star forming region N159 in the LMC. N159-5 was observed at high spatial resolution ∼$0\rlap{.}''11$–$0\rlap{.}''25$ in the K-band using the ESO Very Large Telescope UT4 (VLT), equipped with the NAOS adaptive optics system. Our data reveal that N159-5 has a complex morphology formed mainly by two wings and probably a single central bright star, embedded in diffuse emission of ∼$4\rlap{.}''5$ diameter. A remarkable embedded tight cluster of approximatively the same size, containing at least 38 faint stars coinciding with N159-5, is also detected. Such clusters can be found in galactic HII regions like the star-forming regions SH2 269 or M42. At the location of the radio peak, especially in the bright western wing, this cluster is rich in stars. Spectroscopic observations reveal that the diffuse region is constituted mainly of dust continuum and that the bright star #2-55 could be of type O8 V. A comparison with the radio observation flux of N159-5 published in the literature seems to show that the bright star #2-55 is not the only ionization source of N159-5. Towards N159-5 molecular H_2 emission is detected. A model of the region is proposed.

Key words. galaxies: Magellanic Clouds – ISM: individual objects: N159-5 – stars: formation

1. Introduction

The Large Magellanic Cloud (LMC) is rich in HII regions and young OB associations. Because of its known and relatively small distance (50 kpc) (Storm et al. 2004) and face-on position relatively free from foreground extinction, it is well suited for the study of both individual stars and very compact objects, as well as global structures. The LMC is also an ideal laboratory for investigating the formation and evolution of massive stars in a low-metallicity environment.

Massive stars play a major role in the dynamical evolution of galaxies. They are responsible for the ionization of the interstellar medium while the associated stellar winds and supernovae are dominant sources of mechanical energy. They are also a main driver of chemical evolution in the universe at the end of their lives. Some understanding of the early stages of massive star formation in our galaxy is emerging. However, this is not the case in external galaxies of low-metallicity environment such as the Magellanic Clouds (MCs). There are two main reasons for this dearth of information: one is the lack of the high–spatial-resolution data at a distance of 50–65 kpc, necessary to disentangle the individual massive stars from their surrounding environment; and the other is the strong reddening, typical of young, massive-star regions.

Some progress has been made following the discovery of compact HII regions in the MCs, now generically named HEBs (High Excitation Blobs) (Heydari-Malayeri & Testor 1982). HEBs are characterized by small size, high density, extinction, and excitation. The line ratio [OIII]$\lambda\lambda$4959+5007/Hβ used as excitation parameter ranges typically between ∼7–10. They are probably excited by more than one newborn massive star arriving on the zero-age main sequence (Walborn & Parker 1992). With a diameter of 0.5–2 pc they are at the frontier of compact HII (CHII) and HII regions. HEBs represent the early evolutionary stages of recent star formation (Churchwell 1992) and are important in the context of massive-star formation under low metallicity.

So far, only eight HEBs have been found in the MCs and they are listed in Testor (2001). Optical HST observations of some of them have revealed tight star clusters and complex structures (0.03 pc) and are listed in Meynadier et al. (2004). Nevertheless, due to the reddening, little is known about their exciting sources. In the present paper we focus on the HEB N159-5 (Heydari-Malayeri & Testor 1982), a compact HII region of size ∼6″ (1.5 pc) in the HII region N159 (Henize 1956) coinciding with the IRAS source 05405-6946. This compact HII region features high excitation [OIII](5007+4959)/Hβ ∼ 8 and is affected by the highest extinction of A_V ∼ 5 mag (Heydari-Malayeri & Testor 1985) and 4.5–6.7 mag (Israel & Korneef 1991) among the HEBs. South of 30 Doradus at a distance of ∼600 pc there is a chain of Henize giant HII regions, namely N158, N160 and N159. It is believed that the star formation

---

List of Figures

List of Tables

Bibliography

Abergel, A., Verstraete, L., Joblin, C., Laureijs, R., & Miville-Deschênes, M.-A. 2005, Space Science Reviews, 119, 247

Alfven, H. 1950, Cosmical Electrodynamics (Oxford: Clarendon Press)

Allen, D. A. & Burton, M. G. 1993, *Nature*, 363, 54

Amiaud, L., Dulieu, F., Fillion, J.-H., Momeni, A., & Lemaire, J.-L. 2007, in press, Journal of Chemical Physics

Anders, E. & Grevesse, N. 1989, *Geochim. Cosmochim. Acta*, 53, 197

André, P., Ward-Thompson, D., & Barsony, M. 2000, Protostars and Planets IV, 59

Arce, H. G. & Goodman, A. A. 2002, *ApJ*, 575, 928

Arce, H. G. & Sargent, A. I. 2006, *ApJ*, 646, 1070

Arce, H. G., Shepherd, D., Gueth, F., et al. 2007, Protostars and Planets V, 245

Axon, D. J. & Taylor, K. 1984, *MNRAS*, 207, 241

Ballesteros-Paredes, J., Klessen, R. S., Mac Low, M.-M., & Vazquez-Semadeni, E. 2007, Protostars and Planets V, 63

Bally, J., Cunningham, N., Moeckel, N., & Smith, N. 2005, in IAU Symposium, 12–22

Bally, J., O'Dell, C. R., & McCaughrean, M. J. 2000, *AJ*, 119, 2919

Bally, J., Reipurth, B., & Davis, C. J. 2007, Protostars and Planets V, 215

Bally, J. & Zinnecker, H. 2005, *AJ*, 129, 2281

Banerjee, R. & Pudritz, R. E. 2006, *ApJ*, 641, 949

Bautista, M. A. & Pradhan, A. K. 1998, *ApJ*, 492, 650

Becklin, E. E. & Neugebauer, G. 1967, *ApJ*, 147, 799

Beckwith, S., Persson, S. E., Neugebauer, G., & Becklin, E. E. 1978, *ApJ*, 223, 464

Bertout, C., Robichon, N., & Arenou, F. 1999, *A&A*, 352, 574

Beuther, H., Churchwell, E. B., McKee, C. F., & Tan, J. C. 2007, Protostars and Planets V, 165

Beuther, H., Zhang, Q., Greenhill, L. J., et al. 2004, *ApJ*, 616, L31

Beuther, H., Zhang, Q., Greenhill, L. J., et al. 2005, *ApJ*, 632, 355

Bik, A., Kaper, L., Hanson, M. M., & Smits, M. 2005, *A&A*, 440, 121

Black, J. H. & Dalgarno, A. 1976, *ApJ*, 203, 132

Black, J. H. & van Dishoeck, E. F. 1987, *ApJ*, 322, 412

Blitz, L., Fukui, Y., Kawamura, A., et al. 2007, Protostars and Planets V, 81

Bok, B. J. & Reilly, E. F. 1947, *ApJ*, 105, 255

Boulanger, F. 2007, H2EX: A space mission dedicated to the observation of H_2, `http://www.ias.u-psud.fr/website/modules/content\_mic/index.php?id=55`

Bourke, T. L. 2001, *ApJ*, 554, L91

Bourke, T. L., Garay, G., Lehtinen, K. K., et al. 1997, *ApJ*, 476, 781

Bourke, T. L., Hyland, A. R., & Robinson, G. 1995a, *MNRAS*, 276, 1052

Bourke, T. L., Hyland, A. R., Robinson, G., James, S. D., & Wright, C. M. 1995b, *MNRAS*, 276, 1067

Brand, P. W. J. L., Moorhouse, A., Burton, M. G., et al. 1988, *ApJ*, 334, L103

Brand, P. W. J. L., Toner, M. P., Geballe, T. R., et al. 1989a, *MNRAS*, 236, 929

Brand, P. W. J. L., Toner, M. P., Geballe, T. R., et al. 1989b, *MNRAS*, 236, 929

Briceño, C., Preibisch, T., Sherry, W. H., et al. 2007, Protostars and Planets V, 345

Brown, P. N., Byrne, G. D., & Hindmarsh, A. C. 1989, "SIAM Journal on Scientific and Statistical Computing", 10, 1038

Burton, M. G. 1997, in Astronomical Society of the Pacific Conference Series, Vol. 121, IAU Colloq. 163: Accretion Phenomena and Related Outflows, ed. D. T. Wickramasinghe, G. V. Bicknell, & L. Ferrario, 571–+

Chen, H., Bally, J., O'Dell, C. R., et al. 1998, *ApJ*, 492, L173

Chernoff, D. F. 1987, *ApJ*, 312, 143

Chernoff, D. F., McKee, C. F., & Hollenbach, D. J. 1982, *ApJ*, 259, L97

Chièze, J.-P., Pineau des Forêts, G., & Flower, D. R. 1998, *MNRAS*, 295, 672

Chrysostomou, A., Brand, P. W. J. L., Burton, M. G., & Moorhouse, A. 1993, *MNRAS*, 265, 329

Chrysostomou, A., Burton, M. G., Axon, D. J., et al. 1997, *MNRAS*, 289, 605

Chrysostomou, A., Hough, J. H., Burton, M. G., & Tamura, M. 1994, *MNRAS*, 268, 325

Churchwell, E. & Hollis, J. M. 1983, *ApJ*, 272, 591

Churchwell, E., Wood, D. O. S., Felli, M., & Massi, M. 1987, *ApJ*, 321, 516

Clénet, Y., Le Coarer, E., Joncas, G., et al. 2002, *PASP*, 114, 563

Cole, A. A. 1998, *ApJ*, 500, L137+

Corporon, P. & Reipurth, B. 1997, in IAU Symposium, Vol. 182, Herbig-Haro Flows and the Birth of Stars, ed. B. Reipurth & C. Bertout, 85P–+

Creighan, S. C., Perry, J. S. A., & Price, S. D. 2006, Journal of Chemical Physics, 124, 114701

Crutcher, R. M. 2007, in Engineering and Science, Vol. 23, EAS Publications Series, 37–54

Crutcher, R. M. & Troland, T. H. 2007, in IAU Symposium, Vol. 237, IAU Symposium, ed. B. G. Elmegreen & J. Palous, 141–147

Crutcher, R. M., Troland, T. H., Lazareff, B., Paubert, G., & Kazès, I. 1999, *ApJ*, 514, L121

Cunningham, N. J. 2006, PhD thesis, University of Colorado

de Hoffmann, F. & Teller, E. 1950, Physical Review, 80, 692

Doi, T., O'Dell, C. R., & Hartigan, P. 2002, *AJ*, 124, 445

Dougados, C., Cabrit, S., Lavalley, C., & Ménard, F. 2000, *A&A*, 357, L61

Dougados, C., Lena, P., Ridgway, S. T., Christou, J. C., & Probst, R. G. 1993,
    ApJ, 406, 112

Draine, B. T. 1978, *ApJS*, 36, 595

Draine, B. T. 1980, *ApJ*, 241, 1021

Draine, B. T. & McKee, C. F. 1993, *ARA&A*, 31, 373

Draine, B. T. & Roberge, W. G. 1982, *ApJ*, 259, L91

Draine, B. T., Roberge, W. G., & Dalgarno, A. 1983, *ApJ*, 264, 485

Eiroa, C. & Casali, M. M. 1995, *A&A*, 303, 87

Elitzur, M. & de Jong, T. 1978, *A&A*, 67, 323

Elmegreen, B. G. & Lada, C. J. 1977, *ApJ*, 214, 725

Evans, N. J. 1999, *ARA&A*, 37, 311

Ferland, G. J. 2001, *PASP*, 113, 41

Field, D., Jones, N. C., & Ziesel, J.-P. 2004, *Phys. Rev. A*, 69, 052716

Field, D., Lunt, S. L., Hoffmann, S. V., Ziesel, J. P., & Gulley, R. J. 1999, in
    The Physics and Chemistry of the Interstellar Medium, Proceedings of the
    3rd Cologne-Zermatt Symposium, held in Zermatt, September 22-25, 1998,
    Eds.: V. Ossenkopf, J. Stutzki, and G. Winnewisser, GCA-Verlag Herdecke,
    ISBN 3-928973-95-9, ed. V. Ossenkopf, J. Stutzki, & G. Winnewisser, 367

Flower, D. R. 1997, *MNRAS*, 288, 627

Flower, D. R., Le Bourlot, J., Pineau des Forêts, G., & Cabrit, S. 2003, *Ap&SS*,
    287, 183

Flower, D. R., Le Bourlot, J., Pineau des Forêts, G., & Roueff, E. 2000, *MNRAS*,
    314, 753

Flower, D. R. & Pineau des Forêts, G. 2003, *MNRAS*, 343, 390

Flower, D. R., Pineau des Forêts, G., & Hartquist, T. W. 1985, *MNRAS*, 216, 775

Flower, D. R., Pineau des Forêts, G., & Walmsley, C. M. 2006, *A&A*, 449, 621

Flower, D. R. & Roueff, E. 1998, Journal of Physics B, 31, 2935

Fragile, P. C., Anninos, P., Gustafson, K., & Murray, S. D. 2005, *ApJ*, 619, 327

France, K. & McCandliss, S. R. 2005, *ApJ*, 629, L97

Fukui, Y. 2007, in IAU Symposium, Vol. 237, IAU Symposium, ed. B. G. Elmegreen & J. Palous, 31–39

Garmire, G., Feigelson, E. D., Broos, P., et al. 2000, *AJ*, 120, 1426

Gatley, I., Becklin, E. E., Hyland, A. R., & Jones, T. J. 1981, *MNRAS*, 197, 17P

Gautier, T. N., Fink, U., Larson, H. P., & Treffers, R. R. 1976, *ApJ*, 207, L129

Genzel, R., Reid, M. J., Moran, J. M., & Downes, D. 1981, *ApJ*, 244, 884

Genzel, R. & Stutzki, J. 1989, *ARA&A*, 27, 41

Gezari, D. Y., Backman, D. E., & Werner, M. W. 1998, *ApJ*, 509, 283

Giannini, T., McCoey, C., Caratti o Garatti, A., et al. 2004, *A&A*, 419, 999

Gibb, E. L., Whittet, D. C. B., Schutte, W. A., et al. 2000, *ApJ*, 536, 347

Gómez, L., Rodríguez, L. F., Loinard, L., et al. 2005, *ApJ*, 635, 1166

Gonatas, D. P., Engargiola, G. A., Hildebrand, R. H., et al. 1990, *ApJ*, 357, 132

Greenhill, L. J., Gezari, D. Y., Danchi, W. C., et al. 2004a, *ApJ*, 605, L57

Greenhill, L. J., Reid, M. J., Chandler, C. J., Diamond, P. J., & Elitzur, M. 2004b, in IAU Symposium, 155

Greenhill, L. J., Reid, M. J., Chandler, C. J., Diamond, P. J., & Elitzur, M. 2004c, in IAU Symposium, ed. M. Burton, R. Jayawardhana, & T. Bourke, 155

Gustafsson, M. 2006, PhD thesis, University of Aarhus, Denmark

Gustafsson, M., Brandenburg, A., Lemaire, J. L., & Field, D. 2006a, *A&A*, 454, 815

Gustafsson, M., Kristensen, L. E., Clénet, Y., et al. 2003, *A&A*, 411, 437

Gustafsson, M., Lemaire, J. L., & Field, D. 2006b, *A&A*, 456, 171

Habart, E., Boulanger, F., Verstraete, L., et al. 2003, *A&A*, 397, 623

Habart, E., Walmsley, M., Verstraete, L., et al. 2005, Space Science Reviews, 119, 71

Habing, H. J. 1968, *Bull. Astron. Inst. Netherlands*, 19, 421

Hanson, M. M., Luhman, K. L., & Rieke, G. H. 2002, *ApJS*, 138, 35

Harrison, A., Puxley, P., Russell, A., & Brand, P. 1998, *MNRAS*, 297, 624

Hartigan, P. 2003, *Ap&SS*, 287, 111

Hayes, D. S. 1985, in IAU Symp. 111: Calibration of Fundamental Stellar Quantities, ed. D. S. Hayes, L. E. Pasinetti, & A. G. D. Philip, 225–249

Henize, K. G. 1956, *ApJS*, 2, 315

Henning, T. & Launhardt, R. 1998, *A&A*, 338, 223

Heydari-Malayeri, M., Rosa, M. R., Charmandaris, V., Deharveng, L., & Zinnecker, H. 1999, *A&A*, 352, 665

Heydari-Malayeri, M., Testor, G., Baudry, A., Lafon, G., & de La Noe, J. 1982, *A&A*, 113, 118

Hillenbrand, L. A. 1997, *AJ*, 113, 1733

Hirota, T., Bushimata, T., Choi, Y. K., et al. 2007, ArXiv e-prints, 705

Hoare, M. G., Kurtz, S. E., Lizano, S., Keto, E., & Hofner, P. 2007, Protostars and Planets V, 181

Hoban, S., Reuter, D. C., Mumma, M. J., & Storrs, A. D. 1991, *ApJ*, 370, 228

Hollenbach, D. 1997, in IAU Symp. 182: Herbig-Haro Flows and the Birth of Stars, 181–198

Hollenbach, D. & McKee, C. F. 1979, *ApJS*, 41, 555

Hollenbach, D. & McKee, C. F. 1989, *ApJ*, 342, 306

Hollenbach, D. J., Chernoff, D. F., & McKee, C. F. 1989, in Infrared Spectroscopy in Astronomy, 245–258

Hollenbach, D. J. & Shull, J. M. 1977, *ApJ*, 216, 419

Hollenbach, D. J. & Tielens, A. G. G. M. 1997, *ARA&A*, 35, 179

Hollenbach, D. J. & Tielens, A. G. G. M. 1999, Reviews of Modern Physics, 71, 173

Hora, J. L. & Latter, W. B. 1996, *ApJ*, 461, 288

Hornekær, L., Baurichter, A., Petrunin, V. V., Field, D., & Luntz, A. C. 2003, Science, 302, 1943

Hornekær, L., Rauls, E., Xu, W., et al. 2006, Physical Review Letters, 97, 186102

Hough, J. H., Axon, D. J., Burton, M. G., et al. 1986, *MNRAS*, 222, 629

Howell, S. B. 2000, Handbook of CCD Astronomy (Cambridge University Press)

Indebetouw, R., Johnson, K. E., & Conti, P. 2004, *AJ*, 128, 2206

Israel, F. P. & Koorneef, J. 1991, *A&A*, 250, 475

Israel, F. P., Maloney, P. R., Geis, N., et al. 1996, *ApJ*, 465, 738

Jeans, J. H. 1928, Astronomy and Cosmogony (Cambridge, U.K.: Cambridge Univ. Press)

Jiang, Z., Yao, Y., Yang, J., et al. 2003, *ApJ*, 596, 1064

Jijina, J., Myers, P. C., & Adams, F. C. 1999, *ApJS*, 125, 161

Johansson, L. E. B., Greve, A., Booth, R. S., et al. 1998, *A&A*, 331, 857

Johnston, K. J., Migenes, V., & Norris, R. P. 1989, *ApJ*, 341, 847

Jones, T. J., Woodward, C. E., Boyer, M. L., Gehrz, R. D., & Polomski, E. 2005, *ApJ*, 620, 731

Kaifu, N., Usuda, T., Hayashi, S. S., et al. 2000, *PASJ*, 52, 1

Kaufman, M. J. & Neufeld, D. A. 1996a, *ApJ*, 456, 611

Kaufman, M. J. & Neufeld, D. A. 1996b, *ApJ*, 456, 250

Kaufman, M. J., Wolfire, M. G., Hollenbach, D. J., & Luhman, M. L. 1999, *ApJ*, 527, 795

Kitchin, C. R. 1984, Astrophysical Techniques (Bristol: Hilger)

Kleinmann, D. E. & Low, F. J. 1967, *ApJ*, 149, L1

Krabbe, A., Storey, J., Rotaciuc, V., Drapatz, S., & Genzel, R. 1991, in IAU Symposium, Vol. 148, The Magellanic Clouds, ed. R. Haynes & D. Milne, 205

Kristensen, L. E., Gustafsson, M., Field, D., et al. 2003, *A&A*, 412, 727

Kristensen, L. E., Ravkilde, T. L., Field, D., Lemaire, J. L., & Pineau Des Forêts, G. 2007a, *A&A*, 469, 561

Kristensen, L. E., Ravkilde, T. L., Pineau des Forêts, G., et al. 2007b, accepted for publication in *A&A*

Kwan, J. 1977, *ApJ*, 216, 713

Kwan, J. & Scoville, N. 1976, *ApJ*, 210, L39

Lacombe, F., Gendron, E., Rouan, D., et al. 2004, *A&A*, 417, L5

Latter, W. B., Dayal, A., Bieging, J. H., et al. 2000, *ApJ*, 539, 783

Le Bourlot, J., Pineau des Forêts, G., & Flower, D. R. 1999, *MNRAS*, 305, 802

Le Bourlot, J., Pineau des Forêts, G., Flower, D. R., & Cabrit, S. 2002, *MNRAS*, 332, 985

Le Petit, F., Nehmé, C., Le Bourlot, J., & Roueff, E. 2006, *ApJS*, 164, 506

Lee, C.-F., Stone, J. M., Ostriker, E. C., & Mundy, L. G. 2001, *ApJ*, 557, 429

Lee, J.-K. & Burton, M. G. 2000, *MNRAS*, 315, 11

Lemaire, J. L., Field, D., Gerin, M., et al. 1996, *A&A*, 308, 895

Lemaire, J.-L., Testor, G., Field, D., & Rouan, D. 2007, in Visions for Infrared Astronomy, ed. V. Coudé du Foresto, D. Rouan, & G. Rousset, 31–36

Lenzen, R., Hartung, M., Brandner, W., et al. 2003, in Presented at the Society of Photo-Optical Instrumentation Engineers (SPIE) Conference, Vol. 4841, Instrument Design and Performance for Optical/Infrared Ground-based Telescopes. Edited by Iye, Masanori; Moorwood, Alan F. M. Proceedings of the SPIE, Volume 4841, pp. 944-952 (2003)., ed. M. Iye & A. F. M. Moorwood, 944–952

Lesaffre, P., Chièze, J.-P., Cabrit, S., & Pineau des Forêts, G. 2004, *A&A*, 427, 147

Lim, A. J., Raga, A. C., Rawlings, J. M. C., & Williams, D. A. 2002, *MNRAS*, 335, 817

Liszt, H. S., Wilson, R. W., Penzias, A. A., et al. 1974, *ApJ*, 190, 557

Livingston, W. & Wallace, L. 1991, An Atlas of the Solar Spectrum in the Infrared from 1850 to 9000 cm^{-1}, N. S. O. Technical Report No. 91-001, Tech. rep., National Optical Astronomy Observatories

London, R., McCray, R., & Chu, S.-I. 1977, *ApJ*, 217, 442

Mac Low, M.-M. & Klessen, R. S. 2004, Reviews of Modern Physics, 76, 125

Maddalena, R. J., Moscowitz, J., Thaddeus, P., & Morris, M. 1986, *ApJ*, 303, 375

Manicò, G., Ragunì, G., Pirronello, V., Roser, J. E., & Vidali, G. 2001, *ApJ*, 548, L253

Martin, P. G. & Mandy, M. E. 1995, *ApJ*, 455, L89+

Martín-Hernández, N. L., Vermeij, R., & van der Hulst, J. M. 2005, *A&A*, 433, 205

Masson, C. R., Lo, K. Y., Phillips, T. G., et al. 1987, *ApJ*, 319, 446

Mathis, J. S. 1990, *ARA&A*, 28, 37

Mathis, J. S., Rumpl, W., & Nordsieck, K. H. 1977, *ApJ*, 217, 425

May, P. W., Pineau des Forêts, G., Flower, D. R., et al. 2000, *MNRAS*, 318, 809

McCaughrean, M. J. & Mac Low, M. 1997, *AJ*, 113, 391

McCaughrean, M. J. & Stauffer, J. R. 1994, *AJ*, 108, 1382

McKee, C. F. & Hollenbach, D. J. 1980, *ARA&A*, 18, 219

Menten, K. M. & Reid, M. J. 1995, *ApJ*, 445, L157

Meynadier, F., Heydari-Malayeri, M., Deharveng, L., et al. 2004, *A&A*, 422, 129

Moorhouse, A., Brand, P. W. J. L., Geballe, T. R., & Burton, M. G. 1990, *MNRAS*, 242, 88

Moorwood, A., Cuby, J.-G., Biereichel, P., et al. 1998, The Messenger, 94, 7

Nadeau, D. & Geballe, T. R. 1979, *ApJ*, 230, L169

Nadeau, D., Neugebauer, G., & Geballe, T. R. 1982, *ApJ*, 253, 154

Nakajima, Y., Kato, D., Nagata, T., et al. 2005, *AJ*, 129, 776

Neufeld, D. A., Hollenbach, D. J., Kaufman, M. J., et al. 2007, *ApJ*, 664, 890

Neufeld, D. A., Melnick, G. J., & Harwit, M. 1998, *ApJ*, 506, L75

Nissen, H. D., Gustafsson, M., Lemaire, J. L., et al. 2007, *A&A*, 466, 949

Norris, R. P. 1984, *MNRAS*, 207, 127

O'Dell, C. R. 2001, *ARA&A*, 39, 99

O'Dell, C. R., Wen, Z., & Hu, X. 1993, *ApJ*, 410, 696

Osterbrock, D. E. 1961, *ApJ*, 134, 270

Ostriker, E. C., Lee, C.-F., Stone, J. M., & Mundy, L. G. 2001, *ApJ*, 557, 443

Padoan, P. & Nordlund, Å. 1999, *ApJ*, 526, 279

Parise, B., Belloche, A., Leurini, S., et al. 2006, *A&A*, 454, L79

Penston, M. V. 1973, *ApJ*, 183, 505

Perets, H. B., Biham, O., Manicó, G., et al. 2005, *ApJ*, 627, 850

Perry, J. S. A. & Price, S. D. 2003, *Ap&SS*, 285, 769

Pickles, A. J. 1998, *PASP*, 110, 863

Pijpers, F. P. 1999, *MNRAS*, 307, 659

Pirronello, V., Biham, O., Liu, C., Shen, L., & Vidali, G. 1997a, *ApJ*, 483, L131+

Pirronello, V., Liu, C., Shen, L., & Vidali, G. 1997b, *ApJ*, 475, L69+

Pudritz, R. E., Ouyed, R., Fendt, C., & Brandenburg, A. 2007, Protostars and Planets V, 277

Quinet, P., Le Dourneuf, M., & Zeippen, C. J. 1996, *A&AS*, 120, 361

Raga, A. & Cabrit, S. 1993, *A&A*, 278, 267

Raga, A. C., de Gouveia Dal Pino, E. M., Noriega-Crespo, A., Mininni, P. D., & Velázquez, P. F. 2002, *A&A*, 392, 267

Ramsay, S. K., Chrysostomou, A., Geballe, T. R., Brand, P. W. J. L., & Mountain, M. 1993, *MNRAS*, 263, 695

Rantakyrö, F. T., Rubio, M., Johansson, L. E. B., Chini, R., & Merkel-Ferreira, E. 2005, in Astronomical Society of the Pacific Conference Series, Vol. 344, The Cool Universe: Observing Cosmic Dawn, ed. C. Lidman & D. Alloin, 215–+

Ravkilde, T. L., Kristensen, L. E. Cabrit, S., Pineau des Forêts, G., Lemaire, J. L., & Field, D. 2007, in preparation

Ray, T., Dougados, C., Bacciotti, F., Eislöffel, J., & Chrysostomou, A. 2007, Protostars and Planets V, 231

Reid, M. J., Menten, K. M., Greenhill, L. J., & Chandler, C. J. 2007, *ApJ*, 664, 950

Reipurth, B., Nyman, L.-A., & Chini, R. 1996, *A&A*, 314, 258

Richer, J. S., Shepherd, D. S., Cabrit, S., Bachiller, R., & Churchwell, E. 2000, Protostars and Planets IV, 867

Rigaut, F., Salmon, D., Arsenault, R., et al. 1998, *PASP*, 110, 152

Rodríguez, L. F., Poveda, A., Lizano, S., & Allen, C. 2005, *ApJ*, 627, L65

Röllig, M., Abel, N. P., Bell, T., et al. 2007, *A&A*, 467, 187

Rosenthal, D., Bertoldi, F., & Drapatz, S. 2000, *A&A*, 356, 705

Rousset, G., Lacombe, F., Puget, P., et al. 2003, in Presented at the Society of Photo-Optical Instrumentation Engineers (SPIE) Conference, Vol. 4839, Adaptive Optical System Technologies II. Edited by Wizinowich, Peter L.; Bonaccini, Domenico. Proceedings of the SPIE, Volume 4839, pp. 140-149 (2003)., ed. P. L. Wizinowich & D. Bonaccini, 140–149

Sandstrom, K. M., Peek, J. E. G., Bower, G. C., Bolatto, A. D., & Plambeck, R. L. 2007, ArXiv e-prints, 706

Santos, N. C., Yun, J. L., Santos, C. A., & Marreiros, R. G. 1998, *AJ*, 116, 1376

Savage, B. D. & Sembach, K. R. 1996, *ARA&A*, 34, 279

Scalo, J. M. 1986, Fundamentals of Cosmic Physics, 11, 1

Schild, H., Miller, S., & Tennyson, J. 1997, *A&A*, 318, 608

Schleuning, D. A. 1998, *ApJ*, 493, 811

Schofield, K. 1967, *Planet. Space Sci.*, 15, 643

Schultz, A. S. B., Colgan, S. W. J., Erickson, E. F., et al. 1999, *ApJ*, 511, 282

Sharpless, S. 1959, *ApJS*, 4, 257

Shuping, R. Y., Morris, M., & Bally, J. 2004, *AJ*, 128, 363

Simpson, J. P., Colgan, S. W. J., Erickson, E. F., Burton, M. G., & Schultz, A. S. B. 2006, *ApJ*, 642, 339

Skrutskie, M. F., Cutri, R. M., Stiening, R., et al. 2006, *AJ*, 131, 1163

Smith, M. D. & Brand, P. W. J. L. 1990, *MNRAS*, 242, 495

Smith, M. D., Brand, P. W. J. L., & Moorhouse, A. 1991a, *MNRAS*, 248, 451

Smith, M. D., Brand, P. W. J. L., & Moorhouse, A. 1991b, *MNRAS*, 248, 730

Smith, M. D., Davis, C. J., & Lioure, A. 1997, *A&A*, 327, 1206

Smith, M. D., Khanzadyan, T., & Davis, C. J. 2003, *MNRAS*, 339, 524

Sofia, U. J. & Meyer, D. M. 2001, *ApJ*, 554, L221

Störzer, H. & Hollenbach, D. 1999, *ApJ*, 515, 669

Sternberg, A. & Dalgarno, A. 1989, *ApJ*, 338, 197

Sternberg, A. & Neufeld, D. A. 1999, *ApJ*, 516, 371

Stolovy, S. R., Burton, M. G., Erickson, E. F., et al. 1998, *ApJ*, 492, L151

Stone, J. M., Xu, J., & Mundy, L. G. 1995, *Nature*, 377, 315

Storm, J., Carney, B. W., Gieren, W. P., et al. 2004, *A&A*, 415, 531

Strand, K. A. 1958, *ApJ*, 128, 14

Sweitzer, J. S. 1978, *ApJ*, 225, 116

Takami, M., Usuda, T., Sugai, H., et al. 2002, *ApJ*, 566, 910

Tamura, M., Kandori, R., Kusakabe, N., et al. 2006, *ApJ*, 649, L29

Tan, J. C. 2004, *ApJ*, 607, L47

Testor, G., Lemaire, J. L., Field, D., & Callejo, G. 2005, *A&A*, 434, 497

Testor, G., Lemaire, J. L., Kristensen, L. E., Field, D., & Diana, S. 2007, *A&A*, 469, 459

Tielens, A. G. G. M. 2005, The Physics and Chemistry of the Interstellar Medium (The Physics and Chemistry of the Interstellar Medium, by A. G. G. M. Tielens, pp. . ISBN 0521826349. Cambridge, UK: Cambridge University Press, 2005.)

Timmermann, R. 1998, *ApJ*, 498, 246

Tiné, S., Williams, D. A., Clary, D. C., et al. 2003, *Ap&SS*, 288, 377

Troland, T. H., Crutcher, R. M., & Kazes, I. 1986, *ApJ*, 304, L57

van Dishoeck, E. F., Wright, C. M., Cernicharo, J., et al. 1998, *ApJ*, 502, L173+

Vannier, L., Lemaire, J. L., Field, D., et al. 2001, *A&A*, 366, 651

Voshchinnikov, N. V., Il'in, V. B., Henning, T., & Dubkova, D. N. 2006, *A&A*, 445, 167

Ward-Thompson, D., André, P., Crutcher, R., et al. 2007, Protostars and Planets V, 33

Wen, Z. & O'Dell, C. R. 1995, *ApJ*, 438, 784

Wilgenbus, D., Cabrit, S., Pineau des Forêts, G., & Flower, D. R. 2000, *A&A*, 356, 1010

Wolniewicz, L., Simbotin, I., & Dalgarno, A. 1998, *ApJS*, 115, 293

Wrathmall, S. A., Gusdorf, A., & Flower, D. R. 2007, submitted to *MNRAS*

Yun, J. L., Moreira, M. C., Afonso, J. M., & Clemens, D. P. 1999, *AJ*, 118, 990

Zuckerman, B., Kuiper, T. B. H., & Rodriguez Kuiper, E. N. 1976, *ApJ*, 209, L137